Plasma Physics Reports, Vol. 31, No. 5, 2005, pp. 347–368. Translated from Fizika Plazmy, Vol. 31, No. 5, 2005, pp. 387–408.

TOKAMAKS

An Analytic Approach to Developing Transport Threshold Models of Neoclassical Tearing Modes in Tokamaks

A. B. Mikhailovskii[1, 2], M. S. Shirokov[1, 3], S. V. Konovalov[1, 4], and V. S. Tsypin[5]

[1]*Russian Research Centre Kurchatov Institute, pl. Kurchatova 1, Moscow, 123182 Russia*
[2]*Moscow Institute of Physics and Technology, Institutskiĭ pr. 9, Dolgoprudnyĭ, Moscow oblast, 141700 Russia*
[3]*Moscow Engineering Physics Institute, Kashirskoe sh. 31, Moscow, 115409 Russia*
[4]*Naka Fusion Research Establishment, Japan Atomic Energy Research Institute, Ibaraki 3111-0193, Japan*
[5]*Institute of Physics, University of São Paulo, Rua do Matão, Travessa R, 187, 05508–900, São Paulo, Brazil*

Received February 25, 2004

Abstract—Transport threshold models of neoclassical tearing modes in tokamaks are investigated analytically. An analysis is made of the competition between strong transverse heat transport, on the one hand, and longitudinal heat transport, longitudinal heat convection, longitudinal inertial transport, and rotational transport, on the other hand, which leads to the establishment of the perturbed temperature profile in magnetic islands. It is shown that, in all these cases, the temperature profile can be found analytically by using rigorous solutions to the heat conduction equation in the near and far regions of a chain of magnetic islands and then by matching these solutions. Analytic expressions for the temperature profile are used to calculate the contribution of the bootstrap current to the generalized Rutherford equation for the island width evolution with the aim of constructing particular transport threshold models of neoclassical tearing modes. Four transport threshold models, differing in the underlying competing mechanisms, are analyzed: collisional, convective, inertial, and rotational models. The collisional model constructed analytically is shown to coincide exactly with that calculated numerically; the reason is that the analytical temperature profile turns out to be the same as the numerical profile. The results obtained can be useful in developing the next generation of general threshold models. The first steps toward such models have already been made. © *2005 Pleiades Publishing, Inc.*

1. INTRODUCTION AND GENERAL OVERVIEW OF THE PROBLEM

Transport threshold models of neoclassical tearing modes (NTMs) [1–11] are an important object of modern investigations of the MHD phenomena that restrict the plasma pressure in tokamaks. These investigations include an analysis of the effect of anomalous transverse plasma transport on the excitation of NTMs by the bootstrap current (the so-called bootstrap drive). The transport of the even moments of the particle velocity distribution functions (i.e., the plasma density and the electron and ion temperatures) and the transport of the odd moments (such as the longitudinal plasma momentum) both can be anomalous. In the first case, we are dealing with anomalous transverse diffusion and anomalous transverse heat conduction by electrons and ions, and, in the second case, with anomalous transverse plasma viscosity. Accordingly, investigations of transport threshold models of NTMs go in two directions. The first is centered on the weakening of the bootstrap drive (compared to that predicted for relatively low transport [12, 13]) at a sufficiently rapid transverse diffusion or sufficiently high heat conduction [1–7, 10, 11]. The second is concerned with a modification of the bootstrap drive at a sufficiently high transverse plasma viscosity [8, 9].

The present study follows mainly the first of the above two trends. We investigate a number of effects that compete with transverse heat transport, leading to the establishment of one or another profile of the perturbed temperatures of the electrons and ions, and determine the bootstrap drive corresponding to these profiles. In the above formulation of the problem, the weakening of the bootstrap drive at a high transverse transport can be regarded as a consequence of the fact that such a transport rules out the possibility of the formation of flattened temperature profiles within the separatrix of a magnetic island that correspond to the maximal level of the bootstrap drive. Flattened profiles do not form when the magnetic island width W is less than a certain critical width W_c, which is determined by the competition mentioned above, i.e., by the estimation condition $W < W_c$.

In the original paper on the subject [1], the bootstrap drive was assumed to be governed by the electron plasma component. This assumption is reasonable for a plasma in which the electron temperature is much higher than the ion temperature (i.e., for a plasma with hot electrons). Fitzpatrick [1] considered the competition between the transverse and the longitudinal heat conduction by electrons in terms of the Braginskii collisional hydrodynamics [14]. The transport threshold model of NTMs that takes into account only this com-

peting process (mechanism) can be called the Fitzpatrick model, or the standard electron transport model, or, for simplicity, the collisional model. This model yields the following functional dependence for the critical island width W_{c,T_e}:

$$W_{c,T_e} \sim (\chi_{\perp e}/\chi_{\parallel e})^{1/4}, \quad (1.1)$$

where $\chi_{\perp e}$ and $\chi_{\parallel e}$ are the transverse and longitudinal electron thermal conductivities and the subscript T_e is added to W_c to emphasize that a study is made of the processes that govern the perturbed electron temperature.

Fitzpatrick [1] also pointed out that the assumption about the collisional nature of the longitudinal heat conduction fails to hold when the electron temperature is not too low because, in this case, the mean free path of the electrons exceeds the shear length L_s: $v_{Te}/L_s\nu_e > 1$, where v_{Te} is the electron thermal velocity and ν_e is the electron collision frequency. According to [1], the transverse electron heat conduction in such circumstances should compete with the so-called longitudinal collisionless electron convection rather than with the longitudinal heat conduction. The idea set forth in [1] was then taken up by the investigators who carried out experiments on the COMPASS-D tokamak [3] (see also [15]). The result was a transport threshold model of NTMs that can be called the Fitzpatrick–Gates model, or the electron convective transport model, or, for simplicity, the convective model. In this model, the critical island width W_c is given by a functional dependence of the form

$$W_{c,T_e} \sim \chi_{\perp e}^{1/3}. \quad (1.2)$$

The original views about the longitudinal collisionless convection effect were merely intuitive [1, 3, 15]. A kinetic description of this effect was developed in our study [7]. In a more recent paper [10], it was explained that, in order to give a hydrodynamic description of the longitudinal collisionless convection, it is necessary to take into account the longitudinal collisionless heat flux (see Section 2 for details). To do so, the plasma should be described not by the Braginskii hydrodynamics [14] but by a more general approach such as, for example, the Grad hydrodynamics (for a discussion of this issue, see [10]).

The Fitzpatrick and Fitzpatrick–Gates models can be referred to as single-channel models in the sense that it is only the electron temperature gradient that is assumed to contribute to the bootstrap drive. A more general formulation of the problem requires the use of three-channel models in which the bootstrap drive is assumed to be governed not only by the electron and ion temperature gradients but also by the plasma density gradient. The first step in this direction was taken by Gorelenkov *et al.* [2]. In this context, it is also important to mention a paper by Sauter *et al.* [4], who showed that the quantity Δ_{bs}, which characterizes the bootstrap drive, should have the following structure:

$$\Delta_{bs} = \sum_{A = n_e, T_e, T_i} \Delta_{bs,A}. \quad (1.3)$$

Here, A indicates the Ath channel and

$$\Delta_{bs,A} \sim a_{bs,A}\frac{W}{W^2 + W_{d,A}^2}, \quad (1.4)$$

where $a_{bs,A}$ are certain numerical coefficients and $W_{d,A}$ are certain effective critical island widths, which coincide with the critical widths $W_{c,A}$ to within numerical factors (see expressions (1.1), (1.2)). In formula (1.3), the summation over A indicates that the bootstrap drive can be governed by the following three types of anomalous transport: anomalous transverse diffusion ($A = n_e$), anomalous transverse heat conduction by the electrons ($A = T_e$), and that by the ions ($A = T_i$).

Turning again to the Fitzpatrick and Fitzpatrick–Gates models, we can say that these are single-mechanism models in the sense that they account for only one of the competing processes (mechanisms) whereby the perturbed temperature profile is established. This is why, generally speaking, they should be treated as particular cases (fragments) of more complicated single-channel models.

Later, the Fitzpatrick model [1] began to be incorporated into more general (i.e., generalized) models [4, 16] in which the effects of the polarization current [17–19] and of the magnetic well (the Glasser–Greene–Johnson effect) [20] were accounted for as a channel characterizing the entire plasma, i.e., as a certain general plasma channel.

The Fitzpatrick model [1] described above was used both to interpret experimental data and for prediction purposes in many papers (see, e.g., [16, 21–24]). This model served as a starting point for constructing more complex threshold models, which take into account the influence of the transverse transport on the magnetic well effect [25, 26] as well as the effective increase in the transverse heat conductivity due to external helical fields [6].

It is obvious that the general application of the Fitzpatrick model in plasma theory could be regarded, to some extent, as justified if the role of the general plasma channel were played by the electron heat conduction. In many studies, including those oriented toward applications of the theory to ASDEX-U [23] and DIII-D [24] experiments, it was assumed, however, that the ion temperature is as important as the electron temperature. This is why, in those two papers, it was actually assumed that two-channel processes can be described in terms of single-channel processes by using

the following expression for Δ_{bs} (cf. expressions (1.3), (1.4)):

$$\Delta_{bs} \sim a_{bs}\frac{W}{W^2 + W_d^2}. \quad (1.5)$$

In other words, it was in fact assumed that, instead of expressions of the form (cf. expression (1.1))

$$W_{c,A} \sim (\chi_{\perp,A}/\chi_{\|,A})^{1/4}, \quad (1.6)$$

where $A = (e, i)$, it is possible to use expressions such as

$$W_c \sim (\chi_\perp/\chi_\|)^{1/4}, \quad (1.7)$$

where $\chi_\perp$ and $\chi_\|$ are the transverse and longitudinal plasma thermal conductivities introduced by the relationships $\chi_\perp = \max(\chi_{\perp e}, \chi_{\perp i})$ and $\chi_\| = \max(\chi_{\|e}, \chi_{\|i})$. As a rule, however, we have $\max(\chi_{\perp e}, \chi_{\perp i}) = \chi_{\perp i}$ and $\max(\chi_{\|e}, \chi_{\|i}) = \chi_{\|e}$. Consequently, formula (1.7) means actually that

$$W_c \sim (\chi_{\perp i}/\chi_{\|e})^{1/4}. \quad (1.8)$$

Formula (1.8) can be considered valid provided that the electron–ion heat exchange is sufficiently intensive. In this case, it is possible to describe the plasma in the one-temperature (common-temperature) approximation and to obtain a unified heat conduction equation by adding the electron and ion heat conduction equations. Under experimental conditions, the electron–ion heat exchange is slow, however. This is why the existing general plasma models cannot be considered quite adequate.

The above three-channel models, in which the quantity Δ_{bs} is given by the expressions like formulas (1.3) or (1.4), are not among the most general transport threshold models. The reason is that the basic expression for the perturbed bootstrap current is, on the one hand, determined by the longitudinal electron viscosity (see [9] for details) but, on the other hand, it is reduced to the sum of the contributions from the electron and ion temperature gradients and plasma density gradient only when the transverse ion viscosity is ignored. For a finite (nonzero) transverse ion viscosity, an additional family of more general transport models comes to light, which can be called four-channel models (see below for details) and which were discussed in our earlier papers [8, 9]. In this case, the role of the fourth channel is played by the so-called *E*-channel, which characterizes the contribution of the perturbed electric field of the island to the bootstrap drive.

In [1–3], the islands were considered to be nonrotating, $\omega = 0$, where ω is the island rotation frequency. The investigation of transport threshold models of rotating NTMs ($\omega \neq 0$) was begun in our paper [7], in which we identified transverse transport with the transverse heat conduction. In that paper, we did not address the question of whether the heat conduction is electronic or whether it is ionic, but when we analyzed the physical consequences following from the model developed there, we pointed out that the heat conduction is ionic. We assumed that the process competing with transverse transport is "rotational" heat transport, described by the term with the time derivative in the heat conduction equation. The corresponding model was called the rotational transport threshold model. In this model, the functional dependence of W_c has the form

$$W_c \sim (\chi_\perp/\omega)^{1/2}. \quad (1.9)$$

It was then explained [11] that the model developed in [7] refers to the so-called supersonic NTMs, i.e., to the modes that rotate at frequencies ω higher than the characteristic frequency $\omega_s = c_s k_{\|\mathrm{eff}}$ of acoustic waves, $\omega > \omega_s$, where c_s is the speed of sound and $k_{\|\mathrm{eff}}$ is the characteristic (effective) wavenumber. Accordingly, it was suggested in [11] to call the rotational transport model of [7] the supersonic transport threshold model. In what follows, we will also call it the rotational model, for simplicity. At lower island rotation frequencies, $\omega < \omega_s$, the dominant effect that competes with transverse transport is heat transport described by the term with the longitudinal gradient of the longitudinal plasma velocity $V_\|$ in the heat conduction equation. This gave rise to an additional type of transport threshold models of NTMs; in [11], these were called subsonic transport threshold models. In turn, the equation of longitudinal plasma motion implies that the longitudinal plasma velocity $V_\|$ is determined by the balance between the longitudinal plasma inertia and longitudinal plasma pressure gradient. Therefore, for $\omega < \omega_s$, the problem about the weakening of the bootstrap current should be treated with allowance for the longitudinal plasma inertia (see Section 2 for details). This is why the subsonic model can be called the inertial threshold model. For simplicity, we will also call it the inertial model. According to [11], this model gives the following functional dependence:

$$W_c \sim (\omega\chi_\perp)^{1/4}. \quad (1.10)$$

The calculation procedure carried out in terms of each of the above transport threshold models is as follows. First, the plasma temperature perturbed by the electromagnetic field of a magnetic island is determined from one or another version of the heat conduction equation. Second, some relationships or other that relate the bootstrap current to the temperature gradient are used to calculate the perturbed bootstrap current (see below for details). Third, the bootstrap drive is calculated by integrating the perturbed bootstrap current over space. Hence, the second and third steps of the calculation procedure are the same in all the models. In this sense, the models differ only in the expressions for the perturbed temperature of the electrons or ions.

Generally speaking, the heat conduction equations can be solved numerically or analytically. The latter is possible only when they are "solvable." One of the

main objectives of our study is to investigate the problem of the solvability of the equations. One of the main results of these investigations is that, in all four models under analysis, the corresponding heat conduction equations turn out to be solvable. (For the rotational model, this was shown earlier in [7].) Based on this remarkable fact, we find analytic solutions for each of the four models, thereby making the first step of the above calculation procedure.

Let us explain in more detail what is meant here by solvability. We carry out the calculations under the simplifying assumption $W_c \gg W$. In our problem, we deal with two physically different spatial regions, namely, the near and far regions, which are characterized by spatial scales on the order of W_c and W, respectively. The above effects compete in the far region, which is thus more difficult to describe mathematically. Solvability implies that, in this region, all versions of the heat conduction equation that will be considered below have rigorous analytic solutions. As for the near region, the heat conduction equations in it are fairly simple and can be solved by standard methods. The complete solution to one heat conduction equation or another is obtained by matching the solutions for the far and near regions.

Originally, the heat conduction equation in the collisional model was solved numerically by Fitzpatrick [1]. In [7], we found a model (approximate) analytic solution to this equation. The model analytic solutions to the heat conduction equation were also derived in terms of the convective model (in [7, 10]) and the inertial model (in [11]). Hence, using the results that will be obtained below, we can compare the model and rigorous expressions for the perturbed temperature as well as the relevant expressions for the bootstrap drive that correspond to the above transport models. Such a comparison is one of the objectives of our study. It turns out that the rigorous and model results differ only quantitatively but not qualitatively. Consequently, in applying transport threshold models to interpret the experimental data, to predict the behavior of NTMs in the next generation of tokamaks, or to test numerical codes, it is necessary to use rigorous relationships. On the other hand, for a theoretical analysis of the various aspects of the physics of magnetic islands, it is preferable to utilize the simpler (model) relationships.

In our analysis, anomalous diffusion is ignored. We calculate the island width W_d in each of the above four models without identifying it with W_{d,T_e} or with W_{d,T_i}, i.e., without addressing the question of whether the bootstrap drive mechanism (channel) is electronic or ionic. The corresponding identification is made in the next step of our calculations (i.e., in finding the bootstrap current).

Considering the results of [11], it is clear that the subsonic model should bear on the ion channel. This is largely true for the rotational model, although it may well refer to the electron channel. As for the convective model, it should bear primarily on the electron channel. The question of whether this model should involve the ion channel has not yet been considered.

The question of which of the above channels should play the dominant role in the collisional model still remains unclear. Recall that, in Fitzpatrick's original analysis [1], this model was assumed to include the electron channel. In this case, however, in accordance with what was said above, the collisional model is unable to compete in reliability with the convective model [1, 3]. This was taken into account in interpreting experimental data on the NTMs in a plasma with hot electrons [3, 15, 27, 28]. In [11], the question was discussed of whether the collisional model can be applied to describe the ion mechanism for bootstrap drive at $\omega \neq 0$. As was mentioned in that paper, in this case, it is important to evaluate the relative importance of the collisional and inertial models. According to [11], the inertial model is more realistic than the collisional one provided that the inertial transport predominates over the transport due to longitudinal heat conduction. The corresponding condition has the form

$$\chi_{\|i} < c_s^2/\omega. \tag{1.11}$$

On the other hand, according to [11], the following estimate is valid for finite ω values:

$$\chi_{\|i} \simeq \frac{c_s^2}{\nu_{i\,\mathrm{eff}} + |\omega|}, \tag{1.12}$$

where $\nu_{i\,\mathrm{eff}}$ is the effective ion collision frequency. Estimate (1.12) implies that, in collisional hydrodynamics ($\nu_{i\,\mathrm{eff}} > |\omega|$), condition (1.11) is satisfied. This indicates that the collisional model fails to describe the ion channel for bootstrap drive.

Hence, the collisional model is inapplicable to the ion mechanism for bootstrap drive of the NTMs and is unlikely to be applicable to the electron channel (mechanism). Nevertheless, it is important to analyze this model for at least the following two reasons. First, of all the models in question, this is the only model that has been analyzed numerically and thus the only one against which the analytical results can be tested, so it can be used, to a certain extent, as a reference model. Second, most of the present-day studies on transport models deal precisely with this model. Consequently, it seems inexpedient to ignore the collisional model at the present stage of research on the subject.

In [11], the conditions to which the inertial and rotational models are applicable were also determined, taking into account that the minimal width of a magnetic island, $W_{\min}$, is on the order of the width $\rho_b \simeq \rho q/\epsilon^{1/2}$ of an ion banana orbit, $W_{\min} \simeq \rho_b$ (where ρ is the ion gyroradius, q is the safety factor, and ϵ is the inverse aspect ratio), as well as that the characteristic value of the island rotation frequency is the drift frequency ω_*. In

[11], it was shown that the subsonic model for describing the NTMs should be applicable under the condition

$$W/W_{\min} > \epsilon^{-1/2}, \tag{1.13}$$

and that the applicability condition for the supersonic model is

$$1 < W/W_{\min} < \epsilon^{-1/2}. \tag{1.14}$$

Hence, our main objective here is to derive expressions for the perturbed temperature profiles that are established as a result of the mechanisms outlined above, namely, collisional, convective, inertial, and rotational mechanisms. Having obtained these expressions, we find the corresponding expressions for the perturbed bootstrap current, calculate the bootstrap drive, and finally construct the relevant transport threshold models of the NTMs.

Recall that, knowing the perturbed temperature profile, we should determine the corresponding bootstrap current, average it over the separatrix surface of the magnetic island, and then calculate the bootstrap drive due to this current. In [1], in which only the perturbed electron temperature $\hat{T}_e$ was calculated, it was assumed that the perturbed bootstrap current $\hat{J}_{bs}$ can be found from the relationship

$$\hat{J}_{bs} = -\frac{1.46\epsilon^{1/2} c n_0}{B_\theta}\frac{\partial \hat{T}_e}{\partial x}. \tag{1.15}$$

It is well known that the functional relationships of form (1.15) relating the bootstrap current to the temperature gradient are valid in the problems in which the equilibrium magnetic field geometry is characterized by the only variable, namely, the radial coordinate x; in this case, we have $\hat{J}_{bs} = \hat{J}_{bs}(x)$ and $\hat{T} = \hat{T}(x)$. We are, however, interested in the magnetic island geometry, which involves two variables: the magnetic flux function of the magnetic island, ψ, and the cyclic variable of the island, ξ. A methodologically important question thus arises of whether quasi-one-dimensional formulas like (1.15) can be used in the theory of magnetic islands. This question, too, is to be discussed below. We will show that such quasi-one-dimensional formulas also apply to two-dimensional problems about magnetic islands.

Formula (1.15) raises the question of whether its right-hand side should actually contain the numerical coefficient 1.46. The reason is that the product of this coefficient times $\epsilon^{1/2}$ is the fraction of trapped particles. Following [29], Fitzpatrick [1] described the bootstrap current by the expression containing the same coefficient. He thereby assumed that the fraction of trapped particles is the only numerical factor that characterizes the bootstrap current expressed in terms of the temperature gradient. However, in [30], in accordance with a general analysis carried out in [31], it was pointed out that the bootstrap current should be described by the expression that also contains additional factors determined by a complicated dependence of the Coulomb collision frequencies on the particle velocities. In this case, the portion of the bootstrap current that is related to the electron temperature gradient, $\hat{J}^e_{bs}$, is described not by expression (1.15) but by the relationship

$$\hat{J}^e_{bs} = -0.40 \times 2.46\frac{\epsilon^{1/2} c n_0}{B_\theta}\frac{\partial \hat{T}_e}{\partial x}. \tag{1.16}$$

Analogously, the ion portion of the perturbed bootstrap current, $\hat{J}^i_{bs}$, which is initiated by the perturbed ion temperature $\hat{T}_i$, is equal to

$$\hat{J}^i_{bs} = 0.17 \times 2.46\frac{\epsilon^{1/2} c n_0}{B_\theta}\frac{\partial \hat{T}_i}{\partial x}. \tag{1.17}$$

With allowance for the plasma density perturbation $\hat{n}$, the total perturbed bootstrap current $\hat{J}_{bs}$ is given by the relationship (cf. [30])

$$\hat{J}_{bs} = -2.46\frac{\epsilon^{1/2} c}{B_\theta} \times \left[(T_{0e} + T_{0i})\frac{\partial \hat{n}}{\partial x} + 0.40 n_0 \frac{\partial \hat{T}_e}{\partial x} - 0.17 n_0 \frac{\partial \hat{T}_i}{\partial x}\right]. \tag{1.18}$$

The factors 0.40 and –0.17 in relationships (1.16)–(1.18) can be called the partial factors associated with the electron and ion temperatures, respectively, or simply the electron and ion partial factors.

It is important to stress that the ion partial factor is small and negative. This indicates that, in contrast to the electron temperature gradient, which leads to the bootstrap drive of NTMs, the ion temperature gradient stabilizes the NTMs to a certain extent. When the ion temperature does not exceed the electron temperature, such stabilization is insignificant, but it can be substantial if the ion temperature is much higher than the electron temperature.

Note also that, in [8, 10, 11], the following one-fluid formula was used instead of formulas (1.16)–(1.18):

$$\hat{J}_{bs} = -\frac{\epsilon^{1/2} c n_0}{B_\theta}\frac{\partial \hat{T}}{\partial x}, \tag{1.19}$$

where by $\hat{T}$ was meant the perturbed plasma temperature. In this respect, the analysis carried out below refines the results of those three papers both quantitatively (including the values of the corresponding partial factors) and qualitatively (in particular, this concerns the stabilizing role of the ion temperature gradient).

Above, we were dealing with the effects caused by the anomalous transverse heat transport. According to [8, 9], however, the bootstrap drive is also substantially affected by the anomalous transverse ion viscosity. In order to give insight into the mechanism by

which the transverse ion viscosity influences the bootstrap current, note in advance that, according to [9], formula (1.18) can be regarded as a consequence of a certain, more general, expression for $\hat{J}_{bs}$, specifically,

$$\hat{J}_{bs} = -2.46\frac{\epsilon^{1/2}c}{B_\theta} \times\left[T_{0e}\frac{\partial\hat{n}}{\partial x} + 0.40n_0\frac{\partial\hat{T}_e}{\partial x} + en_0\left(\hat{E}_x - \frac{B_\theta}{c}\hat{U}_{\|i}\right)\right], \quad (1.20)$$

where $\hat{U}_{\|i}$ is the perturbed longitudinal ion velocity and $\hat{E}_x$ is the radial component of the perturbed electric field. The expression for $\hat{U}_{\|i}$ is found from the equation of longitudinal ion motion, which, however, contains the transverse viscosity coefficient. When this viscosity is ignored, the expression in question has the form

$$\hat{U}_{\|i} = \hat{U}_{\|i}^{(0)} \equiv \frac{c}{B_\theta}\left(\hat{E}_x - \frac{T_{0i}}{en_0}\frac{\partial\hat{n}}{\partial x} + \frac{0.17}{e}\frac{\partial\hat{T}_i}{\partial x}\right). \quad (1.21)$$

Substituting expression (1.21) into expression (1.20) yields relationship (1.18). On the other hand, when the transverse ion viscosity is taken into account, we have $\hat{U}_{\|i} \neq \hat{U}_{\|i}^{(0)}$; as a result, relationship (1.18) fails to hold in this case. The expression for the bootstrap current that accounts for both the anomalous transverse heat transport and anomalous transverse ion viscosity will be considered below.

Our paper is organized as follows. In Section 2, we present the general formulas that characterize the geometry of the magnetic islands and that are required for further analysis. We also write out the plasmodynamic equations that are used to derive the basic equations for the perturbed temperature. In Section 3, we convert these basic equations to a form convenient for their analysis. In Section 4, we find rigorous solutions to these equations in the far region. In Section 5, we solve these equations in the near region. Using the procedure for matching the rigorous solutions obtained for the far and near regions, we then determine the integration constants and thereby accomplish the procedure for finding complete rigorous solutions. In the Appendix, we present the known model solutions and discuss the degree to which they are rigorous.

In Section 6, the analytic expressions for the perturbed temperature profiles that were obtained in Sections 4 and 5 are used to calculate the bootstrap drive at a strong transverse heat transport and to construct expressions extrapolating the bootstrap drive to arbitrary values of the ratio between the island width W and critical length W_c. In Section 7, some versions of the transport threshold model for NTMs are developed based on the results derived in Section 6. Section 8 is aimed at explaining how the bootstrap drive is modified by the anomalous transverse ion viscosity. In Section 9, we discuss the results obtained and make final remarks.

2. PRELIMINARY FORMULAS

2.1. Relationships Characterizing the Magnetic Island Geometry

We consider a chain of magnetic islands localized in the vicinity of a certain rational (singular) magnetic surface of radius $r = r_s$ (where r is the radial coordinate). We describe the magnetic islands in terms of their magnetic flux function ψ (see also Section 1) defined by the relationship

$$\psi = \tilde{\psi}\cos\xi - x^2B_0/(2L_s). \quad (2.1)$$

Here, $x = r - r_s$ is the radial deviation from the rational magnetic surface, $\mathbf{B}_0$ is the equilibrium magnetic field, and the perturbation amplitude $\tilde{\psi}$ associated with the island width W is introduced by the relationship (see Section 1)

$$\tilde{\psi} = W^2B_0/(16L_s). \quad (2.2)$$

The function ξ is the above cyclic variable of the island. It is defined as

$$\xi = m\theta - n\zeta - \omega t, \quad (2.3)$$

where m and n are the poloidal and toroidal wavenumbers, θ and ζ are the poloidal and toroidal angles, and the island rotation frequency ω was introduced in Section 1.

Along with the magnetic flux function ψ, we introduce the dimensionless flux function Ω of a magnetic island:

$$\Omega = -\psi/\tilde{\psi}. \quad (2.4)$$

The range $1 < \Omega < \infty$ corresponds to the region outside the separatrix surface of the island, and the range $-1 < \Omega < 1$ corresponds to the region inside the separatrix.

In terms of Ω, relationship (2.1) reads

$$\Omega = 8x^2/W^2 - \cos\xi. \quad (2.5)$$

In terms of the functions Ω and ξ, the radial deviation x has the form

$$x = \sigma_x 2^{-3/2}W(\Omega + \cos\xi)^{1/2}, \quad (2.6)$$

where $\sigma_x = \operatorname{sgn} x = \pm 1$. We also use the longitudinal gradient operator $\nabla_\| \equiv (\mathbf{b}\cdot\nabla)$ and the squared transverse gradient operator $\nabla_\perp^2$, where $\nabla_\perp = \nabla - \mathbf{b}\nabla_\|$, with $\mathbf{b} = \mathbf{B}/B$ being a unit vector pointing along the total magnetic field $\mathbf{B}$. In terms of (Ω, ξ), we have

$$\nabla_\| = k_\|(\partial/\partial\xi)_\Omega, \quad (2.7)$$

$$\nabla_\perp^2(\ldots) = \frac{32}{W^2}(\Omega + \cos\xi)^{1/2}\frac{\partial}{\partial\Omega}\left[(\Omega + \cos\xi)^{1/2}\frac{\partial}{\partial\Omega}(\ldots)\right]. \quad (2.8)$$

Here, the longitudinal wavenumber $k_\parallel$ (i.e., the longitudinal component of the wave vector) is defined by the relationship

$$k_\parallel = -\frac{xk_y}{L_s} \equiv -\frac{\sigma_x W k_y}{2^{3/2} L_s}(\Omega + \cos\xi)^{1/2}, \quad (2.9)$$

where $k_y = m/r_s$ is the poloidal component of the wave vector.

2.2. Basic Time-Dependent Plasma Equations

2.2.1. Collisional mechanism. In collisional hydrodynamics [1], the plasma temperature T is assumed to satisfy the heat conduction equation of the form [14]

$$\nabla \cdot \mathbf{q} = 0. \quad (2.10)$$

Here, $\mathbf{q}$ is the heat flux defined by the relationship

$$\mathbf{q} = -n_0(\chi_\parallel \mathbf{b}\nabla_\parallel + \chi_\perp \nabla_\perp)T, \quad (2.11)$$

where n_0 is the plasma density and the longitudinal and transverse thermal conductivities, $\chi_\parallel$ and $\chi_\perp$, were introduced in Section 1. The quantities n_0, $\chi_\parallel$, and $\chi_\perp$ are assumed to be coordinate-independent.

The total temperature is represented as

$$T = T^{(0)} + \hat{T}, \quad (2.12)$$

Here, $\hat{T}$ is the perturbed temperature and

$$T^{(0)} = T_0(r_s) + xT_0', \quad (2.13)$$

where $T_0' \equiv (dT_0/dr)_{r=r_s}$, with $T_0(r)$ being the equilibrium temperature. With representation (2.12), Eq. (2.10) is transformed into

$$4\frac{\partial}{\partial\Omega}\left[(\Omega + \cos\xi)^{1/2}\frac{\partial\hat{T}}{\partial\Omega}\right] + \frac{1}{\Omega_{\mathrm{col}}^2}\left\{\frac{\partial}{\partial\xi}\left[(\Omega + \cos\xi)^{1/2}\frac{\partial\hat{T}}{\partial\xi}\right] - \frac{\sigma_x W T_0'}{2^{5/2}}\cos\xi\right\} = 0. \quad (2.14)$$

Here,

$$\Omega_{\mathrm{col}} = (W_{\mathrm{col}}/W)^2, \quad (2.15)$$

where W_{col} is a certain characteristic island width that is determined by the competition between the transverse and longitudinal transport and is given by the expression (cf. expression (1.1))

$$W_{\mathrm{col}} = 2^{3/2}\left(\frac{L_s^2\chi_\perp}{k_y^2\chi_\parallel}\right)^{1/4}. \quad (2.16)$$

The subscript "col" stands for "collisional," which means that we are working in collisional hydrodynamics. Note also that the width W_{col} so introduced coincides the width W_c used in [1].

2.2.2. Convective mechanism. In the case of convective mechanism [1, 3], we start with the hydrodynamic equations that were derived in [10] for particles of any of the species (i.e., for electrons or ions):

$$\nabla_\parallel q_\parallel - \frac{3}{2}\chi_\perp\frac{\partial^2 p}{\partial x^2} = 0, \quad (2.17)$$

$$\frac{5}{M}\nabla_\parallel(pT) - \chi_\perp\frac{\partial^2 q_\parallel}{\partial x^2} = 0. \quad (2.18)$$

Here, $q_\parallel$ is the longitudinal heat flux associated with this species of particles (for more detail, see [10]); $p = nT$, n and T are their pressure, density, and temperature, respectively; and M is the mass of a particle.

Instead of $q_\parallel$, we introduce the function X through the relationship $q_\parallel = 3c_s n_0 X$, where c_s is the generalized speed of sound of the corresponding particle species, $c_s = [5T_0/(3M)]^{1/2}$. Equations (2.17) and (2.18) are then reduced to the form

$$\frac{\partial}{\partial\Omega}\left[(\Omega + \cos\xi)^{1/2}\frac{\partial\hat{T}}{\partial\Omega}\right] + \frac{\sigma_x}{\Omega_{\mathrm{conv}}^{3/2}}\frac{\partial X}{\partial\xi} = 0, \quad (2.19)$$

$$\frac{\partial}{\partial\Omega}\left[(\Omega + \cos\xi)^{1/2}\frac{\partial X}{\partial\Omega}\right] + \frac{\sigma_x}{\Omega_{\mathrm{conv}}^{3/2}}\left[\frac{\partial\hat{T}}{\partial\xi} - \frac{\sigma_x T_0' W}{2^{5/2}}\frac{\sin\xi}{(\Omega + \cos\xi)^{1/2}}\right] = 0. \quad (2.20)$$

Here,

$$\Omega_{\mathrm{conv}} = (W_{\mathrm{conv}}/W)^2, \quad (2.21)$$

W_{conv} is a certain characteristic width determined by the competition between the transverse transport and the longitudinal convection and given by the expression (cf. expression (1.2))

$$W_{\mathrm{conv}} = \left(\frac{2^{11/2}\chi_\perp L_s}{c_s k_y}\right)^{1/3}. \quad (2.22)$$

2.2.3. Inertial mechanism. In the case of inertial mechanism, the plasma temperature is described not by Eq. (2.10) but by the heat conduction equation (see [11] for details)

$$\rho_0 c_{is}^2 \nabla_\parallel V_\parallel = -\frac{2}{3}\nabla \cdot \mathbf{q}_\perp. \quad (2.23)$$

Here, the function $\mathbf{q}_\perp$ is given by relationship (2.11) with $\chi_\parallel = 0$; $V_\parallel$ is the longitudinal plasma velocity introduced in Section 1; $\rho_0 = M_i n_0$ is the plasma mass density; M_i is the mass of an ion; and c_{is} is the ion acoustic speed, which is equal in order of magnitude to $c_{is} = (T_0/M_i)^{1/2}$.

Equation (2.23) should be supplemented with the equation of longitudinal plasma motion of the form

$$\rho_0 d_0 V_\parallel/dt = -n_0 \nabla_\parallel T. \quad (2.24)$$

Here, the operator d_0/dt is defined by the relationship $d_0/dt = \partial/\partial t + \mathbf{V}_E \cdot \nabla$, where $\mathbf{V}_E = c(\mathbf{E}_\perp \times \mathbf{B}_0)/B_0^2$ is drift velocity in crossed fields and $\mathbf{E}_\perp = -\nabla\phi$ is the transverse electric field, with ϕ being the electrostatic potential.

As in [7, 11], we use the zero longitudinal electric field approximation, $\mathbf{E} \cdot \mathbf{B} = 0$. In this approximation, the longitudinal Ohm's law yields

$$\phi = \frac{B_0\omega}{ck_y}[x - h(\psi)]. \quad (2.25)$$

Here, $h(\psi)$ is the electrostatic potential profile function, which is defined by the relationship

$$\frac{\partial h}{\partial \Omega} = \begin{cases} \pi\sigma_x w g(\Omega)/8, & \Omega \geq 1, \\ 0, & -1 < \Omega < 1, \end{cases} \quad (2.26)$$

where

$$g(\Omega) = \int_0^\kappa \frac{d\kappa}{\lambda_3(\kappa)}, \quad (2.27)$$

$$\lambda_3(\kappa) = \frac{1}{3}[2(2-\kappa^2)E(\kappa) - (1-\kappa^2)K(\kappa)]^{1/2}, \quad (2.28)$$

with $\kappa = [2/(\Omega + 1)]^{1/2}$, $K(\kappa)$ and $E(\kappa)$ being complete elliptic integrals of the first and second kinds, respectively.

Using the above formulas, we convert the equation of motion (2.24) to the form

$$\left(\frac{\partial V_\parallel}{\partial \xi}\right)_\Omega = -\frac{2\sigma_x}{\pi}\frac{k_y w}{L_s \omega g(\Omega) M_i}\left(\frac{\partial T}{\partial \xi}\right)_\Omega. \quad (2.29)$$

Combining Eqs. (2.23) and (2.29) leads to the following analogue of Eq. (2.14):

$$\frac{\partial}{\partial\Omega}\left[(\Omega + \cos\xi)^{1/2}\frac{\partial \hat{T}}{\partial \Omega}\right] - \frac{1}{\Omega_i^2 g(\Omega)}\frac{\partial \hat{T}}{\partial \xi} = -\frac{\sigma_x T_0' W}{2^{5/2}\Omega_i^2 g(\Omega)}\frac{\sin\xi}{(\Omega + \cos\xi)^{1/2}}. \quad (2.30)$$

Here,

$$\Omega_i = W_{\text{inert}}^2/W^2, \quad (2.31)$$

where W_{inert} is a certain characteristic island width that is determined by the competition between the transverse transport and the longitudinal plasma inertia and is given by the expression (cf. expression (1.10))

$$W_{\text{inert}} = \left(\frac{128\sqrt{2}\pi}{3}\frac{\omega L_s^2 \chi_\perp}{k_y^2 c_{is}^2}\right)^{1/4}. \quad (2.32)$$

This expression formally implies that $W_{\text{inert}} \longrightarrow \infty$ as $\omega \longrightarrow \infty$. For sufficiently high ω values, however, we must switch from expression (2.32) for W_{inert} to the expression W_{rot} for that will be introduced below.

2.2.4. Rotational mechanism. According to [7], in the case of supersonic (rotational) mechanism, the plasma temperature is described not by Eqs. (2.10) and (2.23) but by the heat conduction equation of the form

$$n_0\frac{d_0 T}{dt} = -\frac{2}{3}\nabla \cdot \mathbf{q}_\perp. \quad (2.33)$$

Accordingly, in place of Eqs. (2.14) and (2.30), we have (see [7] for details)

$$\frac{\partial}{\partial\Omega}\left[(\Omega + \cos\xi)^{1/2}\frac{\partial \hat{T}}{\partial \Omega}\right] + \frac{g(\Omega)}{\Omega_r}\frac{\partial \hat{T}}{\partial \xi} - \frac{\sigma_x T_0' W g(\Omega)\sin\xi}{2^{5/2}\Omega_r(\Omega + \cos\xi)^{1/2}} = 0. \quad (2.34)$$

Here,

$$\Omega_r = W_{\text{rot}}^2/W^2, \quad (2.35)$$

where W_{rot} is a certain characteristic island width that is determined by the competition between the transverse transport and the rotation of the island and is given by the expression (cf. expression (1.9))

$$W_{\text{rot}} = \left(\frac{128\sqrt{2}}{3\pi}\frac{\chi_\perp}{\omega}\right)^{1/2}. \quad (2.36)$$

This expression formally implies that $W_{\text{rot}} \longrightarrow \infty$ as $\omega \longrightarrow 0$. For sufficiently low ω values, however, we must switch from expression (2.36) for W_{rot} to expression (2.32) for W_{inert}.

3. TRANSFORMATION OF THE EQUATIONS FOR THE PERTURBED TEMPERATURE

3.1. Collisional Mechanism

Turning to Eq. (2.14), we assume that the width Ω_{col} is a large parameter, $\Omega_{\text{col}} \gg 1$. This assumption allows us to distinguish between two characteristic regions of the perturbation: the far region

$$1 \ll \Omega \simeq \Omega_{\text{col}}, \quad (3.1)$$

and the near region

$$|\Omega| \simeq 1. \quad (3.2)$$

In the far region, Eq. (2.14) is reduced to

$$\partial^2\hat{T}/\partial u^2 + \alpha_{col}^2 u^2 \partial^2\hat{T}/\partial\xi^2 = C_{col} u\cos\xi, \quad (3.3)$$

where $\alpha_{col} = 1/\Omega_{col}$, $C_{col} = \sigma_x W T_0'/(2^{5/2}\Omega_{col}^2)$, and

$$u = \Omega^{1/2}. \quad (3.4)$$

We set

$$\hat{T} = T_c(u)\cos\xi, \quad (3.5)$$

to cast Eq. (3.3) into the form

$$d^2T_c/du^2 - \alpha_{col}^2 u^2 T_c = C_{col} u. \quad (3.6)$$

For $u \gg \Omega_{col}^{1/2}$, this equation has the solution

$$T_c(u) = -\sigma_x W T_0'/(2^{5/2}u). \quad (3.7)$$

It is thus natural to characterize the temperature perturbation by introducing the dimensionless function $y(u)$ through the relationship

$$T_c(u) = -\sigma_x W T_0' y(u)/2^{5/2}, \quad (3.8)$$

with which to transform Eq. (3.6) to

$$d^2y/du^2 - \alpha_{col}^2 u^2 y = -\alpha_{col}^2 u. \quad (3.9)$$

In accordance with solution (3.7) and relationship (3.8), the function $y(u)$ for $u \gg \Omega_{col}^{1/2}$ has the form

$$y(u) = 1/u. \quad (3.10)$$

Equation (3.9) is the basic equation for calculating the perturbed temperature profile in the Fitzpatrick model [1].

3.2. Convective Mechanism

In this case, the far and near perturbation regions are also introduced by relationships (3.1) and (3.2). In the far region, Eqs. (2.19) and (2.20) are reduced to

$$\partial^2\hat{T}/\partial u^2 + \sigma_x\alpha_{conv}^{3/2} u\partial X/\partial\xi = 0, \quad (3.11)$$

$$\partial^2 X/\partial u^2 + \sigma_x\alpha_{conv}^{3/2} u\partial\hat{T}/\partial\xi = C_{conv}\sin\xi, \quad (3.12)$$

where $\alpha_{conv} = 2^{4/3}/\Omega_{conv}$ and $C_{conv} = T_0' W/(2^{1/2}\Omega_{conv}^{3/2})$.

We now represent $\hat{T}$ in the form (3.5) and, in place of X, introduce the function $X_s(u)$ through the relationship

$$X = X_s(u)\sin\xi. \quad (3.13)$$

Equations (3.11) and (3.12) then become

$$d^2T_c/du^2 + \sigma_x\alpha_{conv}^{3/2} u X_s = 0, \quad (3.14)$$

$$d^2X_s/du^2 - \sigma_x\alpha_{conv}^{3/2} u T_c = C_{conv}. \quad (3.15)$$

We see that, for $u \gg \Omega_{conv}^{1/2}$, Eqs. (3.14) and (3.15) have solution (3.7). Consequently, in this case, we can again introduce the dimensionless function $y(u)$ through relationship (3.8). We can also pass over from the function X_s to the dimensionless function $\kappa(u)$ by setting

$$X_s(u) = -\sigma_x W T_0'\kappa(u)/2^{5/2}. \quad (3.16)$$

As a result, Eqs. (3.14) and (3.15) are reduced to

$$d^2y_c/du^2 + \sigma_x\alpha_{conv}^{3/2} u\kappa = 0, \quad (3.17)$$

$$d^2\kappa/du^2 - \sigma_x\alpha_{conv}^{3/2} uy = -\sigma_x\alpha_{conv}^{3/2}. \quad (3.18)$$

These are the dimensionless equations for the perturbed temperature profile in the far region in the convective transport threshold model of NTMs.

3.3. Inertial Mechanism

By analogy with Ω_{col} and Ω_{conv}, we assume that the parameter Ω_i is large, $\Omega_i \gg 1$, so we, as before, can introduce the far and near regions of the perturbation. In the far region, $\Omega \gg 1$, relationship (2.27) becomes

$$g(\Omega) = 2^{3/2}/(\pi\Omega^{1/2}), \quad (3.19)$$

with which Eq. (2.30) simplifies to the equation (cf. Eqs. (3.3), (3.11), (3.12))

$$\partial^2\hat{T}/\partial u^2 - \alpha_i^2 u^2\partial\hat{T}/\partial\xi = -C_i u\sin\xi, \quad (3.20)$$

where $\alpha_i = 2^{1/4}\pi^{1/2}/\Omega_i$ and $C_i = \sigma_x\pi T_0' W/(4\Omega_i^2)$ (see [11] for details).

Instead of formula (3.5), we set

$$\hat{T} = T_c(u)\cos\xi + T_s(u)\sin\xi, \quad (3.21)$$

so Eq. (3.20) splits into the equations (cf. Eqs. (3.14), (3.15))

$$d^2T_c/du^2 - \alpha_i^2 u^2 T_s = 0, \quad (3.22)$$

$$d^2T_s/du^2 + \alpha_i^2 u^2 T_c = -C_i u. \quad (3.23)$$

In the case of inertial mechanism, these two equations play the same role as Eq. (3.6) in the case of collisional mechanism and as Eqs. (3.14) and (3.15) in the case of convective mechanism.

Taking into account that, for $u \gg \Omega_i^{1/2}$, the solution $T_c(u)$ to Eqs. (3.22) and (3.23) is given by formula (3.7), we introduced the function $y(u)$ through equality (3.8) and, by analogy with relationship (3.16), set

$$T_s(u) = -\sigma_x W T_0'\kappa(u)/2^{5/2}. \quad (3.24)$$

Equations (3.22) and (3.23) are then transformed into the equations

$$d^2y/du^2 - \alpha_i^2 u^2 \kappa = 0, \tag{3.25}$$

$$d^2\kappa/du^2 + \alpha_i^2 u^2 y = -\alpha_i^2 u, \tag{3.26}$$

which are analogous to Eqs. (3.17) and (3.18).

3.4. Rotational Mechanism

By analogy with Ω_{col}, Ω_{conv}, and Ω_i, we assume that the parameter Ω_r is large, $\Omega_r \gg 1$. Like in the other models, we can introduce the far and near regions of the perturbation. In the far region, Eq. (2.34) is reduced to the form (cf. Eqs. (3.3), (3.11), (3.12), (3.20))

$$\frac{\partial^2 \hat{T}}{\partial u^2} + \alpha_r \frac{\partial \hat{T}}{\partial \xi} = \frac{C_r}{u}\sin\xi, \tag{3.27}$$

where $\alpha_r = 2^{7/2}/(\pi\Omega_r)$ and $C_r = 2\sigma_x W T_0'/(\pi\Omega_r)$.

When $\hat{T}$ is represented by formula (3.21), Eq. (3.27) splits into the equations

$$d^2T_c/du^2 + \alpha_r T_s = 0, \tag{3.28}$$

$$d^2T_s/du^2 - \alpha_r T_c = C_r/u. \tag{3.29}$$

Note that, for $u \gg \Omega_r^{1/2}$, the solution $T_c(u)$ is given by formula (3.7). Consequently, we can introduce the dimensionless functions $y(u)$ and $\kappa(u)$ in the same manner as in the previous sections. In terms of these functions, Eqs. (3.28) and (3.29) reduce to

$$d^2y/du^2 + \alpha_r \kappa = 0, \tag{3.30}$$

$$d^2\kappa/du^2 - \alpha_r y = -\alpha_r/u. \tag{3.31}$$

These equations, which are analogous to Eqs. (3.17) and (3.18), as well as to Eqs. (3.25) and (3.26), are the basic equations for calculating the perturbed temperature in the rotational model.

4. RIGOROUS EXPRESSIONS FOR THE PERTURBED TEMPERATURE IN THE FAR REGION

4.1. Collisional Mechanism

Homogeneous equation (3.9) (with zero on the right-hand side) has solutions that are expressed in terms of Bessel functions, so the rigorous solution to the inhomogeneous equation can be obtained by the method of variation of constants. As a result, we arrive at the following expression for the function $y(u)$:

$$y(u) = \lambda_{col}(t)/(2\Omega_{col})^{1/2}. \tag{4.1}$$

Here,

$$\lambda_{col}(t) = t^{1/4}\left[I_{1/4}(t)\int_t^\infty K_{1/4}(t_1)t_1^{1/4}dt_1 + K_{1/4}(t)\int_0^t I_{1/4}(t_1)t_1^{1/4}dt_1\right], \tag{4.2}$$

$t = u^2/(2\Omega_{col})$, and $I_{1/4}(t)$ and $K_{1/4}(t)$ are Bessel functions of imaginary arguments of the first and second kinds.

For $u \gg \Omega_{col}^{1/2}$, Eq. (4.1) leads to expression (3.10), while, for $u \ll \Omega_{col}^{1/2}$, it yields

$$y(u) = \frac{1}{\sqrt{2\pi}}\Gamma^2\left(\frac{3}{4}\right)\frac{u}{\Omega_{col}}, \tag{4.3}$$

where Γ is the gamma function. A direct comparison of the analytical asymptotic solution (4.3) with the numerical asymptotic solution (34) from [1] shows that the solutions coincide. The difference between the rigorous asymptotic solution and model solution (A.2) is illustrated by formula (A.3) (see the Appendix).

4.2. Convective Mechanism

Following [10], in place of the real functions $y(u)$ and $\kappa(u)$ in Eqs. (3.17) and (3.18), we introduce the complex function $Y(u)$ through the relationship

$$Y(u) = y(u) + i\kappa(u). \tag{4.4}$$

We sum up Eq. (3.17) and Eq. (3.18) multiplied by the imaginary unit to obtain

$$d^2Y/du^2 - i\sigma_x\alpha_{conv}^{3/2}uY = -i\sigma_x\alpha_{conv}^{3/2}. \tag{4.5}$$

By analogy with Eq. (3.9), homogeneous equation (4.5) has solutions that are expressed in terms of Bessel functions. This allows us to find a rigorous solution to Eq. (4.5) that is analogous to solution (4.1). We represent the sought solution in the form

$$Y(u) = \frac{(\sqrt{3}+i)2^{1/3}}{3^{2/3}\Omega_{conv}^{1/2}}t^{1/3} \times\left[I_{1/3}(t)\int_t^\infty K_{1/3}(t_1)dt_1 + K_{1/3}(t)\int_0^t I_{1/3}(t_1)dt_1\right], \tag{4.6}$$

where $t = 2^{1/2}(1+i)\alpha_{conv}^{3/4}u^{3/2}/3$. In accordance with relationship (4.4), the functions $y(u)$ and $\kappa(u)$ are given by the relationships

$$y(u) = \mathrm{Re}\,Y, \tag{4.7}$$

$$\kappa(u) = \mathrm{Im}\,Y. \tag{4.8}$$

From representation (4.6) we see that the function u varies on a characteristic spatial scale equal to $\Omega_{\text{conv}}^{1/2}$. For $u \gg \Omega_{\text{conv}}^{1/2}$, the expression for the function $y(u)$ that follows from relationships (4.6) and (4.7) coincides with that determined from Eq. (3.20), whereas the function $\kappa(u)$ is as small as Ω_{conv}/u^2 in comparison to the function $y(u)$. In the opposite limit, $u \ll \Omega_{\text{conv}}^{1/2}$, relationships (4.7) and (4.8) yield

$$y(u) = \left(\frac{2}{3}\right)^{1/3}\Gamma\left(\frac{2}{3}\right)\frac{u}{\Omega_{\text{conv}}}, \tag{4.9}$$

$$\kappa(u) = \sqrt{3}\left(\frac{2}{3}\right)^{1/3}\Gamma\left(\frac{2}{3}\right)\frac{u}{\Omega_{\text{conv}}}. \tag{4.10}$$

These asymptotic solutions are rigorous versions of the model asymptotic solutions that are considered in the Appendix (see formula (A.5) and subsequent explanations).

4.3. Inertial Mechanism

According to [11], Eqs. (3.25) and (3.26) with relationship (4.4) lead to the following equation for the complex function Y:

$$d^2Y/du^2 + i\alpha_i^2u^2Y = i\alpha_i^2u. \tag{4.11}$$

By analogy with Eqs. (3.9) and (4.5), homogeneous equation (4.11) has solutions that are expressed in terms of Bessel functions. Applying the method of variation of constants and taking into account the corresponding boundary conditions, we obtain the following solution to Eq. (4.11):

$$Y(u) = -\frac{i\pi}{2^{3/2}a^{3/2}\Omega_i^2}t^{1/4} \times\left[I_{1/4}(t)\int_t^\infty t_1^{1/4}K_{1/4}(t_1)dt_1 + K_{1/4}(t)\int_0^t t_1^{1/4}I_{1/4}(t_1)dt_1\right], \tag{4.12}$$

where $t = au^2$ and $a = (1 - i)2^{-5/4}\pi^{1/2}/\Omega_i$.

For $u \gg \Omega_i^{1/2}$, solution (4.12) and relationships (4.7) and (4.8) lead to expression (3.10) for $y(u)$ and to the function $\kappa(u)$ that is as small as Ω_i/u^2 in comparison to the function $y(u)$. In the opposite limit, $u \ll \Omega_i^{1/2}$, solution (4.12) becomes

$$Y(u) = -\frac{i\pi^{1/2}\Gamma^2(3/4)}{2\Omega_i^2a^{3/2}}t^{1/2}. \tag{4.13}$$

Turning to relationships (4.7) and (4.8), we obtain from expression (4.13) the solution

$$y(u) = -\kappa(u) = \Gamma^2(3/4)u/(2^{3/4}\Omega_i). \tag{4.14}$$

An analogous model asymptotic solution $y(u)$ is given by formula (A.10).

4.4. Rotational Mechanism

In [7], two second-order differential equations (3.30) and (3.31) were reduced to the single fourth-order differential equation

$$d^4y/du^4 + \alpha_r^2y = \alpha_r^2/u. \tag{4.15}$$

The corresponding homogeneous equation has solutions of the form of a plane wave. In [7], it was found that the rigorous solution to Eq. (4.15) is given by formula

$$\frac{dy}{du} = -\frac{2^{5/2}}{\pi\Omega_r}\tau(z), \tag{4.16}$$

where

$$\tau(z) = e^z\left(\cos z\int_\infty^z e^{-t}\sin t\frac{dt}{t} - \sin z\int_\infty^z e^{-t}\cos t\frac{dt}{t}\right) - e^{-z}\left(\cos z\int_{z_0}^z e^{t}\sin t\frac{dt}{t} - \sin z\int_{z_0}^z e^{t}\cos t\frac{dt}{t}\right), \tag{4.17}$$

$$z = 2^{5/4}\pi^{-1/2}(\Omega/\Omega_r)^{1/2}. \tag{4.18}$$

The quantity z_0 is a small parameter that plays the role of the integration constant in the far region and should be determined by matching solution (4.16) with the solution dy/du obtained for the near region. Note also that the right-hand side of equality (4.17) from [7], which leads to solution (4.16) in the present paper, is misprinted: its correct form should include the factor 4.

Combining Eqs. (3.30) and (3.31) and using definition (4.4), we arrive at the following second-order differential equation for the complex function $Y(u)$:

$$d^2Y/du^2 - i\alpha_rY = -i\alpha_r/u. \tag{4.19}$$

It is obvious that Eq. (4.19) also leads to expression (4.16) for the function dy/du, thereby making it possible to determine the function $y(u)$ and, accordingly, the function $\kappa(u)$.

In the region $u \gg \Omega_r^{1/2}$, the expression for the function $y(u)$ that follows from relationship (3.16) coincides with expression (3.10), while the function $\kappa(u)$ in this region is as small as Ω_r/u^2 in comparison to $y(u)$. The asymptotic solutions $y(u)$ and $\kappa(u)$ coincide qualitatively with those predicted by the model that was considered in Section 4.3.

In the region $u \ll \Omega_r^{1/2}$, the function $y(u)$ turns out to diverge logarithmically as $z_0 \longrightarrow 0$. This is why, in order to use formula (4.16) in this region, it is necessary

know the parameter z_0. This parameter will be calculated in Section 5.2.

5. TEMPERATURE PERTURBATION IN THE NEAR REGION

5.1. Collisional, Convective, and Inertial Mechanisms

In the near region, Eq. (2.14), which characterizes the collisional mechanism, reduces to

$$\frac{\partial}{\partial\Omega}\left[(\Omega+\cos\xi)^{1/2}\frac{\partial\hat{T}}{\partial\Omega}\right] = 0. \tag{5.1}$$

The solution to this equation can be represented as

$$\hat{T} = c_{\rm col}(\Omega+\cos\xi)^{1/2}\cos\xi, \tag{5.2}$$

where $c_{\rm col}$ is the integration constant.

For $\Omega \gg 1$, solution (5.2) becomes

$$\hat{T} = c_{\rm col}u\cos\xi. \tag{5.3}$$

The integration constant $c_{\rm col}$ is determined from the requirement that, in the region $\Omega \gg 1$, the solutions for the perturbed temperature $\hat{T}$ in the far and near regions be coincident. Comparing formulas (3.5), (3.7), and (4.3) for $\hat{T}$ with formula (5.3), we then find

$$c_{\rm col} = -\frac{\sigma_x T_0' W\Gamma^2(3/4)}{8\sqrt{\pi}\Omega_{\rm col}}. \tag{5.4}$$

Analogously, in order to derive an equation that is analogous to Eq. (5.1) and describes the convective mechanism in the near region, it is sufficient to take the limit $\Omega_{\rm conv} \longrightarrow \infty$ in Eqs. (2.19) and (2.20). In doing so, instead of solution (5.2), we get

$$\hat{T} = c_{\rm conv}^{(c)}(\Omega+\cos\xi)^{1/2}\cos\xi, \tag{5.5}$$

$$X = c_{\rm conv}^{(s)}(\Omega+\cos\xi)^{1/2}\sin\xi, \tag{5.6}$$

where $c_{\rm conv}^{(c)}$ and $c_{\rm conv}^{(s)}$ are integration constants. Matching the solutions obtained for the far and near regions yields the following expressions for $c_{\rm conv}^{(c)}$ and $c_{\rm conv}^{(s)}$ (cf. expression (5.4)):

$$(c_{\rm conv}^{(c)}, c_{\rm conv}^{(s)}) = -\frac{\sigma_x T_0' W}{2^{5/2}\Omega_{\rm conv}}\left(\frac{2}{3}\right)^{1/3}\Gamma\left(\frac{2}{3}\right)[1, 3^{1/2}]. \tag{5.7}$$

An analogous approximation can be used to describe temperature perturbations in the near region in terms of the inertial model. In this case, instead of using representations (5.2), (5.5), and (5.6), we represent $\hat{T}$ as

$$\hat{T} = (\Omega+\cos\xi)^{1/2}(c_{\rm inert}^{(c)}\cos\xi + c_{\rm inert}^{(s)}\sin\xi), \tag{5.8}$$

so, instead of expressions (5.4) and (5.7), the inertial model gives

$$(c_{\rm inert}^{(c)}, c_{\rm inert}^{(s)}) = -\frac{\sigma_x T_0' W}{2^{13/4}\Omega_i}\Gamma^2\left(\frac{3}{4}\right)[1, -1]. \tag{5.9}$$

Analogous expressions for $c_{\rm inert}^{(c)}$ and $c_{\rm inert}^{(s)}$ can be obtained by using model solution (A.9) in the far region.

In the model description of the perturbed temperature profile in the far region, expressions (5.5), (5.7), and (5.9) for the integration constants $c_{\rm col}$, $c_{\rm conv}^{(c)}$, and $c_{\rm inert}^{(c)}$ are replaced, respectively, by expressions (A.4), (A.8), and (A.12).

5.2. Rotational Mechanism

5.2.1. Solution in the near region. According to [7], the solution to Eq. (2.34) in the near region can be represented as

$$\hat{T} = T^{(1)} + T^{(2)}, \tag{5.10}$$

where $T^{(1)}$ and $T^{(2)}$ are the sine and cosine components of the temperature perturbation. For $|\Omega| \simeq 1$, the expressions for $T^{(1)}$ and $T^{(2)}$ were obtained in [7].

In that paper, it was shown that, for $\Omega \gg 1$, the function $T^{(2)}$ satisfies the equation

$$\frac{dT^{(2)}}{du} = 2\sigma_x\left[c_{\rm rot}^{(c)} - \frac{4\sqrt{2}}{\pi}c^{(2)}c_{\rm rot}^{(s)}\Omega^{1/2} + \frac{48}{\pi^2}c^{(1)}c^{(2)}\Omega\left(1-\frac{1}{3}\ln\Omega\right)\right]\cos\xi, \tag{5.11}$$

where $c_{\rm rot}^{(c)}$ and $c_{\rm rot}^{(s)}$ are integration constants and the parameters $c^{(1)}$ and $c^{(2)}$ are defined as

$$c^{(1)} = \sigma_x W T_0'/(4\sqrt{2}\Omega_r), \tag{5.12}$$

$$c^{(2)} = 1/\Omega_r. \tag{5.13}$$

Following [7], we find

$$c_{\rm rot}^{(c)} = -\sigma_x W T_0'/(8\Omega_r). \tag{5.14}$$

This expression follows from equality (4.17) of [7], provided that it is corrected in the above way.

5.2.2. Simplification of expression (4.16) for $y(u)$ in the limit $z \ll 1$. We convert expression (4.17) to the form

$$\begin{aligned}\tau(z) &= -e^{z}\left\{\cos z\left[\frac{\pi}{4} + I_{-}^{-}(z)\right] + \sin z\left[C + \frac{1}{2}\ln 2 + I_{+}^{-}(z)\right]\right\} \\ &+ e^{-z}\{\cos z[I_{+}^{+}(z) - I_{+}^{+}(z_0)] - \sin z[I_{-}^{+}(z) - I_{-}^{+}(z_0)] \\ &- e^{z_0}\ln z_0 \sin(z - z_0)\},\end{aligned} \tag{5.15}$$

where

$$I_{\pm}^{+}(z) = \int_0^z \ln t e^{t}(\cos t \pm \sin t)dt, \tag{5.16}$$

$$I_{\pm}^{-}(z) = \int_0^z \ln t e^{-t}(\cos t \pm \sin t)dt, \tag{5.17}$$

and C is Euler's constant.

Expanding the right-hand side of equality (5.15) in powers of z, we find

$$\tau(z) = \tau_0 + \tau_1 z + \tau_2 z^2 - 2z^2 \ln z, \tag{5.18}$$

where

$$\tau_0 = -\pi/4 - I_{+}^{+}(z_0) + e^{z_0}\ln z_0 \sin z_0, \tag{5.19}$$

$$\begin{aligned}\tau_1 &= -\left(\frac{\pi}{4} + \frac{1}{2}\ln 2\right) - C + I_{+}^{+}(z_0) - I_{-}^{+}(z_0) \\ &- e^{z_0}\ln z_0(\cos z_0 + \sin z_0),\end{aligned} \tag{5.20}$$

$$\tau_2 = 3 + e^{z_0}\ln z_0 \cos z_0 - I_{-}^{+}(z_0) - C - \frac{1}{2}\ln 2. \tag{5.21}$$

Transforming Eq. (5.11) to Eq. (4.16) gives the following expression for the function $\tau(z)$ in the near region:

$$\begin{aligned}\tau(z) &= \tau_0 + \tau_1\left(\frac{2\Omega}{\bar{\Omega}_r}\right)^{1/2} + \frac{2\Omega}{\bar{\Omega}_r}\left(\tau_2 - \ln\frac{2}{\bar{\Omega}_r}\right) \\ &- \frac{2\Omega}{\bar{\Omega}_r}\ln\Omega,\end{aligned} \tag{5.22}$$

where $\bar{\Omega}_r = 2^{-3/2}\pi\Omega_r$.

5.2.3. Matching of the solutions for the far and near regions. Expressions (5.18) and (5.22) for the function $\tau(z)$ should coincide with one another. We see that, in these expressions, the terms with $\Omega\ln\Omega$ are the same. The conditions for the Ω-independent terms, as well as for those proportional to $\Omega^{1/2}$, to be the same determine the integration constants $c_{\rm rot}^{(c)}$ (see expression (5.14)) and $c_{\rm rot}^{(s)}$ in the near region. Finally, equating the terms that are proportional to Ω, we arrive at the relationship, which should be satisfied by the parameter z_0:

$$\tau_2 + \ln\bar{\Omega}_r - \ln 2 = \frac{3\times 2^{11/2}\sigma_x c^{(1)}c^{(2)}\bar{\Omega}_r^2}{\pi^2 W T_0'}. \tag{5.23}$$

Substituting expressions (5.12) and (5.13) for the parameters $c^{(1)}$ and $c^{(2)}$ into this relationship yields

$$\tau_2 = 3 - \ln(\bar{\Omega}_r/2). \tag{5.24}$$

Since $\bar{\Omega}_r \gg 1$, this relationship can be reduced to the following approximate form:

$$\tau_2 = -2\ln(W_{\rm rot}/W), \tag{5.25}$$

which can be satisfied only when $z_0 \ll 1$. For such z_0 values, expression (5.21) simplifies to

$$\tau_2 = \ln z_0. \tag{5.26}$$

Expressions (5.25) and (5.26) yield

$$z_0 \simeq (W/W_{\rm rot})^2, \tag{5.27}$$

which justifies the above assumption that the matching parameter z_0 is small.

6. CALCULATION OF THE CONTRIBUTION OF THE BOOTSTRAP CURRENT TO THE GENERALIZED RUTHERFORD EQUATION FOR THE ISLAND WIDTH

6.1. Kinetic Approach to Calculating the Perturbed Bootstrap Current at a Strong Transverse Heat Transport

The perturbed temperature $\hat{T}$ is related to the perturbation of the distribution function $\hat{f}$ of the corresponding particle species by the familiar relationship

$$\hat{f}_{+} = \left(\frac{Mv^2}{2T_0} - \frac{3}{2}\right)\frac{\hat{T}}{T_0}F_0. \tag{6.1}$$

Here, the plus sign indicates the part of $\hat{f}$ that is even in the longitudinal particle velocity $v_\parallel$, F_0 is the equilibrium distribution function, v is the absolute value of the particle velocity, and M is the mass of a particle. In order to calculate the bootstrap current, however, it is necessary to know the part of $\hat{f}$ that is odd in $v_\parallel$ (i.e., $\hat{f}_{-}$). In this case, in accordance with [8], the basic expression for the perturbed bootstrap current $\bar{J}_{bs}$, averaged over the separatrix surface of the magnetic island, has the form

$$\bar{J}_{bs} = \sum_{\alpha = e,\, i} \bar{J}_{\parallel}^{\alpha}. \tag{6.2}$$

Here,

$$\bar{J}_{\parallel}^{\alpha} = e_{\alpha}\int d^3\mathbf{v}\, v_{\parallel}\langle\langle \hat{f}_{-}\rangle_{\theta}\rangle, \tag{6.3}$$

the index α stands for the particle species, the symbol $\langle\ldots\rangle$ indicates averaging over the separatrix surface of the island, and the symbol $\langle\ldots\rangle_{\theta}$ denotes averaging over equilibrium poloidal oscillations. The index for the particle species in the function $\hat{f}_{-}$ is omitted for simplicity.

According to [8, 30], the functions $\hat{f}_{-}$ and $\hat{f}_{+}$ are related by the formula

$$\hat{f}_{-} = \hat{g}_{-} + \sigma_v \hat{H}. \tag{6.4}$$

Here,

$$\hat{g}_{-} = -\frac{q v_{\parallel}}{\epsilon}\left[\frac{1}{\omega_B}\frac{\partial \hat{f}_{+}}{\partial x} - \frac{\omega}{k_y}\frac{MF_0}{T_0}(\psi_x h' - 1)\right], \tag{6.5}$$

$\sigma_v = \operatorname{sgn} v_{\parallel}$, $h' \equiv dh/d\psi$, and the function $\hat{H} \equiv \hat{H}(v, \psi)$ satisfies the kinetic equation

$$\left\langle\left\langle \frac{1}{v_{\parallel}} C(\hat{g}_{-} + \sigma_v \hat{H})\right\rangle_{\theta}\right\rangle = 0, \tag{6.6}$$

where C is the collision integral.

Based on the analysis carried out in the previous sections, we represent the perturbed temperature $\hat{T}$ as

$$\hat{T} = \frac{2^{3/2}\sigma_x}{W} c^{(c)} x\cos\xi, \tag{6.7}$$

where the constants $c^{(c)}$ differ between the transport models; i.e., we have $c^{(c)} = c_j^{(c)}$ with j = (col, conv, inert, rot).

In place of $c_j^{(c)}$, we introduce the dimensionless coefficients μ_j through the relationships

$$c_j^{(c)} = -\frac{\sigma_x T_0' W}{2^{3/2}}\mu_j, \tag{6.8}$$

which yield

$$\mu_j = \frac{1}{2^{3/2}}\left[\frac{\Gamma^2(3/4)}{\sqrt{\pi}\Omega_{\mathrm{col}}}, \frac{2^{5/6}\Gamma(2/3)}{3^{1/3}\Omega_{\mathrm{conv}}}, \frac{\Gamma^2(3/4)}{2^{1/4}\Omega_i}, \frac{1}{\Omega_r}\right]. \tag{6.9}$$

In terms of the coefficients μ_j, relationship (6.1) reads

$$f_{+}^{j} = -\frac{T_0'}{T_0}F_0\mu_j\left(\frac{Mv^2}{2T_0} - \frac{3}{2}\right)x\cos\xi. \tag{6.10}$$

We substitute this relationship into expression (6.5) to obtain

$$\hat{g}_{-} = \frac{q v_{\parallel}}{\epsilon k_y}\frac{MF_0}{T_0} \times\left[\omega_{*T}\mu_j\left(\frac{Mv^2}{2T_0} - \frac{3}{2}\right)\cos\xi + \omega(\psi_x h' - 1)\right], \tag{6.11}$$

where $\omega_{*T} = k_y c T_0'/(eB)$ is the diamagnetic drift frequency in terms of the temperature gradient. The difference between expression (6.11) and an analogous expression for the case of weak transverse transport [30] consists in the replacement

$$\psi_x h_R' - 1 \longrightarrow -\mu_j\cos\xi, \tag{6.12}$$

where h_R is the Rutherford profile function. This is why the results from calculating the bootstrap current in [30] can be used here, provided that they are corrected for this replacement. Thus, using formula (5.47) from [30], we obtain

$$\bar{J}_{bs} = \bar{J}_{bs}^{e} + \bar{J}_{bs}^{i}, \tag{6.13}$$

where

$$\bar{J}_{bs}^{e} = 2.46\times 0.40\epsilon^{1/2}\frac{cn_0 T_{0e}'}{B_{\theta}}\mu_j^{e}\langle\cos\xi\rangle, \tag{6.14}$$

$$\bar{J}_{bs}^{i} = -2.46\times 0.17\epsilon^{1/2}\frac{cn_0 T_{0i}'}{B_{\theta}}\mu_j^{i}\langle\cos\xi\rangle. \tag{6.15}$$

According to [30], the parameter Δ_{bs}, which characterizes the bootstrap drive, is related to $\bar{J}_{bs}$ by the relationship

$$\Delta_{bs} = -\frac{2^{3/2}Rq}{cswB_0}\sum_{\sigma_x}\int_{-1}^{\infty} d\Omega\,\bar{J}_{bs}\oint\frac{\cos\xi}{(\Omega + \cos\xi)^{1/2}}d\xi. \tag{6.16}$$

Inserting formulas (6.13)–(6.15) into this relationship leads to the following expression for Δ_{bs}, which is analogous to expression (5.51) from [30]:

$$\Delta_{bs} = \Delta_{bs}^{e} + \Delta_{bs}^{i}. \tag{6.17}$$

Here,

$$\Delta_{bs}^{e} = -2.46\times 0.40\epsilon^{1/2}\beta_{pe}\frac{r}{sw}\frac{T_e'}{T_e}\mu_j^{e}c_{bs}^{\infty}, \tag{6.18}$$

$$\Delta_{bs}^{i} = 2.46\times 0.17\epsilon^{1/2}\beta_{pi}\frac{r}{sw}\frac{T_i'}{T_i}\mu_j^{i}c_{bs}^{\infty}, \tag{6.19}$$

where

$$c_{bs}^{\infty} = 2^{1/2}\int_{-1}^{\infty} S(\Omega)\langle\cos\xi\rangle^2 d\Omega, \tag{6.20}$$

with

$$S(\Omega) = \frac{2^{1/2}}{\pi}\begin{cases}\kappa K(\kappa), & \Omega \geq 1\\ K(k), & -1 < \Omega < 1,\end{cases} \quad (6.21)$$

$\kappa = [2/(\Omega + 1)]^{1/2}$, and $k = [(\Omega + 1)/2]^{1/2}$. The quantity c_{bs}^{∞} is an analogue of the quantity $c_{bs} = 0.79$ in the case of weak transverse transport. We take the integral over Ω in expression (6.20) to obtain

$$c_{bs}^{\infty} = 0.823. \quad (6.22)$$

As a result, we arrive at the following expressions for Δ_{bs}:

$$\Delta_{bs}^{e,j} = 0.40\epsilon^{1/2}\beta_{pe}\frac{r_s W}{sL_{Te}}\left(\frac{1.21}{W_{\rm col}^2}, \frac{2.39}{W_{\rm conv}^2}\right), \quad (6.23)$$

$$j = (\text{col, conv}),$$

$$\Delta_{bs}^{i,j} = -0.17\epsilon^{1/2}\beta_{pi}\frac{r_s W}{sL_{Ti}}\left(\frac{1.80}{W_{\rm inert}^2}, \frac{1.43}{W_{\rm rot}^2}\right), \quad (6.24)$$

$$j = (\text{inert, rot}).$$

Expressions (6.23) and (6.24) for $\Delta_{bs}^{e,j}$ and $\Delta_{bs}^{i,j}$ can also be derived, on the one hand, from formulas like (1.15) by choosing the corresponding coefficients on their right-hand sides and, on the other hand, from relationship (6.16), in which the perturbed bootstrap current $\bar{J}_{bs}$ is replaced with the quantities $\bar{J}_{bs}^{\alpha,j}$, $\bar{J}_{bs}^{\alpha,j}$ given by the formulas

$$\bar{J}_{bs}^{\alpha,j} = -(0.40, -0.17)\frac{2^{5/2}\sigma_x c n_0}{B_\theta W}c_j\langle\cos\xi\rangle. \quad (6.25)$$

Here,

$$c_j = (c_{\rm col}^{c}, c_{\rm conv}^{(c)}, c_{\rm inert}^{(c)}, c_{\rm rot}^{(c)}), \quad (6.26)$$

where the integration constants on the right-hand side are defined by expressions (5.4), (5.7), (5.9), and (5.14).

6.2. Extrapolation Formulas for Δ_{bs} at Arbitrary Transverse Heat Transport

Following [30], we consider the case of weak transverse heat transport, in which, instead of expressions (6.23) and (6.24), we have

$$\Delta_{bs}^{\alpha} = 2.46\times 1.58\epsilon^{1/2}\frac{r_s\beta_{p\alpha}}{sWL_{T\alpha}}(0.40, -0.17), \quad (6.27)$$

where $\alpha = (e, i)$ and the numbers in parentheses refer to the electrons and ions, respectively. Pursuing the idea that was set forth in [1], we can use expressions (6.23), (6.24), and (6.27) to construct extrapolation formulas for the parameters $\Delta_{bs}^{\alpha,j}$ at arbitrary transverse heat transport:

$$\Delta_{bs}^{e,j} = 2.46\times 1.58\times 0.40\epsilon^{1/2}\frac{r_s\beta_{pe}W}{sL_{Te}(W^2 + W_{d,j}^2)}, \quad (6.28)$$

$$\Delta_{bs}^{i,j} = -2.46\times 1.58\times 0.17\epsilon^{1/2}\frac{r_s\beta_{pi}W}{sL_{Ti}(W^2 + W_{d,j}^2)}, \quad (6.29)$$

where

$$W_{d,j} = (W_{d,\rm col}, W_{d,\rm conv}, W_{d,\rm inert}, W_{d,\rm rot}). \quad (6.30)$$

Quantities (6.30) represent the effective critical island width corresponding to the jth competing mechanism. These widths are given by the equalities

$$(W_{d,\rm col}, W_{d,\rm conv}, W_{d,\rm inert}, W_{d,\rm rot}) = (1.80W_{\rm col}, 1.27W_{\rm conv}, 1.47W_{\rm inert}, 1.65W_{\rm rot}). \quad (6.31)$$

The ratio between $W_{d,\rm col}$ and $W_{\rm col}$, which is determined by the first of equalities (6.31), was originally found by Fitzpatrick [1].

6.3. Bootstrap Drive for Model Perturbed Temperature Profiles

We now analyze the difference between the quantities Δ_{bs}^{j} given by expressions (6.23) and (6.24) and those following from the model solutions for the perturbed temperature profile that are presented in the Appendix. By the superscript here is meant j = (col, conv, inert) because, for j = rot, the model solution has not yet been obtained.

We begin the analysis by making redefinitions in relationships (6.25). Specifically, in place of the parameters c_j, we introduce the quantities

$$(c_j)^{\rm model} = [(c_{\rm col})^{\rm model}, (c_{\rm conv})^{\rm model}, (c_{\rm inert})^{\rm model}], \quad (6.32)$$

which are assumed to be given by formulas (A.4), (A.8), and (A.12). As a result, instead of expressions (6.23) and (6.24), we arrive at

$$(\Delta_{bs}^{e,j})^{\rm model} = 0.40\epsilon^{1/2}\beta_{pe}\frac{r_s W}{sL_{Te}}\left(\frac{0.81}{W_{\rm col}^2}, \frac{1.48}{W_{\rm conv}^2}\right), \quad (6.33)$$

$$(\Delta_{bs}^{i,j})^{\rm model} = -0.17\epsilon^{1/2}\beta_{pi}\frac{r_s W}{sL_{Ti}}\frac{1.20}{W_{\rm inert}^2}. \quad (6.34)$$

Analogously, instead of extrapolation formulas (6.28) and (6.29) for $\Delta_{bs}^{\alpha, j}$ at arbitrary transverse heat transport, we now have

$$(\Delta_{bs}^{e, j})^{\text{model}} = 0.40 \times 2.46 \times 1.58\epsilon^{1/2}\frac{r_s\beta_{pe}W}{sL_{Te}\{W^2 + [(W_{d, j})^{\text{model}}]^2\}}, \quad j = (\text{col, conv}), \tag{6.35}$$

$$(\Delta_{bs}^{i, j})^{\text{model}} = -0.17 \times 2.46 \times 1.58\epsilon^{1/2}\frac{r_s\beta_{pi}W}{sL_{Ti}\{W^2 + [(W_{d, \text{inert}})^{\text{model}}]^2\}}, \tag{6.36}$$

where

$$[(W_{d, \text{col}})^{\text{model}}, (W_{d, \text{conv}})^{\text{model}}, (W_{d, \text{inert}})^{\text{model}}] \equiv (2.19W_{\text{col}}, 1.62W_{\text{conv}}, 1.80W_{\text{inert}}). \tag{6.37}$$

Of course, the coefficients in equalities (6.37) differ from those in equalities (6.31). The difference is seen to be not too large, however.

7. SOME VERSIONS OF TRANSPORT THRESHOLD MODELS

In using the parameter Δ_{bs}, which characterizes the bootstrap drive (see the above discussion), the equation for the island width (the generalized Rutherford equation) is written as [19]

$$\frac{dW}{dt} \sim \frac{\Delta'}{4} + \Delta_{bs} + \ldots. \tag{7.1}$$

Here, Δ' is the standard parameter in the theory of tearing modes; the ellipsis points denote the contributions from the polarization current, the magnetic well, the ECR-driven current, and (possibly) from some other effects; and the symbol ~ indicates an equality in which a certain positive factor is omitted.

7.1. Electron Convective Transport Model

Taking into account the results obtained in [10], and those derived in Section 6, we can show that, in the electron convective transport model (the Fitzpatrick–Gates model), the evolution of the magnetic island width is described by the equation

$$\frac{\tau_s}{r_s}\frac{dW}{dt} = r_s\Delta' + 4\beta_{pe}\frac{0.40r_sC_{bs, e}W}{W^2 + W_{d, \text{conv}, e}^2}, \tag{7.2}$$

where τ_s is the resistive diffusion time and the parameter $C_{bs, e}$, which characterizes the electron channel (mechanism) for the bootstrap drive of NTMs, is given by the relationship

$$C_{bs, e} = 2.46 \times 2c_{bs}\epsilon^{1/2}r_s/(sL_{T, e}). \tag{7.3}$$

In deriving Eq. (7.2) from Eq. (7.1), we have omitted the ellipses that indicate the contributions from the polarization current and other effects mentioned above. This will also be done in further analysis, for simplicity.

In [10], the island width $W_{d, \text{conv}, e}$ was calculated by using a model expression for c_{conv}; i.e., it was assumed that $c_{\text{conv}} = (c_{\text{conv}})^{\text{model}}$, where $(c_{\text{conv}})^{\text{model}}$ is given by expression (A.8). In this case, we have

$$W_{d, \text{conv}, e} = (W_{d, \text{conv}, e})^{\text{model}}. \tag{7.4}$$

In analogy with [10], the right-hand side of this relationship has the form (cf. equalities (6.37))

$$(W_{d, \text{conv}, e})^{\text{model}} = 5.96[\chi_\perp^{(e)}L_s/(k_y v_{Te})]^{1/3}, \tag{7.5}$$

which is a refinement to the corresponding result of [10]. If, instead of $(c_{\text{conv}})^{\text{model}}$, we use the rigorous expression for c_{conv} (see the first of equalities (3.7)), then, instead of expression (7.5), we arrive at the following rigorous expression for $W_{d, \text{conv}, e}$ (cf. equalities (6.31)):

$$W_{d, \text{conv}, e} = 4.67[\chi_\perp^{(e)}L_s/(k_y v_{Te})]^{1/3}. \tag{7.6}$$

Hence, the value of $W_{d, \text{conv}, e}$ given by rigorous expression (7.6) is somewhat smaller than the value of $(W_{d, \text{conv}, e})^{\text{model}}$ given by model expression (7.5). In analogy with [10], we compare the island width $W_{d, \text{conv}, e}$ to the width $W_d^{(G)}$ (where the superscript G stands for Gates), given by the expression

$$W_d^{(G)} = 8.76[\chi_\perp^{(e)}L_s/(k_y v_{Te})]^{1/3}, \tag{7.7}$$

which was constructed in [3] (see also [15]) on an intuitive basis and by subsequently fitting the theoretical results to the experimental observations. With allowance for expression (7.5), this comparison yields

$$W_{d, \text{conv}, e} < (W_{d, \text{conv}, e})^{\text{model}} < W_d^{(G)}. \tag{7.8}$$

The inequality $(W_{d, \text{conv}, e})^{\text{model}} < W_d^{(G)}$ was discussed in [10], where it was noted that this inequality should be regarded as being consistent with the experimental conditions. The reason is that, in [10], the contribution of the polarization current was ignored. In [19], it was shown, however, that, in a plasma with hot electrons (as was indeed the case in the experiments of [3]), this contribution is destabilizing. It is assumed that the island rotation frequency is high in comparison to the diamagnetic drift frequency (see [19] for details). Consequently, the two inequality signs in relationships (7.8) should be interpreted as indicating that, in the rigorous formulation of the problem, the polarization current

plays a more important role than in model calculations of the island width $W_{d,\,\mathrm{conv},\,e}$.

One of the parameters that were measured in experiments is the minimum island width $W_{\min}$ corresponding to the threshold for exciting the NTMs. The expression for $W_{\min}$that was obtained experimentally in [3] can be represented as

$$W_{\min}^{\mathrm{exper}} = 76.56F_{\mathrm{conv}}. \tag{7.9}$$

Here,

$$F_{\mathrm{conv}} = \frac{1}{a_1}\frac{(-\Delta' r_s)L_{T,e}}{\beta_p L_q \epsilon^{1/2}}\left(\frac{\chi_\perp^{(e)} L_s}{k_y v_{Te}}\right)^{2/3}, \tag{7.10}$$

where $a_1 = 4 \times 0.40 \times 2.46 \times 1.58$, β_p is the poloidal beta, and L_q is the shear length. In the model approach at hand, Eq. (7.2) and expression (7.5) yield

$$(W_{\min})^{\mathrm{model}} = 35.52F_{\mathrm{conv}}, \tag{7.11}$$

whereas, in the rigorous approach, Eq. (7.2) and expression (7.6) give

$$W_{\min} = 21.85F_{\mathrm{conv}}. \tag{7.12}$$

We can see that the rigorous value of $W_{\min}$ differs from $W_{\min}^{\mathrm{exper}}$ to a greater extent than from $(W_{\min})^{\mathrm{model}}$.

The main result of one or another model is the prediction of the maximum possible β_p value, $\beta_p^{\max}$, above which the NTMs are excited. When there is only one of the competing mechanisms and the polarization current effect is ignored, the maximum value of the poloidal beta, $\beta_p^{\max}$, is determined by the expression

$$\beta_p^{\max} = \frac{1}{a_1}\frac{(-\Delta')L_T}{L_q \epsilon^{1/2}} W_d. \tag{7.13}$$

Turning to model expressions (7.5) and rigorous expression (7.6), we find that the rigorous approach yields a lower $\beta_p^{\max}$ value in comparison to that predicted by the model approach. On the one hand, as expected, accounting for the electron partial factor 0.40 leads to a higher $\beta_p^{\max}$ value.

7.2. Inertial Transport Threshold Model

The basic equation for the inertial transport threshold model of NTMs is constructed in the same way as Eq. (7.2):

$$\frac{\tau_s}{r_s}\frac{dW}{dt} = r_s\Delta' - 4 \times 0.17\beta_p \frac{r_s C_{bs} W}{W^2 + W_{d,\,\mathrm{inert}}^2}. \tag{7.14}$$

In this case, we are dealing not with the bootstrap drive but rather with the bootstrap suppression of NTMs by the ion temperature gradient. Accordingly, Eq. (7.14) has steady solutions only when $\Delta' > 0$.

7.3. Model for Incorporating Both the Inertial and the Electron Dynamics

With allowance for both the inertial and the electron dynamics, we arrive at the following hybrid of Eqs. (7.2) and (7.14):

$$\begin{aligned}\frac{\tau_s}{r_s}\frac{dW}{dt} &= r_s\Delta' - 4 \times 0.17\beta_{pi}\frac{r_s C_{bs,\,i} W}{W^2 + W_{d,\,\mathrm{inert}}^2} \\ &+ 4 \times 0.40\beta_{pe}\frac{r_s C_{bs,\,e} W}{W^2 + W_{d,\,\mathrm{conv}}^2}.\end{aligned} \tag{7.15}$$

Here, β_{pi} and β_{pe} are the ion and electron poloidal betas and the coefficients $C_{bs,\,\alpha}$ (with $\alpha = i, e$) are given by the expressions

$$C_{bs,\,\alpha} = 2 \times 2.46 c_{bs} \epsilon^{1/2} r_s/(sL_{T,\,\alpha}), \tag{7.16}$$

where $L_{T,\,\alpha} = -T_{0\alpha}/T_{0\alpha}'$.

Equation (7.15) implies, in particular, that the inertial dynamics and the electron dynamics can be equally important even when the island widths $W_{d,\,\mathrm{inert}}$ and $W_{d,\,\mathrm{conv}}$ are markedly different. Such a situation can occur for comparable values of the ratios $\beta_{p\alpha}/L_{T,\,\alpha}$. Note also that, as in the models considered above, the electrons lead to bootstrap drive, while the ions lead to bootstrap suppression.

7.4. Model for Incorporating the General Ion Dynamics

When the general ion dynamics (i.e., the inertial dynamics plus the rotational dynamics) is taken into account, but the electron dynamics is ignored, we arrive not at Eq. (7.14) but at the equation

$$\frac{\tau_s}{r_s}\frac{dW}{dt} = r_s\Delta' - 4 \times 0.17\beta_{pi}\frac{r_s C_{bs,\,i} W}{W^2 + W_{d,\,i}^2}, \tag{7.17}$$

where

$$\frac{1}{W_{d,\,i}^2} = \frac{1}{W_{d,\,\mathrm{inert}}^2} + \frac{1}{W_{d,\,\mathrm{rot}}^2}. \tag{7.18}$$

Relationship (7.18) implies that, for $\Delta' > 0$, the effective critical island width related to the ion dynamics is determined by the fastest of the possible ion dynamic processes. This is the main difference between Eqs. (7.17) and (7.15); recall that, in the latter case, the subsonic dynamics and the electron dynamics can play an equally important role.

7.5. Model for Incorporating both the General Ion and the General Electron Dynamics

With allowance for both the general ion and the general electron dynamics, instead of Eqs. (7.15) and (7.17), we obtain the equation

$$\frac{\tau_s}{r_s}\frac{dW}{dt} = r_s\Delta' - 4\times 0.17\beta_{pi}\frac{r_s C_{bs,i} W}{W^2 + W_{d,i}^2} + 4\times 0.40\beta_{pe}\frac{r_s C_{bs,e} W}{W^2 + W_{d,\mathrm{conv}}^2}, \quad (7.19)$$

in which the island width $W_{d,i}$ is given by relationship (7.18).

In Eq. (7.19), as in Eq. (7.17), it is assumed that the electron dynamics is governed by the competition between the electron convection and the transverse electron heat transport. If the electron convection is not the only process that competes with the electron heat transport, then, in Eq. (7.19), we must make the substitution

$$W_{d,\mathrm{conv}}^2 \longrightarrow W_{d,e}^2. \quad (7.20)$$

Here, the width $W_{d,e}$ accounts for all possible competing electron processes and is given by a relationship analogous to relationship (7.18):

$$\frac{1}{W_{d,e}^2} = \sum_j \frac{1}{W_{d,e,j}^2}, \quad (7.21)$$

where the subscript j denotes the jth competing electron process. The effective critical island width $W_{d,e}$ associated with the electron dynamics ($\Delta' < 0$) is determined by the fastest of the competing electron processes, as is the case with the effective critical island width $W_{d,e}$ associated with the ion dynamics ($\Delta' > 0$).

8. BOOTSTRAP DRIVE MODIFIED BY ANOMALOUS TRANSVERSE ION VISCOSITY

According to [9], the equation of the longitudinal motion of the ions with allowance for their longitudinal viscosity has the form

$$\frac{d_0\hat{U}_{\|i}}{dt} = -\epsilon^{1/2}(\hat{U}_{\|i} - \hat{U}_{\|i}^{(0)}) + 4\mu_{\perp i}\frac{\partial^2\hat{U}_{\|i}}{\partial x^2}, \quad (8.1)$$

where $\hat{U}_{\|i}^{(0)}$ is given by expression (1.20) and $\mu_{\perp i}$ is the transverse ion viscosity coefficient. The numerical coefficient in the term with $\epsilon^{1/2}$ in Eq. (8.1) is omitted, for simplicity.

Using the estimate $\partial/\partial x \simeq 1/W$ and ignoring the term with d_0/dt, we obtain from Eq. (8.1) the following qualitative expression (cf. expression (1.20)):

$$\hat{U}_{\|i} = \frac{1}{1 + W_\mu^2/W^2}\frac{c}{B_\theta}\left(\hat{E}_x - \frac{T_{0i}}{en_0}\frac{\partial\hat{n}}{\partial x} + \frac{0.17}{e}\frac{\partial\hat{T}_i}{\partial x}\right), \quad (8.2)$$

where W_μ is the characteristic island width determined by the transverse ion viscosity,

$$W_\mu = \left(\frac{\mu_{\perp i}}{\epsilon^{1/2}\nu_i}\right)^{1/2}. \quad (8.3)$$

Formula (1.19) then is reduced to

$$\hat{J}_{bs} = \hat{J}_{bs}^e + \hat{J}_{bs}^i + \hat{J}_{bs}^E. \quad (8.4)$$

Here, the electron- and ion-related bootstrap current components are given by the expressions (cf. expressions (1.16)–(1.18))

$$\hat{J}_{bs}^e = -2.46\frac{\epsilon^{1/2}c}{B_\theta}\left(T_{0e}\frac{\partial\hat{n}}{\partial x} + 0.40n_0\frac{\partial\hat{T}_e}{\partial x}\right), \quad (8.5)$$

$$\hat{J}_{bs}^i = -\frac{2.46\epsilon^{1/2}c}{B_\theta(1 + W_\mu^2/W^2)}\left(T_{0i}\frac{\partial\hat{n}}{\partial x} - 0.17n_0\frac{\partial\hat{T}_i}{\partial x}\right), \quad (8.6)$$

and the component $\hat{J}_{bs}^E$ is related to the perturbed radial electric field $\hat{E}_x$ by

$$\hat{J}_{bs}^E = -\frac{2.46\epsilon^{1/2}cen_0\hat{E}_x}{B_\theta}\frac{W_\mu^2}{W^2 + W_\mu^2}. \quad (8.7)$$

It is seen that the transverse ion viscosity gives rise to two physically different effects. First, according to expression (8.6), it lowers the ion-related bootstrap current component by a factor of $(1 + W_\mu^2/W^2)$. Second, according to expression (8.7), it acts to trigger an additional bootstrap drive mechanism that is associated with the radial electric field perturbation and was not incorporated into traditional models based on expression (1.3). For simplicity, we call this bootstrap drive mechanism the *E*-channel for bootstrap drive.

We now consider that the anomalous transverse transport of heat and particles reduces both the electron and ion contributions to the bootstrap current; in this case, the contribution of the ions is also reduced because of their transverse viscosity. Consequently, as $W_d \longrightarrow \infty$ and $W_\mu \longrightarrow \infty$ we have $\hat{J}_{bs}^e \longrightarrow 0$ and $\hat{J}_{bs}^i \longrightarrow 0$. On the other hand, according to relationship (8.7), the *E*-channel, being insensitive to the transverse transport of heat and particles, makes a certain (finite) contribution to the bootstrap current. As a result, in the limiting case at hand, relationship (8.7) transforms into

$$\hat{J}_{bs} = -2.46\epsilon^{1/2}cen_0\hat{E}_x/B_\theta. \quad (8.8)$$

With allowance for the relationship $\hat{E}_x = -\partial\phi/\partial x$, where ϕ is described by Eq. (2.25), we obtain from relationship (8.8) the expression

$$\hat{J}_{bs} = -2.46\frac{en_0q\omega}{\epsilon^{1/2}k_y}\left(\frac{\partial h}{\partial x} - 1\right). \quad (8.9)$$

By analogy with formulas (6.14) and (6.15), this expression leads to the following formula for the averaged perturbed bootstrap current $\bar{J}_{bs}$:

$$\bar{J}_{bs} = -2.46\frac{en_0q\omega}{\epsilon^{1/2}k_y}\left(\langle\Omega_x\rangle\frac{\partial h}{\partial\Omega} - 1\right), \quad (8.10)$$

where the derivative $\partial h/\partial\Omega$ is determined by relationships (2.26)–(2.28). Using formula (8.10) and relationship (6.16), we find

$$\Delta_{bs} = \Delta_{bs,E} \equiv -2.46c_{bs}^E\frac{en_0q\omega r_s}{\epsilon^{1/2}k_y swcB_\theta}, \quad (8.11)$$

where

$$c_{bs}^E \equiv -\frac{1}{2^{3/2}\pi}\sum_{\sigma_x}\int_1^\infty d\Omega\left\langle\frac{\partial h}{\partial x}\right\rangle\oint\frac{\cos\xi d\xi}{(\Omega + \cos\xi)^{1/2}} = 0.77. \quad (8.12)$$

Relationship (8.11) implies that, when the magnetic islands rotate in the direction of the diamagnetic ion drift ($\omega/\omega_{*i} > 0$) the E-channel leads to the bootstrap drive ($\Delta_{bs,E} > 0$). When the islands rotate in the direction of the diamagnetic electron drift ($\omega/\omega_{*e} > 0$), it leads to stabilization ($\Delta_{bs,E} < 0$). This result refines the corresponding result of [8, 9], which is somewhat incorrect because of an error in the calculation: in those papers, the derivative $\partial h/\partial\Omega$ was described by a relationship of form (2.26) with the minus sign on its right-hand side.

The above conclusion concerning the sign of $\Delta_{bs,E}$ can be explained based on the following qualitative considerations: Because of their high viscosity, the ions do not contribute to the bootstrap current, which thus turns out to be purely electronic. The triggering of the E-channel at a weak transverse particle transport and a weak transverse electron heat transport indicates qualitatively that the expression for the electron-related bootstrap current component should contain the coefficient $1 - \omega/\omega_{*p_e}$, where ω_{*p_e} is the diamagnetic electron drift frequency in terms of the pressure gradient. For a strong transport of heat and particles, unity drops out of this coefficient, so the expression for the parameter $\Delta_{bs,E}$ differs from the standard expression for the electron-related bootstrap current component in that it contains the factor $(-\omega/\omega_{*p_e})$. If this factor is negative, i.e., $\omega/\omega_{*p_e} > 0$, then the parameter $\Delta_{bs,E}$ is also negative, which is reflected by formula (8.11).

From the above, it also follows that, in order to take the transverse ion viscosity into account, it is necessary to switch from the three-channel model of the bootstrap drive, which is based on expression (1.3), to a four-channel model based on the expression

$$\Delta_{bs} = \sum_{A = n_e, T_e, T_i, E}\Delta_{bs,A}. \quad (8.13)$$

Here, according to expression (8.7), the quantity $\Delta_{bs,E}$ is determined by the perturbed radial electric field $\hat{E}_x$ and, in the limiting case of high transverse ion viscosity, is given by relationship (8.11).

9. FINAL REMARK AND DISCUSSIONS OF THE RESULTS

The above analysis has demonstrated that research on transport threshold models of NTMs occupies a fairly important place in the general theory of magnetic islands in tokamaks. Our contribution to this research consists, first of all, in finding rigorous analytic solutions to the time-independent heat conduction equation for the cases in which transverse heat transport is sufficiently strong and the temperature profile is established as a result of the competition between this heat transport, on the one hand, and the longitudinal heat transport, the longitudinal heat convection, and the heat transport due to the longitudinal gradient of the longitudinal plasma velocity, on the other hand. Together with the rigorous solution to the heat conduction equation that was obtained earlier for the competition between strong transverse heat transport and rotational heat transport, the above rigorous solutions constitute the basis for constructing the corresponding versions of transport threshold models of NTMs with rigorously defined numerical coefficients, which is important for the practical application of such models. The transport threshold models proposed here can in turn serve as fragments of more general threshold models of NTMs, which can be referred to as next-generation transport threshold models. Since, on the whole, the results obtained have been discussed in sufficient detail in the body of the paper, we will say a few words about some questions that lie outside the scope of the present work.

The above formulas for the bootstrap current J_{bs} show that, in transport threshold models of NTMs, this current is independent of the magnetic surfaces of the island. In other words, the bootstrap current has a component that depends on the cyclic variable ξ of the island. This bootstrap current component should perturb the nondissipative component of the longitudinal electric field of the islands [19] (this effect was ignored in our analysis). A description of this nondissipative

electric-field component, as well as of the dissipative component of the longitudinal electric field that is generated by the dissipative component of the longitudinal current [19], could become the subject of an ongoing investigation.

Assuming that magnetic islands rotate across the main magnetic field at frequencies on the order of the drift frequency, we ignored drift effects in the plasma equations used in our analysis. Incorporating drift effects into transport threshold models could be another topic for future research. It is also of interest to generalize transport models to the case in which the NTMs are suppressed by the helical magnetic field of the external coils [6].

As was noted previously, one of the factors governing the evolution of the width of magnetic islands is the effect of the magnetic field line curvature, or, in other terminology, the magnetic well effect. This effect was analyzed in our recent paper [32]. In order to calculate it, it is necessary to know the perturbed temperatures of the electrons and ions. In [32], these temperature perturbations were assumed to correspond to the traditional weak transverse heat transport approximation. From the above analysis, it is clear, however, that strong transverse heat transport modifies the magnetic well effect. The first steps in investigating this problem were taken in [25, 26], where the temperature perturbation was calculated using the Fitzpatrick model [1]. However, the above study showed that the Fitzpatrick model can be used solely for illustrative purposes; the same can be said about the results obtained in [25, 26]. An analysis of the magnetic curvature effect in the case of strong transverse heat transport under more realistic assumptions than those made in [25, 26] could also be the subject of subsequent investigations.

ACKNOWLEDGMENTS

We are grateful to S.E. Sharapov, T. Ozeki, T. Takizuka, R.M.O. Galvão, and I.C. Nascimento for useful discussions. This work was supported in part by the Russian Foundation for Basic Research (project no 03-02-16294), the RF Program for State Support of Leading Scientific Schools (project no. NSh-2024.2003.2), the Department of Atomic Science and Technology of the RF Ministry of Atomic Industry, the U.S. Civilian Research and Development Foundation for the Independent States of the Former Soviet Union (CRDF) (grant no. BRHE REC-011), the National Program of Support for Excellence Groups (PRONEX) of the National Council for Scientific and Technological Development (CNPq) (Brazil), and the State of São Paulo Foundation for the Support of Research (FAPESP) (Brazil).

APPENDIX: MODEL PERTURBED TEMPERATURE PROFILES

A.1. Collisional Mechanism

Following [7], the solution to Eq. (3.9) can be approximated by the model expression

$$y(u) = \frac{u}{u^2 + u_{\rm col}^2}, \qquad (A.1)$$

where the quantity $u_{\rm col}$ is introduced by the relationship $u_{\rm col} = 6^{1/4}\Omega_{\rm col}^{1/2}$. For $u \gg \Omega_{\rm col}^{1/2}$, expression (A.1) passes over to expression (3.10); for $u \ll \Omega_{\rm col}^{1/2}$, it becomes

$$y(u) = u/(\sqrt{6}\Omega_{\rm col}). \qquad (A.2)$$

The difference between the asymptotic behavior of model solution (A.2) and that of analytic solution (4.3) consists in the substitution

$$(3^{1/2})^{-1} \equiv 0.577 \longrightarrow \Gamma^2(3/4)/\sqrt{\pi} \equiv 0.847. \qquad (A.3)$$

It can be seen that this difference is not too large, which justifies the use of model expression (A.1).

Turning to solution (5.2), we can introduce the integration constant $c_{\rm col}$ for the near region. Matching solutions (A.2) and (A.3), we then obtain

$$(c_{\rm col})^{\rm model} = -\frac{\sigma_x T_0' W}{8\sqrt{3}\Omega_{\rm col}}. \qquad (A.4)$$

The superscript "model" indicates that, in deriving relationship (A.4), we have used the model solution in the far region. The difference between the coefficients $(c_{\rm col})^{\rm model}$ and $c_{\rm col}$ can be determined from substitution (A.3).

A.2. Convective Mechanism

According to [10], the function $y(u)$ that satisfies Eqs. (3.17) and (3.18) can be approximated by the model expression (cf. expression (A.1))

$$y(u) = \frac{u}{u^2 + u_{\rm conv}^2}, \qquad (A.5)$$

where $u_{\rm conv} = (5/2)^{1/6}\Omega_{\rm conv}^{1/2}$.

For $u \gg \Omega_{\rm conv}^{1/2}$, expression (A.5) passes over to expression (3.10); for $u \ll \Omega_{\rm conv}^{1/2}$, it takes the form (cf. expression (A.2))

$$y(u) = (2/5)^{1/3}u/\Omega_{\rm conv}. \qquad (A.6)$$

We see that expressions (A.6) and (4.10) are qualitatively the same, which substantiates the use of model expression (A.5). By analogy with substitution (A.3),

the difference between expressions (A.6) and (4.9) can be illustrated by the substitution

$$(2/5)^{1/3} \equiv 0.74 \longrightarrow (2/3)^{1/3}\Gamma(2/3) \equiv 1.18. \quad \text{(A.7)}$$

In describing the temperature perturbation in the near region, we introduce the integration constants $c_{\text{conv}}^{(c)}$ and $c_{\text{conv}}^{(s)}$ in accordance with representations (5.5) and (5.6). Matching the model solution for the far region with the solution given by representations (5.5) and (5.6), we find the coefficients $(c_{\text{conv}}^{(c)})^{\text{model}}$ and $(c_{\text{conv}}^{(s)})^{\text{model}}$, which are analogous to the coefficient $(c_{\text{col}})^{\text{model}}$ determined by formula (A.4). As a result, we arrive, in particular, at the expression

$$(c_{\text{conv}}^{(c)})^{\text{model}} = -\frac{\sigma_x T_0' W}{2^{13/6}5^{1/3}\Omega_{\text{conv}}}. \quad \text{(A.8)}$$

The difference between this expression for $(c_{\text{conv}}^{(c)})^{\text{model}}$ and the rigorous expression for the coefficient $c_{\text{conv}}^{(c)}$ can be inferred from substitution (A.7).

A.3. Inertial Mechanism

Following [11], the solution to Eq. (4.11) can be approximated by the model expression

$$Y(u) = \frac{u}{u^2 + (1+i)u_i^2}, \quad \text{(A.9)}$$

where $u_i = 6^{1/4}\pi^{1/2}\Omega_i^{1/2}$.

For $u \gg \Omega_i^{1/2}$, relationships (4.7), (4.8), and (A.9) imply that the function $y(u)$ is described by expression (3.10) and the function $\kappa(u)$ is as small as Ω_i/u^2 in comparison to the function $y(u)$. The behavior of the function $\kappa(u)$ is thus analogous to that in the case of convective mechanism, which was discussed in Section 4.2 (see expression (4.10)). For $u \ll \Omega_i^{1/2}$, relationships (4.7), (4.8), and (A.9) lead to the expression

$$y(u) = -\kappa(u) = \frac{\pi^{1/2}u}{2^{3/4}3^{1/2}\Omega_i}. \quad \text{(A.10)}$$

This behavior of the function $y(u)$ for $u \ll \Omega_i^{1/2}$ is analogous to that described by expressions (A.2) and (A.6) in the collisional and convective models, respectively. At the same time, expression (A.10) predicts that the behavior of the function $\kappa(u)$ for $u \ll \Omega_i^{1/2}$ is analogous to that described by expression (4.10) in the convective model.

We can see that the only difference between expressions (A.10) and (4.14) consists in the substitution

$$(\pi/3)^{1/2} = 1.02 \longrightarrow \Gamma^2(3/4) = 1.50. \quad \text{(A.11)}$$

Consequently, model expression (A.9) coincides qualitatively with rigorous expression (4.12).

The solution in the near region is given by representation (5.8), so, by analogy with expression (A.8), we find

$$(c_{\text{inert}}^{(c)})^{\text{model}} = -\sigma_x\left(\frac{\pi}{3}\right)^{1/2}\frac{T_0' W}{2^{13/4}\Omega_i}. \quad \text{(A.12)}$$

This expression differs from the rigorous expression for the integration constant $c_{\text{inert}}^{(c)}$ (see the first of expressions (5.9)) in substitution (A.11).

REFERENCES

1. R. Fitzpatrick, Phys. Plasmas **2**, 825 (1995).
2. N. N. Gorelenkov, R. V. Budny, Z. Chang, *et al.*, Phys. Plasmas **3**, 3379 (1996).
3. D. A. Gates, B. Lloyd, A. W. Morris, *et al.*, Nucl. Fusion **37**, 1593 (1997).
4. O. Sauter, R. J. La Haye, Z. Chang, *et al.*, Phys. Plasmas **4**, 1654 (1997).
5. ITER Physics Expert Group on Disruptions, Plasma Control, and MHD and ITER Physics Basis Editors, Nucl. Fusion **39**, 2251 (1999).
6. Q. Yu, S. Gunter, and K. Lackner, Phys. Rev. Lett. **85**, 2949 (2000).
7. S. V. Konovalov, A. B. Mikhailovskii, M. S. Shirokov, and V. S. Tsypin, Plasma Phys. Controlled Fusion **44**, 579 (2002).
8. S. V. Konovalov, A. B. Mikhailovskii, M. S. Shirokov, and V. S. Tsypin, Phys. Plasmas **9**, 4596 (2002).
9. S. V. Konovalov, A. B. Mikhailovskii, M. S. Shirokov, and V. S. Tsypin, Plasma Phys. Controlled Fusion **44**, L51 (2002).
10. A. B. Mikhailovskii, M. S. Shirokov, V. S. Tsypin, *et al.*, Phys. Plasmas **10**, 3790 (2003).
11. A. B. Mikhailovskii, M. S. Shirokov, V. S. Tsypin, *et al.*, Phys. Plasmas **10**, 3975 (2003).
12. R. Carrera, R. D. Hazeltine, and M. Kotschenreuther, Phys. Fluids **29**, 899 (1986).
13. W. X. Qu and J. D. Callen, Report No. UWPR-85-5 (University of Wisconsin, Madison, 1985).
14. S. I. Braginskii, in *Reviews of Plasma Physics*, Ed. by M. A. Leontovich (Gosatomizdat, Moscow, 1963; Consultants Bureau, New York, 1965), Vol. 1.
15. D. A. Gates, B. Lloyd, A. W. Morris, *et al.*, in *Proceedings of the 16th IAEA Fusion Energy Conference, Montreal, 1996* (IAEA, Vienna, 1997), Vol. 1, p. 715.
16. H. Zohm, Phys. Plasmas **4**, 3433 (1997).
17. A. I. Smolyakov, A. Hirose, E. Lazzaro, *et al.*, Phys. Plasmas **2**, 1581 (1995).
18. H. R. Wilson, J. W. Connor, R. J. Hastie, *et al.*, Phys. Plasmas **3**, 248 (1996).

19. A. B. Mikhailovskii, Contrib. Plasma Phys. **43**, 125 (2003).
20. M. Kotschenreuther, R. D. Hazeltine, and P. J. Morrison, Phys. Fluids **28**, 294 (1985).
21. R. J. La Haye, L. L. Lao, E. J. Strait, *et al.*, Nucl. Fusion **37**, 397 (1997).
22. A. Isayama, Y. Kamada, T. Ozeki, *et al.*, Plasma Phys. Controlled Fusion **41**, 35 (1999).
23. S. Gunter, G. Gantenbein, A. Gude, *et al.*, Nucl. Fusion **43**, 161 (2003).
24. A. M. Popov, Phys. Plasmas **9**, 4205 (2002).
25. H. Lutjens, J. F. Luciani, and X. Garbet, Phys. Plasmas **8**, 4267 (2001).
26. H. Lutjens and J. F. Luciani, Phys. Plasmas **9**, 4837 (2002).
27. R. J. La Haye, R. J. Buttery, S. Guenter, *et al.*, Phys. Plasmas **7**, 3349 (2000).
28. R. J. Buttery, M. Valovic, C. D. Warrick, *et al.*, Nucl. Fusion **41**, 985 (2001).
29. M. N. Rosenbluth, R. D. Hazeltine, and F. L. Hinton, Phys. Fluids **15**, 116 (1972).
30. B. N. Kuvshinov and A. B. Mikhailovskii, Fiz. Plazmy **24**, 275 (1998) [Plasma Phys. Rep. **24**, 245 (1998)].
31. S. P. Hirshman, D. J. Sigmar, and J. F. Clarke, Phys. Fluids **19**, 656 (1976).
32. A. B. Mikhailovskii, S. V. Konovalov, M. S. Shirokov, and V. S. Tsypin, Fiz. Plazmy **30**, 595 (2004) [Plasma Phys. Rep. **30**, 549 (2004)].

Translated by I.A. Kalabalyk

Plasma Physics Reports, Vol. 31, No. 5, 2005, pp. 369–381. Translated from Fizika Plazmy, Vol. 31, No. 5, 2005, pp. 409–421.

PARTICLE ACCELERATION IN PLASMA

Ion Acceleration in a Dipole Vortex in a Laser Plasma Corona

S. V. Bulanov[1, 2, 3, 4], D. V. Dylov[1], T. Zh. Esirkepov[1, 2, 3], F. F. Kamenets[1], and D. V. Sokolov[1]

[1]*Moscow Institute of Physics and Technology, Institutskiĭ per. 9, Dolgoprudnyĭ, Moscow oblast, 141700 Russia*
[2]*Advanced Photon Research Center, Japan Atomic Energy Research Institute, Kizu, Kyoto 619-0215, Japan*
[3]*CREST-JST, Kawaguchi, Saitama 332-0012, Japan*
[4]*Prokhorov Institute of General Physics, Russian Academy of Sciences, ul. Vavilova 38, Moscow, 119991 Russia*

Received June 18, 2004; in final form, August 18, 2004

Abstract—Particle-in-cell simulations show that the inhomogeneity scale of the plasma produced in the interaction of high-power laser radiation with gas targets is of fundamental importance for ion acceleration. In a plasma slab with sharp boundaries, the quasistatic magnetic field and the associated electron vortex structure produced by fast electron beams both expand along the slab boundary in a direction perpendicular to the plasma density gradient, forming an extended region with a quasistatic electric field, in which the ions are accelerated. In a plasma with a smooth density distribution, the dipole magnetic field can propagate toward the lower plasma density in the propagation direction of the laser pulse. In this case, the electron density in an electric current filament at the axis of the magnetic dipole decreases to values at which the charge quasineutrality condition fails to hold. In electric fields generated by this process, the ions are accelerated to energies substantially higher than those characteristic of plasma configurations with sharp boundaries. © *2005 Pleiades Publishing, Inc.*

1. INTRODUCTION

The problem of the generation of high-energy ions in the interaction of high-power laser radiation with solid, cluster, and gas targets has been the focus of considerable interest for many years (see [1–12] and reviews [13–16]). This is explained by the development of laser technologies that provide the possibility of generating multiterawatt or even petawatt femtosecond radiation pulses [17] and carrying out experiments on the acceleration of charged particles by such pulses. Laser accelerators of charged particles possess a number of obvious advantages: first, the laser facilities required for such acceleration are widespread because of their compactness and, accordingly, relatively low cost; second, there is no need for the radiation protection of large rooms (in reality, it is sufficient to shield only the chamber where the target is positioned); and last, but not least in importance, laser accelerators are capable of generating high-intensity short-duration fast particle beams and can be further improved to achieve high repetition rates of this beams. These advantages have initiated active discussions about possible application of fast ion beams accelerated in a laser-produced plasma in such areas as controlled fusion research (within the framework of the concept of fast ignition of precompressed thermonuclear targets) [18–20], the hadron therapy of oncological diseases [21–24], the activation of radioactive sources (in particular, for the purposes of electron–positron emission tomography in medicine [25]), proton imaging of ultrafast processes in laser plasmas [26], the transmutation of radioactive elements [25], and for studying neutrino oscillations [27] and for creating an ion–ion collider in high-energy physics [28].

In constructing the theory of ion acceleration by laser pulses, various acceleration regimes have been considered that depend on the type of target and the parameters of laser radiation. In this paper, we restrict ourselves to studying ion acceleration in the interaction of laser pulses with gas targets. Because of the high laser power, the gas of the target is ionized during a very short time (on the order of the optical period). As a result, conditions arise that correspond to the interaction of laser radiation with a subcritical plasma, in which the following inequality holds: $n < n_{cr} = \omega^2 m_e/(4\pi e^2)$, where ω is the laser frequency and m_e and e are the mass and charge of an electron.

In a number of recent papers, the ion acceleration in a subcritical plasma was attributed to the so-called Coulomb explosion [29]. The ion acceleration mechanism proposed in those papers can be described as follow. Coulomb explosion is associated with the disruption of plasma quasineutrality inside the self-focusing channel along which the laser pulse propagates. The plasma quasineutrality is violated because the ponderomotive force of the laser radiation expels electrons from the channel and the resulting charge-separation electric field accelerates the ions in the radial direction. Such an acceleration regime usually occurs under conditions in which the plasma slab is much thicker than the laser pulse depletion length, i.e., when the laser

1063-780X/05/3105-0369$26.00 © 2005 Pleiades Publishing, Inc.

pulse in the plasma is damped (by transferring its energy to the charged particles) before reaching the farther boundary of the plasma slab. The results of computer simulations carried out in [4, 13, 30] showed, however, that fast ions are generated far more efficiently when the laser pulse penetrates through the entire finite-thickness plasma slab. The relativistic electrons that have been accelerated within the self-focusing channel accompany the pulse and reach the farther slab boundary at the same time as the pulse. Fast electrons leave the plasma and then return back into it under the action of the electric field of an unneutralized electric charge. In such motion, the electrons form an electron dipole vortex (or a toroidal vortex in 3D geometry). The electric current of this vortex configuration generates a quasistatic dipole magnetic field. It should be noted that the current produced by fast electrons in the self-focusing channel inside the plasma slab also generates a quasistatic magnetic field [31]. However, near the farther (with respect to the propagation direction of the laser pulse) slab boundary, the magnetic field is generated more efficiently because the current-carrying electrons occupy a larger volume and also because the electrons are accelerated predominantly in the pulse propagation direction. Further evolution of the magnetic field depends substantially on the scale on which the plasma density varies. In a highly inhomogeneous plasma, a cloud of fast electrons and the region of the magnetic field generated by them expand in a transverse direction along the plasma–vacuum interface. The magnetic field partially penetrates into the plasma and displaces the electron plasma component with respect to the heavy plasma ions, thereby producing a quasistatic electric field in a wide region. The direction of the electric field is such that the field simultaneously accelerates the ions and focuses them to the axis. The resulting beam of accelerated ions has a form of a dense thin filament, in which the longitudinal momentum of the ions is much larger than their transverse momentum. This scenario of ion acceleration corresponds to the so-called magnetic acceleration mechanism that was proposed in [30] and was used, in particular, to explain the acceleration of ions observed experimentally in [32].

Since the ion acceleration process depends on many parameters (such as the power, intensity, and energy of the laser pulse; the plasma density; and the plasma slab thickness), this problem requires further investigation. It is clear that plasma targets with smooth density distributions are more suited to conditions of actual experiments.

Although this paper is devoted to studying ion acceleration processes in the interaction of high-power electromagnetic pulses with gas targets, the results obtained can also find application in the problems of the interaction of laser radiation with solid targets. As was noted in [32], a terawatt laser pulse with a relatively low contrast ratio (on the order of 10^{-5}–10^{-6}) has a pedestal of nanosecond duration (and/or a prepulse), which can be focused to an intensity on the order of 10^{13} W/cm^2. This portion of the pulse can completely vaporize the target material and ionize it before the arrival of the main (femtosecond) pulse. As a result, the main pulse begins to interact just with the low-density plasma. Such a scenario is quite natural because actual laser pulses always have a pedestal that is very difficult to eliminate (this is a rather complicated task that has stimulated a great deal of effort [15]). Note that more detailed discussion of the regimes in which the material of a relatively thick solid target evaporates incompletely, giving rise to a plasma corona at the target surface and initiating electron and ion acceleration in it, goes beyond the scope of our study.

The energy of fast particles in a laser plasma is uniquely related to the radiation intensity in the focal plane. In [33], it was pointed out that the relativistic interaction regimes can be achieved even for laser pulses with energies as low as several millijoules, provided that they are focused into a spot with dimensions comparable to the laser radiation wavelength, which corresponds to the so-called λ^3 regime. In this case, in order to prevent the laser pulse from breaking into filaments due to transverse instability, it is necessary to ensure matching between the dimensions of the focal spot, the position of the focal region relative to the plasma boundary, and the diameter of the self-focusing channel. This matching was investigated in detail by Mourou *et al.* [33] for plasma targets with sharp boundaries at which the plasma density falls from a finite value to zero across a narrow layer with a thickness less than or on the order of the laser wavelength. The matching condition implies that the laser input numerical aperture should correspond to the effective waveguide numerical aperture. The aperture of the laser beam is governed by the properties of the optical focusing system. The effective waveguide aperture is determined by the dimensions of the self-focusing channel and the plasma density, which in turn depend on the laser field amplitude.

In what follows, we will consider how the characteristic inhomogeneity scale of the plasma density and the presence of the background plasma affect charged particle acceleration in the collisionless plasma approximation.

2. FORMULATION OF THE PROBLEM AND PARAMETERS FOR NUMERICAL SIMULATIONS

In the case under consideration, the process of the interaction of a laser pulse with a finite-thickness plasma slab can be conditionally divided into three stages. In the first (initial) stage, laser radiation penetrates into the plasma. Depending on whether the matching condition is satisfied or not, the laser pulse in the target either takes the form of a directed beam whose energy is localized within a single channel as a

result of self-focusing or it breaks into several filaments. In the latter case, charged particle acceleration is very inefficient, so we will assume that the parameters of the problem satisfy the optimal matching condition. In the second (intermediate) stage, the laser pulse propagates inside the plasma slab. This stage is accompanied by the generation of fast electron beams, the excitation of a quasistatic magnetic field in the self-focusing channel, and the formation of relativistic electromagnetic solitons. In the third (final) stage, the laser pulse reaches the father boundary of the plasma slab and escapes into a vacuum.

The laser pulse parameters that provide optimal ion acceleration regimes were chosen such as it was done in [30]. The simulations were carried out with a 2D version of the REMP (Relativistic Electro-Magnetic Particle-mesh) code, which is based on the particle-in-cell (PIC) method and on the density decomposition method for calculating the electric current density [34]. The code activates a so-called 2D3V model, in which the electromagnetic fields and the charge and current densities depend on two spatial coordinates and time and each plasma quasi-particle is described by two time-dependent spatial coordinates and three time-dependent momentum components. We considered only circularly polarized laser pulses. The characteristic length of the laser pulse was assumed to be $l_\parallel = 7.5\lambda$. Here and below, the length of the pulse, its width $l_\perp$, and the dimensions of the computation region are expressed in units of the laser wavelength λ. It makes sense to speak about the dimensionless amplitude of the focused laser pulse, $a = eE/(m_e\omega c)$, only for a given effective pulse width $l_\perp$, because the energy conservation equation implies that the relationship $a^2 l_\perp = \text{const}$ holds. In this paper, when speaking about the initial laser pulse amplitude, we will mean the laser amplitude in the focal region, where the pulse width is $l_\perp = 0.6$, which indicates that the pulse is focused into a spot with dimensions on the order of one laser wavelength (for a discussion of the relevant regimes, see [33]). In what follows, we will present results from numerical simulations in which the dimensionless amplitude is $a|_{l_\perp = 0.6} = 3$ and $a|_{l_\perp = 0.6} = 10$. In all simulations, the convergence angle α of a focused laser pulse with respect to its optical axis (the x axis) is relatively small: $-\pi/12 < \alpha < \pi/12$. The geometric center of the focal spot is at the point $(x, y) = (20\lambda, 30\lambda)$. The pulse is modeled by specifying its wave front at the boundary $x = 0$ of the computation region, assuming that, in the vacuum region (on the left from the target), its propagation is described by geometrical optics. The pulse envelope (i.e., the distribution of the pulse amplitude along and across the propagation direction before focusing) is specified as a product of two cosines, $[\cos(2\pi x/l_{\parallel\,\text{full}}) + 1]\cos(2\pi y/l_{\perp\,\text{full}})/4$, for $|x| < l_{\parallel\,\text{full}}/2$ and $|y| < l_{\perp\,\text{full}}/2$, where $l_{\parallel\,\text{full}}$ and $l_{\perp\,\text{full}}$ are the full length of the pulse and its full width, respectively. For the given distribution of the pulse amplitude, the effective pulse dimensions are defined by the formulas $l_\parallel = 0.375 l_{\parallel\,\text{full}}$ and $l_\perp = 0.375 l_{\perp\,\text{full}}$.

The dimensions of the computation region in the x and y directions were $60\lambda \times 60\lambda$, the dimensions of numerical cells were $\lambda/16 \times \lambda/16$, and the number of quasi-particles of each species per cell at the point corresponding to the maximal plasma density was equal to 9. The total number of quasi-particles of each species depends on the specified density distribution; in our simulations, it varied from 10^6 to 2×10^6. The form-factor of the quasi-particles was described by a second-order piecewise polynomial [34]. The ion-to-electron mass ratio was assumed to be that for a proton, $m_i/m_e = 1836.15$. The time step was $dt = 0.025\tau$, where $\tau = 2\pi/\omega$ is the electromagnetic wave period.

The target was a plasma slab of finite length in the pulse propagation direction. The slab width was equal to the transverse size of the computation region, and the slab length was varied from 20λ to 30λ. The plasma density profile inside the target was specified as a superposition of a rectangular and a half-sinusoidal distribution. For a rectangular distribution, the plasma density was uniform inside the slab and was equal to zero outside the slab: $n = n_{\max}\theta(x - x_{\min})\theta(x_{\max} - x)$, where $\theta(x)$ is the Heaviside step function, defined as zero for $x < 0$ and as unity for $x > 0$.

For a smooth plasma slab, the density profile along the pulse propagation direction within the slab was described by a half-sinusoidal distribution: $n(x) = n_{\max}\sin[\pi(x - x_{\min})/(x_{\max} - x_{\min})]$. In all simulations, the maximal plasma density at the target center was equal to $n_{\max} = 0.5 n_{\text{cr}}$.

Below, we present results from numerical simulations of laser–plasma interaction for four types of targets with different plasma density profiles. In the first version, the plasma density was uniform over the entire target volume, specifically, it was equal to $n_{\max} = 0.5 n_{\text{cr}}$ inside the slab and to zero outside it. In the second version, the plasma density profile was described by a half-sinusoidal distribution and the plasma background was absent (as in the first version). In the third version, the central rectangular plasma slab was surrounded by an external (background) plasma of density $n_{\text{bg}} = 0.1 n_{\text{cr}}$. In the fourth version, the central slab of a smoothly inhomogeneous plasma (whose density profile was described by a half-sinusoidal distribution) also was surrounded by a background plasma of density $n_{\text{bg}} = 0.1 n_{\text{cr}}$.

The boundary conditions used in simulations corresponded to complete absorption of both the electromagnetic field and the particles at the boundary of the computation region. The field absorption was modeled using Tajima and Lee's method from [35].

3. NUMERICAL RESULTS: EFFECTS OF THE TARGET PLASMA INHOMOGENEITY SCALE AND OF THE BACKGROUND PLASMA ON THE ION ACCELERATION

Recall that we are considering here two laser pulses with the same effective length but with two different focal intensities corresponding to the dimensionless amplitudes $a|_{l_\perp = 0.6} = 3$ and $a|_{l_\perp = 0.6} = 10$. The pulses interact with four types of targets: a uniform target with sharp boundaries and a smoothly nonuniform target, both with and without a background plasma.

We begin with the case of a laser pulse with the dimensionless amplitude $a|_{l_\perp = 0.6} = 3$ at the focal spot. For a typical laser wavelength of $\lambda = 1$ μm, this corresponds to a radiation intensity in the focal region of about $I \approx 1.8 \times 10^{19}$ W/cm^2. In this case, the laser power and laser energy are rather moderate: $P \approx 200$ GW and $E \approx 2$ mJ.

3.1. Interaction of a Laser Pulse with a Plasma Target with Sharp Boundaries in the Absence of a Background Plasma

Here, we consider the interaction between a laser pulse with an amplitude of $a|_{l_\perp = 0.6} = 3$ and a rectangular plasma slab whose density is $n = n_{\max} = 0.5n_{cr}$ inside the interval $15.45 < x < 34.55$ and is zero outside it. The laser pulse is focused onto the left boundary of the plasma slab. For the given plasma density, the laser radiation power exceeds the threshold for relativistic self-focusing. As a result, the electromagnetic field becomes localized in a narrow channel. Over a time of about 60τ, the laser pulse reaches the farther target boundary, having lost a considerable portion of its initial energy. Figure 1 shows the distributions of (a) the z component of the electric field, (b) the ion density, and (c) the electron density at the time $t = 60\tau$. We can see that the pulse self-focusing occurs at the very beginning of the interaction. In the self-focusing channel, relativistic electromagnetic solitons [13, 36–45] in the form of local maxima of the electric field are generated (see Fig. 1a). The ponderomotive pressure of the laser radiation gives rise to channels in the ion and electron densities. As a result, the pulse becomes greatly depleted and, by the time $t = 60\tau$, when the laser radiation approaches the right plasma boundary, the channels become very narrow.

However, although the laser pulse power at the exit from the plasma slab is much lower than that at the entrance to the slab, the spontaneous magnetic field produced in the laser–plasma interaction creates a sufficiently strong charge-separation electric field at the right plasma boundary. This electric field accelerates the ions [30], which form a narrow beam. Such an ion beam can easily be seen in Figs. 2c and 2d, which display the ion phase planes (p_x, x) and (p_x, y) at the time $t = 120\tau$. In the case at hand, the maximal momentum acquired by the ions is about $p_x \approx 0.04m_ic$ (Figs. 2c, 2d), which corresponds to an energy of about $E = 0.8 \times 10^{-3}m_ic^2 \approx 800$ keV. Figures 2a and 2b display the ion and electron density distributions in the (x, y) plane at the time $t = 120\tau$. We can see that the width of the ion and electron channels increases with time. In the region where the solitons have been generated, the electron and ion densities become depressed, giving rise to expanding cavities. The origin of the cavities is attributed to the ponderomotive force of the electromagnetic radiation trapped inside a soliton, and the cavities themselves correspond to the so-called postsolitons (see [42–44]). Postsolitons were first observed by proton imaging [26] in experiments on the interaction of high-intensity laser radiation with plasma [44]. The ions inside postsolitons are also accelerated, which is illustrated by the peaks in the dependence of p_x on x in the central region in Fig. 2c. In postsolitons, however, the ions are usually accelerated to energies that are approximately four times lower than those of the ions generated at the farther boundary of the target.

The main properties of the regime that has been discussed in this section correspond to the case investigated in [30], where it was pointed out that the quasistatic magnetic field plays a fundamentally important role in the ion acceleration at the plasma–vacuum interface.

3.2. Interaction of a Laser Pulse with a Plasma Target Having Sharp Boundaries in the Presence of a Background Plasma

We now discuss the features of the interaction between a laser pulse with an amplitude of $a|_{l_\perp = 0.6} = 3$ and a plasma target whose density is $n = n_{\max} = 0.5n_{cr}$ inside the interval $15.45 < x < 34.55$ and is equal to $0.1n_{cr}$ outside it. As in the case considered in Section 3.1, the laser pulse is focused onto the left boundary of the dense plasma slab. The simulation results are illustrated in Fig. 3.

In the presence of a background plasma, the interaction between laser radiation and a highly inhomogeneous plasma at the instants just before and just after the time $t = 100\tau$ has interesting properties. As in the previous case, the laser pulse reaches the right boundary of the dense plasma slab, having formed self-focusing channels, which are clearly seen in the ion and electron density distributions in Figs. 3b and 3c. At the interface between the higher density plasma slab and the lower density background plasma, wide magnetic field regions are observed (see Fig. 3a, which presents the distribution of the magnetic field component B_z in the (x, y) plane). On the opposite sides of the laser pulse axis, the magnetic field points in opposite directions. This structure is a magnetic dipole, which, in spite of the presence of the plasma background, expands along

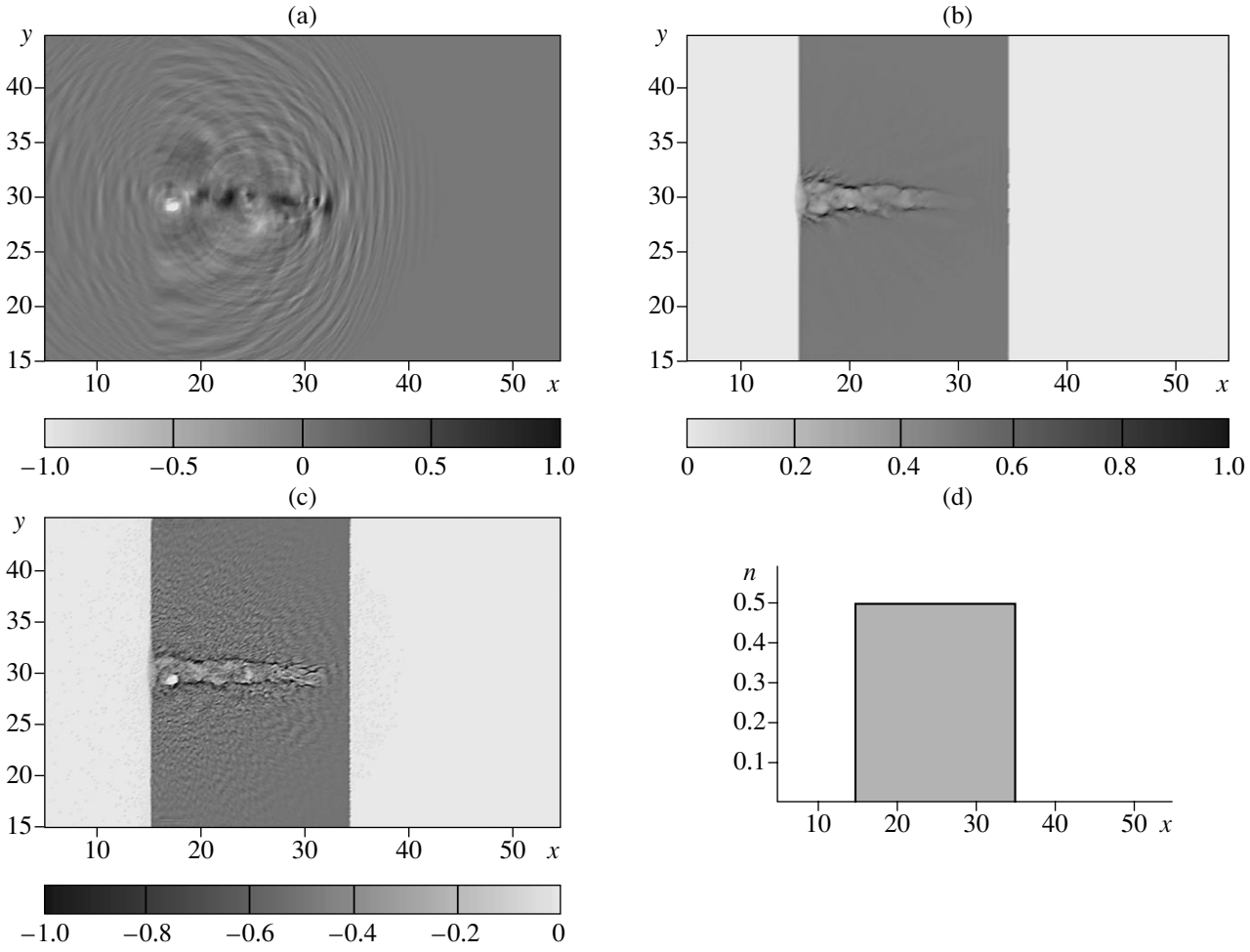

Fig. 1. Distributions of (a) the z component E_z of the electric field, (b) the ion density n_i, and (c) the electron density n_e in the (x, y) plane at the time $t = 60\tau$. Plot (d) shows the plasma density profile n within the target.

the y axis in a direction orthogonal to the local electron density gradient. Under the action of the magnetic pressure force, which is proportional to the gradient of the magnetic field squared, $\propto -\nabla B^2/8\pi$, the electron plasma component (and, after a certain time delay, the ion plasma component too) is displaced into the plasma slab, giving rise to a large-scale quasistatic electric field. The electric field so generated accelerates the ions from the axial region along the x axis and focuses them to it. This acceleration scenario corresponds to the ion acceleration regime described in [30]. The ion phase plane (p_x, y) at the time $t = 100\tau$ is shown in Fig. 3d. The maximal ion energy in the beam is equal to $E = 0.2 \times 10^{-3} m_i c^2 \approx 200$ keV.

3.3. Interaction of a Laser Pulse with a Smoothly Nonuniform Plasma Target in the Absence of a Background Plasma

Here, we discuss the interaction between a laser pulse with an effective length of $l_\parallel = 7.5\lambda$ and amplitude of $a|_{l_\perp = 0.6} = 3$ and a smoothly nonuniform target in the absence of a background plasma. Figure 4 illustrates typical distributions of (a) the quasistatic magnetic field, (b) the ion density, and (c) the electron density in the (x, y) plane at the time $t = 120\tau$ and also shows the ion phase planes (d) (p_x, x) and (e) (p_x, y) at the same time.

Let us consider Figs. 4a–4c. By the time $t = 120\tau$, the laser pulse has already escaped from the computation region. It can be seen that, in the electron and ion density distributions, there is a long-lived plasma filament at the channel axis, in which the current is produced by fast electrons. In Fig. 4a, we can see a large-amplitude spontaneous magnetic field and the electron vortices associated with it [45–47]. The dimensionless amplitude of the z component of the magnetic field is approximately equal to $B_z \approx 0.6$. The magnetic field is normalized to $m\omega c/e$; i.e., the ratio of the electron gyrofrequency to the laser frequency is equal to about $\omega_{Be}/\omega \approx 0.6$. Taking into account that the maximum

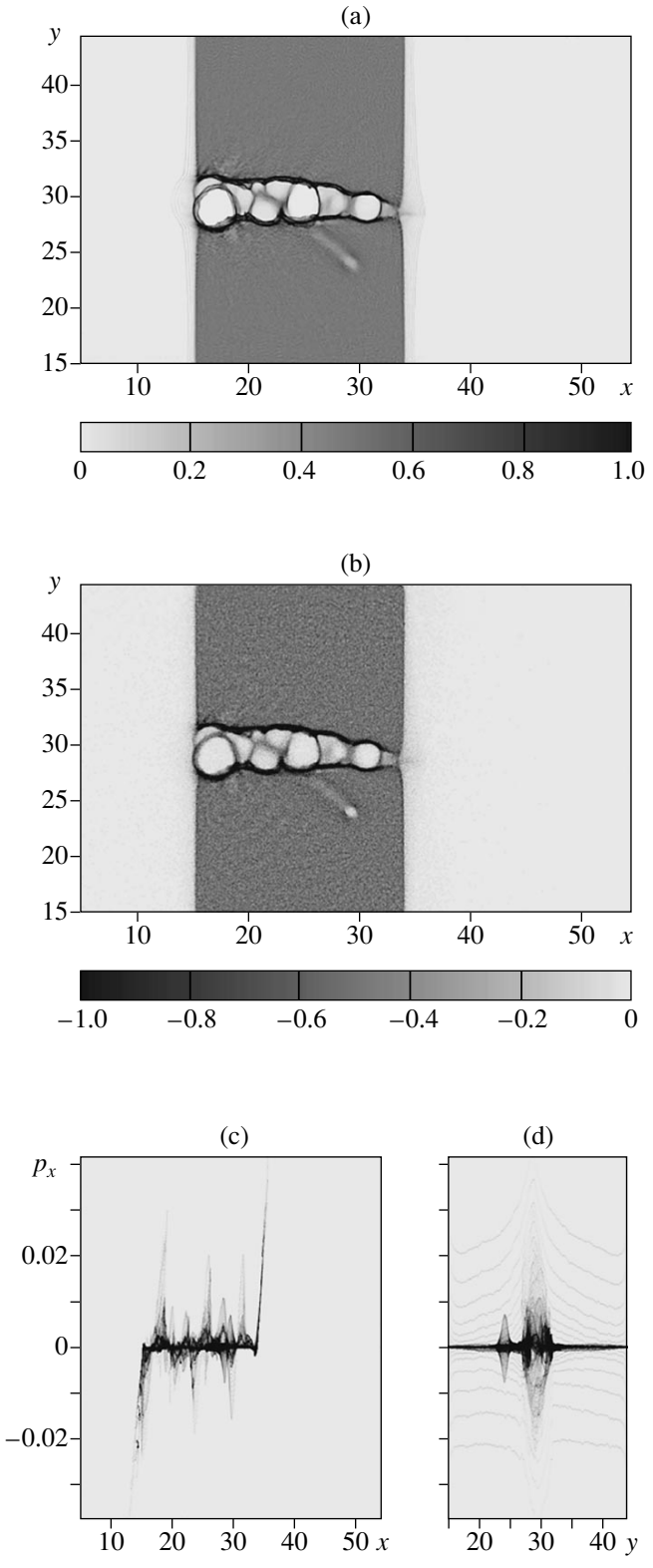

Fig. 2. Distributions of (a) the ion density n_i and (b) the electron density n_e in the (x, y) plane and (c, d) the ion phase planes (p_x, x) and (p_x, y) at the time $t = 120\tau$. Here and in the subsequent figures, the ion momentum is normalized to $m_i c$.

laser radiation amplitude in the focal region is equal to $a|_{l_\perp = 0.6} = 3$, this indicates that a substantial portion of the energy of the incident laser pulse is converted into the energy of the magnetic dipole and the kinetic energy of the electron vortex motion.

Note that, in the regime under consideration, the quasistatic magnetic field is localized inside the plasma (rather than in a vacuum, as in the case with a rectangular plasma slab). A comparison between the electron and ion density distributions at the times $t = 60\tau$, $t = 120\tau$, and $t = 300\tau$ shows that the electron density within the magnetic dipole progressively decreases. The ion density also decreases, but far more gradually than does the electron density. This process results in the formation of a thin dense plasma shell, which separates the target from the region occupied by the spontaneous magnetic field. The region where the magnetic field is localized expands across the plasma density gradient. The expansion, however, is not as rapid as that in the regimes discussed above.

The charge-separation electric field that is generated in the magnetic dipole region accelerates ions in both forward and backward directions. In the phase planes (p_x, x) and (p_x, y) (see Figs. 4d, 4e), the beams of accelerated ions are seen to have the shape of wings. The maximum momentum of the ions accelerated at the magnetic dipole axis by the time $t = 120\tau$ is equal to about $p_x \approx 0.015 m_i c$, which corresponds to an energy of about $E = 0.1 \times 10^{-3} m_i c^2 \approx 100$ keV. As time progresses, the plasma filament decays.

By the time $t = 300\tau$, the maximum momentum of the ions that have formed the filament is approximately equal to $p_x \approx 0.02 m_i c$. At the magnetic dipole boundary, the ions are accelerated to the same maximum momentum.

3.4. Interaction of a Laser Pulse with a Smoothly Nonuniform Plasma Target in the Presence of a Background Plasma

We proceed with the analysis of the interaction between a laser pulse with an effective length of $l_\parallel = 7.5\lambda$ and amplitude of $a|_{l_\perp = 0.6} = 3$ and a smoothly nonuniform target in the presence of a background plasma. The numerical results that were obtained for the time $t = 300\tau$ are presented in Fig. 5.

At all earlier times (e.g., at $t = 120\tau$), the structures in the plasma develop in much the same way as in the above regime of the interaction of a laser pulse with a smoothly nonuniform target in the absence of a background plasma. In particular, the magnetic dipole forms in the same region. In the absence of a background plasma, however, the dipole expands in a transverse direction along the target boundary. The effect of the plasma background is to drive the magnetic dipole into motion along its axis. This difference reflects the fundamental properties of the motion of vortex structures

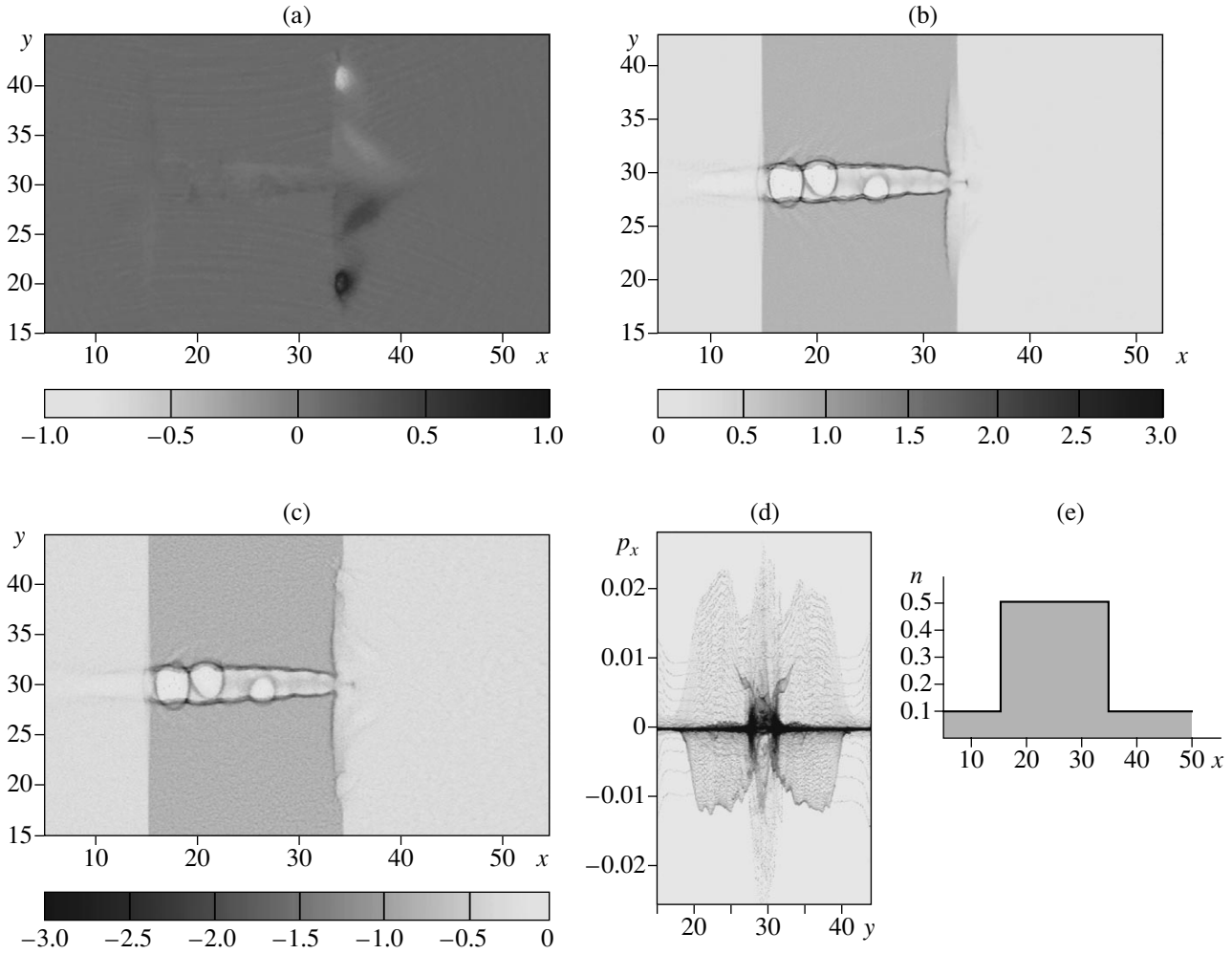

Fig. 3. Distributions of (a) the z component B_z of the magnetic field, (b) the ion density n_i, and (c) the electron density n_e in the (x, y) plane and (d) the ion phase plane (p_x, y) at the time $t = 100\tau$. Plot (e) shows the plasma density profile n within the target.

[48]. When the plasma target boundary is sharp, the vortices move along it. In a homogeneous plasma, a dipole (a pair of vortices) moves along its axis. Hence, in the case in question, the conditions in a smoothly nonuniform plasma target in the presence of a background plasma are close to those characteristic of a homogeneous medium.

From Fig. 5, which displays the (a) electron and (b) ion density distributions, we can see that, by the time $t = 300\tau$, large-scale cavities from which the plasma is expelled form inside the magnetic dipole. The process by which the plasma is expelled from the cavities is similar to that described in [49, 50] for a single vortex. In contrast to a solitary isolated vortex, a fundamental property of the dipole structure is that there is an electric current that flows along the dipole axis and is localized in a thin plasma filament. As the dipole vortex propagates toward the plasma region with a lower density, the number of particles at the filament axis decreases. The electrons escape from the current-carrying filament faster than do the ions. As a result, the current filament becomes electrically charged and undergoes a Coulomb explosion. The ions expand in a transverse direction with respect to the filament and gain a certain energy. The energy acquired by the ions in the vicinity of the point ($x = 42$, $y = 30$) in Fig. 5b is the highest. In the vicinity of this point, the region with a strong quasistatic electric field forms and starts propagating along the x axis. The beam of fast ions accelerated in this region at the magnetic dipole axis is clearly seen in Fig. 5d. The maximum ion momentum in such a spike is equal to about $p_x \approx 0.056 m_i c$, which corresponds to an energy of about $E \approx 1.5$ MeV.

3.5. Interaction of a High-Power Laser Pulse with a Plasma Target

Finally, in analogy with the previous section, we consider the interaction between a laser pulse with an amplitude of $a|_{l_\perp = 0.6} = 10$ and a smoothly nonuniform

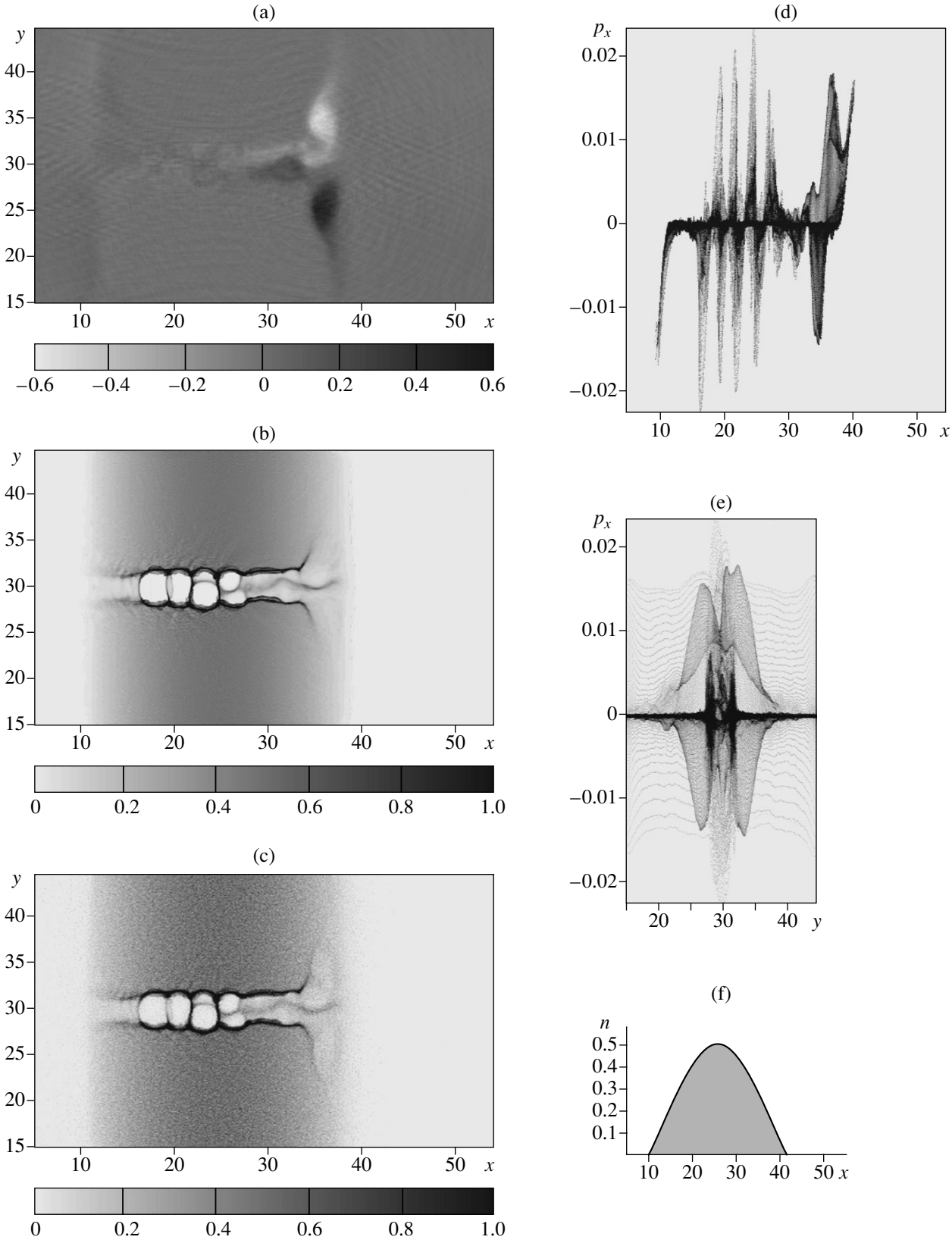

Fig. 4. Distributions of (a) the z component B_z of the magnetic field, (b) the ion density n_i, and (c) the electron density n_e in the (x, y) plane and (d, e) the ion phase planes (p_x, x) and (p_x, y) at the time $t = 120\tau$. Plot (f) shows the plasma density profile n within the target.

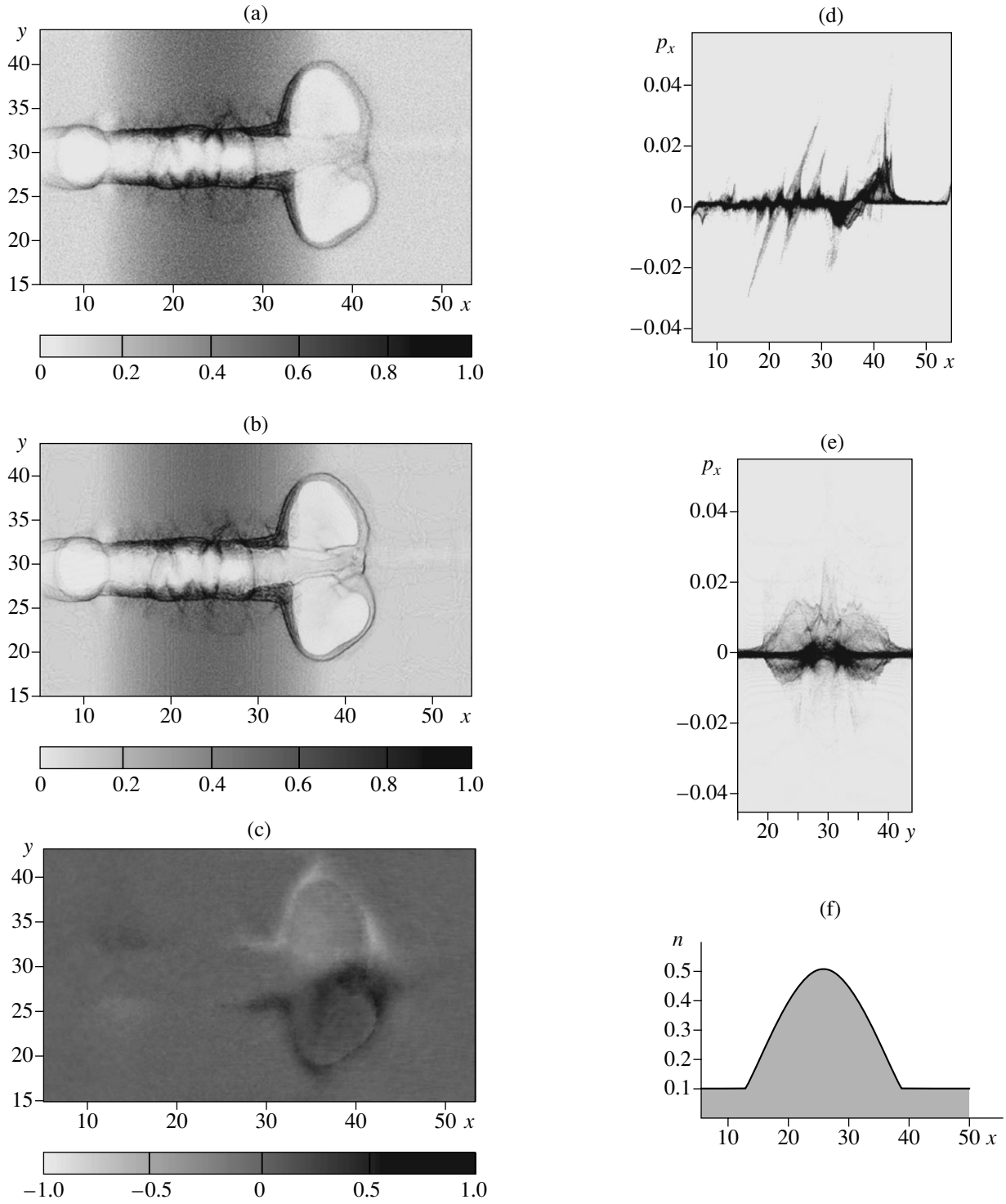

Fig. 5. Distributions of (a) the electron density n_e, (b) the ion density n_i, and (c) the z component B_z of the magnetic field in the (x, y) plane and (d, e) ion phase planes (p_x, x) and (p_x, y) at the time $t = 300\tau$. Plot (f) shows the plasma density profile n within the target.

target in the presence of a background plasma. For a laser wavelength of $\lambda = 1$ μm, this corresponds to a laser intensity in the focal region of $I \approx 2 \times 10^{20}$ W/cm^2 and a power of $P \approx 2$ TW.

The results of computer simulations for this case are illustrated in Figs. 6 and 7, which refer to the times $t = 120\tau$ and 300τ, respectively. In this case, a decisive role is played by the generation of a quasistatic magnetic

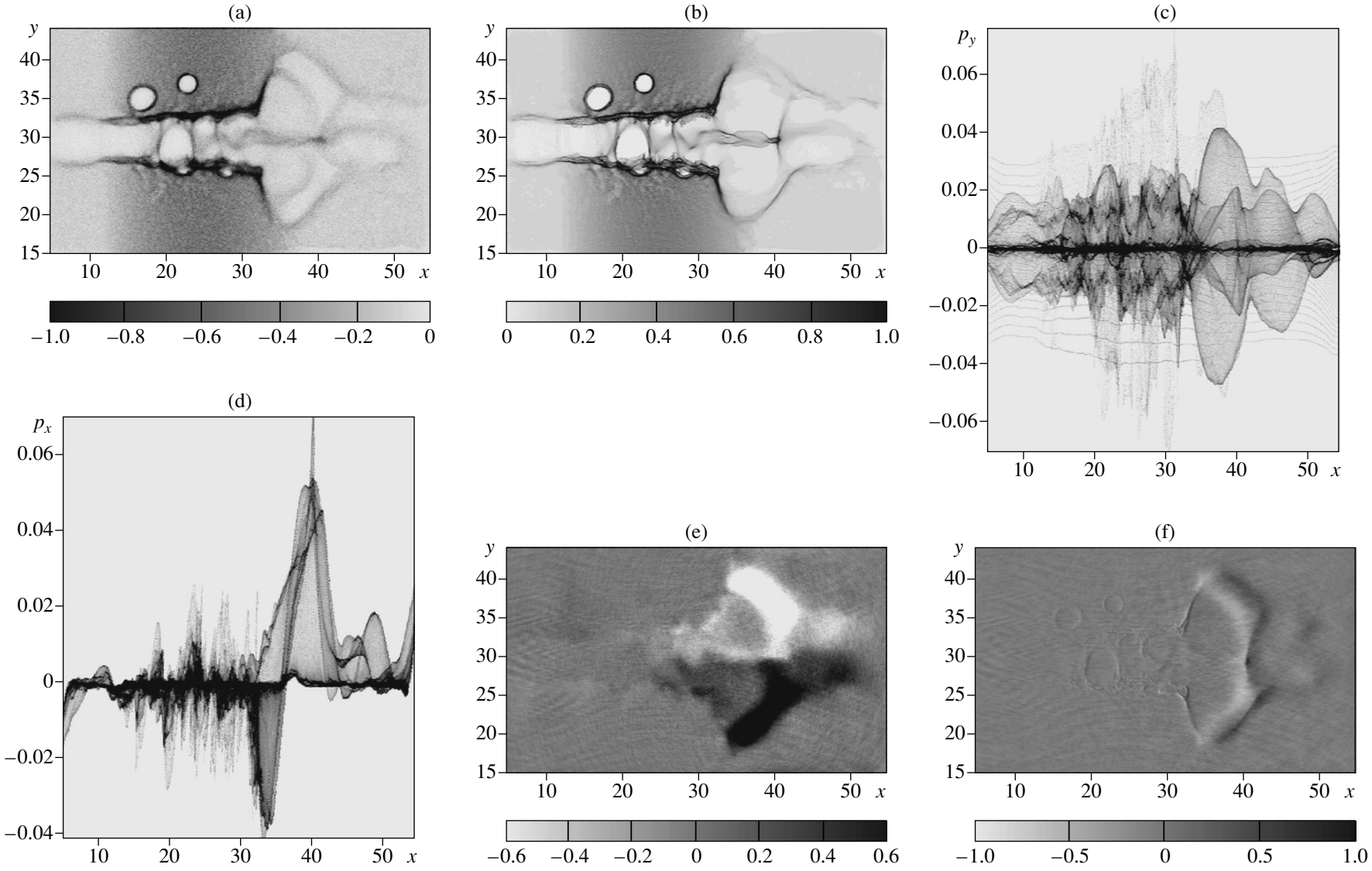

Fig. 6. Distributions of (a) the electron density n_e, (b) the ion density n_i, (e) the z component B_z of the magnetic field, and (f) the x component E_x of the electric field in the (x, y) plane and (c, d) ion phase planes (p_y, x) and (p_x, x) at the time $t = 120\tau$.

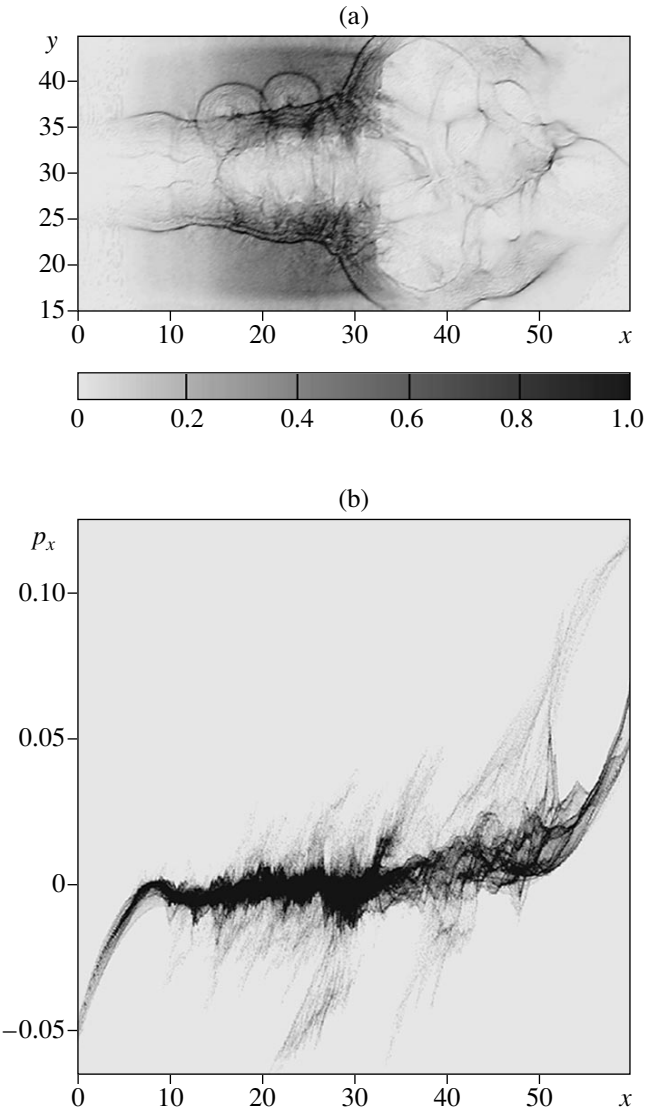

Fig. 7. (a) Distribution of the ion density n_i in the (x, y) plane and (b) ion phase plane (p_y, x) at the time $t = 300\tau$.

field and by the nonlinear evolution of the current-carrying vortex structures associated with it. The electron and ion density distributions in Figs. 6a and 6b clearly show the formation of the self-focusing channel, the postsoliton-related cavities, and a dipole current-carrying vortex structure on the right side of the computation region. In the phase plane (p_y, x) (Fig. 6c), we observe the ion beams ejected in the transverse direction from the postsolitons and the ion spikes in the shell of the magnetic dipole. One can see the beams of fast ions accelerated across the self-focusing channel; these beams are similar to those discussed in [51]. The energy of the ions generated during the decay of the current filament at the axis of the magnetic dipole is the highest. These ions are observed to form a short beam in the vicinity of the point $(x = 42, y = 0)$ (see Fig. 6d). Presumably, the oppositely directed components of the magnetic field in this region, annihilate one another: Fig. 6e clearly shows a highly nonuniform magnetic field that changes its sign there. The rapidly varying magnetic field produces a strong electric field (Fig. 6f), that accelerates the ions. This is followed by the merging and splitting of the current vortex structures, accompanied by the formation of a system of thin plasma filaments at the boundaries of the cavities from which the plasma has been expelled. These filaments are seen in the ion density distribution in the (x, y) plane (Fig. 7a). By the time $t = 300\tau$, fast ions have acquired an energy of about $E \approx 6$ MeV, as can be inferred from Fig. 7b. Although in this case (as in all the cases considered above) the ions at the left and right interfaces between the plasma and vacuum are also accelerated, the energy of the ions generated during the decay of the current filament at the axis of the magnetic dipole turns out to be appreciably higher.

4. CONCLUSIONS

We have presented the results from PIC simulations of ion acceleration in the interaction of terawatt laser pulses a subcritical plasma. In simulations, short laser pulses were focused onto the target surface, into a focal spot with dimensions comparable to the laser radiation wavelength. Such interaction conditions correspond to the so-called λ^3 regime, which makes it possible to achieve unsurpassed laser intensities for given values of the pulse power and energy [15, 33]. Under these conditions, the interaction of a relativistically strong laser pulse with the target material is accompanied by the generation of numerous nonlinear structures. In particular, a self-focusing channel forms and relativistic electromagnetic solitons develop and then evolve into postsolitons. In addition, strong electric fields are generated at the plasma–vacuum interfaces. In all these structures, electrical quasineutrality is locally violated. The most efficient ion acceleration, however, is associated with the generation of a quasistatic magnetic field. In this case, the electric current in the plasma is produced by fast electron beams according to the scenario described in [31]. In an inhomogeneous plasma, the magnetic field evolves into a large-scale dipole structure. In a highly inhomogeneous plasma such that its density varies on a spatial scale less than or on the order of the characteristic diameter of the self-focusing channel, the magnetic field region expands along the plasma boundary in a direction perpendicular to the plasma density gradient. The magnetic pressure displaces the electron plasma component with respect to the plasma ions, thereby producing a long-lived large-scale electric field that accelerates the ions at the plasma–vacuum interface [30]. In a plasma with a smooth density profile (the density varies on a scale greater than the characteristic diameter of the self-focusing channel), the magnetic dipole and the associated electron vortex dipole move

in the propagation direction of the laser pulse. As the magnetic dipole propagates toward the lower plasma density and expands in a transverse direction, the electron density in the current filament at the dipole axis decreases to values at which the charge quasineutrality condition fails to hold. As a result, the current filament undergoes a Coulomb explosion and the magnetic field vanishes. The rapid decrease in the magnetic field induces a strong electric field at the dipole axis, which accelerates ions to maximal energies. In this respect, such ion acceleration is analogous to the acceleration of charged particles in high-current plasma discharges [52]. Hence, our investigations have further confirmed the conclusion made earlier in [30, 53] about the fundamentally important role of the generation of spontaneous magnetic fields in a laser plasma in the relativistic interaction regime.

ACKNOWLEDGMENTS

We are grateful to M. Borghesi, K. Koyama, and P. Norreys for valuable discussions. This work was supported in part by INTAS (grant no. 0233), MEXT (Japan), and CREST-JST (Japan).

REFERENCES

1. A. V. Gurevich, L. V. Pariĭskaya, and L. P. Pitaevskiĭ, Zh. Éksp. Teor. Fiz. **49**, 647 (1965) [Sov. Phys. JETP **22**, 449 (1966)].
2. J. Denavit, Phys. Rev. Lett. **69**, 3052 (1992).
3. W. S. Lawson, P. W. Palumbo, and D. J. Larson, Phys. Plasmas **4**, 788 (1997).
4. T. Zh. Esirkepov, I. Sentoku, K. Mima, *et al.*, Pis'ma Zh. Éksp. Teor. Fiz. **70**, 80 (1999) [JETP Lett. **70**, 82 (1999)].
5. A. G. Zhidkov, A. Sasaki, T. Tajima, *et al.*, Phys. Rev. E **60**, 3273 (1999).
6. P. Mora, Phys. Rev. Lett. **90**, 185002 (2003).
7. V. E. Kovalev and V. Yu. Bychenkov, Phys. Rev. Lett. **90**, 185 004 (2003).
8. M. Passoni, V. T. Tikhonchuk, M. Lontano, and V. Yu. Bychenkov, Phys. Rev. E **69**, 026411 (2004).
9. T. Tajima, Jpn. J. Soc. Therap. Rad. Oncol. **9**, 83 (1998).
10. A. Maksimchuk, S. Gu, K. Flippo, *et al.*, Phys. Rev. Lett. **84**, 4108 (2000).
11. E. L. Clark, K. Krushelnick, M. Zepf, *et al.*, Phys. Rev. Lett. **85**, 1654 (2000).
12. R. A. Snavely, M. H. Key, S. P. Hatchett, *et al.*, Phys. Rev. Lett. **85**, 2945 (2000).
13. S. V. Bulanov, F. Califano, G. I. Dudnikova, *et al.*, in *Reviews of Plasma Physics*, Ed. by V. D. Shafranov (Kluwer Academic, New York, 2001), Vol. 22, p. 227.
14. J. Mendonca, J. Davies, and M. Eloy, Meas. Sci. Technol. **12**, 1801 (2001).
15. G. Mourou, T. Tajima, and S. V. Bulanov, submitted to Rev. Mod. Phys.
16. R. Bingham, J. T. Mendonca, and P. K. Shukla, Plasma Phys. Controlled Fusion **46**, R1 (2004).
17. G. A. Mourou, C. P. J. Barty, and M. D. Perry, Phys. Today **51**, 22 (1998).
18. M. Roth, T. E. Cowan, M. H. Key, *et al.*, Phys. Rev. Lett. **86**, 436 (2001).
19. V. Yu. Bychenkov, W. Rosmus, A. Maksimchuk, *et al.*, Fiz. Plazmy **27**, 1076 (2001) [Plasma Phys. Rep. **27**, 1017 (2001)].
20. S. Atzeni, M. Temporal, and J. J. Honrubia, Nucl. Fusion **42** (2002).
21. S. V. Bulanov and V. S. Khoroshkov, Fiz. Plazmy **28**, 493 (2002) [Plasma Phys. Rep. **28**, 453 (2002)].
22. S. V. Bulanov, T. Zh. Esirkepov, V. S. Khoroshkov, *et al.*, Phys. Lett. A **299**, 240 (2002).
23. E. Fourkal, B. Shahine, M. Ding, *et al.*, Med. Phys. **29**, 2788 (2002).
24. V. Malka, S. Fritzler, E. Lefebvre, *et al.*, Med. Phys. **31**, 1587 (2004).
25. K. W. D. Ledingham, P. McKenna, and R. P. Singhal, Science **300**, 1107 (2003).
26. M. Borghesi, D. H. Campbell, A. Schiavi, *et al.*, Phys. Plasmas **9**, 2214 (2002).
27. S. V. Bulanov, T. Esirkepov, P. Migliozzi, *et al.*, hep-ph/0404190 (2004-04-27); Nucl. Instrum. Methods Phys. Res. A (in press).
28. T. Esirkepov, M. Borghesi, S. V. Bulanov, *et al.*, Phys. Rev. Lett. **92**, 175003 (2004).
29. G. S. Sarkisov, V. Yu. Bychenkov, V. N. Novikov, *et al.*, Phys. Rev. E **59**, 7042 (1999).
30. A. V. Kuznetsov, T. Zh. Esirkepov, F. F. Kamenets, and S. V. Bulanov, Fiz. Plazmy **27**, 225 (2001) [Plasma Phys. Rep. **27**, 211 (2001)].
31. G. A. Askar'yan, S. V. Bulanov, F. Pegoraro, and A. M. Pukhov, Pis'ma Zh. Éksp. Teor. Fiz. **60**, 240 (1994) [JETP Lett. **60**, 251 (1994)].
32. K. Matsukado, T. Zh. Esirkepov, H. Daido, *et al.*, Phys. Rev. Lett. **91**, 215001 (2003).
33. G. Mourou, Z. Chang, A. Maksimchuk, *et al.*, Fiz. Plazmy **28**, 14 (2002) [Plasma Phys. Rep. **28**, 12 (2002)].
34. T. Zh. Esirkepov, Comput. Phys. Commun. **135**, 144 (2001).
35. T. Tajima and Y. C. Lee, J. Comput. Phys. **42**, 406 (1981).
36. J. H. Marburger and R. F. Tooper, Phys. Rev. Lett. **35**, 1001 (1975).
37. N. L. Tsintsadze and D. D. Tskhakaya, Zh. Éksp. Teor. Fiz. **72**, 480 (1977) [Sov. Phys. JETP **45**, 252 (1977)].
38. V. A. Kozlov, A. G. Litvak, and E. V. Suvorov, Zh. Éksp. Teor. Fiz. **76**, 148 (1979) [Sov. Phys. JETP **49**, 75 (1979)].
39. T. Zh. Esirkepov, F. F. Kamenets, S. V. Bulanov, and N. M. Naumova, Pis'ma Zh. Éksp. Teor. Fiz. **70**, 80 (1999) [JETP Lett. **70**, 82 (1999)].
40. D. Farina and S. V. Bulanov, Phys. Rev. Lett. **86**, 5289 (2001).
41. S. Poornakala, A. Das, P. K. Kaw, *et al.*, Phys. Plasmas **9**, 3802 (2002).

42. N. M. Naumova, S. V. Bulanov, T. Zh. Esirkepov, *et al.*, Phys. Rev. Lett. **87**, 185004 (2001).

43. T. Zh. Esirkepov, K. Nishihara, S. V. Bulanov, and F. Pegoraro, Phys. Rev. Lett. **89**, 275002 (2002).

44. M. Borghesi, S. Bulanov, D. H. Campbell, *et al.*, Phys. Rev. Lett. **88**, 135002 (2002).

45. S. V. Bulanov, M. Lontano, T. Zh. Esirkepov, *et al.*, Phys. Rev. Lett. **76**, 3562 (1996).

46. S. K. Venkatesan, Phys. Plasmas **4**, 3001 (1997).

47. A. V. Gordeev and T. V. Losseva, Fiz. Plazmy **26**, 1030 (2000) [Plasma Phys. Rep. **26**, 965 (2000)].

48. H. Lamb, *Hydrodynamics* (Cambridge University Press, Cambridge, 1932).

49. A. V. Gordeev and T. V. Losseva, Pis'ma Zh. Éksp. Teor. Fiz. **70**, 669 (1999) [JETP Lett. **70**, 684 (1999)].

50. J. I. Sakai, S. Saito, H. Mae, *et al.*, Phys. Plasmas **9**, 2959 (2002).

51. F. Pegoraro, S. V. Bulanov, F. Califano, *et al.*, IEEE Trans. Plasma Sci. **28**, 1226 (2000).

52. B. A. Trubnikov and S. K. Zhdanov, Zh. Éksp. Teor. Fiz. **70**, 92 (1976) [Sov. Phys. JETP **43**, 48 (1976)].

53. G. A. Askar'yan, S. V. Bulanov, F. Pegoraro, and A. M. Pukhov, Comm. Plasma Phys. Controlled Fusion **17**, 35 (1995).

Translated by O.E. Khadin

Plasma Physics Reports, Vol. 31, No. 5, 2005, pp. 382–391. Translated from Fizika Plazmy, Vol. 31, No. 5, 2005, pp. 422–431.

PLASMA DYNAMICS

Study of X-ray and Neutron Emission in Experiments with Al Wires in an MA Plasma Focus

P. Kubeš[1], J. Kravárik[1], D. Klír[1], P. Barvir[1], M. Scholz[2], M. Paduch[2], K. Tomaszewski[2], I. Ivanova-Stanik[2], B. Bieńkowska[2], L. Karpinski[2], L. Juha[3], J. Krása[3], M. J. Sadowski[4], L. Jakubowski[4], A. Szydłowski[4], A. Banaszak[4], H. Schmidt[5], and V. M. Romanova[6]

[1] *Czech Technical University, Technicka 2, 166 27 Prague, Czech Republic*

[2] *Institute of Plasma Physics and Laser Microfusion, 23 Hery St., 00908 Warsaw, Poland*

[3] *Institute of Physics, Academy of Sciences of the Czech Republic, Na Slovance 2 182 21 Prague 8, Czech Republic*

[4] *Andrzej Soltan Institute of Nuclear Studies, 05-400 Otwock-Swierk, Poland*

[5] *International Center on Dense Magnetized Plasma, 23 Hery St., 00908 Warsaw, Poland*

[6] *Lebedev Physical Institute, Russian Academy of Sciences, Leninskiĭ pr. 53, Moscow, 119991 Russia*

Received January 22, 2004; in final form, April 20, 2004

Abstract—Results are presented from experimental studies of the correlation between X-ray and neutron emissions generated in the implosion of a deuteron plasma shell onto an Al wire. The experiments were carried out on the PF-1000 facility at currents of 1.5–1.8 MA. An Al wire 80 μm in diameter and 7–9 cm in length was placed at the end of the inner electrode. During the implosion of the plasma shell, Al *K*-shell X-rays were first emitted at the dip of the current derivative. After the X-ray pulse, a relatively stable corona with a diameter of 2–3 mm and lifetime of a few hundred nanoseconds formed around the wire. The presence of the wire did not considerably reduce the total neutron yield (at most 10^{11} neutrons per shot) in comparison to discharges without a wire. As a rule, the intensity of neutron emission was maximal a few tens of nanoseconds after the peak of X-ray emission. A detailed comparison of two shots with low and high neutron yields have shown that the neutron yield depends on the configuration and dynamics of the discharge. The possible influence of the self-generated axial component of the magnetic field on the development of the plasma focus and the acceleration of fast deuterons is discussed. © *2005 Pleiades Publishing, Inc.*

1. INTRODUCTION

Interest in plasma focus (PF) discharges is motivated by the high efficiency of X-ray generation, the high energy of the accelerated electrons and ions, and (when deuterium is used as a working gas) the production of neutrons in such discharges. In recent years, a number of interesting results have been obtained in experiments with PF discharges, e.g., in experiments on liner implosion carried out on the PF-3 facility [1] at the Kurchatov Institute of Atomic Energy (Moscow) and in studies performed under the program of the International Center for Dense Magnetized Plasmas on the PF-1000 facility at the Institute of Plasma Physics and Laser Microfusion (Warsaw). PF-1000 experiments are mainly concentrated on studying the PF dynamics with the help of comprehensive X-ray and neutron diagnostics. In some experiments performed in recent years, a fine wire was placed at the end of the inner electrode. The presence of the wire allows one to study the influence of the dense plasma formed around the wire on the generation of high-energy particles and photons. The wire also serves as an active diagnostic probe in the PF axial region. The dense cylindrical plasma shell and the central part of the wire, which remains in a solid state, also reduce the instability growth rate. In experiments carried out on PF 1000, X-ray emission in the *K*-shell lines of Al ions [2] was observed. It was demonstrated that the presence of an Al or a C wire has little effect on the neutron yield. In [3–6], results from the neutron measurements were presented and the acceleration of fast deuterons in different pinch devices was discussed. In [3], it was supposed that neutrons were produced in the dense plasma column and a model was proposed for the acceleration of deuterons by the axial electric field generated outside the dense plasma in the course of the $m = 0$ instability when the pinch radius decreased below 500 μm. It was observed that the neutron yield reduced in the presence of impurities or a weak external axial magnetic field. It was also assumed that electrons and deuterons were accelerated simultaneously. In [4], neutron emission was observed simultaneously with X-ray emission at the instant at which the current time derivative dI/dt vanished. This instant also coincided with the onset of the fast $m = 0$ instability. In contrast, in [5], neutron emission was observed after the hot spot phase, when no rapid pinching or expansion of the plasma occurred. In this stage, the pinch seemed to be composed of high-density regions interspersed in the axial direction with tenuous regions (islands), in which the plasma density was at least two orders of magnitude lower. The characteristic size of these islands was a few

millimeters. One or two hard X-ray pulses with a photon energy of above 1 MeV and duration of 20–100 ns were observed between 120 and 200 ns. Neutrons with an upper energy of 5 MeV were assumed to be generated due to the deceleration of the beam in the plasma target. They were emitted simultaneously with the beginning of the first hard X-ray (HXR) pulse. Two conceptual models were proposed to explain the energy and duration of the HXR and neutron pulses. The first model supposes that MeV deuterons are accelerated by the induction field arising due to the rapid pinch contraction to a radius of less than 1 μm. According to the second model, the accelerating electric field is generated due to the local explosive increase in $\partial B/\partial t$ in a tenuous plasma region. In this case, however, the question arises about the duration of the neutron pulses. A detail study of the fusion processes in the Poseidon PF device was carried out in [6], in which results from measurements of fast deuterons, as well as fusion protons and neutrons produced in D–D reactions, were described. The dissipation of the fast deuterium beam in a pinching PF discharge was explained by the interaction of the beam with the target plasma and the gyration of particles in the self-generated magnetic field. In those experiments, two neutron pulses were observed. The first pulse was generated in the quiet phase at the drop of dI/dt, while the second one was detected in the unstable (disruption) pinch phase, 100 ns after the first pulse. The authors of [6] noted good agreement between theory and experiment for deuterons with energies of 15–60 keV in the quiet phase and 40–120 keV in the unstable phase. Neutrons and protons were assumed to be generated mainly in the dense plasma in the quiet phase and in the low-density plasma surrounding the pinch in the unstable phase. The radial deflection of the protons trajectories that was detected by a pinhole camera was explained by the presence of an azimuthal current, which comprised 40–60% of the axial current. The absolute number of fast deuterons was about 0.1% of the initial number of ions in the PF pinch, and their energy was about 1% of the energy stored in the capacitor bank.

At present, mechanisms for fusion reactions and the generation of fast electrons and deuterons in Z-pinches are still under discussion. In this paper, we describe results from the studies of XUV, X-ray, and neutron emission on the PF-1000 facility and compare them to the results obtained in [3–6].

2. EXPERIMENTAL SET UP

The experiments were performed on the PF-1000 facility with a stored electrical energy of 600–650 kJ, voltage of 30–33 kV, and maximal current of 1.5–1.8 MA. Both the anode and cathode were 600 mm in length. The outer electrode (cathode) 400 mm in diameter was assembled of 24 stainless-steel rods. The inner annular electrode (anode) 230 mm in diameter was made of copper and was mounted on an aluminum insulator. An Al wire 80 μm in diameter and 7–9 cm in length was placed at the end of the anode along its axis and had no galvanic contact with the anode. The working chamber was filled with deuterium at a pressure of 3 torr.

The diagnostics used allowed us to measure side-on radiation in a wide spectral range (from visible to HXR range) with temporal, spatial, and spectral resolution. The arrangement of the diagnostics is shown in Fig. 1a. We employed two soft X-ray (SXR) microchannel-plate (MCP) detectors (henceforth referred to as MCP1 and MCP2). The sensitive surface of the first detector was divided into four quadrants and that of the second detector was divided into four strips. Both detectors were covered with a 5.2-μm polyester (C_8H_8) film, which transmitted photons with energies of 200–300 eV and above 600 eV [7]. The exposure time and the time interval between exposures were 2 and 10 ns, respectively. A PIN silicon diode with a 10-μm Be filter detected X-ray emission with photon energies above 600 eV. Two optical frame cameras with a gating time of 1 ns and a time interval between frames of 20 ns imaged the emitting plasma in the visible spectral range. A Ne102a scintillator with a 10-μm Al filter detected X-ray emission with photon energies of 1.0–1.8 keV and above 3 keV. The slit of the optical streak camera was oriented perpendicular to the wire and imaged the plasma region at a distance of 1.5 cm from the anode end. A 2D time-integrating mica crystal spectrograph with a 10-μm Be filter recorded Al *K*-shell lines. Fast electrons with energies above 100 keV were recorded with a Cherenkov detector. Three scintillation probes (SPs) located a distance of 7 m from the discharge (downstream probe SP1, upstream probe SP3, and side-on probe SP2) were used to perform time-resolved measurements of HXR emission (behind a 7.5-cm Pb screen) and neutron emission (see Fig. 1b). The neutron yield was measured with indium- and silver-activation counters. The diagnostic setup is described in more detail in [7].

3. EXPERIMENTAL RESULTS

In order to correctly interpret results obtained in experiments with Z-pinch discharges (each of which shows its own specific features), it is necessary to use comprehensive diagnostics with temporal, spatial, and spectral resolution. Here, we report on the results from eight shots with a wire and a few tens of shots without a wire. Results from shot nos. 2057 and 2074 will be described in more detail because of the most comprehensive data set obtained in these discharges, their suitable images, and their interesting specific features: one discharge with a very low neutron yield and another with a high neutron yield. The data on shot no. 2057 (with a neutron yield of 10^9) are presented in Figs. 2–6, and those on shot no. 2074 (with a neutron yield of 10^{11}) are presented in Figs. 7–11.

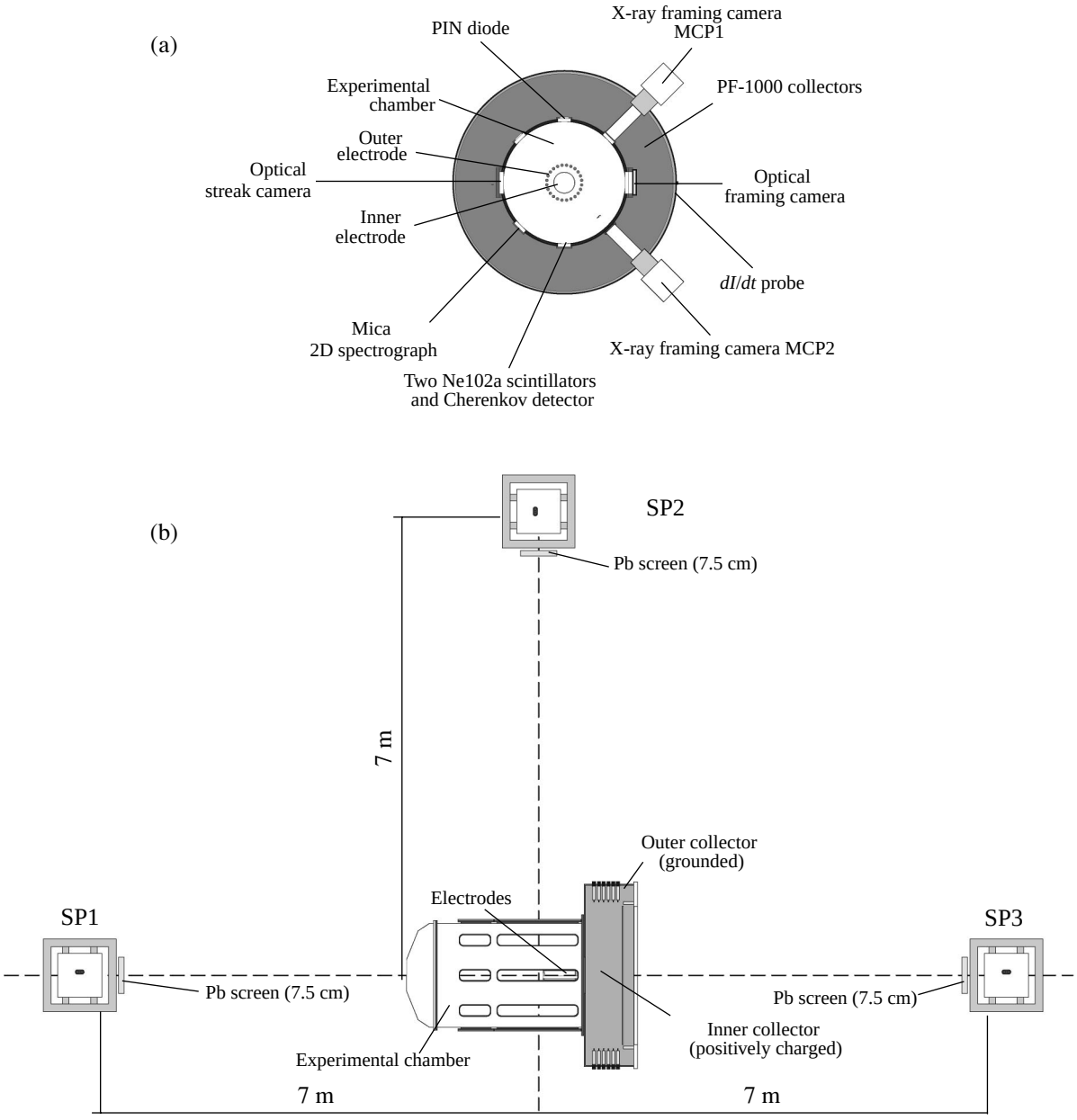

Fig. 1. Schematic of the experimental facility and diagnostics: (a) end view and (b) side view.

The time positions of the images displayed in Figs. 3, 4, and 5 (see Table 1) are shown by the markers in Fig. 2. The instant at which the PIN detector signal reached its maximum was assumed to be the zero time ($t = 0$). The full width at half-maximum (FWHM) of this signal was 80 ns, and the filtered energy emitted into the total solid angle was estimated to be 0.35 J. An appreciable drop in the *dI*/*dt* signal was observed 50 ns after the maximum of the PIN diode signal. This time delay varied from shot to shot in the range from –50 to +50 ns. SXR emission with photon energies above 3 keV was recorded with a scintillator covered with a 10-μm Al foil. The signal from this scintillator had a peak at 30 ns with an FWHM of 50 ns (see Fig. 2).

Figure 3 shows four frames recorded with the MCP1 detector at 84, 94, 104, and 114 ns (at the instant corresponding to the last frame, the PIN diode signal has already decreased below 15%). Radiation (partially in the photon energy range from 200 to 300 eV and partially above 600 eV) was emitted only from the plasma region around the wire (interpreted as the wire corona) that was in front of the electrodes, at a distance of 4–8 cm from them. The diameter of this emitting region varied from 200 to 500 μm.

Figure 4 shows four frames recorded with the MCP2 detector, which is more sensitive than the MCP1. These frames correspond to a later time interval than the frames presented in Fig. 2: they were exposed at 167, 177, 187, and 197 ns, when the PIN signal was almost zero. In Fig. 3, we can see only a part of the plasma corona, whereas in Fig. 4, the other two parts of the emitting corona can be seen. The first is close to the inner electrode and the second is at a distance of 6–9 cm from it. Both parts are ≈3 cm in length and ≈2 mm in diameter. Since the PIN diode signal was small within this time interval (i.e., the radiation filtered with a 10-μm Be foil was weak), we conclude that the detected radiation was mostly emitted in the photon energy range of 200 to 300 eV. The central part of the wire corona, which was located at 3 to 6 cm from the anode and which radiated 80 ns before, did not radiate in the XUV range during this time interval.

In Fig. 5, two visible frames exposed at 200 and 220 ns are displayed. At these instants, the radiation came from the plasma region 7 cm in length. Therefore, we may conclude that the corona plasma was created along the entire Al wire. Moreover, it seems that the axial part of the wire remained in a solid state till that time. In the region located a distance of 0 to 3 cm from the electrode, the visible diameter of the emitting corona was estimated to be 3–5 mm. In the visible spectral range, the middle part of the wire, whose radiation was detected only by MCP1 (see Fig. 3), had a two-layer structure. The first (more intense) layer 2 mm in diameter formed just around the wire, while the second layer formed from a sausage-like structure and had three little light disks ≈2 cm in diameter. Both these layers remained almost unchanged over a time period of 20 ns. A radial umbrella-like structure that can be seen in Figs. 3 and 5 at a distance of 7–11 cm from the electrode may be interpreted as the part of the plasma shell connecting the wire corona with the outer electrode.

Figure 6 shows a time-integrated spectrum recorded with the X-ray spectrograph, which detected the spectral lines of He-like Al ions and their Li- to F-like satellites. Clearly, the time during which these lines were emitted should correspond to the duration of the PIN diode signal. An analysis of the axial and radial structure of the plasma region emitting these spectral lines showed that they were emitted from the three disks that can be seen in the second layer in Fig. 5. It can also be seen that images obtained in the He_α resonance and intercombination lines had sharper boundaries than those obtained in the satellites.

In shot no. 2057, the intensities of neutron emission and HXR emission with photon energies above 30 keV were very low, and the total neutron yield (assuming the neutron emission to be isotropic) was as low as 10^9.

Figure 7 shows waveforms of the signals recorded in shot no. 2074 (cf. waveforms recorded in shot no. 2057 and presented in Fig. 2). The SXR signal detected with the PIN diode consisted of three pulses with a total

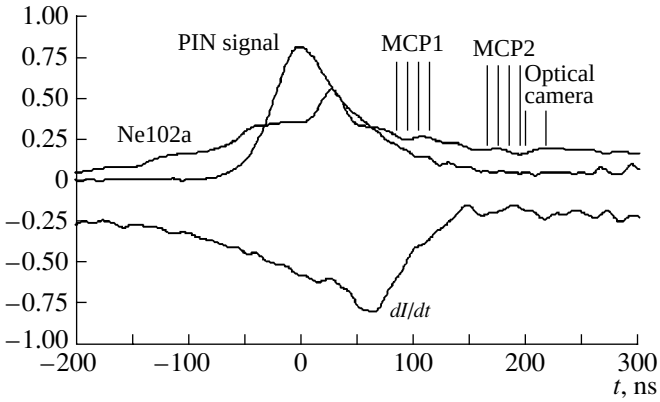

Fig. 2. Waveforms of the current derivative *dI*/*dt*, PIN diode signal, and X-ray signal in the photon energy range higher than 3 keV (shot no. 2057). Three vertical lines mark the instants at which MCP1, MCP2, and optical frames were exposed.

energy of ~0.3 J. The FWHM of the first pulse was 35 ns. The instant at which the PIN detector signal reached its first maximum was assumed to be the zero time. The second and third pulses (both with an FWHM of 20 ns) reached their maxima at 120 and 160 ns after the first maximum, respectively. A dip in the current time derivative *dI*/*dt* was detected 30 ns after the peak of the first pulse. The frames taken with the optical camera and the MCP1 detector were exposed at the trailing edge of the first SXR pulse, whereas the frames taken with the MCP2 detector were exposed during the second SXR pulse and at the leading edge of the third pulse. The time positions of the optical and SXR frames are marked in Fig. 7 are summarized in Table 2.

In shot no. 2074, the neutron yield was as high as 10^{11}. The position of the neutron pulse in Fig. 7 is shown with a correction for the time of flight (for a neutron energy of 2.45 MeV). Neutrons emission (which was detected with the Ne102a scintillator and filtered

Table 1. Time positions of frames in Figs. 3–5

Diagnostics	Figure	Frame	Time, ns
MCP1	3	1	84
	3	2	94
	3	3	104
	3	4	114
MCP2	4	1	167
	4	2	177
	4	3	187
	4	4	197
Optical frame	5	1	200
	5	2	220

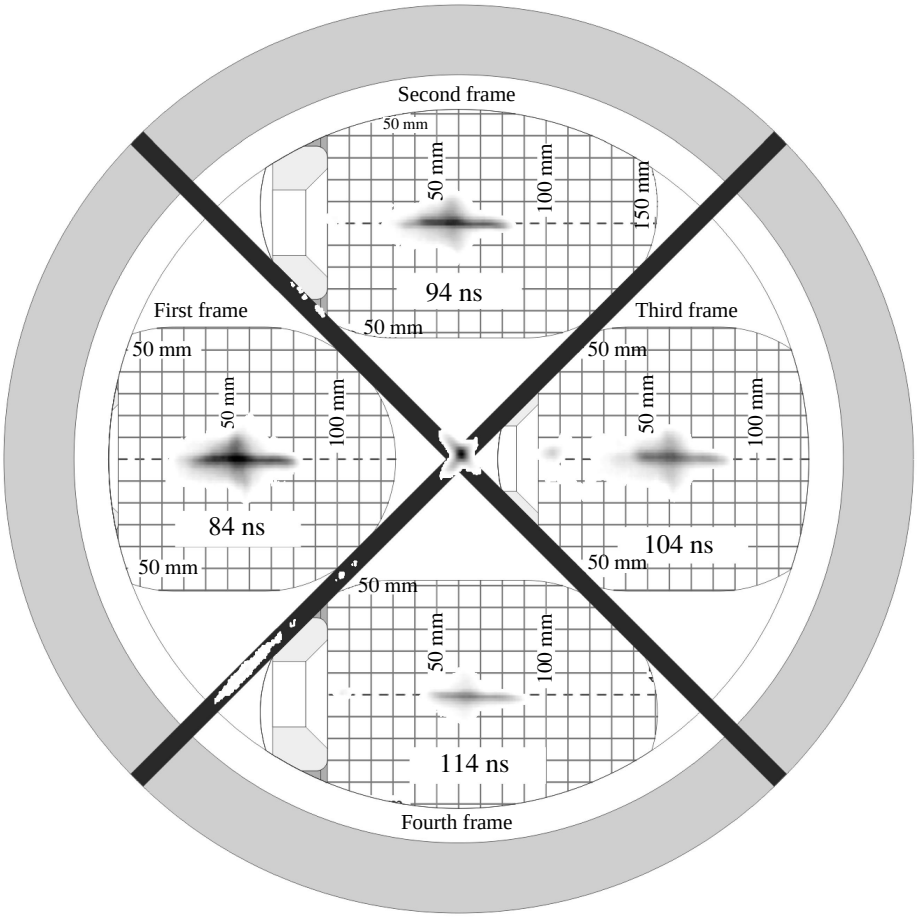

Fig. 3. MCP1 frames (shot no. 2057).

with a 7.5-cm Pb screen, absorbing γ photons) appeared during the first SXR pulse and reached its maximum with an FWHM of 140 ns at 170 ns (during the third SXR pulse).

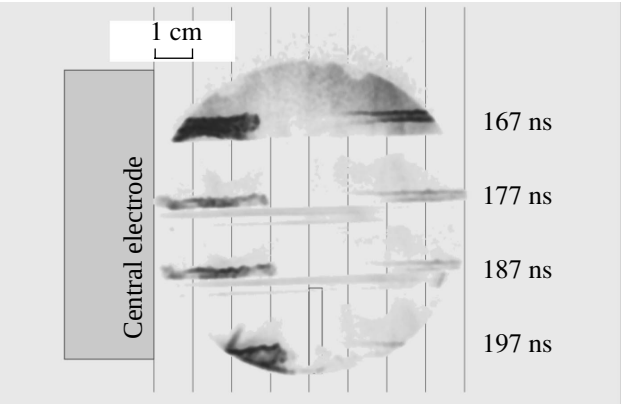

Fig. 4. MCP2 frames (shot no. 2057).

Figure 8 shows two frames recorder by the optical camera at 36 and 56 ns. The plasma corona was observed along the entire 7-cm-long wire. The corona diameter was estimated to be ~3 mm. The region with a larger diameter corresponds to the plasma shell that connects the corona with the outer electrode (cf. Figs. 3, 5).

Figure 9 shows frames obtained with the four quadrants of the MCP1 detector. The quadrants were gated at 35, 45, 55, and 65 ns. One can see a radiating plasma corona 1–1.5 cm in diameter and 7 cm in length, whose intensity gradually decreases with time.

Figure 10 shows four interesting frames obtained with the MCP2 detector. The frames were exposed at 114, 124, 134, and 144 ns (i.e., 80 ns later than those shown in Fig. 9). Both of the radiating structures (the wire corona and the helical tube winding around it) were observed during the second and third SXR pulses, when the intensity of neutron emission rapidly increased. The period of the helical tube was 5 cm, and the diameters of both the tube and the wire corona were estimated to be ~2 mm. No significant evolution of either structure was observed over 30 ns. Note that such

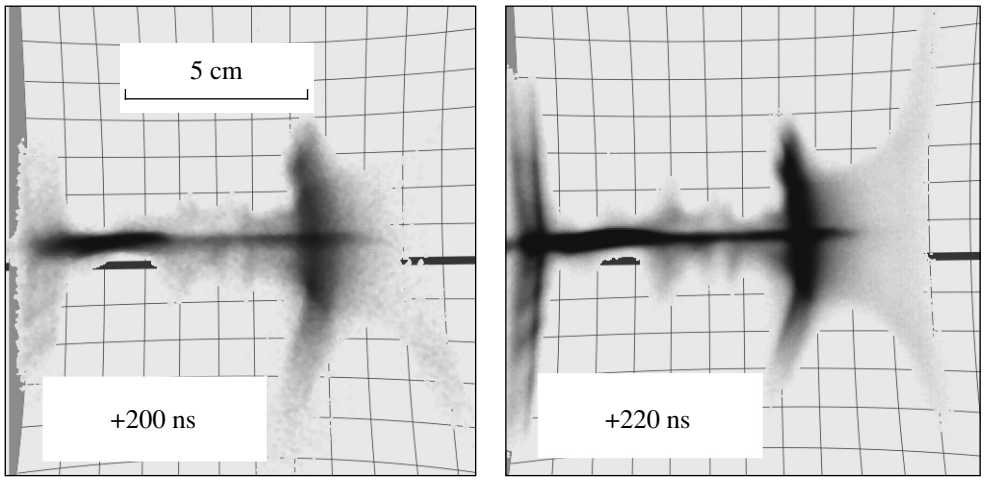

Fig. 5. Optical frames (shot no. 2057). The anode is on the left.

behavior is not typical of our experiments with a wire load. During the neutron pulse, we usually failed to record SXR images of the plasma because of too week XUV emission. The photograph obtained in this shot is the only one from which the pinch structure during the intense neutron pulse can be inferred.

Figure 11 shows a spectrum recorded with the time-integrating spectrograph. It can easily be seen that the lines of H- and He-like Al ions were radiated only from a spot located a distance of 2 cm from the inner electrode. The lines were radiated during the pulses detected with the PIN diode. From the fact that there was no imprint of the helical tube in the *K*-shell spectrum, we can infer that the observed tube radiated in the *L*-shell lines, i.e., in the 200- to 300-eV transparency window of the polyester filter. The intensity of *K*-shell emission in this shot was probably weaker than in shot no. 2057.

4. DISCUSSION

Our experiments with a deuterium current-carrying shell imploding onto an Al wire have shown that the presence of the Al wire does not substantially affect the neutron yield. Eight-shot statistics is not quite reliable, but the neutron yield of 10^{11} per shot was an absolute maximum also for shots without a wire. The ionization of the Al wire considerably decreases the temperature of the wire corona in the axial region of the pinch, and the long-lived cold plasma with a diameter of 2–3 mm probably prevent a decrease in the pinch diameter to lower than 500 μm in accordance with the theoretical model [3, 5]. For this reason, fast deuterons could not be generated near the axis and their source was certainly located outside this region.

As regards X-ray emission, it was not necessarily generated together with neutrons. X-ray pulses with photon energies below 10 keV had a smaller FWHM

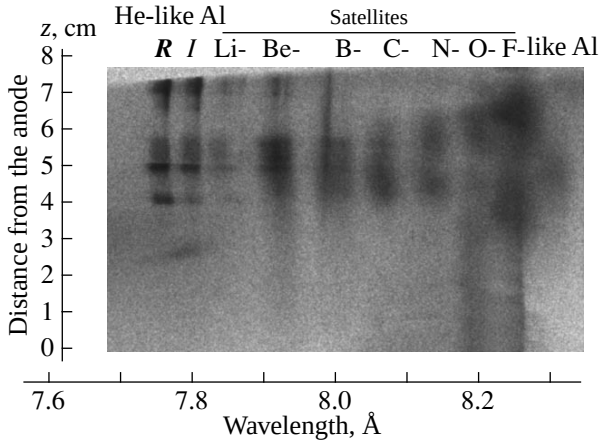

Fig. 6. Plasma image in the spectral lines of He- to F-like Al ions (shot no. 2057).

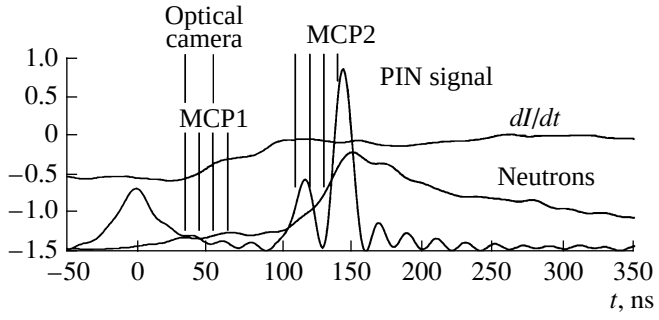

Fig. 7. Waveforms of the current derivative *dI*/*dt*, PIN diode signal, and neutron time-of-fly signal (shot no. 2074). The vertical lines mark the instants at which MCP1, MCP2, and optical frames were exposed.

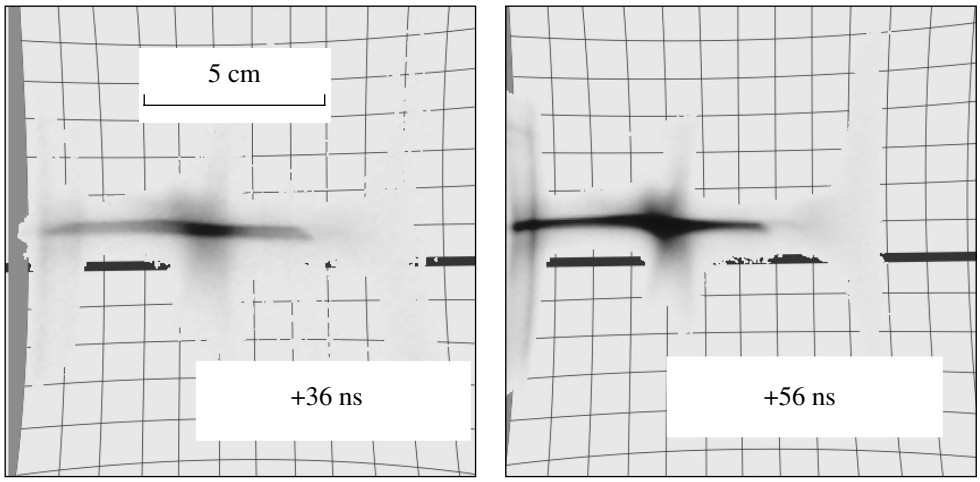

Fig. 8. Optical frames (shot no. 2074). The anode is on the left.

than neutron pulses, and the maximum of neutron emission was usually reached later than the maximum of X-ray emission. This confirms the conclusion made in [5] that neutron emission follows the formation of hot spots and agrees with the observation of the second neutron pulse during the unstable phase on the Poseidon facility [6]. Electrons with energies above 100 keV were detected only in some shots, as a rule, together with a high neutron yield and together with one of the SXR pulses.

Let us discuss two above shots in more detail. First, we consider shot no. 2057 (with a low neutron yield). The images recorded by the MCP1 detector spatially correlated with the corona region that emitted the lines of He-like Al ions (see Figs. 3, 6). Therefore, the MCP1 detector imaged the plasma during the pulse of *K*-shell emission. Taking into account that we used the same filter with the PIN detector and the X-ray spectrograph, we may conclude that the *K*-shell Al lines were emitted in the radial direction from a region with a diameter of 2 cm during the SXR pulse detected with the PIN diode (see Fig. 6). It can be seen in Fig. 5 that this region of the wire corona corresponds to the outer plasma layer with a sausage-like configuration, which therefore lasts from 100 ns to the exposure of frames in Fig. 5, i.e. up to 200–220 ns. Hence, we may conclude that this structure was probably created during the PIN-diode pulse and the emission of intense kiloelectronvolt radiation caused a substantial decrease in the plasma temperature. This long-lived (~100 ns) structure with three little disks is similar to that observed in the spectral lines (see Fig. 6). As regards the observed spectrum, Al lines were emitted from plasma regions with an electron temperature of 100–150 eV and electron density of ~10^{20} cm^{-3}. Thus, the energy density in the radiating plasma was $nkT \sim 10^7$–10^8 Pa. The satellites were presumably generated by superthermal electron beams propagating in the recombining plasma [8]. Apparently, the highest electron energy was a few keV.

Table 2. Time positions of frames in Figs. 8–10

Diagnostics	Figure	Frame	Time, ns
MCP1	9	1	35
Optical frame	8	1	36
MCP1	9	2	45
MCP1	9	3	55
Optical frame	8	2	56
	9	4	65
MCP2	10	1	114
	10	2	124
	10	3	134
	10	4	144

Shot no. 2074 was performed under the same initial conditions as shot no. 2057; however, the time behavior of the plasma focus in these shots was quite different. In shot no. 2074, the PIN-diode signal displayed three pulses. The emission energies measured by the PIN diode in these shots were almost the same. Since the intensity of Al *K*-shell emission in shot no. 2074 was lower than in shot no. 2057 (cf. Figs. 6 and 11 and SXR signals in Figs. 2, 7), we may conclude that, in shot no. 2074, the intensity of XUV radiation in the photon energy range of 200–300 eV was much higher. During the first SXR pulse, photons in the energy range of 200–300 eV were emitted only from the wire corona (see Fig. 9). Later (from 100 to 150 ns), radiation was emitted from both the wire corona and the helical tube (see Fig. 10). The radiating helical tube was probably formed during the expansion of the wire corona

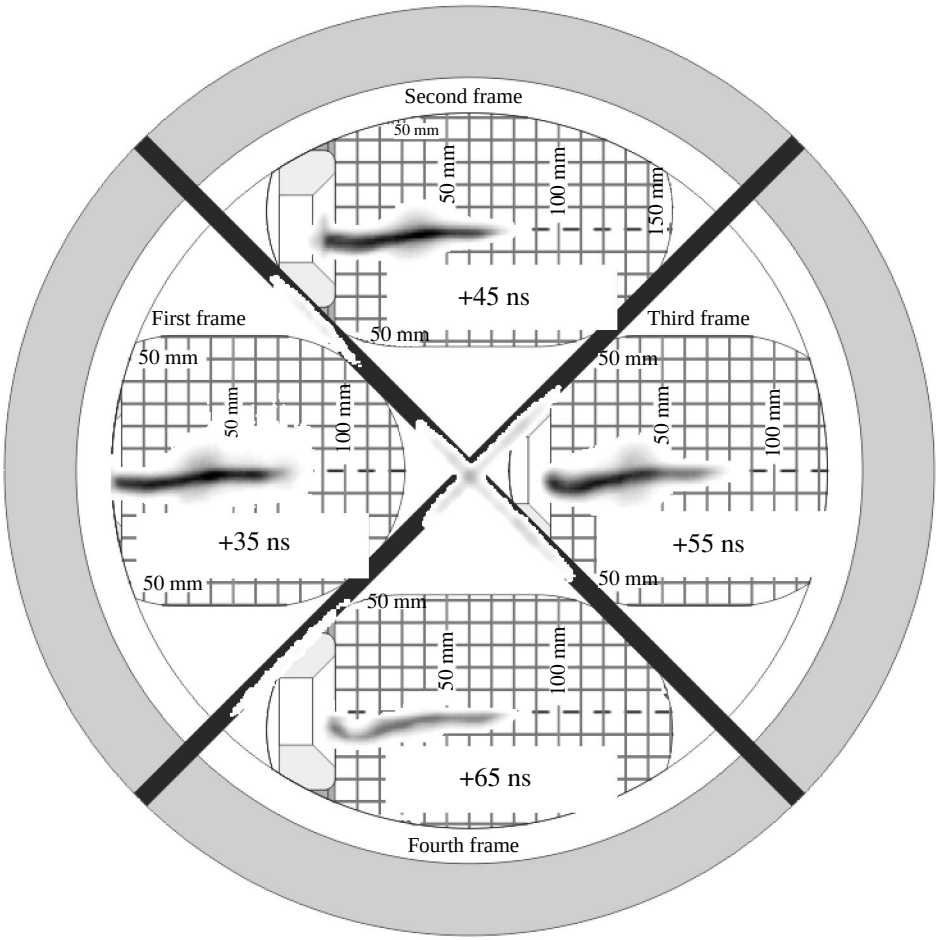

Fig. 9. MCP1 frames (shot no. 2074).

(between 65 and 110 ns). Its origin is not yet completely understood; we think, however, that it developed from the wire corona. The helical tube was fairly uniform in the longitudinal direction over the entire time interval during which the intensity of neutron emission increased. A slow radial expansion of its right edge was only observed (see Fig. 10).

Having described specific features of plasma evolution in both shots, we will try to find out what is the reason for the very different neutron yields in these shots. When the pinch configuration remained compact after the implosion of the plasma shell onto the wire and did not undergo dramatic changes (shot no. 2074), the neutron yield was high. On the other hand, when the evolution of the plasma focus exhibited the onset a few rapidly evolving instabilities (shot no. 2057), the neutron yield was substantially lower. This conclusion may not have general validity; it only indicates the issues to which particular attention should be paid in future research.

As was shown earlier (see, e.g., [3]), the neutron yield reduces considerably when a weak external axial magnetic field is applied to the pinch. However, there are phenomena that can be attributed to the presence of a self-generated (internal) magnetic field B_z, e.g., the existence of the above helical tube or the radial deflection of proton trajectories observed in [6]. As was shown in [9, 10], the spontaneously generated magnetic field B_z should increase the neutron yield. Helical magnetic plasma structures possess a higher stability than those with a dominant azimuthal component. They also are able to store energy with a high density equivalent to a pressure of 10^7–10^8 Pa in the pinch volume. This corresponds to a mean magnetic field of higher than 20 T.

The conceptual model presented below assumes that the generation of fast deuterons is related to the transformation and dissipation of the helical magnetic field inside the plasma focus after the pinch phase. We suppose that deuterons are accelerated by the induction electric field that is generated by the rapidly varying magnetic field. The magnetic field $B \approx 20$ T induces the electric field that accelerates a fraction of deuterons to an energy of $(5–10) \times 10^4$ eV, which is necessary for the

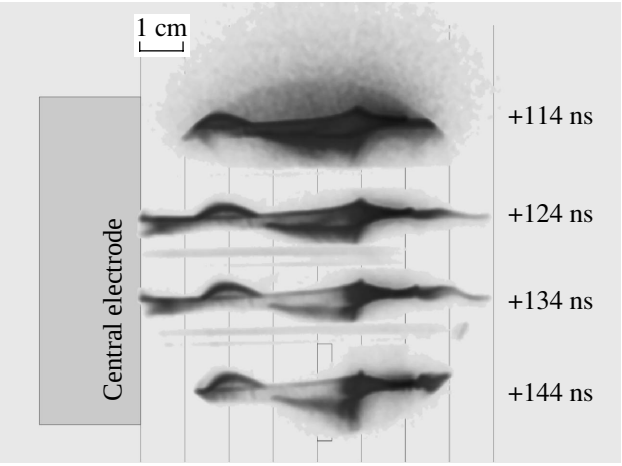

Fig. 10. MCP2 frames (shot no. 2074).

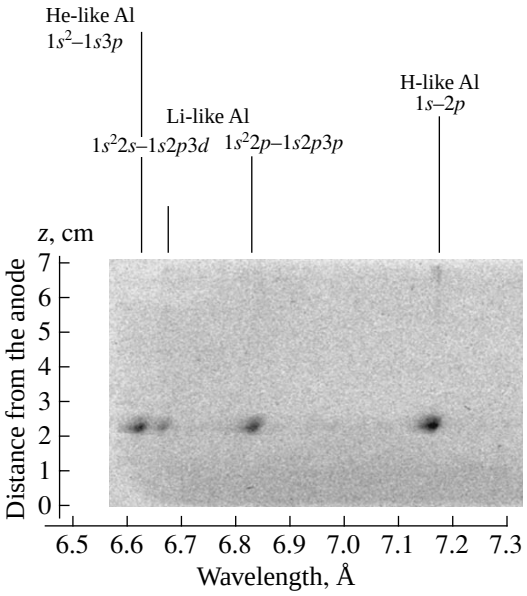

Fig. 11. Plasma image in the spectral lines of H-, He-, and Li-like Al ions (shot no. 2074).

D–D fusion reaction. In our case, the typical velocity with which the plasma moves across the magnetic field during the development of instabilities is ~10^5 m/s. The accelerating electric field E is then

$$E = |\mathbf{v} \times \mathbf{B}| = 2 \times 10^6 \text{ V/m}.$$

According to [6], the most probable energy of the fast deuterons in the plasma focus is 5×10^4 eV, which corresponds to the voltage drop of $U = 5 \times 10^4$ V. The path l along which they are accelerated to this energy is equal to

$$l = \frac{U}{E} = 25 \text{ cm}.$$

The time t during which the deuterons are accelerated to the velocity $v = 2 \times 10^6$ m/s (which corresponds to a kinetic energy of 5×10^4 eV) is

$$t = 2\frac{l}{v} = 25 \quad \text{ns}.$$

Let us now estimate the diffusion time of the magnetic field. During deuteron acceleration, the radiation intensity is maximal in the photon energy range of 50–100 eV (XUV range). It follows from this that the plasma temperature is on the order of 10–20 eV. The Spitzer conductivity of the deuteron plasma is then $\gamma = (1–3) \times 10^5\ \Omega^{-1}\ \text{m}^{-1}$. Hence, the diffusion time of the magnetic field from regions a few millimeters in size is [11]

$$\Delta t = \mu\gamma L^2 \approx 300–400 \text{ ns}.$$

This value agrees with the time during which the experimentally observed structure exists. Collisions between fast and thermal deuterons by the mechanism considered in [6] in terms of the gyrating particle model can produce the observed neutron yield.

5. CONCLUSIONS

Our experiments have shown that the presence of an Al wire at the end of the inner electrode has no appreciable effect on the neutron yield. The acceleration of fast deuterons is unlikely to occur in the cold dense axial plasma region with a diameter below 2–3 mm.

X-ray photons with energies above 3 keV were not necessarily emitted together with neutrons because the maximum of neutron emission was usually reached a few tens of nanoseconds after the maximum of X-ray emission. In order to more exactly determine the time at which neutron emission reaches its maximum, it is necessary to estimate the energy distribution of the emitted neutrons. Electrons with energies above 100 keV were detected only in some shots, as a rule, together with a high neutron yield and together with one of the SXR pulses.

In order to explain the results obtained, we have assumed that an axial magnetic field is generated in Z-pinch discharges. In terms of this model, we have discussed the influence of the self-generated axial component of the magnetic field on the acceleration of fast deuterons and the neutron yield.

ACKNOWLEDGMENTS

This study was supported in part by the research program no. J04/98:212300017 (Research of Energy Consumption Effectiveness and Quality) of the Czech Technical University in Prague; the INGO research program no. 1P2004LA235 (Research in Frame of the International Center for Dense Magnetized Plasmas) and the LN00A100 program of the Research Center of Laser Plasma of the Ministry of Education, Youth, and

Sport of the Czech Republic; and the GACR grant no. 202-03-H162 (Advanced Study in Physics and Chemistry of Plasma).

REFERENCES

1. M. A. Karakin, E. Y. Khantiev, V. I. Krauz, *et al.*, Czech. J. Phys. **52D**, 255 (2002).
2. M. Scholz, L. Karpinski, K. Tomaszewski, *et al.*, Czech. J. Phys. **50** (S3), 150 (2000).
3. O. A. Anderson, W. R. Baker, S. Colgate, *et al.*, Phys. Rev. **110**, 1375 (1958).
4. J. D. Seithan, A. E. Robson, K. A. Gerber, and A. W. DeSilva, Phys. Rev. Lett. **59**, 892 (1987).
5. I. H. Mitchel, R. Aliaga-Rossel, J. P. Chittenden, *et al.*, IEEE Trans. Plasma Sci. **26**, 1267 (1998).
6. U. Jager and H. Herold, Nucl. Fusion **27**, 407 (1987).
7. K. Tomaszewski, G. Kowalewski, J. Kaczmarczyk, *et al.*, Proc. SPIE **4948**, 160 (2002).
8. J. Abdallah, Jr., R. E. H. Clark, A. Ya. Faenov, *et al.*, J. Quant. Spectrosc. Radiat. Transf. **62**, 85 (1999).
9. P. Kubeš, J. Kravárik, Yu. L. Bakshaev, *et al.*, Fiz. Plazmy **28**, 329 (2002) [Plasma Phys. Rep. **28**, 296 (2002)].
10. P. Kubeš, J. Kravárik, D. Klír, *et al.*, in *Dense Z-Pinches*, Ed. by J. Davis, Ch. Deeney, and N. Pereira (AIP, New York, 2002); AIP Conf. Proc. **651**, 197 (2002).
11. T. G. Cowling, *Magnetohydrodynamics* (Adam Hilger, Bristol, 1976).

Translated by the authors

Plasma Physics Reports, Vol. 31, No. 5, 2005, pp. 392–411. Translated from Fizika Plazmy, Vol. 31, No. 5, 2005, pp. 432–452.

DUSTY PLASMA

Helical Structures in Complex Plasma I: Noncollective Interaction

N. G. Guseĭn-zade and V. N. Tsytovich

Prokhorov Institute of General Physics, Russian Academy of Sciences, ul. Vavilova 38, Moscow, 119991 Russia

Received January 5, 2004; in final form, March 15, 2004

Abstract—The conditions for the formation and stability of helical quasi-crystals in a complex plasma containing dust grains of equal size are investigated. A study is made of both the confinement of such helical structures in a direction transverse to the cylinder axis by means of an external parabolic potential well and the possibility of their self-confinement. Computer simulations of the helical dust structures were carried for two cases: for a structure of infinite length along the symmetry axis (or a closed structure in toroidal geometry) and for a structure of finite length. The dust grains were assumed to interact through a potential that is a superposition of the non-Debye nonlinear screened potential and the nonscreened noncollective attractive potential (the Lesage effect). Molecular dynamics simulations showed that, in the presence of dissipation, any initial random distribution of the dust grains interacting through such a potential in cylindrical geometry evolves to an equilibrium helical structure. When the external control parameter was varied smoothly, the pitch angle of the helix was observed to bifurcate (i.e., to undergo sharp jumps). The structure of the helix was also observed to bifurcate when the external parameter was varied: a helix changed into two interwoven helices, which then changed into three interwoven helices, etc. The smaller the confinement parameter (and, accordingly, the larger the radius of the helical structures) and the stronger the attractive forces between the grains, the larger the number of bifurcations. The results of analytical calculations of the parameters of the equilibrium structures and of their energies are in complete agreement with numerical results. It is also shown that noncollective attraction between dust grains makes it probable that helical structures will exists when the external confinement parameter is zero or even when it is negative. Bifurcations in such systems may provide the possibility of creating new types of memory elements. © *2005 Pleiades Publishing, Inc.*

1. INTRODUCTION

Up to now, the experimental and theoretical efforts in the relevant line of research on dusty plasmas have focused mainly on studying two-dimensional (2D) strongly correlated structures. The formation of 2D plane Coulomb quasi-crystals of ultracold atomic ions was observed in different confinement devices (see, e.g., [1]), in particular, in Penning and Paul traps and storage rings [1–5]. Simplest three-dimensional (3D) structures of atomic ions, such as helical structures and their particular forms—one-dimensional linear chains (strings)—were also studied in these devices. Interest in such structures stems primarily from their applications in microcomputers.

2D quasi-crystals were also observed in colloids [6, 7] and dusty plasmas (see [8–10]). Among the first papers devoted to a theoretical description of quasi-crystals on the basis of the Debye screened potential of the interaction between dust grains was that by Schweigert and Peters [11]. Although the large grain charges in such complex systems are nonlinearly screened, the question of whether this screening is of a Debye nature at that time remained open [10]. A general theory of 2D structures with an arbitrary interaction potential between dust grains was developed by Amiranashvili *et al.* [12], who determined the conditions for the existence of 2D quasi-crystals (clusters) composed of a small number of dust grains and found the spectra of their small oscillations.

In most experiments, quasi-crystalline structures are observed to form in an external parabolic confining potential well. Experiments with plane quasi-crystals have revealed the following picture of the formation of shells as the number N of dust grains increases. First, a single shell (ring) forms. As N increases, this ring becomes energetically unfavorable, so a second ring shell forms inside it. The third shell then forms inside the second, and so on. In some respects, this structure is analogous to that of an atom.

In recent years, 3D crystalline structures (plasma crystals) have been produced in RF discharges [13, 14] and in dc glow discharges [15]. A distinctive feature of such crystals is that they contain a large number of grains, the interaction between which is of a collective nature. 3D structures composed of a small number of dust grain (3D clusters) differ from plasma crystals in that the interaction between the grains in them is noncollective and is determined by all possible combinations of pairwise interactions.

In the present paper, the properties of 3D cluster structures are studied both theoretically and numerically for a simple system of identical grains without

1063-780X/05/3105-0392$26.00 © 2005 Pleiades Publishing, Inc.

allowance for the plasma dynamics, whose only role is to set up a certain type of intergrain interaction.

Experiments [6, 7] and numerical simulations [11] showed that the shells in 3D spherical structures form in a way analogous to that in 2D plane structures. Specifically, as N increases, a single spherical shell becomes energetically unfavorable, so a second shell forms inside it; the third shell then forms inside the second; and so on. It is thus possible to speak of an analogue of Mendeleev's periodic table of elements: for a given number N of grains, it is possible to establish exactly how many grains compose each shell for a particular type of intergrain interaction.

In long cylindrical systems, the dust grains can be prevented from expanding in a transverse direction by a simple type of external potential: the grains can be confined by a parabolic potential well or at the expense of solid walls. In such systems, the simplest 3D structure is a helical structure.

A uniform structure consisting of N interwoven helices is composed of grains lying in planes that are perpendicular to the symmetry axis of the cylinder and are equally spaced along it at a uniform spacing Δ. In each plane, the grains lie on a circle (the radii of the circles in the planes being the same) and generally occur at the vertices of a regular polygon (N-gon). For two interwoven helices, this is a segment of a straight line (digon) (see Fig. 1). In the general case, this is an N-gon. In each pair of neighboring planes, the polygons are turned through the same constant angle φ relative to one another. For $N = 2$ (Fig. 1), the two interwoven helices resemble the DNA helix.

Similar structures of ultracold atomic ions have been observed in linear systems [1] and in spherical and toroidal traps [2]. In recent years, such structures have also been observed to form in dusty plasmas. This is why the problem about the mechanism for their formation requires a separate study.

The objective of the present paper is to prove that, in cylindrical and toroidal systems, a steady dust structure exists for an arbitrary interaction potential between the grains. The structure has the form of a helical quasicrystal with a fixed period, the constant of the lattice being determined by the mean number of grains per unit length of the structure. The limiting case of an extended helical structure is a 1D linear configuration (a string).

By varying the external control parameter (e.g., the number of grains per unit length of the helical structure or the parameters of the confining potential), a wide variety of equilibrium configurations can be obtained, from 1D strings to complex structures consisting of several interwoven helices.

In this paper, we present results from numerical investigations of the possibility of forming helical structures in a complex plasma (i.e., a plasma with dust grains) and of confining them in a direction transverse to their symmetry axis by an external parabolic potential well. The constant determining the confining potential can be arbitrary; in particular, it can be negative. In this case, however, equilibrium helical structures can exist only when the interaction between the dust grains is attractive and is sufficiently strong at large distances between them. The subject of the investigations is the problem of how various types of intergrain interactions affect different equilibrium configurations and their bifurcations. The investigations were carried out under the assumption that the interaction between dust grains can be described by summing all the pairwise interactions (the collective interactions being weak). In order for such an assumption to be valid, the number of grains in a 3D structure must be small enough for the mean free path of the plasma particles that take part in the charging of dust grains to be much larger than the radius of the helical structure.

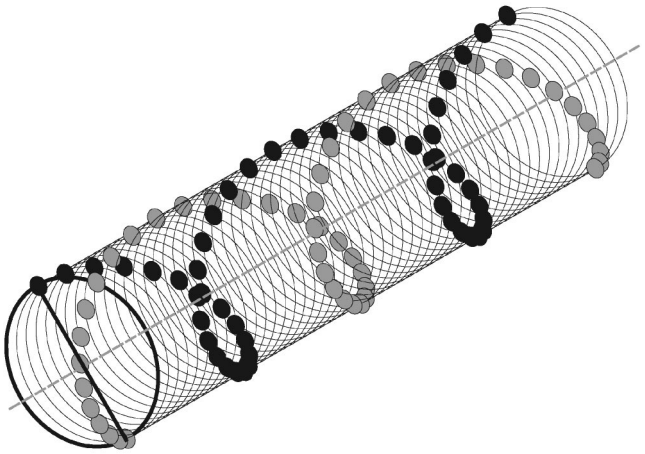

Fig. 1. Example of $N = 2$ helical structure.

Helical structures of finite length were investigated numerically under the assumption that the confinement in the transverse direction is far better than that along the symmetry axis of the structure.

The results of numerical simulations show that, regardless of the type of pairwise interaction, any random distribution of the dust grains evolves into a helical structure.

We begin by discussing the question about the interaction between the grains. We also touch on the questions concerning numerical simulations of the dust grains and present results on the effects that were revealed numerically, namely, bifurcations of the pitch angle and global bifurcations (the onset of new shells). Finally, we discuss analytic methods for investigating equilibrium helical structures and analyze the role of attraction between the grains in the formation of self-confining structures.

2. INTERACTION BETWEEN DUST GRAINS IN A PLASMA

Here, we consider the distinguishing features of the interaction between dust grains in a complex plasma containing (in addition to electrons and ions) an appreciable amount of dust (or aerosol).

Since the electrons and ions have different mobilities and different temperatures, dust grains in a plasma acquire a significant charge. For instance, grains with a radius of about 10 μm can carry a charge of about 10^4 electron charges. The interaction between each pair of grains with such a large charge is strong and, when there are many such grains, the correlations between them are so close that, under certain circumstances, they can induce gas–liquid–crystal phase transitions, i.e., can lead to the formation of spatially ordered structures analogous to those in liquids or solids. Under such conditions, the electrons and ions remain in a gas state but exhibit new correlations that are initiated by the correlations between the grains. The interaction potential, the shape of which can have a considerable impact on phase transitions in a plasma, can differ markedly from that in a classical plasma. The interaction between particles in a Coulomb plasma is usually described by using the one-component plasma model or the model with a screened (Debye) potential, which is often called the Yukawa model. These models are inapplicable to most experiments with complex plasmas. For the sake of comparison, however, we will utilize the Yukawa model in further analysis.

2.1. Debye Screening

If we regard the dust grains simply as heavy ions with a large charge, then we can assume that the potential around a grain is determined by the Debye screening. In this case, for $a \ll \lambda_D$ (where a is the grain radius), the potential of the grain can be represented as

$$\Phi_Y(r) = \psi_Y \frac{Z_d e}{r} = \frac{Z_d e}{r} \exp\left(-\frac{r}{\lambda_D}\right), \quad (1)$$

where ψ_Y is the Yukawa screening (Debye screening) factor, λ_D is the Debye length, e is an elementary charge, and Z_d is the grain charge number.

The assumption regarding the Debye screening of the Coulomb potential can be considered approximately correct if the grain charge is sufficiently small and the ratio of the grain radius to the screening length, as well as the ion-to-electron temperature ratio, is not too small. The applicability conditions for the Debye interaction approximation can be presented in an explicit form. They follow naturally from the possibility of linearizing Poisson's equation, which describes the screening of a charge.

2.2. Nonexponential (Non-Debye) Screening

The main serious restriction on the applicability of the assumption regarding the Debye screening of the Coulomb potential of a dust grain is associated with the condition for the ion polarization charge to be linear, $e\Phi/T_i \ll 1$, where Φ is the potential around the grain and T_i is the ion temperature. At the grain surface, we have $e\Phi/T_i \approx (Z_d e^2/aT_e)(T_e/T_i) = z/\tau \gg 1$, where $\tau = T_i/T_e$ and $z = Z_d e^2/aT_e$.

Under actual experimental conditions, the dimensionless charge z is on the order of unity (for xenon, which is often used in experiments, this charge is on the order of 4, and, for argon, it is about 2.8) and the temperature ratio $\tau = T_i/T_e$ is on the order of 10^{-2}. Consequently, the Boltzmann exponent $\exp(e\Phi/T_i)$ at the grain surface can be on the order of 400, so the screening cannot be described by expanding the potential in a standard fashion. Under the assumption that the potential decreases away from the grain surface according to the law $1/r$, the distance from the grain over which the standard expansion of the potential is valid is one thousand times larger than the grain radius, whereas the Debye screening length is usually larger than the grain radius by a factor of only six to ten. This example shows that the Yukawa potential, which is based on this expansion, is inapplicable to the grain charges observed in actual experiments. Another quantitative estimate can be derived from the assumption that the condition $e\Phi/T_i \ll 1$ holds at least at a distance from the grain surface equal to the Debye screening length, i.e., that there exists a certain region (at least, at distances from the grain surface that are on the order of or larger than the Debye length) to which the linear approximation is applicable. As a result, we can arrive at the inequality $Z_d \ll 3N_{D,i}$ where $N_{D,i}$ is the total number of ions in the Debye sphere. This inequality is actually satisfied for an individual ion in a plasma; in this case, the grain charge Z_d can be replaced by unity and the condition $N_{D,i} \gg 1$ usually holds (by the definition of a weakly correlated plasma). For a dusty plasma, the grain charge Z_d is on the order of $Z_d \approx 10^3$–10^5, whereas the quantity $N_{D,i}$ is about ten, so the inequality in question fails to hold. In practical units, the applicability condition for the assumption of the Yukawa screening can be written as

$$Z_d \ll 52\left(\frac{10^9\ \text{cm}^{-3}}{n_i}\right). \quad (2)$$

In experiments, the ion density lies within the range $10^8\ \text{cm}^{-3} < n_i < 10^9\ \text{cm}^{-3}$, so this inequality does not hold. The solution to the problem about the nonlinear screening under the inequality opposite to inequality (2) is known (see [16]); unfortunately, however, it has often been ignored in describing the screening of the grain charge. In the present paper, the approach developed in [16] is simplified and a simpler solution is

obtained that is more suitable for numerical simulations.

We introduce the screening factor $\psi(r)$ into the dust grain potential $\Phi = (Z_d e/r)\psi(r/\lambda_{Di})$, where $\lambda_{Di} = \sqrt{T_i/(4\pi n_i e^2)}$ is the ion Debye length, which is equal to the total Debye screening length in the limit $\tau \ll 1$. Poisson's equation can then be written as the equation for the screening factor [16]:

$$\frac{d^2\psi(r)}{dr^2} = R(\psi(r), r), \qquad (3)$$

where the distance r from the grain is normalized to the ion Debye length. The function $R(\psi)$ describes the nonlinear screened potential. In the Yukawa approximation, we have $R(\psi) \approx \psi$, so solution (3) becomes $\psi = \exp(-r)$. According to [17], the interval of integration over ion velocities should be restricted by the condition that the only ions that screen the dust grain potential are those capable of reaching the grain from infinity, $m_i v^2/2 > -e\Phi$. As a result, we obtain

$$R(\psi, r) = \frac{r\tau}{az}(I(x_i) - \exp(-\tau x_i)),$$

$$I(x_i) = \exp(x_i)(1 - \mathrm{erf}(\sqrt{x_i})) + \frac{2}{\sqrt{\pi}}\sqrt{x_i}, \qquad (4)$$

$$x_i = \frac{za\psi}{r\tau}.$$

The last term in parentheses in the first of expressions (4) is the electron contribution, which is on the order of unity. The limit $x_i \ll 1$ corresponds to the Yukawa approximation. Recall that, at the grain surface, we have $x_i = z/\tau \approx 400 - 200$. Figure 2 shows the Yukawa approximation $R(\psi) \approx \psi$, as well as the potential $I(x)$ and its asymptotic form $I_{as}(x_i) = 2\sqrt{x_i}/\sqrt{\pi}$ (which is valid in the limit $x_i \gg 1$) over a wide range of x values, from 0.1 to 400.

According to Fig. 2, the exact expression for the potential $I(x)$ can be approximated by the function $I_{as}(x)$ over a broad range of x values. Equation (3) can then be simplified by renormalizing the distance r:

$$\frac{d^2\psi(r)}{dr^2} = \sqrt{\psi(r)r}. \qquad (5)$$

Numerical investigations of this equations show that its solution differs significantly from the Yukawa solution. Specifically, at short distances from the grain, the screening factor ψ is larger than the Yukawa screening factor (this corresponds to stronger screening), but, at a finite distance (say, at r_0), it becomes zero. This property of the screening factor is important for two reasons. First, the Yukawa exponent is usually not too small when the intergrain interaction is taken into account. Second, if the screening factor approaches zero at a finite distance from the grain, then all other relatively weak collective effects such as collective grain attraction become dominant (roughly speaking, their contributions should be compared to zero rather than to a small exponent). Solution (5) depends on the choice of the boundary conditions at the grain surface $r = a$. One of the boundary conditions is simply $\psi(a) = 1$ and the other is that for the magnitude of the derivative of the screening factor at the surface.

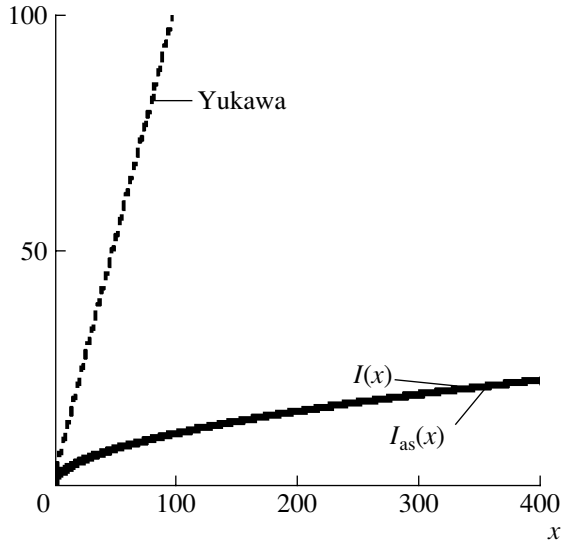

Fig. 2. Function $I(x)$ (solid curve) and its analytical approximation $I_{as}(x)$ (dotted curve, which almost coincides with the solid curve). The dashed curve corresponds to the Yukawa approximation and is seen to differ considerably from the first two curves. The difference between the curves $I(x)$ and $I_{as}(x)$ is quite insignificant: it can only be seen at $\sqrt{x} \ll 1$. Such a remarkably close coincidence between the curves $I(x)$ and $I_{as}(x)$ over almost the entire range of x values, in which the nonlinearity of the screening is important, is used to construct an approximate model of nonlinear screening.

We choose this derivative to be negative and then adjust its value iteratively in such a way that the decrease in the solution at short distances does not become an increase in its value at longer distances and the solution itself does not fall below zero (i.e., does not become negative, which is physically meaningless). The first derivative of ψ at the grain surface, which determines the screening near the grain, can thus be calculated numerically with an accuracy of six digits to the right of the decimal point (see Fig. 3, which displays exact and approximate solutions for the nonlinear screening). For distances at which the screening factor ψ becomes close to zero, Eq. (5) fails to hold and its solution should be matched with the linearized Yukawa solution.

The main result is that the solutions should be matched at a finite distance from the grain surface, namely, at a distance at which the grain charge is screened almost completely, so the remaining nonscreened charge is only about 10^{-3} that of the grain.

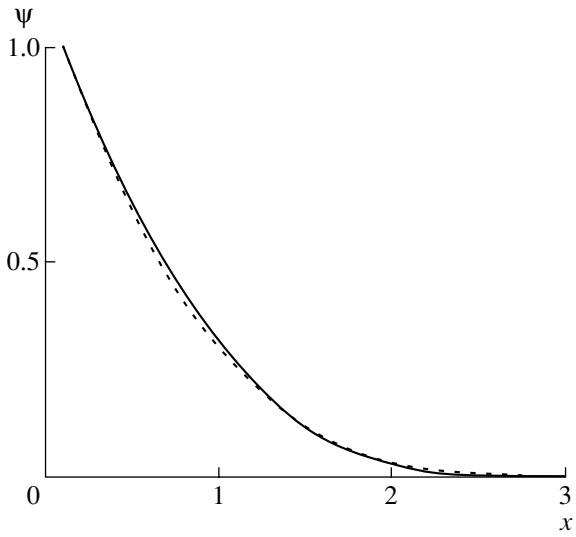

Fig. 3. Screening factor ψ as a function of distance $x \equiv r$ from the grain. The solid curve shows the solution to exact equation (5) for the screening factor, and the dotted curve describes the approximate solution $(1 - (x - a)/3.4)^4$, where the distances are normalized in the same manner as in expression (7) and the numerical coefficient is obtained from the condition for the approximate solution to give a best fit to the exact solution and differs only slightly from the numerical coefficient that enters expression (7) and is found by bringing this expression into correspondence with the asymptotic solution at $r \longrightarrow r_0$.

Under these conditions, the Yukawa screened potential exhibits a tail, whose effect, however, turns out to be insignificant in comparison to the other effects that occur in all types of grain–grain interaction and that were ignored up to this point. In order of magnitude, the ratio between the attractive interaction potential and the nonscreened central-force interaction potential is $(1–10)a^2/\lambda_{Di}^2$. For certain degrees of ionization of a plasma containing a large number of neutral atoms and dust grains with rough (irregular) surfaces, the coefficient of attachment of neutrals to grains is fairly large. The ratio of the contribution from the grain attraction effects to that from the Coulomb repulsion effects can be as large as unity or even greater. However, the attraction effects are usually important at long distances, while the Coulomb effects are essential at short distances. Consequently, in our analysis, the tail of the Yukawa potential at $r \gg r_0$ plays an insignificant role, so we can assume that the Coulomb screened potential vanishes at distances longer than the distance $r = r_0$, at which the solution becomes zero, $\psi = 0$. The interaction model can be further simplified by making the replacement $r = r_0$ on the right-hand side of Eq. (5).

Having made this replacement and having renormalized the distances in the above manner, we write Eq. (5) in the form

$$\frac{d^2\psi(r)}{dr^2} = \sqrt{\psi(r)}. \quad (6)$$

Equation (6) has analytic solutions that possess the same qualitative properties as the solution to Eq. (5). Taking into account the fact that the potential should decrease with distance and using the boundary condition $\psi(a) = 1$ and the asymptotic solution to Eq. (5) at $r \longrightarrow r_0$, we find

$$\psi = \left(1 - \frac{r-a}{\sqrt{12}}\right)^4, \quad (7)$$

where the distance is normalized to $\lambda_{Di}\left(\frac{\pi}{4}\frac{a}{\lambda_{Di}}\frac{z}{\tau}\right)^{1/5}$.

As a result, we arrive at the following approximation for the screening factor:

$$\psi = \left(1 - \frac{r-a}{\lambda_{\rm scr}}\right)^4. \quad (8)$$

A comparison of solution (8) to solution (7) (see Fig. 3) yields the numerical coefficient in the expression for $\lambda_{\rm scr}$:

$$\lambda_{\rm scr} = 3.4\lambda_{Di}\left(\frac{\pi}{4}\frac{a}{\lambda_{Di}}\frac{z}{\tau}\right)^{1/5}. \quad (9)$$

At distances of $r > \lambda_{\rm scr}$, the attractive forces usually play a dominant role. Expression (9) means that, under actual experimental conditions, $\lambda_{\rm scr}$ is about $(8–10)\lambda_{Di}$. The quantity $\lambda_{\rm scr}$ is close to the spatial separation between the grains in a dust plasma crystal.

Solution (8) was used in our numerical simulations. For comparison, we also carried out calculations for the Yukawa screening factor

$$\psi_Y = \exp(-D_Y r). \quad (10)$$

For the Yukawa interaction, we have $D_Y = 1/\lambda_{Di}$, so, in order to compare the nonlinear screening with the Yukawa screening, it is necessary to keep in mind the fact that the screening distance $D = 1/\lambda_{\rm scr}$ in solution (8) is ten times less than the Yukawa distance D_Y in solution (10) (for the actual experiments, at least).

2.3. Noncollective Grain Attraction Model

Since the electrons and ions have different mobilities, dust grains in a plasma rapidly become charged. Thus, the charge of micron-size grains can be fairly large, up to about 10^6 electron charges. For this reason, the grains should strongly repel each other. Numerous experimental data, however, give evidence of the existence of attraction between the grains, which results, in particular, in the formation of compact dust clouds.

One of the models of long-range forces of attraction between like charges is the model of noncollective attraction due to the shadow effect [18].

The model suggests that a plasma flux forms around an isolated dust grain that converges radially to the grain surface, where the ions recombine. Any other

object (e.g., another grain) in the vicinity of the test grain experiences a drag force that attracts it to the test one. When the plasma density is sufficiently low, the volume recombination is negligible, so the conservation of the total flux implies that the velocity of charged particles in the converging flux and, accordingly, the attractive force decrease in inverse proportion to the square of the distance. This attraction mechanism is known as the Lesage gravity, because it resembles that proposed by George Louis Lesage in formulating his universal law of gravitation.

As may be seen, this attraction model does not include the screening effects and thereby assumes that the attractive force is not screened at all. However, in order to describe the noncollective attraction in terms of screening, the usual practice is to introduce the screening factor ψ_{att} through the relationship ($\Phi(r) \approx \psi_{att}(Z_d e/r)$). The screening factor ψ_{att} is negative ($\psi_{att} = -\alpha$) and constant because the contribution of the shadow effect is inversely proportional to the shadow solid angle and the attractive potential is proportional to $1/r$. For a shadowed ion flux, the quantity α is equal in order of magnitude to a^2/λ_{Di}^2. The shadow effects associated with a neutral atom flux depend on both the coefficient of attachment of atoms to a grain and the gas pressure. Under typical experimental conditions (namely, for an attachment coefficient on the order of 10^{-4} and a pressure corresponding to a neutral-to-ion density ratio on the order of 10^6), the attractive force driven by the neutral particle flux is of the same order of magnitude as that driven by the ion flux. When, however, the attachment coefficient is on the order of 10^{-2} or even larger (for fractal-shaped grains with irregular surfaces), the neutral-flux-related attraction is predominant; in this case, the quantity α may be on the order of unity.

2.4. Interaction Potential Model

In computer simulations, we used the normalized intergrain interaction potential

$$V(r) = \frac{1}{r}\left[(1-Dr)^4\frac{1}{2}\left(1+\frac{1-Dr}{|1-Dr|}\right)-\alpha\right]. \quad (11)$$

Here, the potential is expressed in units of $Z_d^2 e^2/\Delta$, and the radial coordinate r is given in units of the distance (spacing) Δ between the planes of the helical structure. The approximation used for the nonlinear screening in this expression implies that the grain size is much less than the distance between the planes.

In the limiting case $D = 0$ and $\alpha = 0$, expression (11) describes the Coulomb interaction.

We will compare potential (11) with the Yukawa screened potential of the interaction between the grains with ($\alpha \neq 0$) and without ($\alpha = 0$) allowance for attraction:

$$V_Y(r) = \frac{1}{r}\exp(-D_Y r) - \frac{\alpha}{r}. \quad (12)$$

This comparison is meaningful only for the parameter values such that $D \ll D_Y$, e.g., for $D = 0.1D_Y$.

3. NUMERICAL SIMULATIONS

Here, we describe the results from simulations of a system of charged dust grains that are initially distributed in space in a random manner and interact by means of the above potentials.

We consider a system consisting of a large number of likely charged dust grains of the same radius a that are prevented from expanding by an external potential well $U(\mathbf{r}_\perp)$. Near the bottom of an axisymmetric potential well, the confining potential can always be approximated by a parabolic potential, $U_{foc} = -\frac{1}{2}K(x^2 + y^2)$, where K is a confinement constant (parameter), which depends on the parameters of the trap (the case of self-confinement of dust grains by attractive forces corresponds to $K \leq 0$).

In most experiments, the grains are confined by an external potential well; however, the confinement parameter K can in principle be varied over a wide range, including the range of its negative values, $K \leq 0$.

In simulations, we utilized the standard technique of molecular dynamics for a one-component plasma. The equation of motion of the nth grain has the form

$$m\frac{\partial^2 \mathbf{r}_n}{\partial t^2} + qK\mathbf{r}_{\perp n} + 2q^2\sum_{n\neq k} F_{nk}(|\mathbf{r}_n - \mathbf{r}_k|) = 0, \quad (13)$$

where r_k is the coordinate of the kth grain. This equation implies that the interaction between the grains is described by summing all their pairwise interactions and that the collective interactions are ignored.

3.1. Periodic Boundary Conditions

Let us consider an axisymmetric grain system with an infinite length along the z axis. It is convenient to perform simulations for a cylindrical system with periodic boundary conditions. Although the problem so formulated does not allow aperiodic solutions, there are several arguments supporting this approach. An actual system (a circular toroidal trap, for example) is always finite; in the case under consideration, however, the radius of the torus is assumed to be infinity large, i.e., the toroidal curvature is ignored.

The initial grain positions were chosen randomly. We considered a system of 400 grains and tested the results obtained against the results calculated for N = 1000. The sums were calculated by a standard method

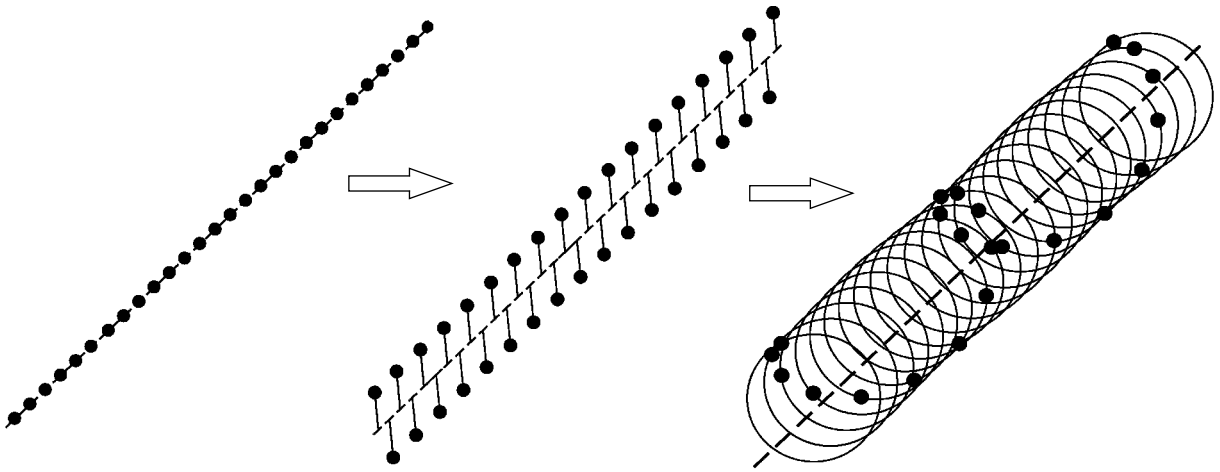

Fig. 4. Configurational bifurcations of the structures that occur as the radial confinement parameter is decreased.

Fig. 5. Grain distribution obtained by the molecular dynamics method for a finite system of grains confined in the *z* direction by a parabolic potential at a very large value of the radial confinement parameter.

similar to the Ewald method [19, 20]. The temperature was calculated as the mean kinetic energy. In order for the system to be capable of evolving to a steady equilibrium state, we introduced friction into the model. The case of purely Coulomb interactions was investigated by Hasse and Schiffer [20].

For all the interaction potentials that were considered in our analysis (namely, those given by expressions (11) and (12) with different values of the parameters α, D, and D_Y), the simulations yielded final one-shell equilibrium configurations in the form of N interwoven helices with a constant pitch angle and a constant spacing between the lattice planes z_0. No other one-shell equilibrium configurations were obtained.

We thus computed a family of steady states for different values of the external parameter K.

For purely Debye screening ($\alpha = 0$ and $z_0/\lambda_{Di} = 0.1$), we decreased the value of the confinement parameter K and observed the following sequence of bifurcations: helix I $\longrightarrow$ tetrahedral configuration (a limiting case of an $N = 2$ helix with the maximum possible turning angle equal to $\pi/2$ $\longrightarrow$ helix I $\longrightarrow$ tetrahedral configuration $\longrightarrow$ helix II $\longrightarrow$ helix I $\longrightarrow$ helix III $\longrightarrow$ $N = 3$ helix with the maximum possible turning angle equal to $\pi/3$ (see Fig. 4).

After this, we observed the formation of a second shell: first, a string formed within a primary helix; then, this string also transformed into a helix. Thus, there were two nested shells, each consisting of several interwoven helices.

It should be noted that, for some values of the external parameter, helical configurations were observed to evolve to different shapes, depending on the initial positions of the grains.

Hence, our computer simulations showed that, in the 3D case under analysis, the simplest configurations are helices (one helix or two, three, etc., interwoven helices), which are analogues of the simplest configurations (regular polygons) in 2D plane geometry.

Note that mechanisms for such jumplike transitions from one type of helix to another are not completely clear.

It is, however, obvious that, under conditions in which the repulsive interaction of the grains with their nearest neighbors is predominant, the turning angle between two neighboring planes is equal to π/N. Consequently, as the confinement parameter K decreases, interactions with remote grains begin to play an increasingly important role, so the bifurcations can be strongly influenced by the character of screening (either the Yukawa or nonlinear screening) and also by the nonscreened attraction. Generally, both these effects increase the number of bifurcations (i.e., decrease the difference between the values of the confinement parameter at which two subsequent bifurcations occur); this is indeed confirmed by our numerical simulations.

3.2. Finite Systems

The results that have been obtained for infinite systems are, strictly speaking, inapplicable to actual finite

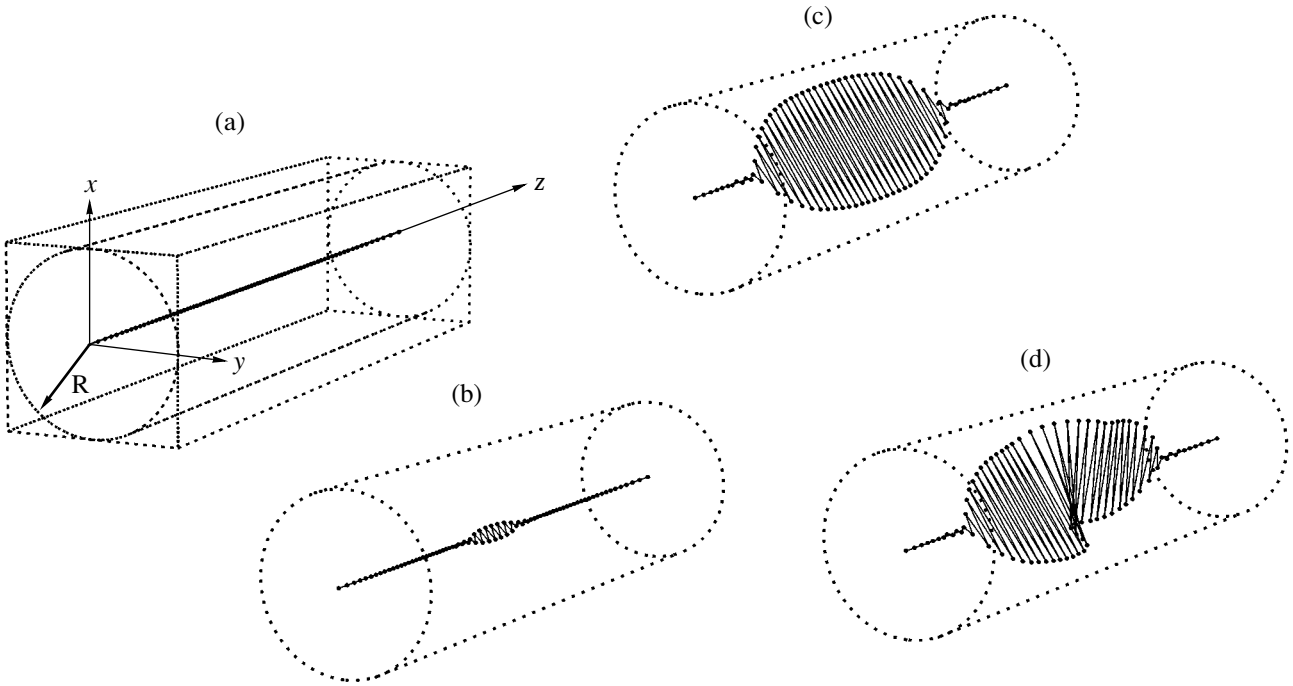

Fig. 6. Results of molecular dynamics simulations for the Yukawa screened potential with $D_Y = 0.1$ for K = (a) 3, (b) 1, (c) 0.45, and (d) 0.3. For illustrative purposes, the scales along the axes in the (x, y) plane are 40 times larger than that along the z axis.

systems; qualitatively, however, the regular features revealed above are also characteristic to the latter.

In our simulations, we analyzed several different models of systems of finite dimensions.

3.2.1. Confinement in the *z* direction by a parabolic potential well. As in the case of infinite systems, we introduced friction into the model in order to achieve a steady equilibrium state.

We simulated axisymmetric finite grain systems for which the confining potential well had the form $U \sim -1/2(d(x^2 + y^2) + z^2)$ and the intergrain interaction potential was given by expression (11). Figure 5 illustrates the results of simulation of a finite chain of 80 grains that is in equilibrium in this potential well at a large value of the radial confinement parameter (all the existing analytic formulas for describing the grain distribution in such a chain are valid only approximately). It can be seen that the distance between the grains increases in the region where the axial confinement (along the z axis) becomes essential.

Figure 6 shows how a grain system evolves as the external parameter (the radial confinement constant) is decreased.

In this figure, we present the results from simulations of a system of 80 grains interacting through the Yukawa potential with $D_Y = 0.1$. The calculations were carried out for $\alpha = 0$ and $K \approx$ (a) 3, (b) 1, (c) 0.45, and (d) 0.3. For illustrative purposes, the scales along the axes in the (x, y) plane are 40 times larger than that along the z axis.

We can see from Fig. 6 that the grain system evolves through all of the above stages: from a string to a system of several interwoven helices. Because of the different line densities (the density per unit length in the z direction), all these stages were often observed to occur simultaneously.

3.2.2. Solid walls. Let us consider an axisymmetric grain system in which the confining potential is proportional to $U \sim -1/2(d(x^2 + y^2) + z^{2L})$. For $L \gg 1$, we deal with a system that is bounded in the z direction by solid walls. In this case, in contrast to the case of confinement by a parabolic potential well, the grain density near the ends of the cylinder is higher than that in its center. This is why the bifurcation process starts precisely at the ends. If we now consider the confinement potential in the form $U \sim -1/2(d(x^2 + y^2)^M + z^{2L})$, we will be dealing with a system bounded by a cylindrical solid wall in the transverse direction and by solid walls along z. In such a system, the grains immediately occupy such positions that the distances between them are the largest. The calculations were carried out for $L = 40$ and $M = 40$. The cylindrical wall in fact determines the radius of the structure. Accordingly, the type of structure is determined by its radius. For a cylinder of very small radius, we arrive at structures similar to those shown in Fig. 7.

In the problem as formulated, the structures are fairly difficult to classify, but it is possible to draw an analogy with infinite structures. As may be seen, the system evolves through all of the above stages: a string

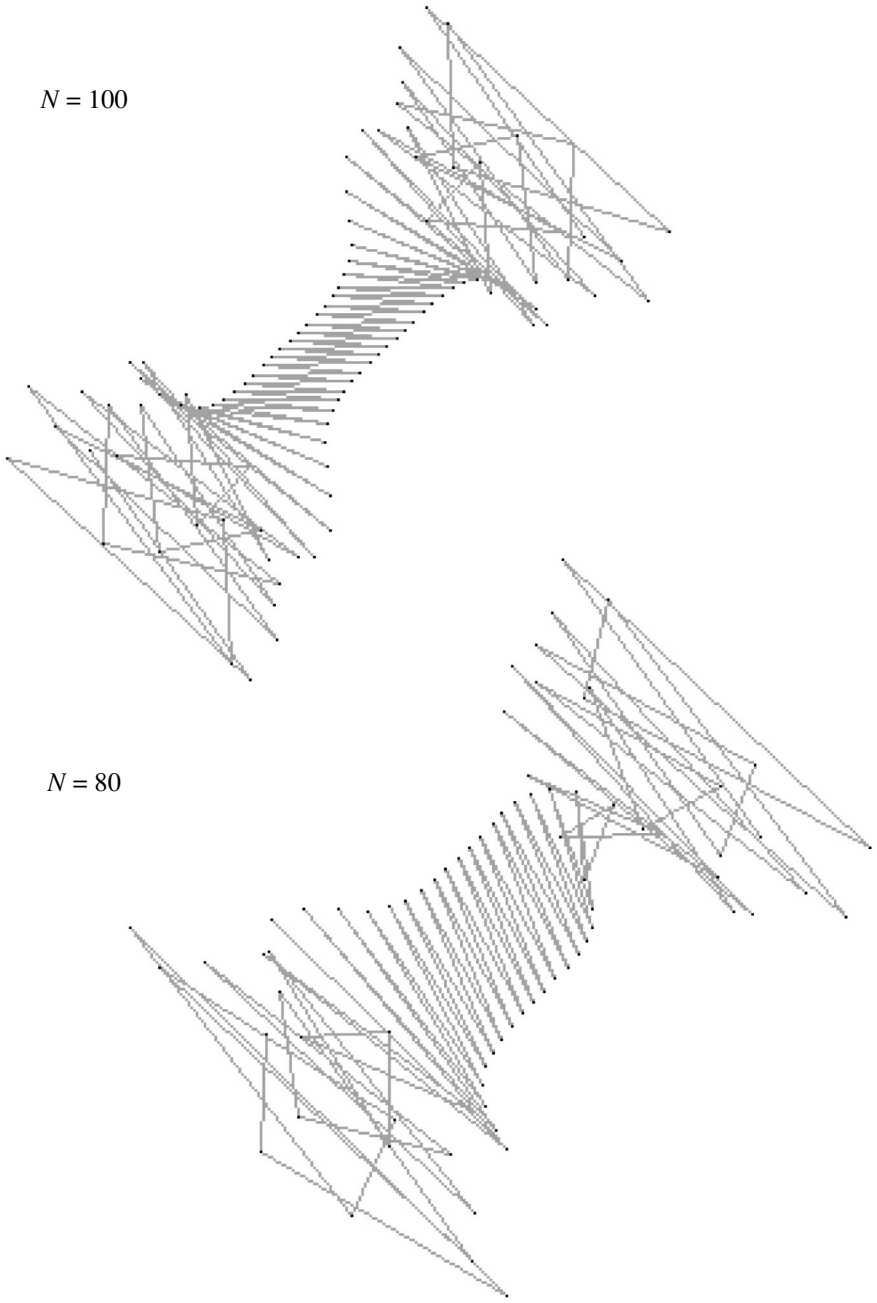

Fig. 7. Results of molecular dynamics simulations for confinement by solid walls at the cylinder ends ($L = 40$). The numbers of grains is $N = 80$ and 100.

changes into a zigzag, which in turn transforms into a helix as the external parameter changes. This bifurcation process starts at the point at which the grain density is higher. For the case of Fig. 5, the bifurcations start at the center of the string; for the case with solid walls, the bifurcational evolution begins at the cylinder ends. For a higher density, at which z_0 is smaller and the dimensionless diameter $u = 2R_0/z_0$ is larger, the conditions favorable for bifurcations of such grains are attained sooner. The values of the external parameter at which a string bifurcates into a zigzag were estimated for an infinite grain system with the same density as that at the center of a finite system; the estimate obtained turns out to be fairly realistic.

4. HELICES

Since in numerical simulations (as in experiments), steady configurations are observed that have the form of a helix with a constant period and a constant pitch angle, it is reasonable to try to analytically describe only this type of configurations.

Let us consider a system of N interwoven helices with a constant period. To do this, we substitute into the general equation of motion (13) the coordinates of the grains that have already formed such a system. In this case, several different equilibrium states are possible. It can be shown, however, that, among all possible equilibrium configurations, the one in which the grains in the (x, y) plane are at the vertices of a regular polygon has minimum energy and, accordingly, is most stable. This is why we restrict ourselves to considering only such configurations.

The configurations of interest can be represented as follows:

$$\mathbf{r}_{1,n} = (x_{1,n}, y_{1,n}, z_{1,n})$$
$$= (R_{1,n}\cos(\varphi_{1,n}), R_{1,n}\sin(\varphi_{1,n}), z_{1,n});$$
$$\mathbf{r}_{2,n} = (x_{2,n}, y_{2,n}, z_{2,n})$$
$$= (R_{2,n}\cos(\alpha + \varphi_{2,n}), R_{2,n}\sin(\alpha + \varphi_{2,n}), z_{2,n});$$
$$\mathbf{r}_{3,n} = (x_{3,n}, y_{3,n}, z_{3,n})$$
$$= (R_{3,n}\cos(2\alpha + \varphi_{3,n}), R_{3,n}\sin(2\alpha + \varphi_{3,n}), z_{3,n});$$
$$\ldots\ldots\ldots\ldots\ldots\ldots\ldots\ldots\ldots\ldots\ldots\ldots\ldots\ldots\ldots\ldots$$
$$\mathbf{r}_{N,n} = (x_{N,n}, y_{N,n}, z_{N,n})$$
$$= (R_{N,n}\cos((N-1)\alpha + \varphi_{N,n}),$$
$$R_{N,n}\sin((N-1)\alpha + \varphi_{N,n}), z_{N,n});$$

where $z_{1,n} = z_{2,n} = z_{3,n} = \ldots = z_{N,n} = z_0 Nn$. Hereinafter, we assume that the grain density along the z axis is constant; i.e., there are N_0 grains over an interval of length L. For an $N = 1$ helix, we have $z_0 = L/N_0$.

For the same linear grain density as in an $N = 1$ helix, the charged grains in a system of N interwoven helices are separated along the z axis by the distance Nz_0.

The rest of the notation is as follows:

$R_{1,n} = R_{2,n} = R_{3,n} = \ldots = R_{N,n} = R$ = const is the radius of a system of N interwoven helices;

$\alpha = 2\pi/N$ is the angle between each two neighboring grains at the vertices of a regular N-gon in the same (x, y) plane; and

$\varphi_{1,n} = \varphi_{2,n} = \varphi_{3,n} = \ldots = \varphi_{N,n} = \varphi n$ is the turning angle of the nth plane (where φ is the angle through which the polygons formed by the grains in the neighboring planes are displaced relative to one another in the (x, y) plane).

We are considering the equilibrium conditions for a helical structure that does not rotate as a whole ($\dot{\varphi} = 0$) because it is always possible to pass over to a frame of reference in which the structure is nonrotating.

The conditions for the existence of a steady equilibrium state have the form

$$\frac{\partial U}{\partial \varphi_n} = 0; \quad \frac{\partial U}{\partial R_n} = 0; \quad \frac{\partial U}{\partial z_n} = 0. \tag{14}$$

As may be seen that there is in fact only one equilibrium condition,

$$\frac{\partial U}{\partial R_n} = 0,$$

because z_n and φ_n always satisfy the force balance equation.

A full analysis of the properties of a helix and its linear stability is a fairly complicated task and is to be done separately. This is why we perform here only a qualitative analysis of the possible types of stable configurations and the evolution from one structure to another when one or several external parameters are varied.

In order to study this problem, we utilize the following familiar mechanical principle: in a stable equilibrium state, the system has a minimal potential energy. Systems with dissipation naturally evolve into this state.

When the grains in such configurations interact through potential (11), the energy of each grain can be written as

$$E = Ku^2 + (1 - \delta_{N,1})\sum_{k=1}^{N-1}\frac{1}{\Delta r_{0,k}}$$
$$\times\left[(1 - D\Delta r_{0,k})^4\frac{1}{2}\left(1 + \frac{1 - D\Delta r_{0,k}}{|1 - D\Delta r_{0,k}|}\right) - \alpha\right]$$
$$+ \sum_{k=0}^{N-1}\sum_{l=1}^{\infty}\frac{2}{\Delta r_{l,k}}$$
$$\times\left[(1 - D\Delta r_{l,k})^4\frac{1}{2}\left(1 + \frac{1 - D\Delta r_{l,k}}{|1 - D\Delta r_{l,k}|}\right) - \alpha\right], \tag{15}$$

where

$$\Delta r_{l,k} = \left(N^2 l^2 + u^2\sin^2\left(\frac{l\varphi}{2} + \frac{\pi k}{N}\right)\right)^{1/2}.$$

For convenience, we have introduced the notation $u = \dfrac{2R}{z_0}$, where R is the radius of the helix.

Accordingly, for interactions through the Debye screened potential given by expression (12), the energy per grain is equal to

$$E = Ku^2 + (1 - \delta_{N,1})\sum_{k=1}^{N-1}\frac{\exp(-D\Delta r_{0,k}) - \alpha}{\Delta r_{0,k}}$$
$$+ 2\sum_{k=1}^{N-1}\sum_{l=1}^{\infty}\frac{\exp(-D\Delta r_{l,k}) - \alpha}{\Delta r_{l,k}}. \tag{16}$$

Since the infinite sums in these two expressions for the grain energy diverge, it is meaningful to calculate only the difference between the energy of N interwoven

helices and the energy of a string, $E_{N\text{–helix}} - E_{\text{string}}$. This allows us to set aside problems associated with the divergence of the infinite sums.

For a helix, the condition under which the energy takes an extremal value has the form

$$\frac{\partial E}{\partial \varphi} = 0. \tag{17}$$

The stability analysis requires knowledge not only of the extremal value of the energy but also of its minimal value. The corresponding criterion has a definite physical meaning: it gives nothing more than the minimal energy per elementary cell, or, in other words, a minimum in the Madelung energy.

Equation (17) yields phase diagrams in the (u, φ) plane. The situation in which two or more different values of the variables (u, φ) correspond to one value of the external parameter K will be regarded as a bifurcation. As will be clear later, the smaller the confinement parameter K, the larger the number of possible bifurcations.

On the other hand, the expression for the external parameter K is determined by the radial force balance equation. Consequently, the parameter K depends to a greater extent on the radius of the structure and on the type of the intergrain interaction potential. In the simplest cases, the parameter K is inversely proportional to the dimensionless radius u of the structure. This is why it is convenient to classify structures in terms of their radius: the larger the radius of the structure, the larger the number of possible bifurcations. We thus have

$$\begin{aligned} K = &-\frac{1}{2}(1-\delta_{N,1})\sum_{k=1}^{N-1} V_1(\Delta r_{l,k})\sin^2\left(\frac{\pi k}{N}\right) \\ &- \sum_{k=0}^{N-1}\sum_{l=1}^{\infty} V_1(\Delta r_{l,k})\sin^2\left(\frac{l\varphi}{2}+\frac{\pi k}{N}\right), \end{aligned} \tag{18}$$

where

$$V_1(r) = -\frac{1}{r^3}\left[(1-Dr)^3(1+3Dr)\frac{1}{2}\left(1+\frac{1-Dr}{|1-Dr|}\right)-\alpha\right].$$

In contrast to molecular dynamics simulations, in which the equilibrium values of the variables (u, φ) were calculated from the preset values of K, it is now expedient to carry out simulations in exactly the opposite way: to calculate the external parameter K from formula (18) with the preset equilibrium values of (u, φ).

Since the intergrain interaction potentials can be not only repulsive but also attractive (see the above discussion of this latter point), there may also exist equilibrium structures for negative K values.

If radial force balance conditions (14) and condition (17) for the existence of an extremum yield the equilibrium values of (u, φ) at $K \le 0$, then self-confining structures, including those in the absence of any external potential ($K = 0$), are possible too.

The stability condition for a configuration is the condition for its energy to be minimal. Accordingly, for a two-parameter equation, the minimum-energy conditions have the form

$$\begin{aligned} E_{\varphi\varphi}E_{uu} - E_{u\varphi}E_{\varphi u} \equiv K'(u,\varphi) > 0, \\ E_{\varphi\varphi} \equiv F'(u,\varphi) > 0. \end{aligned} \tag{19}$$

For intergrain interaction potential (11), we find

$$\begin{aligned} F'(u,\varphi) = &\sum_{k=0}^{N-1}\sum_{l=1}^{\infty}\frac{1}{2}V_1(\Delta r_{l,k})u^2l^2\left[1-\left(\sin\left(\frac{l\varphi}{2}+\frac{\pi k}{N}\right)\right)^2\right] \\ &+\frac{1}{2}V_2(\Delta r_{l,k})\left[u^2 l\sin\left(\frac{l\varphi}{2}+\frac{\pi k}{N}\right)\cos\left(\frac{l\varphi}{2}+\frac{\pi k}{N}\right)\right]^2, \end{aligned} \tag{20}$$

where

$$V_2(r) = \frac{3}{r^5}\left[(1-Dr)^2(1+2Dr+D^2r^2)\frac{1}{2}\left(1+\frac{1-Dr}{|1-Dr|}\right)-\alpha\right].$$

Finally, we obtain

$$\begin{aligned} K'(u,\varphi) = F'(u,\varphi)\Bigg[&-2K(u,\varphi) \\ &+ u^2(1-\delta_{N,1})\sum_{k=1}^{N-1}V_2(\Delta r_{0,k})\left(\sin\left(\frac{\pi k}{N}\right)\right)^4 \\ &+ 2u^2\sum_{k=0}^{N-1}\sum_{l=1}^{\infty}V_2(\Delta r_{l,k})\left(\sin\left(\frac{l\varphi}{2}+\frac{\pi k}{N}\right)\right)^4\Bigg] \\ -\Bigg[\sum_{k=0}^{N-1}\sum_{l=1}^{\infty}&\left[2V_1(\Delta r_{l,k})+V_2(\Delta r_{l,k})u^2\left(\sin\left(\frac{l\varphi}{2}+\frac{\pi k}{N}\right)\right)^2\right] \\ &\times lu\sin\left(\frac{l\varphi}{2}+\frac{\pi k}{N}\right)\cos\left(\frac{l\varphi}{2}+\frac{\pi k}{N}\right)\Bigg]^2. \end{aligned} \tag{21}$$

We thus have determined the minimum of the Madelung energy.

5. NUMERICAL SIMULATIONS OF EQUILIBRIUM HELICAL STRUCTURES

It is important to emphasize the following general features of the structures that have been revealed by both molecular dynamics simulations and numerical calculations based on analytical formulas:

The results of molecular dynamics simulations show that any random grain distribution evolves into

one of the possible steady helical structures. No finite configurations other than helical structures were obtained. On the other hand, it is obvious that, for any type of interaction potential, there exists a steady helical configuration with a constant period, the constant of the lattice of such a quasi-crystal being determined by the mean number of grains per unit of length along the symmetry axis. As the depth of the external confining potential (the confinement parameter) decreases, the patterns of the grains in the (u, φ) plane begin to bifurcate. For the same K value, a system of N interwoven helices can be in one of several possible equilibrium states. When the interaction between the grains is attractive, they can form steady helical structures in the absence of an external confining potential and even in the presence of a parabolic repulsive potential.

5.1. Dynamics of the Onset of Bifurcations

Figure 8 shows a typical dependence of φ on $u = 2R/z_0$. We can see that, for sufficiently large u values, φ can take on several different values, whose number increases with u. As the parameter u is smoothly changed, bifurcations occur suddenly. They can serve as marks in the helical structure and thereby can provide a method for storing information.

Each type of the interaction potentials under consideration was simulated for different values of the parameters D and α. The curves in (u, φ) plane that correspond to the minimal Madelung energy are qualitatively similar in shape, but the instants at which bifurcations occur, their number, and their sequence all depend on the values of these parameters (as a rule, the number of bifurcations increases with the screening distance D and with the grain attraction coefficient α). Even for $D \geq 0.3$ and $\alpha = 0$, the grains in the structure that has undergone two or three bifurcations are almost insensitive to their neighbors, so the radius of the structure becomes uncertain, i.e., the slope of the curve $\partial E/\partial\varphi$ in the vicinity of the point where $\partial E/\partial\varphi = 0$ becomes very gentle and small perturbations in equilibrium produce large grain displacements. In this case, the minimum energy states are only slightly pronounced and any state of the system is close to an indifferent equilibrium state. However, when there is even a weak long-range interaction (for instance, an attractive interaction such that $D \geq 0.3$ and $\alpha = 0.001$), the energy states of the system are very different. For $D = 0.1$, the attraction effect is far weaker. Consequently, there exists a certain critical value of the parameter D above which the attraction is fairly strong. The situation with the Yukawa screened interaction is analogous: in this case, the critical value of the parameter D_Y is equal to three (a comparative discussion of the Yukawa screening and nonlinear screening will be given below).

In order to describe the grain system graphically, it is convenient to plot the bifurcation curves and the family of the characteristic curves of the equilibrium equation (which are obtained by determining the K values from formula (18) with the equilibrium values of u and φ) in the same figure. The resulting plot can thus be conveniently scaled by the value of the external parameter K of the system.

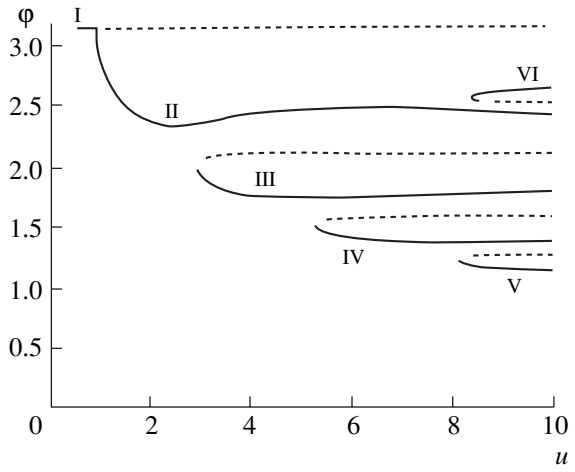

Fig. 8. Solutions in the phase plane composed of two coordinates: the angle φ through which the polygons formed by the grains in the neighboring (x, y) planes are displaced relative to one another and the dimensionless diameter $u = \frac{2R}{z_0}$ of the helical structure (here, z_0 is the spatial separation in the z direction between the grains in the neighboring planes and R is the radius of the helix). The Roman numerals I, II, III, IV, … correspond to different branches of the equilibrium solutions describing a helix (zigzag, helix I, helix II, helix III, etc.). As the external confinement parameter K decreases, a pair of new equilibrium positions appear, one of which (as well as the corresponding branch of the solutions) is unstable (dashed curves) and the other is stable (solid curves). The calculations were carried out for $D = 0.1$ and $\alpha = 0$.

Figure 9 illustrates the extremal-energy condition for a helical structure (the stable branches are given by heavy solid curves, and the unstable branches are given by heavy dashed curves) and also shows the contours of the constant value of the parameter K by light dashed curves. The calculations were carried out for the Yukawa screened potential with $D_Y = 0.1$ and $\alpha = 0$. For such a low screened potential, there are a large number of branches and many bifurcations.

It is also possible to graphically demonstrate the difference between the bifurcation curves calculated for different types of interaction potentials with different values of D and α. For $\alpha > 0$, the equilibrium is possible for the values of the external parameter lying in the range $K \leq 0$ (see Fig. 10). This indicates that the grains interacting by means of attractive forces can evolve into steady structures in the absence of an external confining potential. Nevertheless, in order to obtain a conclusive answer to the question about the stability of such structures, it is necessary to conduct a separate study in which account should be taken not only of criteria (19)

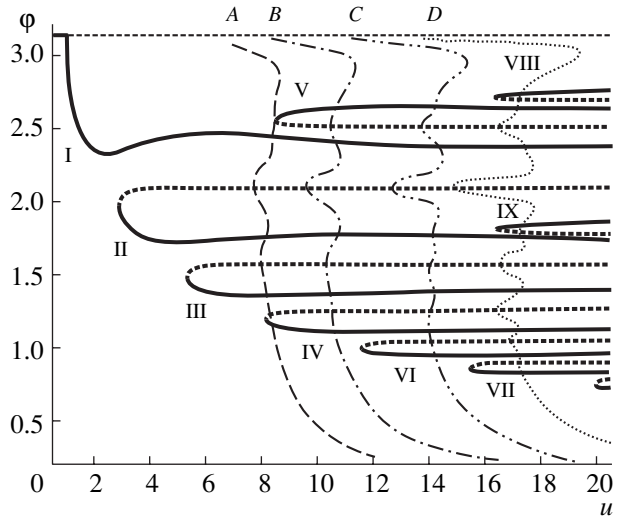

Fig. 9. Contours of the constant value of the equilibrium parameters of helical structures in a system of grains that interact through the Yukawa screened potential and do not experience attractive forces. The calculations were carried out for $N = 1$, $D_Y = 0.1$, and $\alpha = 0$. The stable branches are shown by heavy solid curves, and the unstable branches are shown by heavy dashed curves. The contours of the constant value of the parameter K are given by light dotted curves; curves A, B, C, and D were calculated for $K = 0.009$, 0.005, 0.0025, and 0.0015, respectively.

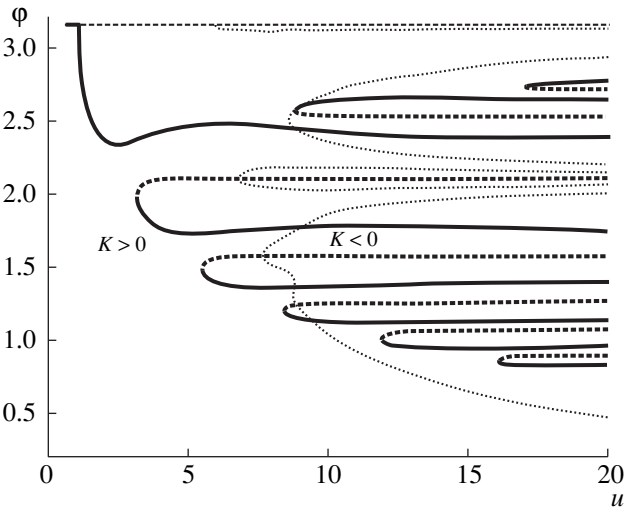

Fig. 10. Contours of the constant value of the equilibrium parameters of helical structures in a system of grains that interact through the Yukawa screened potential lower than that in Fig. 9 and are subject to attractive interactions. The calculations were carried out for $N = 1$, $D_Y = 1$, and $\alpha = 0.01$. The stable branches are shown by heavy solid curves, and the unstable branches are shown by heavy dashed curves. The light dotted curve is for $K = 0$.

(in the case at hand, they are also satisfied for continuous curves in the range $K \le 0$) but also of the stability criteria for different modes.

From Figs. 9 and 10, we can see that several equilibrium conditions can be satisfied for the same value of the external parameter. The smaller the external parameter, the larger the number of possible equilibrium conditions. Most likely, the grain system will try to evolve into a steady configuration that is most favorable from the energy standpoint, but whether or not this will occur depends, of course, on the initial grain distribution and on other parameters of the system. This will inevitably occur, however, if there is any dissipation in the system. Figures 9 and 10 also clearly illustrate how one grain configuration bifurcates into another.

Let us examine in detail all phase transitions that were revealed in our numerical simulations. To do this, we analyze the final steady configurations.

We begin our analysis with a string, which is a limiting case of an $N = 1$ helix.

5.1.1. String. We consider an infinitely long chain of charged grains separated by the same distance z_0. In this case, the solution to Eq. (13) can be represented as

$$\mathbf{r}_n = (0, 0, z_n) = (0, 0, z_0 n).$$

In Fig. 8, our analysis begins immediately with a zigzag—a particular case of an $N = 1$ helix in which the angle φ (i.e. the angle through which two neighboring grains are displaced relative to one another in the (x, y) plane) is equal to π. Let us estimate the parameter values at which a string bifurcates into a zigzag. From the above analysis, it is logical to conclude that this bifurcation should occur when the energy per grain in a string becomes equal to that in a zigzag:

$$E_{\text{zigzag}} - E_{\text{string}} = 0.$$

We can obtain from this the stability condition (or, more correctly, the instability criterion), i.e., the value of the external parameter K at which the string becomes unstable (for certain types of interactions, this value can be explicitly expressed in terms of special functions).

For particular D and α values, it is an easy matter to compare the K value so obtained with that found from an analytic formula in accordance with [21].

5.1.2. Zigzag. We have shown above how to derive the value of the external confinement parameter at which a string becomes a zigzag. Let us now estimate the value of this parameter at which a zigzag changes into a helix of the general form. To do this, we must determine when the extremum (minimum) point ($E_{\varphi\varphi}E_{uu} - E_{u\varphi}E_{\varphi u} > 0$, $E_{\varphi\varphi} > 0$) of the potential energy becomes a saddle point ($E_{\varphi\varphi}E_{uu} - E_{u\varphi}E_{\varphi u} < 0$). Applying the corresponding formula to each particular type of interaction, we can then find the values of u and, consequently, the values of the external parameter K, at which a bifurcation occurs [21] (e.g., for purely Coulomb interaction, we obtain $u = 0.965$).

5.1.3. $N = 1$ helix. We can see that an evolving $N = 1$ helix actually loses its stability only when it undergoes a Y-type bifurcation, namely, a zigzag ⟶ helix I bifur-

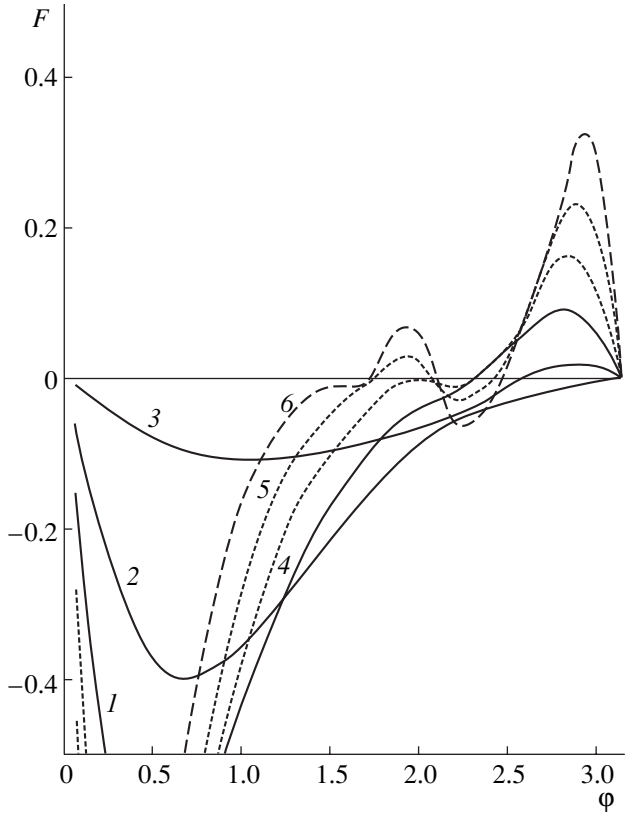

Fig. 11. Function $F(\varphi)$ for different values of the parameter u. The calculations were carried out for the Yukawa screened potential with $D_Y = 1$ and for $N = 1$ and $\alpha = 0$. The equilibrium points are determined by the condition $F = 0$. Curve *1* is for $u = 0.6$ (a stable zigzag with $\varphi = \pi$), curve *2* is for $u = 1.4$ (a stable $N = 1$ helix with $\varphi < \pi$), curve *3* is for $u = 2$, curve *4* is for $u = 2.8$, curve *5* is for $u = 3.6$, and curve *6* is for $u = 5$.

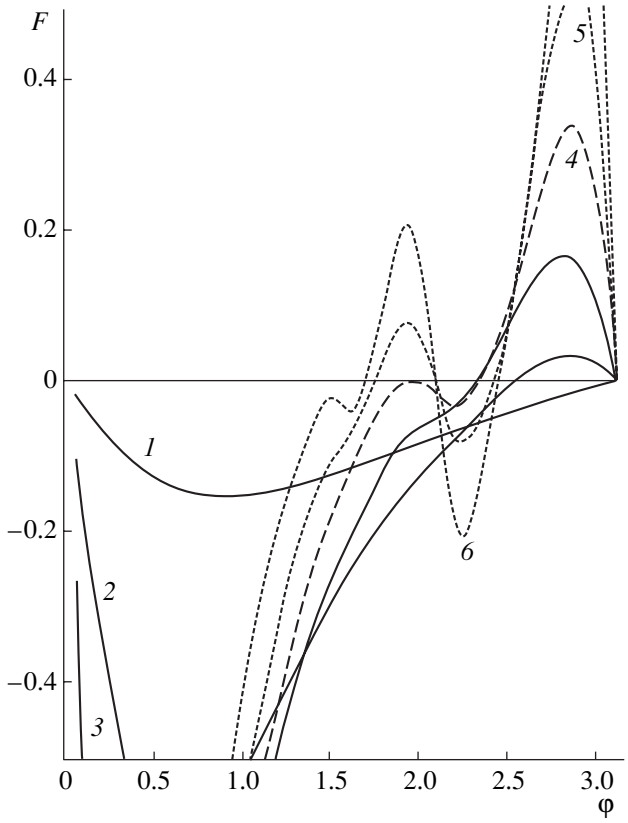

Fig. 12. Function $F(\varphi)$ for different values of the parameter u. The calculations were carried out for the nonlinear screened potential with $D = 0.1$ and for $N = 1$ and $\alpha = 0$. The equilibrium points are determined by the condition $F = 0$. Curve *1* is for $u = 0.6$ (a stable zigzag with $\varphi = \pi$), curve *2* is for $u = 1.4$ (a stable $N = 1$ helix with $\varphi < \pi$), curve *3* is for $u = 2$, curve *4* is for $u = 2.8$, curve *5* is for $u = 3.6$, and curve *6* is for $u = 5$.

cation. In this case, the solution $\varphi = \pi$ becomes unstable and splits into two symmetric branches: stable and unstable. This is most clearly seen by looking at the evolution of the function $F(\varphi) = \partial E/\partial\varphi$ when the parameter u is increased step by step (see Fig. 11, which was obtained for the Yukawa screened potential with $D_Y = 1$ and for $N = 1$ and $\alpha = 0$, and Fig. 12, which was obtained for the nonlinear screened potential with $D = 0.1$ and for $N = 1$ and $\alpha = 0$; recall that, for the same values of the physical parameters of the system, the coefficient D is approximately ten times less than the coefficient D_Y). Note that, for the chosen examples of the Yukawa screened potential and nonlinear screened potential, the state of a homogeneous chain is always unstable, even for small u values (in contrast to a Coulomb system). This conclusion is logical, since the derivative of the function just introduced, $\partial F/\partial\varphi$, is positive at $\varphi = 0$ and is negative at $\varphi = \pi$. However, as the parameter u increases above a certain critical value, the function begins to exhibit a small maximum in the vicinity of $\varphi = \pi$, so another stable solution arises such that the derivative of $F(\varphi)$ in the region $\varphi < \pi$ is positive, which corresponds to a zigzag $\longrightarrow$ helix I bifurcation. As the parameter u increases further, a second maximum in the function arises that corresponds to the next bifurcation, and so on. In Figs. 11 and 12, this bifurcational dynamics is followed up to a value of $u = 5$. One can clearly see the differences between the cases of Yukawa screening and nonlinear screening: the bifurcations occur at different critical values of the pitch of the structure and the equilibrium states in Fig. 12 are more stable than those in Fig. 11 (the values of the derivative $\partial F/\partial\varphi$ at the point where $F = 0$ are larger, $\partial F/\partial\varphi > 0$). For comparison, Figs. 13 and 14 show analogous curves calculated for different values of the Yukawa screening factor, $D_Y = 1$ and 3, and of the attraction coefficient, $\alpha = 0.1$ (weak attraction) and $\alpha = 0.5$ (strong attraction). Figures 15 and 16 show analogous curves calculated for different values of the nonlinear screening factor, $D = 0.1$ and 0.3, and of the attraction coefficient, $\alpha = 0.1$ (weak attraction) and $\alpha = 0.5$ (strong attraction). We can see that attraction has the strongest effect on bifurcations when the screening factors are increased (the screening length is decreased)

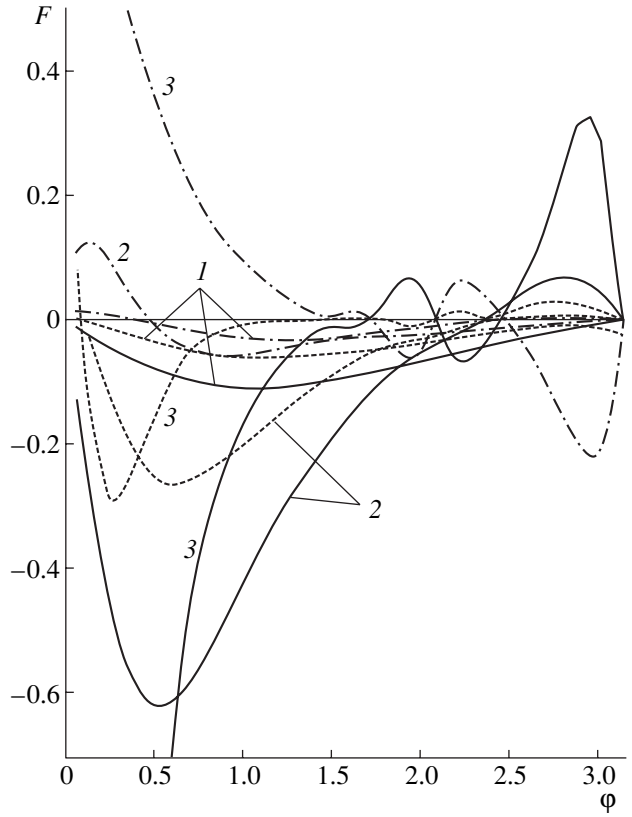

Fig. 13. Function $F(\varphi)$ for different values of the grain attraction coefficient and the parameter u. The calculations were carried out for the Yukawa screened potential with $D_Y = 1$ and for $N = 1$ and $\alpha = 0$ (solid curves), 0.1 (dotted curves), and 0.5 (dashed curves). Curves *1*, *2*, and *3* are for $u = 0.6$, 2, and 5, respectively.

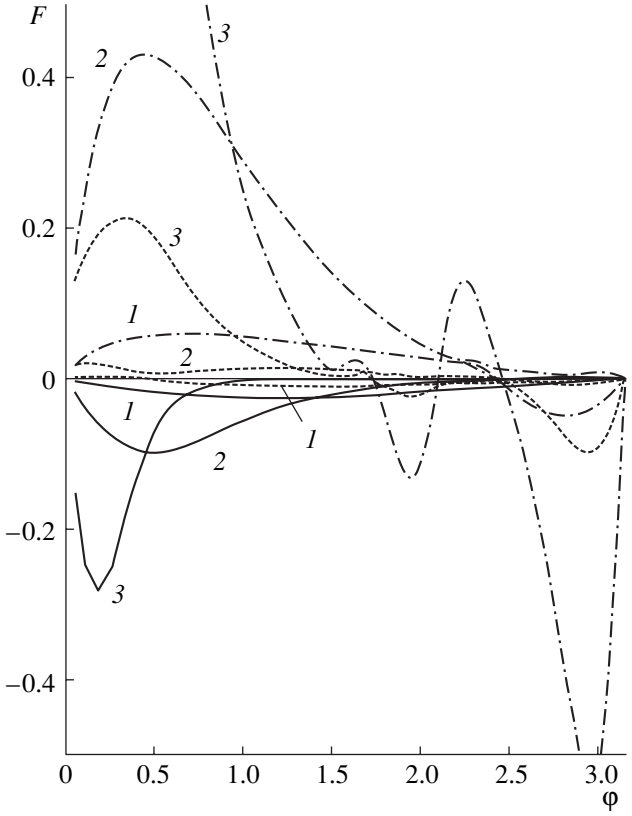

Fig. 14. The same as in Fig. 13, but for $D_Y = 3$. The attraction is seen to have a far stronger effect on bifurcations. Along a substantial portion of solid curve *3*, the function F is close to zero, so the position of the equilibrium point, at which $F = 0$, is fairly uncertain. This uncertainty is removed when even a weak absorption is taken into account (see the dotted curves).

and approach the values at which Coulomb repulsion is substantially suppressed. This situation is quite natural. An essential point is, however, that the screening distances D and D_Y can be controlled experimentally by varying z_0 (because they are normalized to z_0) or, equivalently, the number of grains per unit length of the system. It is now clear that attraction can radically change the behavior of a grain system; it can even cause unstable branches of the solution to become stable (see the cases $u = 5$, $\varphi = \pi$ in Figs. 11 and 12). The difference between the effects of the Yukawa screening and nonlinear screening is also very pronounced.

Such transitions as the numerically calculated sequence of helix I ⟶ helix II ⟶ helix I ⟶ helix III, etc., where the Roman numerals I, II, III, … label the stable branches of $N = 1$ helical structures on the (u, φ) plane, are nothing more than jumps of the system from one stable state to another, provided that the latter is more favorable energetically. In other words, the system tends to change to a configuration that possesses a minimal energy at a fixed value of the external confinement parameter. However, it is the initial grain distribution that points to the branch to which of the solution the system will evolve in molecular dynamics simulations; the subsequent transition to a lower energy state can be initiated by finite-amplitude perturbations. It sometimes happens (especially for large values of the parameter u) that stable branches differ in energy by less than one percent; therefore, in actual experiments, there may be several (rather than one) different stable grain configurations corresponding to the same external conditions.

We thus have completely explained why, for certain values of the external confinement parameter, our numerical simulations yielded different steady configurations of grains, depending on their initial distribution.

5.1.4. $N = 2$ helix. The next simple equilibrium configuration into which an $N = 1$ helix bifurcates is an $N = 2$ helix.

A particular (limiting) case of an $N = 2$ helix is a tetrahedral configuration, in which the grains in the neighboring planes of the lattice are turned through an angle of $\varphi = \pi/2$ in the (x, y) plane. In this case, two pairs of grains in the neighboring planes lie at the vertices of a

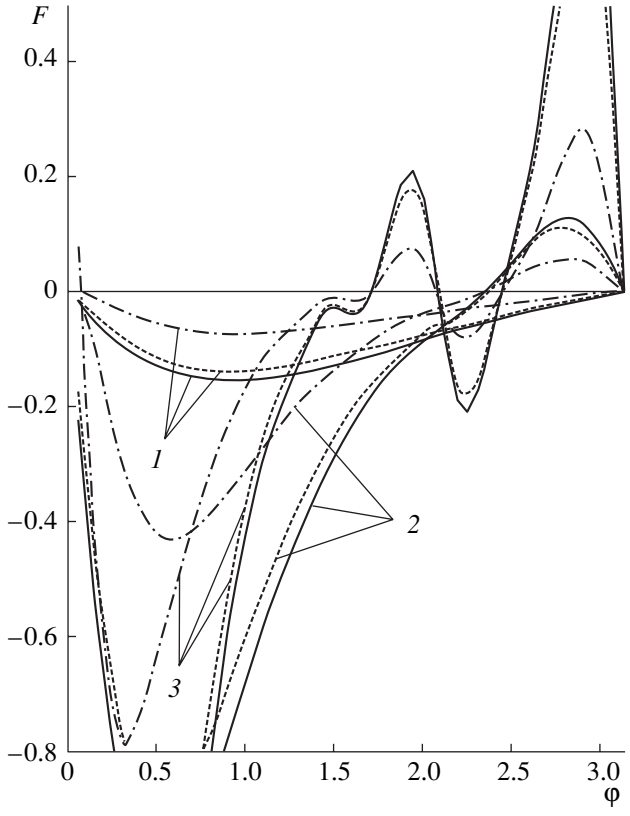

Fig. 15. Function $F(\varphi)$ for different values of the grain attraction coefficient and the parameter u. The calculations were carried out for the nonlinear screened potential with $D = 0.1$ and for $N = 1$ and $\alpha = 0$ (solid curves), 0.1 (dotted curves), and 0.5 (dashed curves). Curves *1*, *2*, and *3* are for $u = 0.6$, 2, and 5, respectively. The general pattern of the curves is only slightly affected by absorption. The nonlinear screened potential differs substantially from the Yukawa potential for which Fig. 14 was obtained.

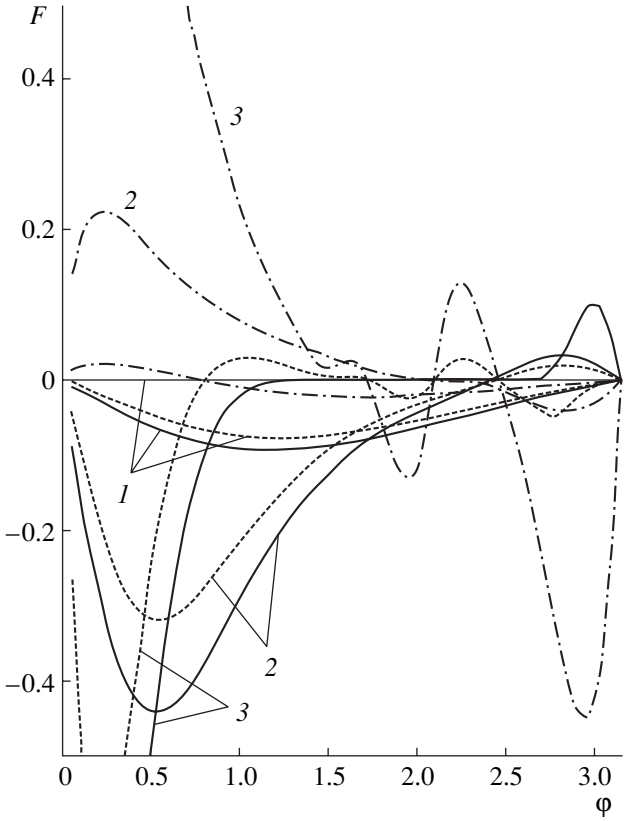

Fig. 16. The same as in Fig. 15, but for $D = 0.3$. The attraction is seen to have a far stronger effect on bifurcations. Along a substantial portion of solid curve *3*, the function F is close to zero, so the position of the equilibrium point, at which $F = 0$, is fairly uncertain. This uncertainty is removed when even a weak absorption is taken into account (see the dotted curves). The nonlinear screened potential differs substantially from the Yukawa potential for which Fig. 14 was obtained.

tetrahedron. It is expedient to emphasize a direct analogy between the particular cases of an $N = 1$ and an $N = 2$ helix, namely, a tetrahedral configuration and a zigzag.

The situation in question is similar to that with a conventional $N = 1$ helix. Simulations carried out for different D and α values showed that grain systems may suffer Y-type bifurcation: a transition from a tetrahedral configuration to a general $N = 2$ helix. One can easily obtain the critical value of the external parameter at which the tetrahedral configuration loses its stability, i.e., the value u_{crit}, at which the system exhibits an instability analogous to that of a zigzag.

The solutions in the phase plane $\{\varphi, u\}$ that were calculated for two-pole ($N = 2$) helical structures in the case of nonlinear screening ($D = 0.1$) and attractive interaction ($\alpha = 0.01$) are shown in Fig. 17, which is similar to Fig. 10 for $N = 1$ helical structures. We can see that, as the external parameter K decreases, two new equilibrium states (stable and unstable) arise, as is the case in Fig. 10. The smaller the external parameter, the larger the number of possible equilibrium states. For $\alpha > 0$, the equilibrium is possible for $K \le 0$. As was mentioned above, this indicates that a system of grains interacting by means of attractive forces can evolve into a steady structure in the absence of an external confining potential.

The bifurcations of $N = 2$ helical structures have the same general qualitative features as the bifurcations of $N = 1$ structures, which have been described above (see Figs. 13–16). The bifurcation process, however, begins to occur at larger values of the parameter u; for relatively small values of this parameter (on the order of those for the $N = 1$ case), the number of bifurcations is smaller. As before, it is possible to determine the critical values of the screening factors at which a weak attraction substantially changes the phase diagrams of the bifurcations.

5.1.5. *N* interwoven helices. Of course, structures consisting of N interwoven helices possess the same regular features as $N = 1$ and $N = 2$ helices. In other words, the bifurcation process begins with a limiting

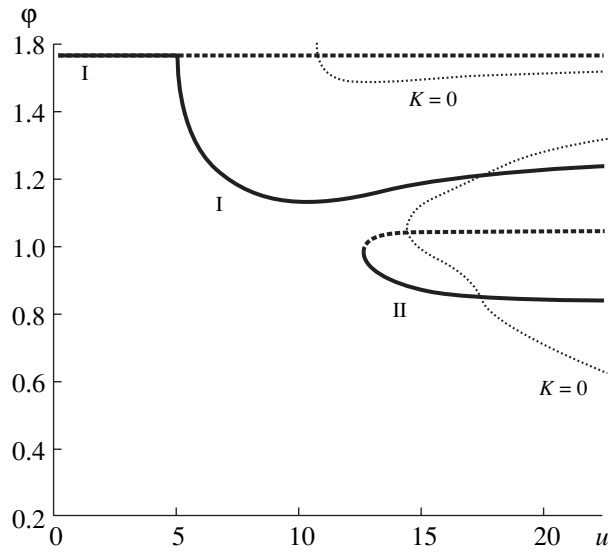

Fig. 17. Solutions in the phase plane $\{\varphi, u\}$ for $N = 2$ helical structures. The calculations were carried out for the nonlinear screened potential ($D = 0.1$) and for attractive interactions between the grains ($\alpha = 0.01$). The stable branches are shown by heavy solid curves, and the unstable branches are shown by heavy dashed curves. The curve $K = 0$ is given by the light dotted curve; the external parameter is negative ($K < 0$) on the right of this curve and is positive ($K > 0$) on the left.

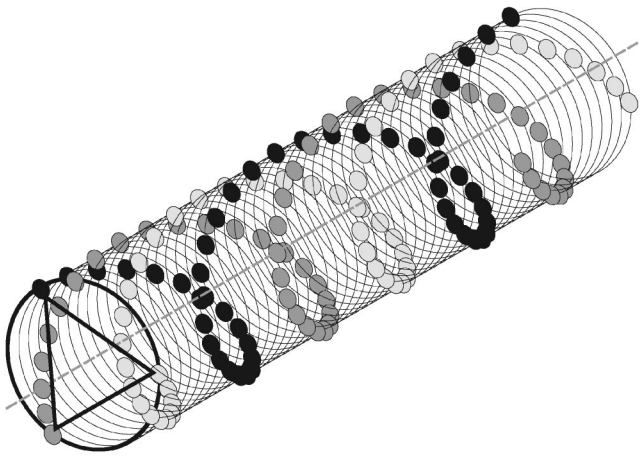

Fig. 18. Schematic representation of an $N = 3$ helical structure.

configuration (similar to a zigzag or a tetrahedral configuration), which changes into a helical structure with a larger number of interwoven helices at a certain value of the external parameter.

The simplest possible structure into which an $N = 2$ helical configuration can evolve is three interwoven helices ($N = 3$) (see Fig. 18). Similar structures were observed in experiments that were performed by Birkl *et al.* [2] with ultracold atomic ions interacting by means of Coulomb repulsive forces. More precisely, the structures observed in those experiments were a limiting case of three interwoven helices: an octahedral configuration, in which the grains in the neighboring planes of the lattice are turned through an angle of $\varphi = \pi/3$ in the (x, y) plane (see Fig. 19). In this case, as in the cases of a string, a zigzag, and a tetrahedral configuration, we can also find the value u_{crit} at which the octahedral configuration loses its stability.

The results of numerical simulations and the data from experiments with purely Coulomb systems show that there are several possible types of helical structures. The particles often form a two-shell structure that is energetically more favorable than a one-shell helical structure. In the planar case, this roughly corresponds to a transition from five particles at the vertices of a regular pentagon to four particles at the vertices of a square and one particle at the center of the square. The situation with helical dust structures is, in a sense, similar, the only difference being that, along with $N = 2$ structures, the structures with a larger number of interwoven helices can be energetically favorable. Most frequently, the results depend strongly on the type of screened potential and on the efficiency of attraction between the grains. In the case of Yukawa screening, the final results differ radically from those in the case of nonlinear screening, especially when the screening parameters are close to their critical values (a situation similar to that considered above for $N = 1$ helical structures). The critical values are determined by the number of grains per unit length of the system; they can easily be achieved in actual laboratory experiments and under microgravity conditions in space.

5.1.6. Formation of the second shell. The second shell begins to form as a string (a limiting case of an extended helical structure) inside a helix.

As the control parameter varies, the spatial separation between grains in the string decreases and the system can bifurcate into a configuration consisting of two helices, one inside the other. In numerical simulations, such a configuration has not been observed, however. The external shell in the form of a helix then evolves into a system of several interwoven helices, or, more precisely, into a hexagonal shell with a string inside it. As the external parameter varies further, two nested shells form, which is followed by the formation of a string inside them; then, by the formation of three nested shells; and so on. We thus can again draw an analogy with the planar case: as the external parameter varies, a particle appears at the center of the ring, inside which the second ring then forms, which is followed by the appearance of a particle at its center and, then, by the formation of the third ring inside it, and so on.

We are interested here in the formation of the second shell only from the standpoint of determining the parameter range in which one-shell structures exist. In order for the force balance in the z direction to be pro-

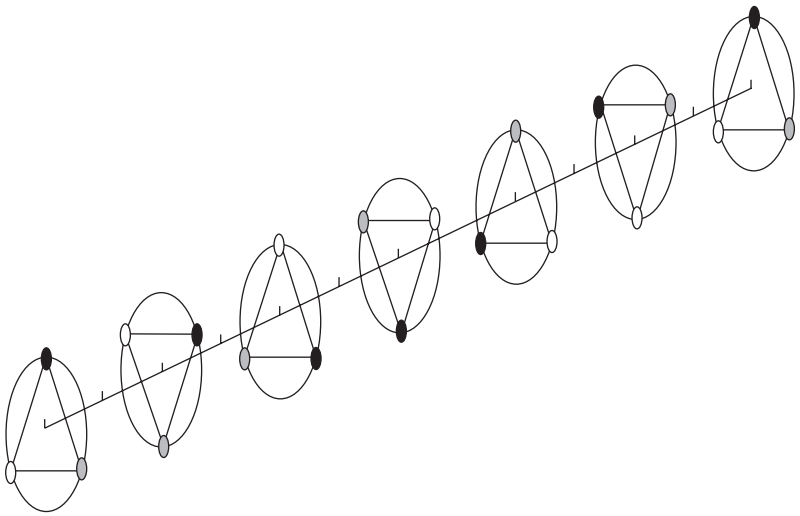

Fig. 19. Schematic representation of an octahedral helical structure.

vided automatically, we restrict ourselves to symmetric configurations such that N_h is a multiple of N_s. It follows from general considerations that the spatial separation between the grains in a string and in a helix are uncorrelated (in the general case, they are disproportionate). Without loss of generally, we can, however, consider only proportionate chains, i.e., we assume that the system in question is periodic with a certain characteristic period L. We can try to estimate the energy of such a configuration by assuming again that the grain density along the z axis is constant. The above assumption implies that there are N grains within the interval of length L ($z_0 = L/N$), but now we deal with a situation in which there are N_s grains of a string and N_h grains of a helix within the interval of the same length L. In order to calculate the mean energy of a grain, we calculate the energy of all the grains within the period L and divide the result by the total number of grains, $N_0 = N_s + N_h$. The estimate thus obtained can be somewhat incorrect because the only symmetric configurations are those in which the number of grains in the helix, N_h, is a multiple of the number of grains in the string, N_s. Even in this special case, however, the helix should be deformed, although to a much lesser extent than when N_h is not a multiple of N_s.

5.2. Comparison of energies

Figure 20 compares the energies of all the above grain configurations in the case of interaction with the parameters $D = 0.1$ and $\alpha = 0$. As is seen, these different configurations are very close in energy. As the external confinement parameter varies, the structure evolves through the following configurations: string $\longrightarrow$ zigzag $\longrightarrow$ helix I $\longrightarrow$ tetrahedral configuration, etc. Since the energies of some configurations differ by a few percent, it is possible to experimentally observe equilibrium stable configurations whose energies exceed the minimal energy. This was indeed observed in numerical simulations: for the same values of the external parameter, they yielded different configurations, depending on the initial grain positions. The results of the computations agree quite well with our analytical estimates, which in turn are physically more transparent and explain all phase transitions from one configuration to another. We stress that, for different configurations, we are comparing the energies per grain, because the structures under analysis are infinitely long in the z direction and thereby have infinite total energies. In numerical simulations, as well as in actual experiments, a study is made of systems with a finite number of grains (N_0), so the difference between the total energies of different configurations is given by the product $N_0\Delta E$. A comparison of the bifurcational pictures in the phase plane $\{u, \varphi\}$ for the cases of nonlinear screening and Yukawa screening with the same physical parameters shows that the bifurcation process in the case of the nonlinear screened potential with $D = 0.1$ sometimes resembles that in the case of the Yukawa screened potential with $D_Y = 1$. In order for the comparison to be adequate, it is necessary to keep in mind that the nonlinear screening parameter D is physically determined by the screening distance and also by z_0, (i.e., by the number of grains per unit length). Since the parameter z_0 can be controlled experimentally, the absolute values of D and D_Y for fixed plasma parameters depend greatly on it. Under actual conditions, however, the ratio between D and D_Y, which is independent of z_0, depends on the sizes of the grains and on their charges. This is why the estimated value of this ratio (about 0.1) is somewhat arbitrary, because it merely corresponds to the parameter values close to those known from the most familiar experiments. With some other ratio between these parameters, the results

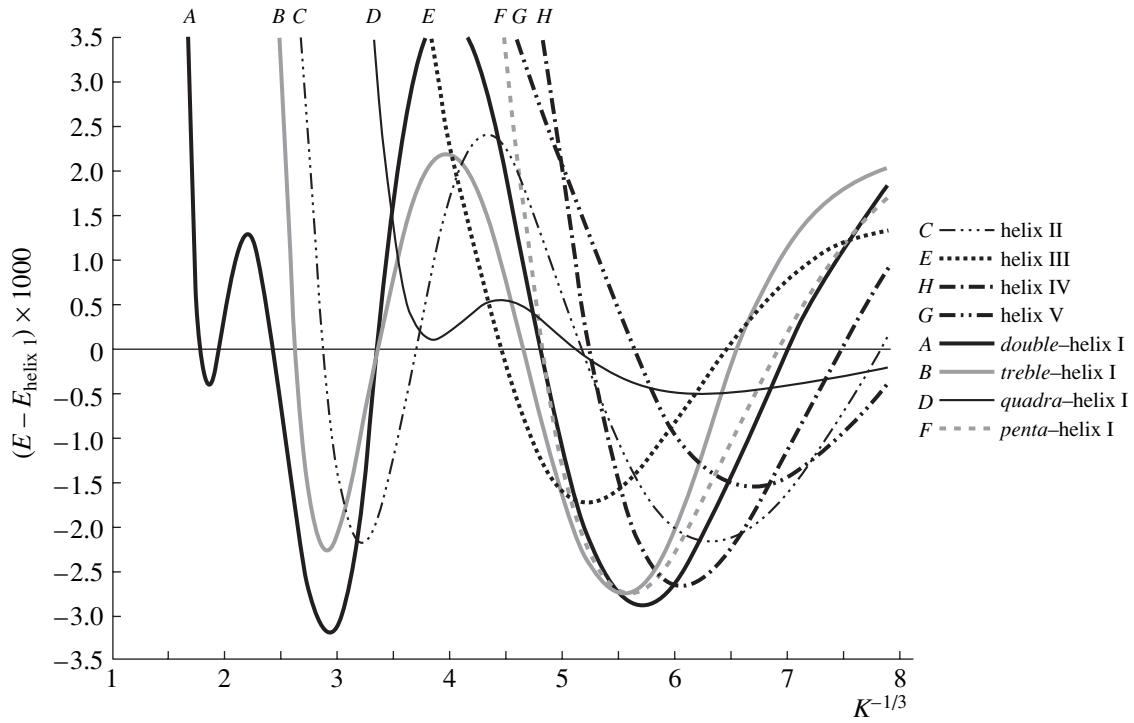

Fig. 20. Comparison between the energies per grain in different types of helical structures for $D = 0.1$ and $\alpha = 0$.

obtained for the Yukawa screening will differ strongly from those obtained for the nonlinear screening.

6. ANALYSIS OF THE RESULTS OBTAINED

In the this paper, we have investigated typical equilibrium configurations of a system of correlated likely charged dust grains. We have derived stability criteria for several configurations (such as a string and a zigzag) and have given a physical interpretation of transitions from one configuration to another that occur when the external parameters are varied. It may be said that transitions of a string into a zigzag and of a zigzag into $N = 1$ helix are analogues of first-kind phase transitions, whereas transitions between different types of helical configurations resemble second-kind phase transitions.

We have carried out a comparative analysis of the mean energies of a grain in each of the helical configurations under study. All analytical estimates are fully confirmed by the results of numerical simulations.

We have shown that systems of finite dimensions should possess all regular features revealed in our investigations of infinite systems. We have described the initial stage of the development of instability. With the results obtained for an infinitely long string, it is possible to correctly estimate the values of the external confinement parameter at which the configuration undergoes transitions from one state to another.

In actual systems, the kinetic energy of a dust grain suspended, e.g., in an ion flux increases (oscillations are excited). Experimental data [22] show that there is a mechanism whereby a grain oscillates at an increasingly large amplitude and escapes from the potential well. Molecular dynamics simulations [23] also show that an initially immobile grain acquires energy and (due to collisions with plasma ions and electrons) begins to oscillate about its equilibrium position. Hence, our results take on a somewhat new meaning. Specifically, if the system has acquired sufficient energy, then it evolves into a new steady configuration with a minimal kinetic energy. If, however, the energy acquired by the system is insufficient for it to evolve into another steady configuration, then the grains in it begin to oscillate about their previous steady-state positions.

It is important to emphasize the general features that have been revealed in our numerical simulations:

(i) In all cases, it was found that any random distribution of the grains evolves into one of the possible steady helical configurations. No final configurations other than helical ones were observed.

(ii) When the interaction between the dust grains is attractive, they can form steady helical structures in the absence of an external confining potential and even in the presence of a parabolic repulsive potential. This possibility has a simple physical interpretation: at short distances, the interaction between the grains is repulsive, and only at sufficiently long distances does attraction become comparable to repulsion. Moreover, nonlinear screening enhances the effect of attraction.

(iii) In helical configurations, the dust grain distribution has a shell structure.

(iv) The most characteristic property of the helical structures under investigation is associated with the bifurcations of the pitch angle, which result from the interactions of grains with numerous remote grains rather than with their nearest neighbors. This is why long-term nonscreened attraction between the grains operates to increase the number of bifurcations.

(v) Bifurcational marks in the structures can provide a method for storing information and can find application in computer technology. They can also be used to study self-sustaining structures in which the grains are subject to attractive interactions (as is the case in space dusty plasmas under natural conditions).

ACKNOWLEDGMENTS

This work was supported by the Russian Foundation for Basic Research grant no. 02-02-16439.

REFERENCES

1. J. J. Bolinger, D. J. Wineland, and D. H. E. Dubin, Phys. Plasmas **1**, 1403 (1994).
2. G. Birkl, S. Kassner, and H. Walther, Nature **357**, 310 (1992).
3. J. D. Prestage, G. J. Dick, and L. Maleki, J. Appl. Phys. **66**, 1013 (1989).
4. M. G. Raizen, J. M. Gilligan, J. C. Bergquist, *et al.*, Phys. Rev. A **45**, 6493 (1992).
5. S. L. Gilbert, J. J. Bollinger, and D. J. Wineland, Phys. Rev. Lett. **60**, 2022 (1988).
6. N. A. Clark, A. J. Hurd, and B. J. Ackerson, Phys. Rev. B **42**, 688 (1990).
7. S. Neser, T. Palberg, C. Blechinger, and P. Leiderer, Prog. Colloid. Polim. Sci. **104**, 194 (1997).
8. V. N. Tsytovitch, Usp. Fiz. Nauk **167**, 57 (1997) [Phys. Usp. **40**, 53 (1997)].
9. A. P. Nefedov, O. F. Petrov, and V. E. Fortov, Usp. Fiz. Nauk **167**, 1215 (1997) [Phys. Usp. **40**, 1163 (1997)].
10. V. N. Tsytovitsh, G. Morfill, and H. Thomas, Fiz. Plazmy **28**, 675 (2002) [Plasma Phys. Rep. **28**, 623 (2002)]; G. Morfill, V. N. Tsytovitsh, and H. Thomas, Fiz. Plazmy **29**, 3 (2003) [Plasma Phys. Rep. **29**, 1 (2003)]; H. Thomas, G. Morfill, and V. N. Tsytovitsh, Fiz. Plazmy **29**, 963 (2003) [Plasma Phys. Rep. **29**, 895 (2003)]; V. N. Tsytovitsh, G. Morfill, and H. Thomas, Fiz. Plazmy **30**, 877 (2004) [Plasma Phys. Rep. **30**, 816 (2004)].
11. V. Schweigert and F. Peters, Phys. Rev. B **51**, 7700 (1995).
12. Sh. Amiranashvili, N. Gusein-zade, and A. Ignatov, Phys. Rev. A **59**, 3098 (1999); Sh. G. Amiranashvili, N. G. Gusein-zade, and V. N. Tsytovich, Phys. Rev. E **64**, 016407 (2001).
13. J. H. Chu and I. Lin, Phys. Rev. Lett. **72**, 4009 (1994).
14. H. Thomas, G. Morfill, and V. Demmel, Phys. Rev. Lett. **73**, 652 (1994).
15. V. E. Fortov, A. P. Nefedov, V. M. Torchinskiĭ, *et al.*, Pis'ma Zh. Éksp. Teor. Fiz. **64**, 86 (1996) [JETP Lett. **64**, 92 (1996)].
16. Ya. L. Al'pert, A. V. Gurevich, and L. P. Pitaevsky, *Space Physics with Artificial Sattelites* (Nauka, Moscow, 1964; Consultants Bureau, New York, 1965); J. Lafranbose and L. Parker, Phys. Fluids **16**, 629 (1973).
17. V. N. Tsytovitch, U. de Angelis, and R. Bingham, J. Plasma Phys. **42**, 429 (1989).
18. A. M. Ignatov, Comm. Plasma Phys. Controlled Fusion **17**, 249 (1996).
19. E. L. Pollock and J. P. Hansen, Phys. Rev. A **8**, 3110 (1973); W. L. Slattery, G. D. Dooley, and H. E. DeWitt, Phys. Rev. A **21**, 2087 (1980).
20. R. W. Hasse and J. P. Schiffer, Ann. Phys. (New York) **203**, 419 (1990).
21. N. G. Gusseĭn-zade and A. M. Ignatov, Kratk. Soobshch. Fiz., No. 11, 13 (2002); N. G. Gusseĭn-zade and A. M. Ignatov, Fiz. Plazmy **29**, 521 (2003) [Plasma Phys. Rep. **29**, 485 (2003)].
22. S. Nunomura, T. Misawa, N. Ohno, and S. Takamura, Phys. Rev. Lett. **83**, 1970 (1999).
23. S. V. Vladimirov, N. Kramer, and S. A. Maĭorov, Kratk. Soobshch. Fiz., No. 9, 33 (2002).

Translated by O.E. Khadin

Plasma Physics Reports, Vol. 31, No. 5, 2005, pp. 412–416. Translated from Fizika Plazmy, Vol. 31, No. 5, 2005, pp. 453–457.

BEAMS IN PLASMA

Geometry of a Cylindrical Ion Beam in a Radial Magnetic Field at a Low Hall Current

V. P. Shumilin

Lenin All-Russia Electrotechnical Institute, Krasnokazarmennaya ul. 12, Moscow, 111250 Russia

Received June 18, 2004

Abstract—The divergence of an ion beam in a cylindrical accelerator with a closed Hall current is considered under the assumption that the Hall current does not substantially change the external magnetic field. It is shown that the tangent of the angle of inclination of the ion trajectories to the cylinder axis is on the order of the ratio of the electron gyroradius in terms of the total energy of an electron to the characteristic radius of the acceleration channel. The beam divergence can be prevented by applying an external magnetic field in a direction parallel to the cylinder axis. *© 2005 Pleiades Publishing, Inc.*

1. The problem of the motion of a quasineutral plasma in an external magnetic field was considered in [1, 2] in relation to the theory of magnetic substorms. In this problem, the field of a magnetic dipole was modeled by an external magnetic field in cylindrical [1] or in planar [2] geometry. A similar problem about the structure of the boundary sheath between a cold quasineutral plasma flow and a uniform magnetic field was considered in [3].[1] It was found that, in a quasineutral boundary sheath, a fairly strong electric field can exist that is perpendicular to the magnetic field. Under certain conditions, this field can be used to accelerate the ions. This problem has substantially contributed to the development of plasma physics, in particular, to the theory of electrojet plasma engines with a closed Hall current [4–8]. In practice, however, Hall accelerators are always cylindrical in shape; in this case, the magnetic field is a radial one and the Hall current is an azimuthal current, so electrons move in circles whose radii are specified by the design of the device. This results in the onset of a radial electric field and, consequently, leads to the divergence of an ion beam. In the literature [4–8], there is no indication that this effect has been studied earlier.

[1] Formula (4.70) on page 123 of monograph [3] was misprinted. Its correct form is

$$f(v_{ye}) = \sqrt{2}\left(\sqrt{1+\sqrt{1-\frac{m_e}{m_i}\frac{v_{ye}^2}{v_0^2}}}-1\right) + \ln\frac{\sqrt{1-\sqrt{1-\frac{m_e}{m_i}\frac{v_{ye}^2}{v_0^2}}}}{(\sqrt{2}-1)\left(\sqrt{2}+\sqrt{1+\sqrt{1-\frac{m_e}{m_i}\frac{v_{ye}^2}{v_0^2}}}\right)}.$$

The expected divergence of an ion beam can be estimated in the following way: The radial electric field should act to balance the centrifugal force experienced by the moving electrons, $\bar{E}_r \sim m v_{\mathrm{dr}}^2/eR$, where $v_{\mathrm{dr}} \sim c\bar{E}_z/H_0 \sim (2e\varphi_0/m)^{1/2}$ is the electron drift velocity, H_0 is the characteristic strength of the radial magnetic field, $\bar{E}_z$ is the mean strength of the longitudinal electric field in the boundary sheath, R is the mean radius of the acceleration channel, φ_0 is the potential drop across the sheath, c is the speed of light, and m and e are the mass and charge of an electron. Consequently, we have $\bar{E}_r/\bar{E}_z \sim \rho_e(\varphi_0)/R$, where $\rho_e(\varphi_0)$ is the gyroradius of electrons with the energy $e\varphi_0$ or, in other words, the sheath thickness. For actual devices, this ratio can be as large as several tenths, so the radial electric field can give rise to a quite pronounced divergence of the ion beam. Such divergence can be prevented by applying a longitudinal magnetic field that satisfies the condition $\bar{E}_r \sim H_z v_{\mathrm{dr}}/c$, or $H_z/H_0 \sim \rho_e(\varphi_0)/R$; i.e., the longitudinal magnetic field required to keep an ion beam from diverging is much weaker than the radial magnetic field H_0.

2. In what follows, a problem similar to that considered by Chapman and Ferraro will be treated in cylindrical geometry. With the purpose of practical implementation, we assume that the ions are produced only at the surface where the longitudinal and radial velocities of a monoenergetic electron flow vanish (the electron cutoff surface). This is why, in order for the boundary sheath to be regarded as quasineutral (in accordance with [1–3]), we will treat the problem as if there were two identical ion beams.

In the planar model [3], the charged particles move in the same plane, so the quasineutrality condition for the sheath implies that the longitudinal (normal to the magnetic wall) velocities of the ions and electrons are

1063-780X/05/3105-0412$26.00 © 2005 Pleiades Publishing, Inc.

the same, provided that their fluxes are equal. Consequently, for the cutoff plane $z = 0$, we have

$$v_e(z) = \pm v_i(z),$$

where the minus sign corresponds to the incident electron flow and the plus sign corresponds to the reverse electron flow (from the cutoff plane to the cathode plasma). We assume that, in cylindrical geometry, the quasineutral boundary sheath forms in an analogous manner: the ions and electrons move in nested cylindrical surfaces of radii $r(z)$ (where r, ϕ, and z are cylindrical coordinates). In this case, the electrons return along the same surface back into the cathode plasma, provided that the following conditions are satisfied at the cutoff point ($r = r_0$, $z = z_0$):

$$\dot{r}(r_0, z_0) = 0; \quad \dot{z}(r_0, z_0) = 0, \tag{1}$$

where the superior dot denotes differentiation over time. By analogy with [1–3], we are interested here in a class of solutions such that, at each point of the sheath, the ions and electrons have equal longitudinal and equal radial velocities. In accordance with what was said above, the ion and electron motion will be described by assuming that $r_i(t) = r_e(t) \equiv r(t)$ and $z_i(t) = z_e(t) \equiv z(t)$.

Let us consider one of the nested surfaces. Let the coordinates $r = r_c$ and $z = z_c$ correspond to the cathode plasma boundary. To write the equations of motion for electrons and ions in cylindrical coordinates, we take into account the longitudinal and radial electric fields, E_z and E_r, the longitudinal magnetic field H_z = const, and the radial magnetic field

$$H_r = \frac{H_0 R_0}{r}, \tag{2}$$

Here, the amplitude $H_0 = H_r(R_0)$ is assumed to be constant, which indicates that we are considering the case where the Hall current does not affect the external magnetic field. The equations of electron motion can thus be written as

$$\ddot{r} - r\dot{\phi}^2 = -\frac{eE_r}{m} - \frac{e}{mc} r\dot{\phi} H_z, \tag{3a}$$

$$r\ddot{\phi} + 2\dot{r}\dot{\phi} = -\frac{e}{mc}\dot{z}H_r + \frac{e}{mc}\dot{r}H_z, \tag{3b}$$

$$\ddot{z} = -\frac{eE_z}{m} + \frac{e}{mc} r\dot{\phi} H_r. \tag{3c}$$

With allowance for the fact that the magnetic field has essentially no impact on the heavy ions, the equations of ion motion have the form

$$\ddot{r} = \frac{e}{M}E_r, \tag{4a}$$

$$\ddot{z} = \frac{e}{M}E_z, \tag{4b}$$

where M is the mass of an ion. By virtue of Eq. (4a), we can ignore the term $\ddot{r}$ in Eq. (3a), and Eq. (4b) enables us to ignore the term $\ddot{z}$ in Eq. (3c). From Eq. (3b) we readily obtain the equation

$$r^2\dot{\phi} + \frac{eH_0R_0}{mc}z - \frac{eH_z r^2}{2mc} = \text{const}.$$

Since we have $\dot{\phi} = 0$ at the cathode plasma boundary $z = z_c$, we can reduce this equation to

$$\dot{\phi} = \frac{eH_0R_0}{mc}\frac{(z_c - z)}{r^2} - \frac{eH_z}{2mc}\frac{(r_c^2 - r^2)}{r^2}.$$

The electric field components then become

$$E_r = \frac{m}{e}\left(\frac{eH_0R_0}{mc}\right)^2 \times \left(\frac{(z_c - z)^2}{r^3} - \frac{H_z}{H_0}\frac{r_c^2(z_c - z)}{r^3} + \frac{H_z^2}{H_0^2}\frac{(r_c^4 - r^4)}{4r^3}\right),$$

$$E_z = \frac{m}{e}\left(\frac{eH_0R_0}{mc}\right)^2\left(\frac{(z_c - z)}{r^2} - \frac{H_z}{H_0}\frac{(r_c^2 - r^2)}{2r^2}\right).$$

Hence, the sought surface $r(z)$ is described parametrically by the set of Eqs. (4) in the following form:

$$\frac{d^2\rho}{d\tau^2} = \frac{(\zeta_c - \zeta)^2}{\rho^3} - \frac{h\rho_c^2(\zeta_c - \zeta)}{\rho^3} + \frac{h^2(\rho_c^4 - \rho^4)}{4\rho^3}, \tag{5a}$$

$$\frac{d^2\zeta}{d\tau^2} = \frac{(\zeta_c - \zeta)}{\rho^2} - \frac{h(\rho_c^2 - \rho^2)}{2\rho^2}, \tag{5b}$$

where we have introduced the dimensionless variables

$$\rho = \frac{r}{R_0}, \quad \zeta = \frac{z}{R_0}, \quad \tau = \frac{t}{T}, \quad T = \sqrt{\frac{M}{m}}\frac{mc}{eH_0},$$

$$h = \frac{H_z}{H_0}.$$

In accordance with relationships (1), Eqs. (5) should be supplemented with the boundary conditions

$$\rho(0) = \rho_0, \quad \zeta(0) = \zeta_0, \quad \left.\frac{d\rho}{d\tau}\right|_{\tau = 0} = 0, \quad \left.\frac{d\zeta}{d\tau}\right|_{\tau = 0} = 0. \tag{6}$$

The set of equations (5) has the first integral

$$\left(\frac{d\rho}{d\tau}\right)^2 + \left(\frac{d\zeta}{d\tau}\right)^2 + 2\psi(\rho, \zeta) = 2\psi(\rho_0, \zeta_0),$$

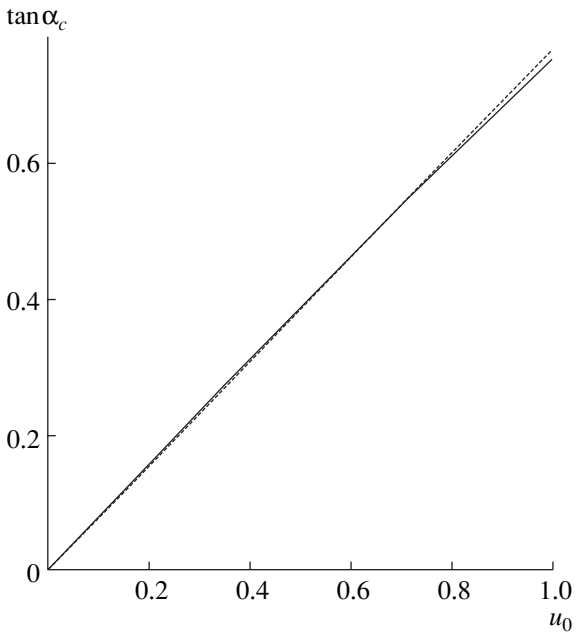

Fig. 1. Dependence of the tangent of the angle of inclination of the ion trajectories at the plasma boundary on the parameter u_0 for $h = 0$ (solid curve) and a linear approximation for this dependence (dashed line).

where

$$\psi(\rho, \zeta) = \frac{1}{2\rho^2}\left[(\zeta_c - \zeta) - \frac{h(\rho_c^2 - \rho^2)}{2}\right]^2 \quad (7)$$

is the dimensionless electric field potential.

We now find the equation for the cutoff surface $\rho_0(\zeta_0)$. Since the potential at this surface has the form

$$\psi(\zeta_0) = \psi[\rho_0(\zeta_0), \zeta_0],$$

we obtain

$$\frac{d\psi}{d\zeta_0} = \frac{\partial\psi}{\partial\rho}\bigg|_{\rho_0, \zeta_0}\frac{d\rho_0}{\partial\zeta_0} + \frac{\partial\psi}{\partial\zeta}\bigg|_{\rho_0, \zeta_0}.$$

On the other hand, expression (7) gives

$$\frac{\partial\psi}{\partial\rho} = -\frac{2\psi(\rho, \zeta)}{\rho} + h\sqrt{2\psi(\rho, \zeta)},$$

$$\frac{d\psi}{\partial\zeta} = -\frac{\sqrt{2\psi(\rho, \zeta)}}{\rho}.$$

Therefore, if the potential distribution over the cutoff surface, $\psi(\zeta_0)$, is prescribed, this surface should satisfy the equation

$$\rho_0(\zeta_0)u_c(\zeta_0) + \zeta_0 - \frac{h}{2}\rho_0^2(\zeta_0) = \text{const},$$

where

$$u_c(\zeta_0) = \sqrt{2\psi(\zeta_0)}$$

is the dimensionless ion velocity at the cathode boundary of the sheath. For definiteness, we set

$$\rho_0(0) = 1, \quad u_c(0) = u_0.$$

As a result, we obtain

$$\zeta_0 = u_0 - \rho_0 u_c(\zeta_0) - \frac{h}{2}(1 - \rho_0^2). \quad (8)$$

The equation for the equipotential cutoff surface, $u_c(\zeta_0) = u_0$, has the form

$$\zeta_0 = u_0(1 - \rho_0) - \frac{h}{2}(1 - \rho_0^2). \quad (9)$$

Using this equation and also relationship (7), which, for the equipotential cutoff surface, has the form

$$u_0 = \frac{\zeta_c - \zeta_0}{\rho_0} - \frac{h}{2}\frac{\rho_c^2 - \rho_0^2}{\rho_0},$$

we easily arrive at the equation for the plasma boundary:

$$\zeta_c = u_0 - \frac{h}{2}(1 - \rho_c^2). \quad (10)$$

3. Let us consider the case $h = 0$, i.e., the divergence of an ion beam in the absence of a longitudinal magnetic field. Taking into account Eq. (9) for the cutoff surface and Eq. (10) for the plasma boundary, we see that the set of equations (5) and (6) exhibits the following obvious symmetry property: if, for one trajectory (e.g., for $\rho_1(\tau)$ and $\zeta_1(\tau)$), a solution such that $\rho_1(0) = 1$ and $\zeta_1(0) = 0$ is known, then, for $\rho_0 \neq 1$, the functions

$$\rho(\tau) = \rho_0\rho_1(\tau/\rho_0),$$

$$\zeta(\tau) = u_0 - \rho_0(u_0 - \zeta_1(\tau/\rho_0))$$

are also solutions to the equations; moreover, the point $(\rho_0, \zeta(0))$ lies in cutoff surface (9). Hence, the trajectories are similar. The tangent of the angle of inclination of the ion trajectories at the cutoff surface is equal to

$$\tan(\alpha_0) = \frac{\ddot{\rho}(0)}{\ddot{\zeta}(0)} = u_0.$$

By virtue of the similarity of the trajectories, the angle of their inclination at the plasma boundary, α_c, is independent of ρ_0 and is a function of u_0 alone:

$$\tan(\alpha_c) = \frac{\dot{\rho}(\tau_c\rho_0)}{\dot{\zeta}(\tau_c\rho_0)} = f(u_0),$$

where the time τ_c is determined from the relationship $\zeta_1(\tau_c) = u_0$. In Fig. 1, the solid curve shows the dependence of the tangent of the angle of inclination of the ion trajectories at the plasma boundary on the parameter u_0, calculated by numerically solving Eqs. (5) and (6) for $h = 0$. The dashes represent the line

$$\tan(\alpha_c) = 0.77u_0,$$

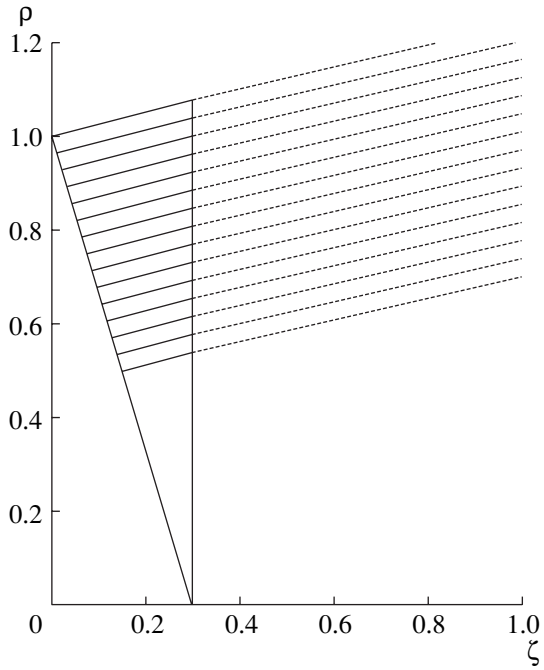

Fig. 2. Ion trajectories for $u_0 = 0.3$ and $h = 0$.

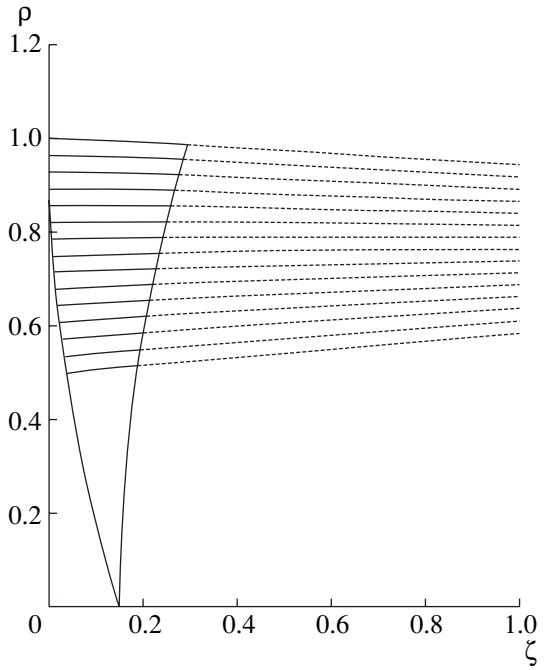

Fig. 3. Ion trajectories for $u_0 = 0.3$ and $h = u_0$.

which is a good approximation for the numerically calculated dependence in the range $u_0 \le 1$.

Figure 2 displays the ion trajectories calculated in dimensionless coordinates by numerically solving Eqs. (5) with boundary conditions (6) for $u_0 = 0.3$ and $h = 0$.

By applying a longitudinal magnetic field in a direction parallel to the longitudinal ion velocity, it is possible to prevent the beam divergence. It is sufficient for this to satisfy the condition $h \approx u_0$. This is illustrated by Fig. 3, which presents the ion trajectories calculated in dimensionless coordinates by numerically solving Eqs. (5) with boundary conditions (6) for $u_0 = 0.3$ and $h = u_0$. When the longitudinal magnetic field is applied in the opposite direction, it leads to additional divergence of the ion beam (Fig. 4).

The main parameter of the problem, u_0, determines the maximum dimensionless ion velocity: it is equal to the ratio of the gyroradius of electrons with the energy $e\varphi_0$ in a constant magnetic field H_0 to the radius R_0:

$$u_0 = \frac{\rho_e(\varphi_0)}{R_0},$$

where

$$\rho_e(\varphi_0) = \sqrt{\frac{2e\varphi_0}{m}}\frac{mc}{eH_0}.$$

In the units in which the potential difference is expressed in volts, the magnetic field strength is given in gausses, and the radius is in centimeters, this parameter is

$$u_0 \approx 3.37\frac{\sqrt{\varphi_0}}{H_0 R_0}.$$

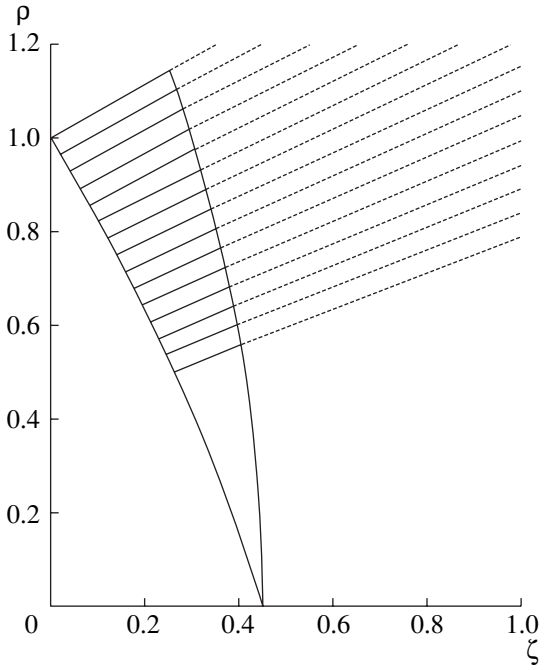

Fig. 4. Ion trajectories for $u_0 = 0.3$ and $h = -u_0$.

Thus, for $R_0 = 2.6$ cm and $H_0 = 100$ G, we have $u_0 \approx 0.290$ for $\varphi_0 = 500$ V and $u_0 \approx 0.205$ for $\varphi_0 = 250$ V.

4. In this paper, we have shown that, due to the neutralization of the centrifugal force, which causes a cloud of Hall electrons in a cylindrical accelerator to expand, a radial electric field arises, which leads to a substantial (10°–20°) divergence of an ion beam. This divergence can be prevented by a longitudinal magnetic field that is applied in a direction parallel to the longitudinal ion velocity and whose strength is 10–30% of that of the radial magnetic field.

It has been found that the equipotential cutoff surface is not perpendicular to the accelerator axis and that, in the presence of an external longitudinal magnetic field, it has a fairly complicated shape. In practice, the anodes most often used are those with a planar surface perpendicular to the system axis [4–6]. Such anodes introduce additional difficulties in exciting discharges of the desired shape in the acceleration channel. It therefore seems expedient to use inclined anodes.

ACKNOWLEDGMENTS

I am grateful to A.V. Zharinov for fruitful discussions and to A.S. Chikhachev and A.N. Ermilov for their sympathetic attitude and encouragement of this study. The work was supported in part by the Russian Foundation for Basic Research, project no 01-02-16014.

REFERENCES

1. S. Chapman and V. C. A. Ferraro, Terr. Magn. Atmos. Electr. **45** (3), 245 (1940).
2. V. C. A. Ferraro, J. Geophys. Res. **57**, 15 (1952).
3. L. A. Artsimovich, *Controlled Thermonuclear Reactions*, Ed. by A. Kolb and R. S. Pease (Fizmatgiz, Moscow, 1961; Gordon & Breach, New York, 1964).
4. A. I. Morozov, in *Encyclopedia of Low-Temperature Plasma*, Ed. by V. E. Fortov (Nauka, Moscow, 2000), Vol. 3, p. 383.
5. S. D. Grishin, in *Encyclopedia of Low-Temperature Plasma*, Ed. by V. E. Fortov (Nauka, Moscow, 2000), Vol. 4, p. 291.
6. A. I. Morozov, Fiz. Plazmy **29**, 261 (2003) [Plasma Phys. Rep. **29**, 235 (2003)].
7. A. V. Zharinov and Yu. S. Popov, Zh. Tekh. Fiz. **37**, 294 (1967) [Sov. Phys. Tech. Phys. **12**, 208 (1967)].
8. M. A. Vlasov, A. V. Zharinov, and Yu. A. Kovalenko, Zh. Tekh. Fiz. **71** (12), 34 (2001) [Tech. Phys. **46**, 1522 (2001)].

Translated by O.E. Khadin

Plasma Physics Reports, Vol. 31, No. 5, 2005, pp. 417–424. Translated from Fizika Plazmy, Vol. 31, No. 5, 2005, pp. 458–465.

ISOTOPE SEPARATION

Axisymmetric Plasma-Optic Mass Separators

A. I. Morozov[1] and V. V. Savel'ev[2]

[1] *Nuclear Fusion Institute, Russian Research Centre Kurchatov Institute, pl. Kurchatova 1, Moscow, 123182 Russia*
[2] *Keldysh Institute of Applied Mathematics, Russian Academy of Sciences, Miusskaya pl. 4, Moscow, 125047 Russia*

Received July 29, 2004; in final form, October 27, 2004

Abstract—A systematic description is given of the principles of operation of axisymmetric plasma-optic mass separators with azimuthators that are compatible with stationary plasma thrusters with closed electron drift. Two schemes of plasma-optic separators (with electrostatic and with magnetic ion focusing) are considered. Results are presented from calculations of the parameters of model devices for separating ions whose masses are on the order of those of xenon ions. © *2005 Pleiades Publishing, Inc.*

1. INTRODUCTION

Industrial-scale mass separators are now used for different purposes, e.g., for obtaining superpure materials for medicine and scientific investigations, for creating isotopically pure engineering materials for atomic industry, for processing nuclear wastes, and so on. There are many mass separation schemes: centrifugal, diffusive, laser-based, ion resonant, etc. Among these schemes, the electromagnetic isotope separation method [1] is notable for its conceptual simplicity, its single-stage design, and its "panoramic" mode of operation—the ability to simultaneously separate many isotopes with different masses. This method is illustrated graphically in Fig. 1. The mass separator system consists of three blocks. The natural substance (an isotopic mixture) is fed into an ion source, where it is ionized to produce ions and electrons, which are accelerated and formed into a high-quality quasineutral electron–ion beam. This beam moves into a separator, where it becomes subject to a uniform magnetic field oriented perpendicular to its path. In the strong magnetic field of the separator, the beam ions revolve along their Larmor semicircles, while the beam electrons, which neutralize the ion space charge, are essentially immobile. The gyroradius of a singly charged ion depends on its mass,

$$\rho_i = \frac{V_i}{\omega_{Hi}} = \frac{Mc}{eH_0}\sqrt{\frac{2eU_a}{M}} \propto \sqrt{\frac{M}{e}}, \qquad (1)$$

where U_a is the accelerating voltage, H_0 is the magnetic field in the separator, and M and e are the mass and charge of an ion. Finally, the ions are deposited on collectors.

Figure 1 and formula (1) demonstrate that it is, in principle, possible to create a single-stage separator capable of operating in a "panoramic" mode (i.e., over a broad range of ion masses). However, the electromagnetic separator fabricated in the 1940s has a fundamental drawback: a very low productivity. The characteristic ion currents are $J_i \le 0.01$–0.1 A. The charge per gram atom is equal to 10^5 C; consequently, even with a current of $J_i \approx 0.1$ A, the processing of this amount of matter will require about 15 days. It is clear that the productivity should be increased by at least three to four orders of magnitude.

The low productivity of the classical electromagnetic separators stems from the fact that there are only ions in the acceleration gap of the ion source. The electric field of these ions restricts the current density by the so-called 3/2 law:

$$j = \frac{g}{9\pi}\sqrt{\frac{2e}{M}}\frac{U_a^{3/2}}{d^2}, \qquad (2)$$

where d is the distance between the electrodes and $g \approx 1$ is a geometrical factor. Attempts to increase the current density in such sources led to an increase in the accelerating voltage and, consequently, in the energy expenditure; in this way, however, it is unrealistic to expect

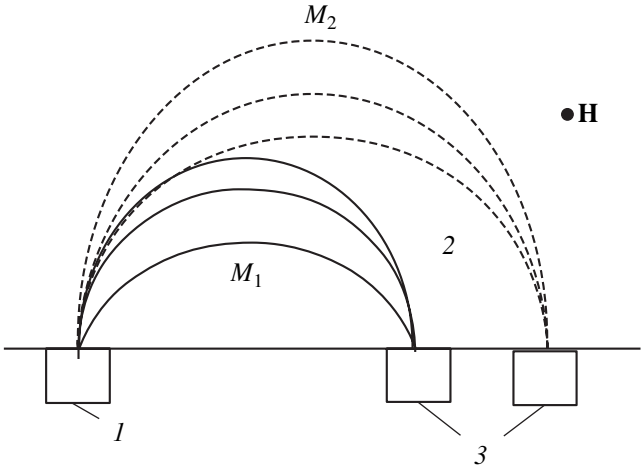

Fig. 1. Artsimovich's electromagnetic separator: (*1*) ion source, (*2*) separating region, and (*3*) ion collectors.

1063-780X/05/3105-0417$26.00 © 2005 Pleiades Publishing, Inc.

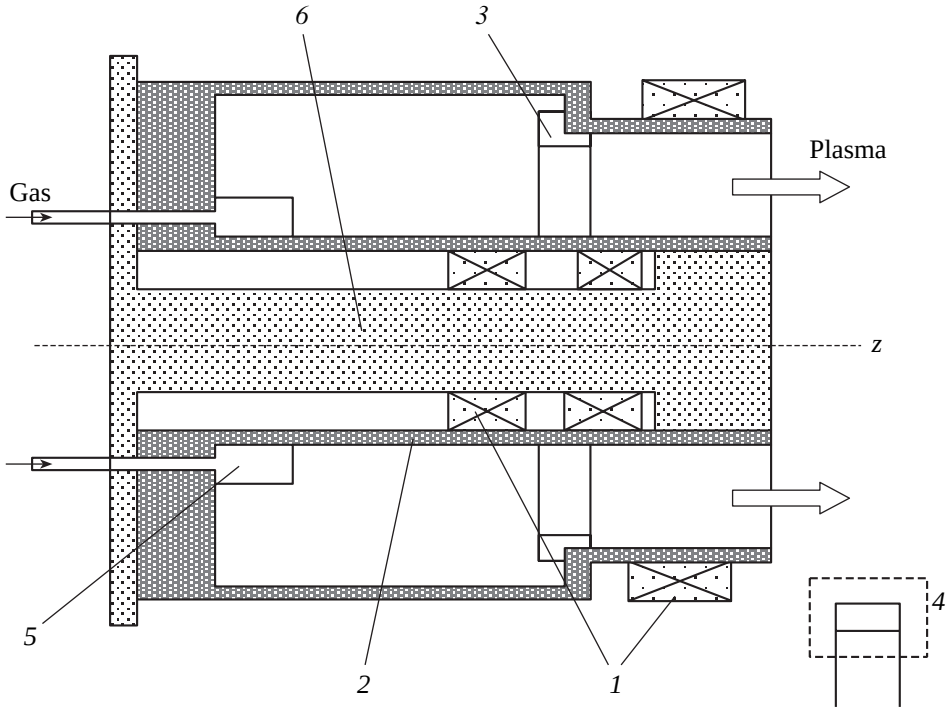

Fig. 2. Schematic of an SPT: (*1*) magnetic poles, (*2*) dielectric channel, (*3*) anode, (*4*) cathode, (*5*) gas distributor, and (*6*) magnetic conductor.

that the current could be increased by several orders of magnitude.

Classical electromagnetic separators began to be built in the mid-1940s; 20 years later (in the 1960s), plasma accelerators were developed in which the acceleration region contained a quasineutral plasma. These developments were stimulated by the need for space electrojet engines. The devices most suitable for solving the separation problem in question are stationary plasma thrusters (SPTs) [2] and anode-sheath thrusters (ASTs) [3]. These are axisymmetric systems with ring-shaped acceleration channels with a quasi-radial magnetic field (Fig. 2). Deep in the acceleration channel, there is an anode in the vicinity of which the working gas is fed into the channel. A hollow cathode is positioned outside the channel near its exit end. The potential difference applied between the anode and the cathode creates an electric field in the channel. When the E and H fields are switched on and the working gas is injected, the electrons emitted from the heated cathode enter the channel and ionize the gas particles. At the same time, they begin to drift in the azimuthal direction in the crossed E and H fields and to diffuse slowly toward the anode. The ionization-produced ions are accelerated in the E field. By the time they arrive at the exit end of the channel, they acquire an energy of

$$\varepsilon \approx e\phi, \tag{3}$$

where ϕ_* is the potential at the point at which the gas particle was ionized. The cathode potential is assumed to be zero. The magnetic field strength in the channel is chosen so as to magnetize the electrons and not to magnetize the ions to any significant extent, the corresponding condition being

$$\rho_e \ll L \ll \rho_i, \tag{4}$$

where L is the channel length and $\rho_{e,i}$ are the electron and ion gyroradii.

The magnitude of the ion current at the exit from the channel is determined primarily by the flow rate of the working gas injected into the channel. In a well-optimized model channel, the degree of gas ionization is close to 95%. Consequently, for singly charged ions, we have

$$J_i \approx \dot{m}\frac{e}{M}. \tag{5}$$

Hence, there is no restriction on the magnitude of the ion current density because the plasma in the channel is quasineutral. In stationary thrusters, the factor that restricts the current density is simply the heating of the channel. The typical current density values are about 0.1–0.2 A/cm^2. For a channel with a cross-sectional area of ~20 cm^2, the total ion current is about 3–4 A.

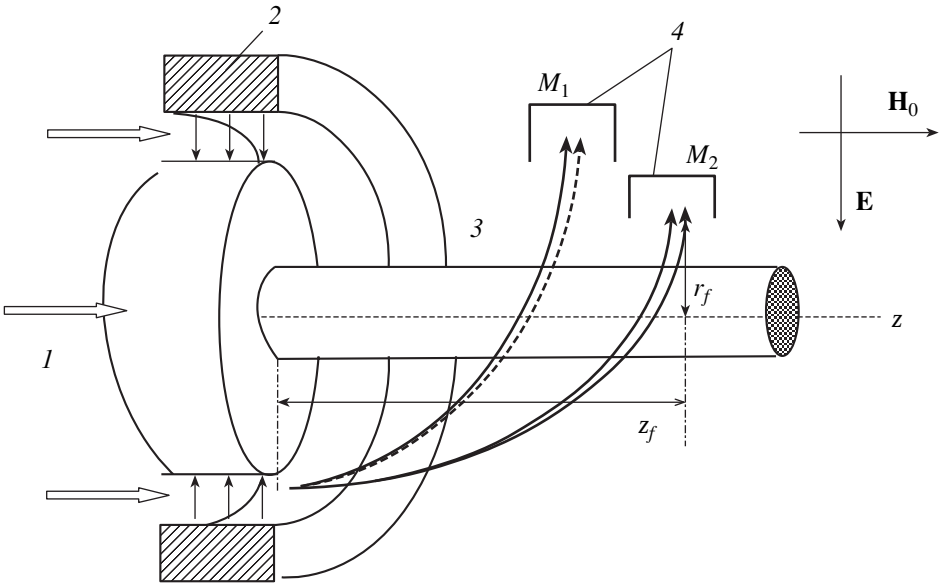

Fig. 3. Schematic of an A-system (POMS): (*1*) ion source, (*2*) azimuthator, (*3*) separating region, and (*4*) ion collectors.

At ion energies of ~300–400 eV, such parameters are achievable in a standard M-70 SPT, in which the diameter of the outer wall of the channel is 70 mm. Model SPTs have already been created in which this diameter is 300 mm and which are capable of producing ion currents of about 30 A. At present, SPTs and ASTs are being optimized in two main parameters: the efficiency and the operation time. In this way, efficiencies of about 70% and continuous operation times of more than 10000 hours have been achieved in laboratory experiments. As for space exploration, from 1971 to the present day, about 200 thrusters have operated or continue to operate onboard more than 30 satellites.

Plasma accelerators for separators must be optimized mainly with respect to other parameters. Specifically, it is necessary to reduce the noise level and to minimize the beam divergence and the spread in the particle energy. There is no doubt that, by using SPTs and ASTs, it will be possible to produce beams with the desired parameters in the future. Beam divergence angles of $\alpha \sim \pm 7°$ have already been achieved, which are close to those ($\alpha \sim \pm 3°$) required for a number of plasma-optics mass separator (POMS) schemes.

In addition to optimizing a plasma accelerator (PA), it is necessary to choose a separator scheme in such a way that the separator would be compatible with the accelerator; would improve the shortcomings of the accelerator; and, at the same time, would allow further modifications to an ultimate physical limit (without changing the basic principles), i.e., to a panoramic mode of operation with $\Delta M = 1$. In other words, the separator scheme should be, on the one hand, analogous to the electromagnetic mass separator proposed by Artsimovich and his collaborators and, on the other hand, it should have high separating productivity. It is these properties that should be possessed by the POMSs described below.

2. PRINCIPLES OF A-SYSTEMS (PROTOTYPES OF PLASMA-OPTICS MASS SEPARATORS)

The POMS developed here is supposed to be based on the A-system scheme proposed in [4].[1] This system, which is illustrated graphically in Fig. 3, is axisymmetric and is intended to operate in the quasineutral mode with electric (*E*) and magnetic (*H*) fields. The axisymmetric geometry of the system makes it possible to close the electron drift orbits and is consistent with the annular geometry of the ion beams produced by a PA with closed electron drift. In the A-system, the ions in the beam are separated according to mass in a simple field configuration: a superposition of a uniform longitudinal magnetic field *H* and a radial electric field *E*:

$$H = H_0, \quad \phi = E_0 R \ln\left(\frac{r}{R}\right), \tag{6}$$

where ϕ is the electrostatic potential. This field configuration possesses an important property: it remains the same in vacuum operating modes and in operating modes with a quasineutral plasma (see [3] for details).

Along with the conductors producing the field configuration, the A-system involves a special block that was called an azimuthator: a coaxial dipole magnet placed at the entrance to the separating section. In the region between the poles of the azimuthator, a transverse (radial) magnetic field is created. In crossing this

[1] For the most recent results on the subject, see [5, 6].

field, the ions acquire an azimuthal velocity determined by the angular momentum conservation law:

$$MrV_\theta + \frac{e}{c}\psi = MRV_{\theta 0} + \frac{e}{c}\psi_0 \equiv D = \text{const}, \quad (7)$$

where $\psi = rA_\theta$ is the magnetic flux function, R is the radius of the particle trajectory in the gap of the azimuthator, and $V_{\theta 0}$ is the initial azimuthal ion velocity at the entrance to the azimuthator. If the gap is sufficiently narrow, then the radius R, as well as the flux function ψ_0, can be assumed to be approximately the same for all ions. Using relationship (7) and assuming that the azimuthal ion velocity component is small, we find the azimuthal velocity of the ions that have passed through the azimuthator:

$$V_{\theta 1} = \frac{e\psi_A}{cMR}, \quad (8)$$

where ψ_A is the magnetic flux in the azimuthator. Hence, the projection of the azimuthal ion velocity onto the (r, θ) plane is independent of the energy spread ε_0 of the ions at the exit from the source and depends on their masses. Since the E and H fields in the focusing section are independent of z, the longitudinal velocity V_z of the ions is conserved as they move in the z direction. We can thus restrict ourselves to considering the ion focusing only in the (r, θ) plane.

Moreover, by virtue of the azimuthal symmetry, it is sufficient to consider the ion motion only in the radial direction (along the radius r) because the motion along the θ coordinate is in fact described by relationship (7). The equation for $r(t)$ has the form

$$M\ddot{r} = -\frac{\partial}{\partial r}(U + e\phi), \quad (9)$$

where $U = \frac{1}{2Mr^2}\left(D - \frac{e}{c}\psi\right)^2$. We choose an ion with a mass M_0 as a reference ion and assume that its trajectory lies at a reference cylindrical surface of radius $r = R$. In this case, the following condition should be satisfied:

$$\left.\frac{\partial(U + e\phi)}{\partial r}\right|_{r = R} = 0, \quad (10)$$

and the motion of an ion near the reference surface is described by the equation

$$M\ddot{\rho} = -\rho\frac{\partial^2}{\partial r^2}(U + e\phi), \quad \rho = r - R. \quad (11)$$

We assume that the angular spread of the ions around the reference ion in the (r, z) plane is small.

Taking into account the expression for the electrostatic potential (the second of expressions (6)) and the relationship $\psi = \frac{H_0}{2}(r^2 - R^2)$,[2] we can readily verify that the equilibrium condition has the form

$$\frac{D^2}{MR^3} + \frac{eDH_0}{McR} = eE_0, \quad (12)$$

and that the equation for ρ can be written as

$$\ddot{\rho} + \Omega^2\rho = 0. \quad (13)$$

Here,

$$\Omega^2 = \omega_H^2 - s\chi^2, \quad (14)$$

where $\omega_H = \frac{eH_0}{Mc}$ is the gyrofrequency, $s = \operatorname{sgn} E$ and $\chi^2 = \frac{e|E|}{MR}$. Equation (13) has an obvious solution,

$$\rho = A\sin\Omega t, \quad (15)$$

and the position of the ion focus is determined from the condition

$$\Omega t_f = \pi. \quad (16)$$

Setting $t_f = \theta_f/\dot{\theta}_0$, we obtain the azimuthal position of the ion focus:

$$\theta_f = \frac{\pi}{\Omega}\dot{\theta}_0, \quad (17)$$

where $\dot{\theta}_0$ is the angular velocity of an ion that moves along the reference trajectory determined by Eq. (12).

We restrict ourselves to considering two limiting cases: purely magnetic focusing ($E = 0$) and purely electric focusing (when the magnetic field H_0 is negligibly weak and serves merely to magnetize the electrons). In these cases, the separators will be referred to as POMS-H and POMS-E systems, respectively.

3. POMS-H SYSTEM

The POMS-H system is analogous to Artsimovich's separator in all respects, including the passive motion in the z direction. From expression (14) we have $\Omega = \omega_H$, and equilibrium equation (12) obviously yields the relationship $V_\theta = R\omega_H$. On the other hand, expression (8) gives $V_\theta = e\psi_A/(cMR)$, so we have

$$R^2 = \frac{\psi_A}{H_0}. \quad (18)$$

[2] This choice of expression for ψ corresponds to the pattern of the closed magnetic fluxes in Fig. 5 and is valid for the vacuum region around a surface of radius $r = R$.

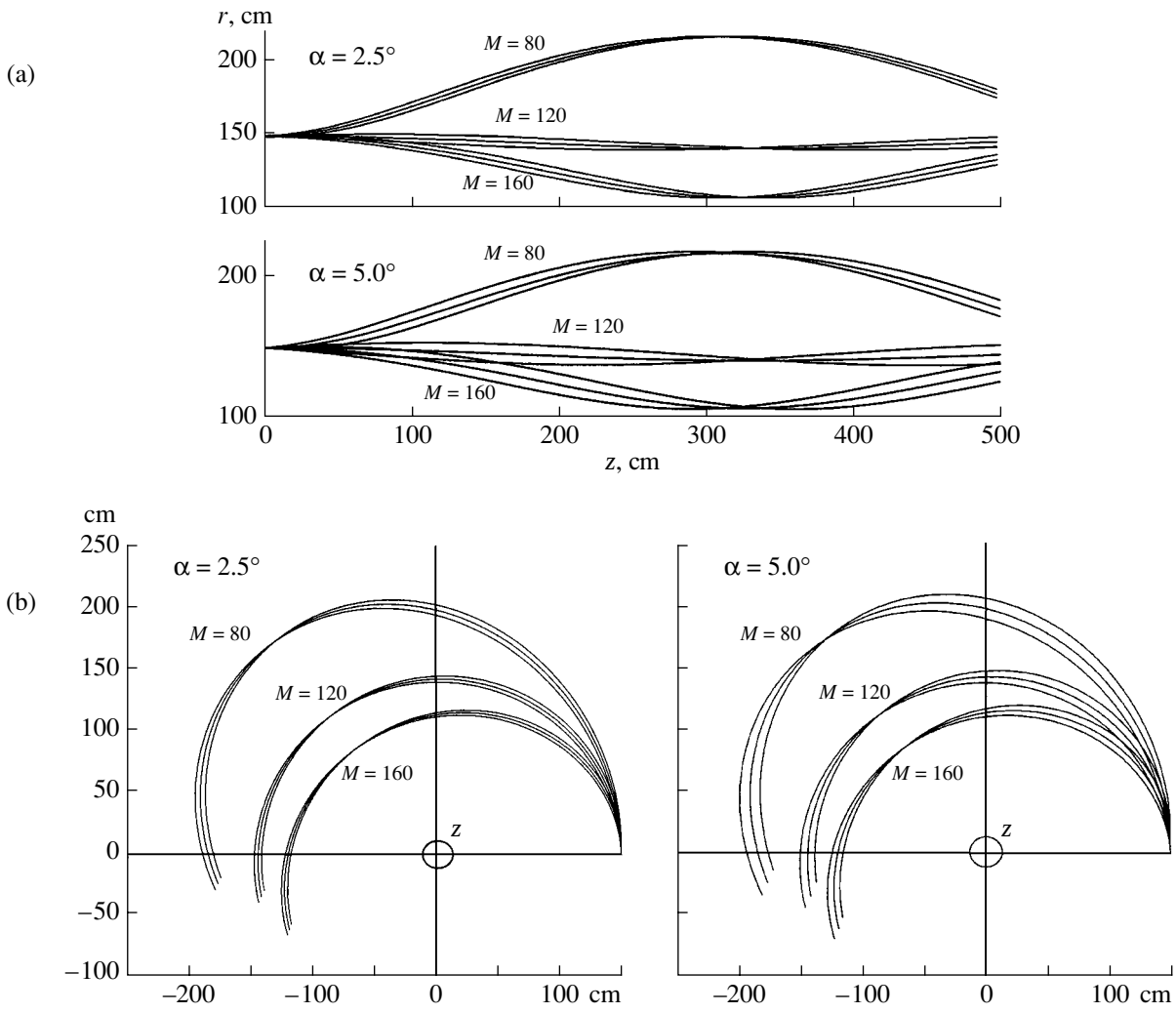

Fig. 4. Ion focusing in a POMS-E for different divergence angles of a beam escaping from the azimuthator ($\alpha = \pm 2.5°, \pm 5°$) and for $M_0 = 113$, $\varepsilon_0 = 400$ eV, and $R = 150$ cm: (a) projections of ion trajectories onto the (r, z) plane, (b) projections of ion trajectories onto the (r, θ) plane, and (c) magnified fragment of the focusing region in the (r, z) plane for $\alpha = \pm 2.5°$.

Hence, all of the ions are focused at the reference cylindrical surface. However, the position of the circles at which the ions are focused, z_f, depend on M:

$$z_f(M) = V_{z0}\frac{\pi}{\omega_H} = \frac{\pi}{\omega_H}\sqrt{\frac{2}{M}\left(\varepsilon_0 - \frac{MV_{\theta 1}^2}{2}\right)}. \qquad (19)$$

We assume that all the ions in the source acquire the same energy ε_0, regardless of their masses. Taking into account expression (8), we can write

$$z_f = \frac{\pi c}{eH_0}\sqrt{2\left(\varepsilon_0 M - \frac{e^2\psi_A^2}{2c^2R^2}\right)}. \qquad (20)$$

Accordingly, variations in the mass and energy of an ion lead to variations in the position of the focal point:

$$\frac{\delta z_f}{z_f} = \left(\frac{\delta M}{M} + \frac{\delta\varepsilon_0}{\varepsilon_0}\right)\frac{M\varepsilon_0}{2\left(M\varepsilon_0 - \dfrac{e^2\psi_A^2}{2c^2R^2}\right)}. \qquad (21)$$

Hence, in order to separate two ions with masses M and $M + \delta M$, it is necessary to satisfy the inequality

$$\frac{\delta\varepsilon_0}{\varepsilon_0} < \frac{\delta M}{M}. \qquad (22)$$

4. POMS-E SYSTEM

In this system, the ion behavior in the (r, θ) plane is similar to that in the Hughes–Rozhansky energy ana-

(c)

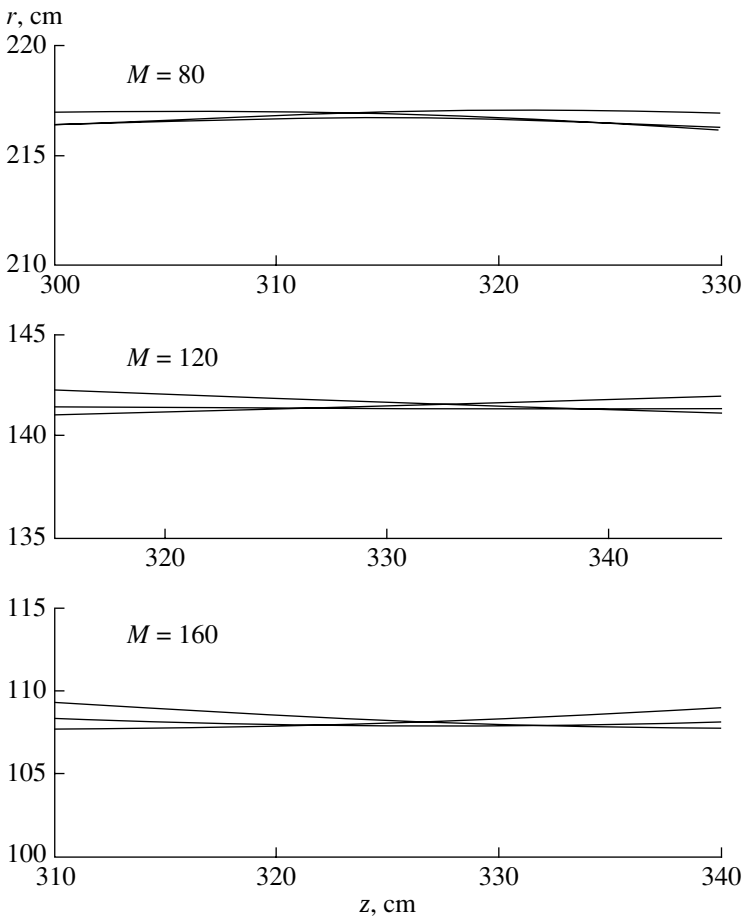

Fig. 4. (Contd.)

lyzer. We can easily see from Eq. (12) and expression (14) that the ions are focused when they move around the $\theta_f = \pi/\sqrt{2}$ azimuth, regardless of their masses. The radial positions at which the ions of different masses are focused differ by the amount

$$\delta R = \frac{\delta M}{M} R. \quad (23)$$

This formula was obtained by taking into account the fact that the ions whose mass $M_0 + \delta M$ differs from the mass M_0 of the reference ion have an angular momentum D differing from that of the reference ion:

$$D = D_0 + \delta D. \quad (24)$$

The ions of different masses are focused at different positions along the z axis:

$$z_f = \frac{\pi V_{z0}}{\sqrt{2}\dot{\theta}} = \frac{\pi}{\sqrt{2}} \frac{\sqrt{\frac{2}{M}\left(\varepsilon_0 - \frac{e^2\psi_A^2}{2c^2MR^2}\right)}R^2M}{\frac{e}{c}\psi_A}. \quad (25)$$

The above formulas for z_f were derived under the assumption that the difference between the mass M and the reference mass is sufficiently small. In order to understand how important is the above assumption that the ion trajectories only slightly differ from the reference trajectory, we have numerically calculated the trajectories of three ions having unequal masses but the same energy (ε_0 = 400 eV). The ions were modeled to escape from an azimuthator, starting from the radial position $r_A = R$ = 150 cm, the divergence angles in the (r, z) plane being $\alpha = \pm 2.5°$ and $\pm 5°$. The reference mass was accepted to be M_0 = 113. The magnetic flux ψ_A was chosen such that, in passing through the azimuthator, a reference ion acquires an azimuthal energy equal to one-half the total energy. The calculated results are illustrated in Figs. 4a–4c, which show the projections of the ion trajectories onto the (r, z) and (r, θ) planes and a magnified fragment of the pattern of ion trajectories in the focal region in the (r, z) plane.

The above analytical and numerical results point to the following three important properties of the focusing in a POMS-E:

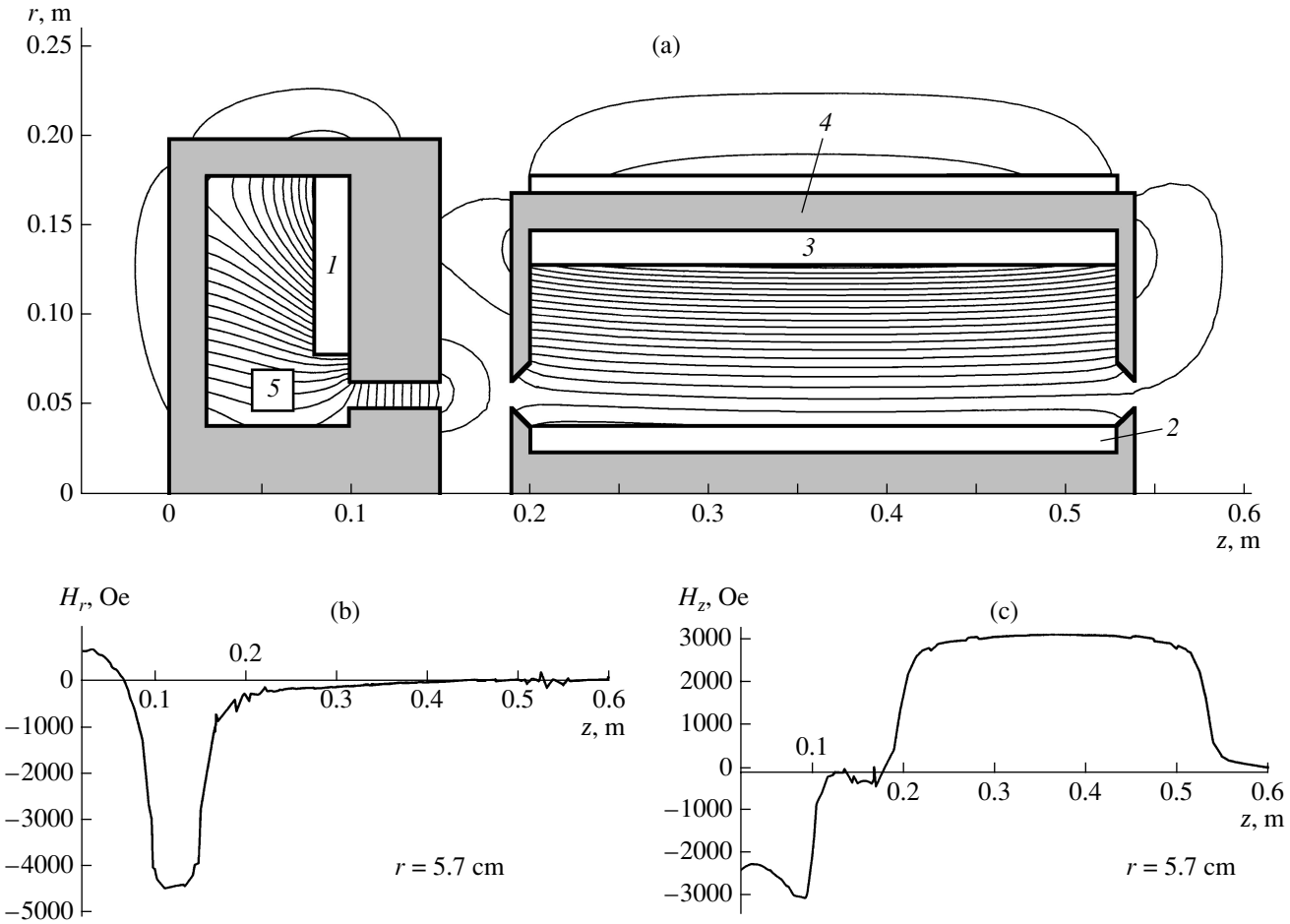

Fig. 5. Design of a POMS-H experimental magnetic system: (a) system geometry and magnetic field lines ((*1–3*) magnetic coils, (*4*) magnetic core, and (*5*) annular plasma source) and (b) radial and (c) longitudinal components of the magnetic field as functions of z at $r = 5.7$ cm. The current densities in the coils are $j_1 = -13$ MA/m^2, $j_2 = -18$ MA/m^2, $j_3 = 14$ MA/m^2, and $j_4 = -3$ MA/m^2.

(i) Over a wide parameter range, ions of different masses are focused approximately in the plane $z_f \approx$ const.

(ii) The angle by which the particles are displaced in the azimuthal direction in moving from the exit from the azimuthator up to the point at which they are focused is essentially independent of M,

$$\theta_f \approx \frac{\pi}{\sqrt{2}}. \quad (26)$$

(iii) Simulations show that it is in principle possible to separate isotopes in a panoramic mode of operation such that $\Delta M \sim 1$; this concerns the elements in the middle of Mendeleyev's periodic table ($M \sim 80$–160). In our study, however, we will neither consider the question about the smearing of the ion focus in the presence of plasma nor even perform a systematic analysis of aberrations in the single-particle approximation. Note only that, since ions of different masses are focused almost in the same cross section, $z \approx$ const, the smearing of the ion focus due to the spread in the longitudinal ion energies in a POMS-E should be less than that in a POMS-H.

5. CALCULATION OF THE EXPERIMENTAL MODELS OF POMS-H AND POMS-E

In order to give a more realistic insight into the above fundamental separator schemes, we designed a model version of a POMS-H and carried out a detailed calculation of its magnetic system. We also estimated the parameters of the magnetic system of a POMS-E. The reference mass was chosen to be $M = 113$.

5.1. POMS-H

The POMS-H magnetic system consists of two blocks: an azimuthator and a separator. The geometry of the blocks and the magnetic field lines in them are shown in Fig. 5. This separator is aimed at experimental investigations of the beams of ions having a mass on the

order of 100, with currents in the ampere range. For simulations, the magnetic field in the azimuthator was set equal to $H_A \approx 5 \times 10^3$ Oe, and the field in the working section of the separator was chosen to be $H_0 \approx$ 3400 Oe. The radius of the azimuthator gap was 5.7 cm, the gap width being 1.5 cm. The distance from the azimuthator to the ion focus was about 30 cm, and the diameter of the separating section was 26 cm. The current densities in four magnetic conductors are indicated in Fig. 5.

The magnetic field was calculated by the Galerkin version of the second-order finite-element method on a triangular mesh. We solved the following equation for the vector potential A_θ (in SI units):

$$\frac{\partial}{\partial r}\left(\frac{1}{\mu_0\mu(B)r}\frac{\partial rA_\theta}{\partial r}\right) + \frac{\partial}{\partial z}\left(\frac{1}{\mu_0\mu(B)}\frac{\partial A_\theta}{\partial z}\right) = -j_\theta(r, z). \quad (27)$$

Here, j_θ is the known electric current density (in the conductors), B is the magnetic induction, $\mu_0 = 4\pi \times 10^{-7}$ H/m is the vacuum magnetic permeability, and $\mu(B)$ is the relative permeability of the iron conductors. For the relative permeability, we used the simple analytical dependence

$$\mu(B) = \mu_1 + \frac{\mu_2}{1 + \kappa B^2}. \quad (28)$$

The results presented in Fig. 5 were calculated for $\mu_1 = 0$, $\mu_2 = 6000$, and $\kappa = 150$.

5.2. POMS-E

In this version of a separator, two blocks (the PA and the azimuthator) are the same as those in the POMS-H. In the POMS-E, the magnetic field is supposed to be 10 to 15 times lower, so the magnetic system will accordingly be lighter in weight. However, the POMS-E in question also includes a system of two coaxial electrodes. For the scales and energies chosen, the voltage between the electrodes is determined from condition (14) and is equal to

$$U = E_0 R \ln\left(\frac{r_a}{r_c}\right), \quad (29)$$

where r_a and r_c are the anode and cathode radii, respectively.

ACKNOWLEDGMENTS

We are grateful to N.N. Semashko for useful discussions of the questions concerning POMS systems. We also thank V.P. Smirnov for the encouragement of this study. This work was supported in part by the Russian Foundation for Basic Research, project nos. 03-01-00063 and 02-07-90027.

REFERENCES

1. L. A. Artsimovich and S. Yu. Luk'yanov, *Charged Particle Motion in Electric and Magnetic Fields* (Nauka, Moscow, 1972) [in Russian].
2. A. I. Morozov, in *Encyclopedia of Low-Temperature Plasma*, Ed. by V. E. Fortov (Nauka, Moscow, 2000), Vol. 3, p. 435.
3. S. D. Grishin, in *Encyclopedia of Low-Temperature Plasma*, Ed. by V. E. Fortov (Nauka, Moscow, 2000), Vol. 4, p. 291.
4. A. I. Morozov and S. V. Lebedev, in *Reviews of Plasma Physics*, Ed. by M. A. Leontovich (Atomizdat, Moscow, 1974; Consultants Bureau, New York, 1980), Vol. 8.
5. A. I. Morozov and N. N. Semashko, Pis'ma Zh. Tekh. Fiz. **28** (24), 63 (2002) [Tech. Phys. Lett. **28**, 1052 (2002)].
6. A. I. Morozov, V. K. Naumov, V. V. Savel'ev, and N. N. Semashko, in *Proceedings of the 7th All-Russia Conference on Physical and Chemical Problems of Separating Atoms and Molecules, Zvenigorod, 2002*, p. 148.

Translated by G.V. Shepekina

Plasma Physics Reports, Vol. 31, No. 5, 2005, pp. 425–435. Translated from Fizika Plazmy, Vol. 31, No. 5, 2005, pp. 466–477.

LOW-TEMPERATURE PLASMA

Experimental and Theoretical Study of a Quasi-Steady Electron-Beam Plasma in Hot Argon

N. L. Aleksandrov, M. N. Vasil'ev, S. L. Lysenko, and A. Kh. Makhir

Moscow Institute of Physics and Technology, Institutskiĭ pr. 9, Dolgoprudnyĭ, Moscow oblast, 141700 Russia

Received June 16, 2004; in final form, September 22, 2004

Abstract—An argon plasma produced by a quasi-steady high-energy electron beam was studied experimentally. The plasma density was measured using an open barrel-shaped microwave cavity. The gas temperature was shown to be a few times higher than room temperature. Electron beam propagation, as well as heat-transfer and kinetic processes in plasma, is modeled self-consistently for the actual experimental conditions. It is shown that the plasma density is largely governed by the conversion rate of the atomic ions into molecular ones. The calculated results are compared to the experimental data. © *2005 Pleiades Publishing, Inc.*

1. INTRODUCTION

Weakly ionized plasmas produced in dense gases irradiated by relativistic electron beams are widely used in practice, e.g., for pumping gas lasers [1, 2], in plasmochemical reactors [3, 4], for surface treatment [5], for cleaning gases of harmful substances [6], etc.

When considering the irradiation of a gas by pulsed electron beams, gas heating can usually be ignored. In some applications, however, it is expedient to use continuous electron beams; in this case, gas heating should necessarily be taken into account. This makes plasma simulations more difficult because nonuniform heating leads to nonuniformity of the neutral gas, and, accordingly, the beam scattering by the gas and the parameters of the plasma produced are nonuniform too. An extra effect to be taken into account is the dependence of the rate constants for elementary processes on the gas temperature. Thus, the effect of gas heating on the parameters of the beam plasma should be investigated in a self-consistent manner, by simultaneously taking into account the gas nonuniformity and the nonuniformities of electron-beam scattering and the kinetic properties of the plasma produced. When a plasma is produced in a small-sized chamber, it is also necessary to incorporate the beam scattering by the chamber wall, as well as the accompanying effects of chamber heating and electron reflection from the wall. The problem as formulated has not yet been considered experimentally or theoretically. Though there have been many numerical studies (generally, by the Monte Carlo method) devoted to the propagation of electrons through matter, all of them were restricted mainly to considering either a gaseous [7, 8] or a solid medium [9, 10].

In this paper, we present the results from experimental and theoretical studies of a plasma produced by a 25-keV continuous electron beam in a cylindrical chamber filled with argon. The severalfold increase in the gas temperature under the action of the beam affects both the scattering of high-energy electrons and the properties of the plasma produced. In our experiments, we measured the longitudinal profiles of the plasma electron density and of the gas temperature at the chamber wall. We also performed calculations for actual experimental conditions. Electron beam propagation in the gas and the chamber wall was simulated by the Monte Carlo method, the plasma composition was determined by kinetic simulations, and the heating of the chamber wall and of the gas was calculated by solving heat conduction equations. The calculated results are compared to the experimental data.

2. EXPERIMENT

2.1. Experimental Setup

A schematic of the experimental setup is shown in Fig. 1. A focused continuous electron beam generated by an electron gun was introduced into the working chamber through the outlet pipe of the high-vacuum chamber. Inside the working chamber, a reaction chamber (a 25-cm-long quartz tube with a wall thickness of 2 mm and an inner diameter of 2.6 cm) was placed. The open end of the reaction chamber faced the outlet pipe, whereas the other end was closed with a Faraday cup. In some experiments, the outer surface of the quartz tube was covered with a multilayer thermal insulation in order to reach a higher temperature.

The outlet pipe was a gas-dynamic window consisting of a two-stage gate system with the differential evacuation of the gas leaking into an intermediate chamber placed between the stages [5]. The input and output apertures of the gas-dynamic window, through which the electron beam was injected, were 1-mm-diameter channels made in 10-mm-thick graphite disks.

The high-vacuum chamber was continuously pumped out by an oil diffusion pump to balance the leaking of the gas through the outlet pipe. The pressure

1063-780X/05/3105-0425$26.00 © 2005 Pleiades Publishing, Inc.

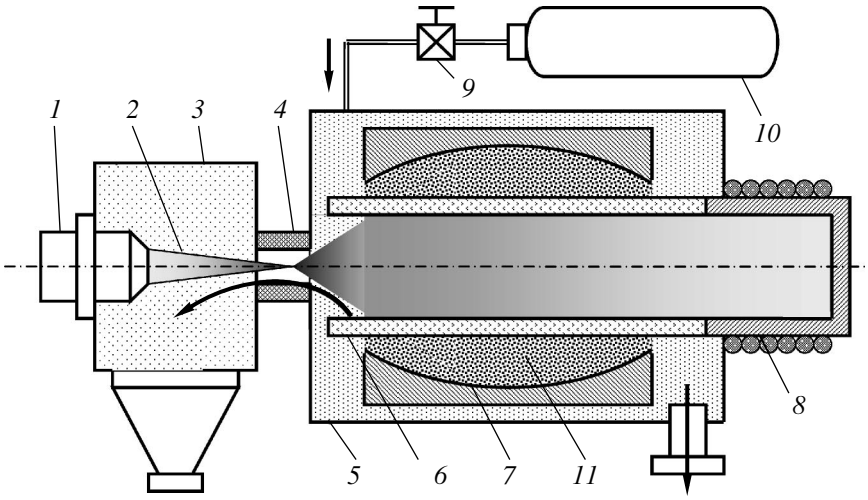

Fig. 1. Schematic of the experimental setup: (*1*) electron gun, (*2*) electron beam, (*3*) high-vacuum chamber, (*4*) outlet pipe, (*5*) working chamber filled with argon, (*6*) quartz shell, (*7*) cavity, (*8*) Faraday cup, (*9*) inlet valve, (*10*) vessel with argon, and (*11*) radio-transparent ceramics.

in the chamber was maintained at a level of $\leq 10^{-4}$ torr, required for stable operation of the electron gun. The working chamber was pumped out by a fore pump. Argon was supplied to the working chamber from a gas vessel through a controlled valve.

2.2. Measurement Technique

The main parameter characterizing the plasma properties in our experiments was the plasma electron density n_e averaged over the chamber cross section at a distance z from the point of electron beam injection. We measured n_e as a function of the gas pressure p and the electron-beam current I_b in different cross sections z for several accelerating voltages U between the cathode and anode of the electron gun. The initial beam electron energy E_b, which was determined by the accelerating voltage, was varied from 20 to 30 keV. The gas pressure and the beam current were varied in the ranges of 1–50 torr and 1–50 mA, respectively.

The electron density n_e was measured by the multimode probing of the plasma volume with microwave electromagnetic radiation at a wavelength of $\lambda \approx 0.8$ cm. For this purpose, we used an open barrel-shaped cavity [11] enclosing the quartz tube. The coaxiality between the tube and the cavity was enabled with the help of special heat-insulating holders (not shown in Fig. 1). The space between the tube and the inner wall of the cavity was filled with ceramic powder that was radio-transparent in the wavelength range under study. This enabled reliable heat-insulation of the cavity from the hot wall of the reaction chamber, whose temperature could be as high as 1000 K (see below).

The open barrel-shaped cavity used in our experiments is described in detail in [11]. The diameter of its central cross section is $2a = 68$ mm, the meridional radius is $r = 204$ mm, and the cavity length is $L = 70$ mm. The inner dimensions of the feeding and receiving rectangular waveguides are 3.8×7.6 mm. To rarefy the spectrum, we used a spatially distributed coupling (eight coupling openings spaced apart by 11.05 mm) between the cavity volume and the waveguide both when exciting the cavity and when recording the signal. The spectrum was additionally rarefied because the cavity was open and the distributed coupling resided close to the equatorial plane; in this case, a number of modes are not excited and recorded.

A fragment of the cavity spectrum without a plasma is shown in Fig. 2. Mode *1* is the one that was used to measure the electron density. The frequency of this mode depends on the plasma density. Mode *2* is a cavity mode with a large azimuthal number. The electric field of this mode is located near the cavity surface. In the middle of the cavity, where the quartz tube is located, this field is very low; hence, mode *2* does not interact with electrons and its frequency does not depend on the plasma density. Therefore, this mode can be used as a reference point.

The electron density was measured as follows: First, the microwave generator was switched on when the gas pressure in the working chamber was minimal ($p <$ 1 torr). Next, the electron beam was switched on and the gas pressure in the working chamber was slowly increased. As a result, the frequencies of the modes excited in the cavity shifted gradually depending on their coupling with the plasma in the working chamber. The frequency of the main mode also shifted gradually; this enabled its identification even at electron densities as high as 5×10^{12} cm^{-3} ($\Delta\omega = 2$ GHz). Indeed, the distance between modes *1* and *2* in Fig. 2 is about 1.5 GHz, and there are no modes with an appreciable amplitude between them. As the electron density increases, the frequency of mode *1* shifts, whereas its amplitude

decreases because its absorption in the plasma increases and the frequency of the mode shifts beyond the bandwidth of the distributed coupling [11]. The plasma density was increased to a value at which mode *1* overlapped mode *2*. Note that these modes did not interact with one another because the fields of the different modes of a cavity with a nonuniform permittivity distribution were mutually orthogonal.

The electron density n_e was determined from the measured frequency shift $\Delta\omega$ by the formula

$$\frac{\Delta\omega}{\omega} = \frac{1}{2}\frac{n_e}{n_e^*}\frac{V_p}{V_r}F_V, \quad (1)$$

where n_e is the electron density averaged over the cavity cross section, V_r is the cavity volume, V_p is the plasma volume inside the cavity, F_V is the cavity form-factor, and n_e^* is the critical electron density.

Formula (1) is applicable when $\omega \gg \nu$ (where ν is the transport frequency of electron collisions in plasma) and $n_e \le (0.2\text{–}0.3)n_e^*$. These conditions determine the maximum measurable electron density: $(n_e)_{\max} \approx (3\text{–}5) \times 10^{12}$ cm^{-3}.

Besides the electron density, we also measured the gas pressure in the reaction chamber, the total electron-beam current (using a water-cooled Faraday cup), and the temperature of the reaction chamber wall at the outer surface of the quartz tube. Several thermal detectors were set at different points z; this allowed us to study the temperature of the outer wall $T_w(z)$ as a function of the gas pressure p and the electron-beam power.

2.3. Experimental Results

Figures 3–5 show the results from measuring of the temperature at the outer surface of the chamber wall and the electron density under different experimental conditions. The wall temperature is several times higher than room temperature; this indicates that the gas in the chamber is significantly heated. Under our experimental conditions, the electron density was in the range 10^{11}–10^{13} cm^{-3} and was approximately proportional to the electron-beam current I_b. Within any cross section z, the function $n_e = n_e(p)$ has a pronounced maximum at a certain pressure p_m, which depended on the beam current and the accelerating voltage U: the higher U or I_b, the higher p_m.

3. SIMULATIONS OF THE INTERACTION OF A HIGH-ENERGY ELECTRON BEAM WITH MATTER

The interaction of an electron beam with matter under actual experimental conditions can be described in as follows: A high-energy electron beam is injected into a quartz tube filled with a gas and propagates along its axis. The injected electrons undergo elastic, inelastic, and ionizing collisions with gas atoms; the latter give rise to secondary electrons. In the absence of an external electric field, the electrons between collisions move along straight lines. After a collision event, an electron is assigned a new propagation direction and an energy loss that depends on the kind of process. As a result, the electron motion is represented by a broken line that can cross the tube wall. In this case, the electron enters another medium and undergoes similar processes but with other parameters. The simulation of electron motion is stopped when its energy becomes lower than the atomic excitation energy.

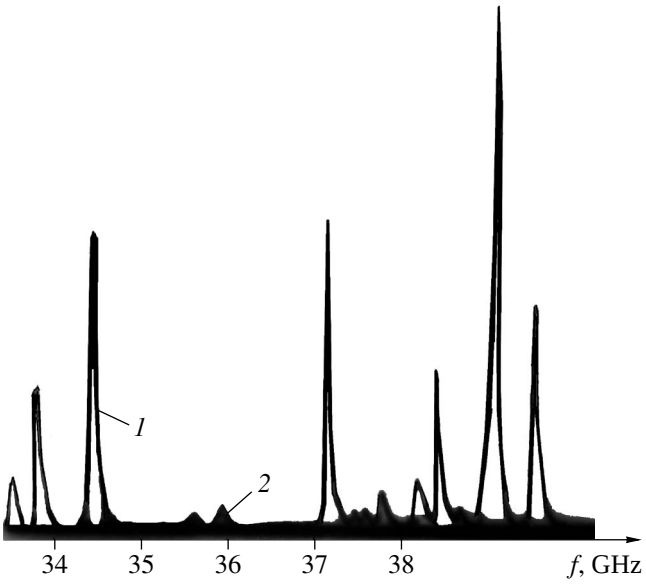

Fig. 2. Fragment of the cavity spectrum without plasma: (*1*) mode used to measure the electron density (*2*) mode used as a reference point.

To describe the electron trajectory, it is necessary to define the algorithm for calculating the electron free path between collisions. Generally, in modeling the propagation of electrons with an energy E in a homogeneous medium, the free path s and, consequently, the point at which the next collision occurs are determined from the condition [7, 8]

$$s = -\lambda(\varepsilon)\ln\xi,$$

where $\lambda(\varepsilon) = [\sigma(\varepsilon)n(\varepsilon)]^{-1}$ is the mean free path for a given electron energy, $\sigma(\varepsilon)$ is the total cross section for electron scattering, $n(\varepsilon)$ is the density of the scattering particles, and ξ is a random value evenly distributed within the interval [0, 1]. For an inhomogeneous medium (e.g., in the case of a nonuniform gas density or when an electron passes from the gas to a solid wall), this condition is naturally generalized to

$$\int_0^s \sigma(\eta)n(\eta)d\eta = -\ln\xi,$$

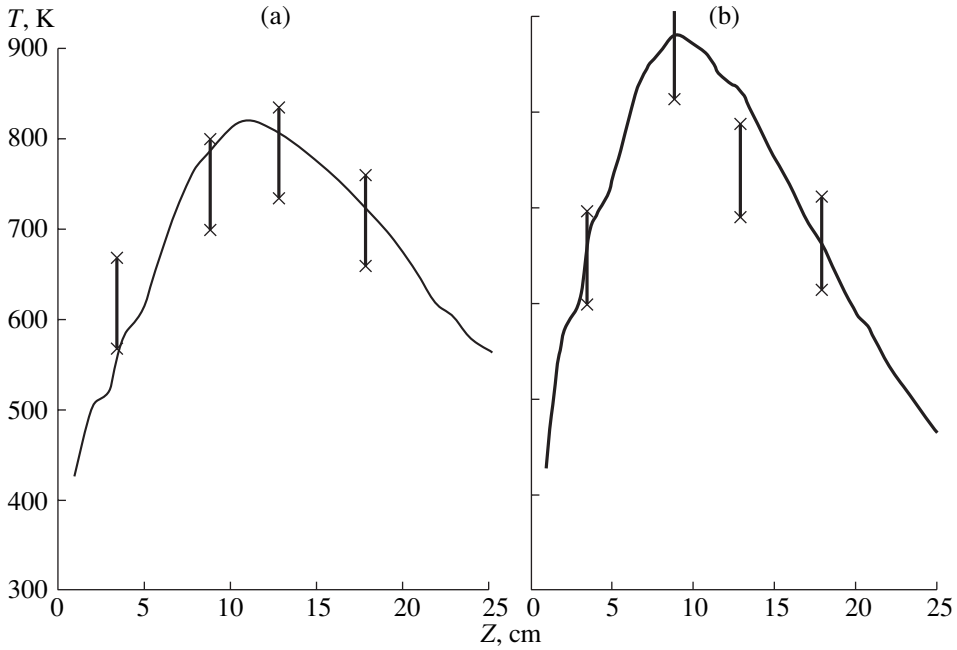

Fig. 3. Longitudinal profile of the temperature at the outer surface of the chamber for the case of an electron beam with a current of 8.8 mA and an electron energy of 25 keV at gas pressures of (a) 5.2 and (b) 11 torr. The solid curves show the simulation results, and the vertical bars show the experimental results.

where η is the spatial coordinate in the electron propagation direction.

When an electron crosses the interface between two media, a fraction of the integral is first calculated in the first medium with its proper parameters and the remaining fraction is then calculated in the second medium with another parameters. Thus, on crossing the interface, only the medium parameters (rather than the simulation algorithm) change. In our simulations, many electrons repeatedly penetrated into the wall and returned back into the gas.

When calculating electron motion in the gas, we took into account variations in the gas density due to the nonuniform heating by the beam. To do this, the gas density at a given point was determined for a given gas pressure and calculated temperature using the equation of state. Self-consistency in simulating the propagation of electrons was achieved as follows: First, electron propagation in the gas and in the wall material was calculated using the Monte Carlo method. The acquired data were then statistically processed and the spatial distribution of the heat released in the gas and at the wall surface was simulated. Finally, the temperature distribution and the gas density were determined throughout the entire volume. This procedure was repeated after calculating each ten trajectories. After 100 trajectories, the temperature distribution relaxed to a quasi-steady state. The temperature relaxation was also provided by heat conduction and radiative heat transfer between different parts of the inner surface of the working chamber (these mechanisms partially balanced the nonuniformity of energy deposition caused by insufficient statistics). In our simulations, we calculated from 5000 to 500000 trajectories. Such a large statistics is necessary, e.g., to obtain smooth spatial distributions of the ionization rate; at the same time, the temperature distribution in the working chamber was already established after calculating 100 trajectories. In other respects, the Monte Carlo algorithm was the same as in the previous simulations [7, 8].

In simulations, we sometimes observed the effect of the so-called burning-through of the gas by the electron beam because of the elevated temperature and the reduced gas density in regions with an increased electron-beam current density. This led to an increase in the penetration depth of high-energy electrons along the tube axis.

Based on the gathered statistical data, we determined the distributions of the ionization and excitation rates of gas atoms over the quartz tube volume, as well as the power dissipated per unit gas volume or unit area of the inner surface of the quartz tube.

4. CROSS SECTIONS FOR ELECTRON SCATTERING BY ARGON ATOMS AND IN A SOLID MEDIUM

4.1. Elastic Collisions

To find the integral and differential cross sections for elastic scattering at energies higher than 10 keV, the Rutherford formula with allowance for screening is usually employed. According to this formula, the dif-

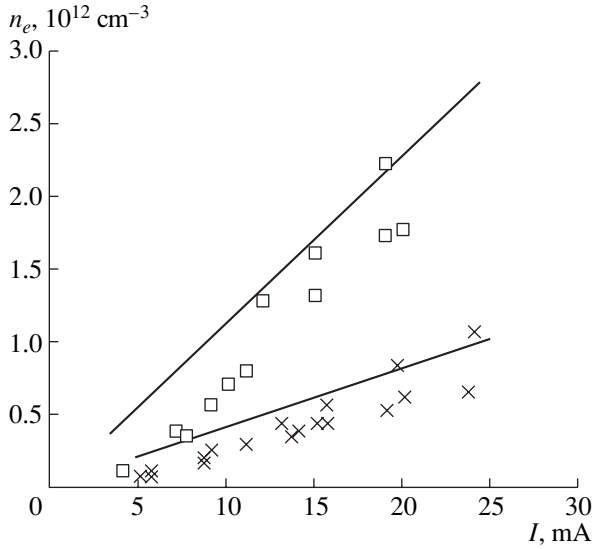

Fig. 4. Electron density as a function of the current of a 29-keV electron beam. The solid lines and symbols show simulation and experimental results, respectively, for p = 12 torr and z = 9 cm (the upper line, squares) and for p = 8 torr and z = 16.5 cm (the lower line, crosses).

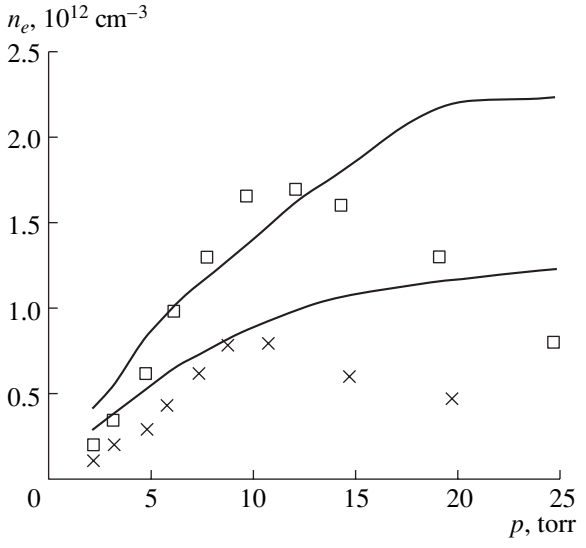

Fig. 5. Electron density vs. gas pressure at z = 9 cm for the case of a 25-keV electron beam. The solid curves and symbols show simulation and experimental results, respectively, for currents of 15 mA (the upper curve, squares) and 7.5 mA (the lower curve, crosses).

ferential cross section for elastic collisions between electrons and atoms is

$$\frac{d\sigma_{el}}{d\Omega} = r_0^2 Z^2 \frac{1-\beta^2}{\beta^4(1-\cos\theta+2\eta)^2}, \qquad (2)$$

where r_0 is the classical radius of an electron, Z is the atomic number,

$$\beta^2 = \frac{E(2mc^2+E)}{(mc^2+E)^2}$$

is the squared ratio of the electron velocity to the speed of light c, m is the electron mass, E is the electron kinetic energy before the collision, θ is the polar angle of scattering with respect to the electron velocity before the collision, and η is the screening parameter. The expression for η as a function of Z and β was taken from [9, 10].

The total cross section for elastic collisions is determined by integrating (2) over solid angle Ω and is equal to

$$\sigma_{el} = \pi r_0^2 \frac{1-\beta^2}{\beta^4}\frac{Z^2}{\eta(1+\eta)}. \qquad (3)$$

The applicability of formula (2) at low energies is questionable because it does not include polarization effects and spin–orbit interaction. Therefore, at low energies, it is expedient to use experimental data. However, the differential and integral cross sections for elastic scattering in argon were measured only for energies E < 100 eV [12, 13]. To bridge the gap between this energy range and the high-energy range where formula (3) is valid, the energy dependence of σ_{el} measured in [12, 13] was extrapolated by a power-law function $\sigma_{el} = AE^{-\delta}$ toward higher energies up to an energy of ~3 keV, at which the extrapolated value was equal to that calculated by formula (3). When calculating electron motion, σ_{el} was determined using the data from [12, 13] (and their extrapolation) at E < 3 keV and using formula (3) at E > 3 keV. At high energies (E > 3 keV), the differential cross section was calculated by formula (2), whereas for E < 3 keV, the measured electron distribution function over the scattering angle at E = 100 eV was used [12, 13].

4.2. Collisional Excitation

We considered only the excitation of the $1s_2$ state of Ar because its cross section is significantly larger than that for any other state [14, 15]. The integral cross section was calculated by the formula [16]

$$\sigma_{ex} = 4\pi a_0^2\left(\frac{E_H}{E_{ex}}\right)^2 \alpha\left(1-\frac{E_{ex}}{E}\right)\frac{E_{ex}}{E}\ln\left(\frac{E}{E_{ex}}\right), \qquad (4)$$

where a_0 is the Bohr radius, E_{ex} is the threshold energy for the transition into the $1s_2$ state, E_H is the ionization energy for a hydrogen atom, and α = 0.265 is the constant describing the oscillator strength of the transition.

The angular distribution of the electrons after a collisional excitation was taken from the measurements [17] of the corresponding differential cross section $d\sigma_{ex}/d\Omega$ at E < 100 eV. For high energies, we used the

angular distribution corresponding to $E = 100$ eV. Of course, such an approach introduces an error. Estimates show however that, when the electron-impact excitation of Ar plays an important role, the angular distribution is mainly determined by elastic collisions (rather than inelastic ones); hence, the error introduced by such an approach is small.

4.3. Ionizing Collisions

The ionization of an atom by an electron with an energy E leads to the generation of a secondary electron with an energy of no higher than $(E - E_i)/2$, where E_i is the ionization energy (the electron with a higher energy is regarded as a primary one). To calculate the electron trajectory, it is necessary to know the ionization cross section $\sigma_{ion}(E)$, the differential cross section $\sigma_{ion}(E, E_2)$ for the generation of a secondary electron with an energy E_2 (here, E is the electron energy before the collision), and the angular distribution of the electrons after the collision.

The ionization processes in Ar were described by analogy to [16]. We used the analytical formula proposed in [18], in which the parameters were somewhat changed in order to fit the experimental data on the differential cross section from [19] and to bring them (after integrating over solid angle) into coincidence with the measured integral ionization cross section in Ar [20].

After a collision event, the propagation directions of the primary and secondary electrons with respect to the velocity of the ionizing electron were determined by analogy to [7].

4.4. Scattering in a Solid Medium

To describe electron propagation in the chamber wall, it is necessary to know both the integral and differential cross sections for elastic and inelastic scattering. The elastic scattering was described by formula (2), whereas the electron energy loss for ionization and excitation were determined using the Bethe–Bloch approximation for continuous energy losses [21]. The average loss at SiO_2 molecules was determined as a sum of the losses at Si and O atoms.

To prove the reliability of the approximation used, energy losses were also calculated using the data (obtained by processing optical spectra [22]) on the differential cross sections for inelastic electron collisions in quartz. It turned out that, for electron energies higher than 300 eV, the data obtained using the latter procedure differed from those obtained using the Bethe–Bloch approximation by no more than 10%.

5. CALCULATIONS OF THE SPATIAL DISTRIBUTION OF THE GAS TEMPERATURE

In a two-dimensional, axially symmetric approximation, the steady-state distribution of the temperature in the gas and the chamber wall was described by the heat conduction equation

$$\frac{1}{r}\frac{\partial}{\partial r}\left(\lambda r\frac{\partial T}{\partial r}\right) + \frac{\partial}{\partial z}\left(\lambda\frac{\partial T}{\partial z}\right) + q = 0, \qquad (5)$$

where r is the distance from the tube axis, z is the longitudinal coordinate counted from the beam input window, λ is the thermal conductivity of a medium, T is the medium temperature, and q is the power dissipated per unit volume.

For the gas in the tube, the power q dissipated per unit volume was determined by the Monte Carlo method. The penetration depth of the beam electrons into the chamber wall was small; hence, it was assumed that $q = 0$ in the quartz tube. The thermal conductivities of argon and quartz were taken from [23].

The boundary condition at the inner surface of the quartz tube, which was in contact with the gas, was written as

$$-\lambda_g\left(\frac{\partial T}{\partial r}\right)_g + q_1 + q_2 = -\lambda_w\left(\frac{\partial T}{\partial r}\right)_w, \qquad (6)$$

where q_1 and q_2 are the heating powers (per unit area) of the tube surface by the electron beam and the radiation emitted from the other parts of the tube surface, respectively. The first term on the left-hand side of Eq. (6) and the term on the right-hand side describe the heat flux in the gas and the wall, respectively. The value of q_1 was determined by the Monte Carlo method, and the value of q_2 was determined assuming the wall radiation to be equilibrium.

At the outer surface of quartz tube, we set

$$-\lambda_w\left(\frac{\partial T}{\partial r}\right)_w = \sigma T^4, \qquad (7)$$

where σ is the Stefan–Boltzmann constant.

The axial and radial temperature profiles were obtained by numerically solving Eq. (5) with boundary conditions (6) and (7) using the method of upper relaxation with a sweep along the transverse coordinate [24].

6. PLASMA KINETIC MODEL

The main purpose of our kinetic model was to determine the steady-state distribution of the electron density in the plasma produced by an electron beam in argon. The problem was solved for pressures of 1–50 torr and gas temperatures of 300–1000 K.

The model is based on the kinetic scheme used in [25, 26] to describe the formation of Ar_2^* excimers and charged species in argon irradiated by an intense pulsed electron beam. This scheme allowed the authors of [25, 26] to describe the temporal evolution of the electron

Reactions and their rate constants. Gas temperature T, K, electron temperature T_e, eV

Reaction	Rate constant	References
1. $e_b + Ar \longrightarrow e_b + e + Ar^+$	Q_{ion} [cm^{-3} s^{-1}]	Monte Carlo
2. $e_b + Ar \longrightarrow e_b + Ar^*$	Q_{ex} [cm^{-3} s^{-1}]	Monte Carlo
3. $Ar^+ + 2Ar \longrightarrow Ar_2^+ + Ar$	$k_3 = 2.5 \times 10^{-31}(300/T)^{0.75}$ cm^6 s^{-1}	[26, 27]
4. $Ar_2^+ + 2Ar \longrightarrow Ar_3^+ + Ar$	$k_4 = 7 \times 10^{-32}(300/T)^{0.75}$ cm^6 s^{-1}	[26, 27]
5. $Ar_2^+ + Ar \longrightarrow Ar^+ + 2Ar$	$k_5 = 9.3 \times 10^{-10}(1.4 \times 10^4/T)^{0.5} \times \exp(-1.4 \times 10^4/T)$ cm^3 s^{-1}	[28]
6. $Ar_3^+ + Ar \longrightarrow Ar_2^+ + 2Ar$	$k_6 = 9.3 \times 10^{-10}(2.3 \times 10^3/T)^{0.5} \times \exp(-2.3 \times 10^3/T)$ cm^3 s^{-1}	[28]
7. $Ar_2^+ + e \longrightarrow Ar^* + Ar$	$k_7 = 7.3 \times 10^{-8} T_e^{-0.67}$ cm^3 s^{-1}	[26]
8. $Ar_3^+ + e \longrightarrow Ar^* + 2Ar$	$k_8 = 1.6 \times 10^{-7} T_e^{-0.54}$ cm^3 s^{-1}	[26]
9. $Ar^+ + 2e \longrightarrow Ar^* + e$	$k_9 = 2.61 \times 10^{-22}(0.086/T_e)^{4.5}$ cm^6 s^{-1}	[27]
10. $Ar^* + e \longrightarrow Ar + e$	$k_{10} = 4.5 \times 10^{-10} T_e$ cm^3 s^{-1}	[26]
11. $Ar^* + Ar^* \longrightarrow Ar_2^+ + e$	$k_{11} = 6 \times 10^{-10}$ cm^3 s^{-1}	[26]
12. $Ar_2^+ + e \longrightarrow Ar^+ + Ar + e$	$k_{12} = 9 \times 10^{-8}\exp(-1.2/T_e)$ cm^3 s^{-1}	Calculations
13. $Ar_3^+ + e \longrightarrow Ar^+ + 2Ar + e$	$k_{13} = 9 \times 10^{-8}\exp(-1.2/T_e)$ cm^3 s^{-1}	Calculations
14. $Ar^+ + N_2 \longrightarrow Ar + N_2^+$	$k_{14} = 5 \times 10^{-11}$ cm^3 s^{-1}	[29]
15. $Ar^+ + O_2 \longrightarrow Ar + O_2^+$	$k_{15} = 7 \times 10^{-11}$ cm^3 s^{-1}	[29]
16. $N_2^+ + O_2 \longrightarrow N_2 + O_2^+$	$k_{16} = 6 \times 10^{-11}(300/T)^{0.5}$ cm^3 s^{-1}	[30]
17. $e + N_2^+ \longrightarrow N + N$	$k_{17} = 4.5 \times 10^{-8} T_e^{-0.5}$ cm^3 s^{-1}	[30]
18. $e + O_2^+ \longrightarrow O + O$	$k_{18} = 5.2 \times 10^{-9} T_e^{-1}$ cm^3 s^{-1}	[30]

density, as well as the densities of Ar_2^+ and Ar_3^+ ions and Ar* and Ar_2^* excited particles. Note that the experimental conditions in [25, 26] differed from our experimental conditions in a higher gas pressure (1 atm and more), a lower gas temperature (300 K and less), and a shorter electron-beam pulse duration (a few hundred nanoseconds). For this reason, we modified the kinetic scheme. In particular, we included the dependence of the rate constants for some processes on the gas temperature and ignored the production of Ar_2^*, because the latter process does not affect the formation of charged species at low gas pressures. Moreover, we included the effect of a small (~0.1%) air admixture on the electron density.

The rate constants for the processes taken into account in our study are listed in the table. The irradiation of argon by a high-energy electron beam leads to the generation of secondary electrons, Ar^+ ions, and excited atoms (processes (1), (2)). The plasma electron density is determined by both ionization processes and electron–ion recombination. The recombination of an electron with an Ar^+ atomic ion is a three-body reaction; under our experimental conditions, its rate is several orders of magnitude less than the rate of dissociative recombination with Ar_2^+, Ar_3^+ molecular ions. Hence, it is of importance to include the production of molecular ions in reactions (3) and (4) and their loss in collisions with atoms (reactions (5), (6)) and electrons (reactions (12), (13)). Note that processes (5) and (6) are of importance only in a hot gas. Therefore, we should include these processes, although they were not considered in modeling excimer lasers [25, 26]. The kinetics of the excited atoms can also be important because of associative ionization (reaction (11)), through which charged particles are produced. The excited atoms are produced in collisions with the beam electrons (reaction (2)) and via electron–ion recombi-

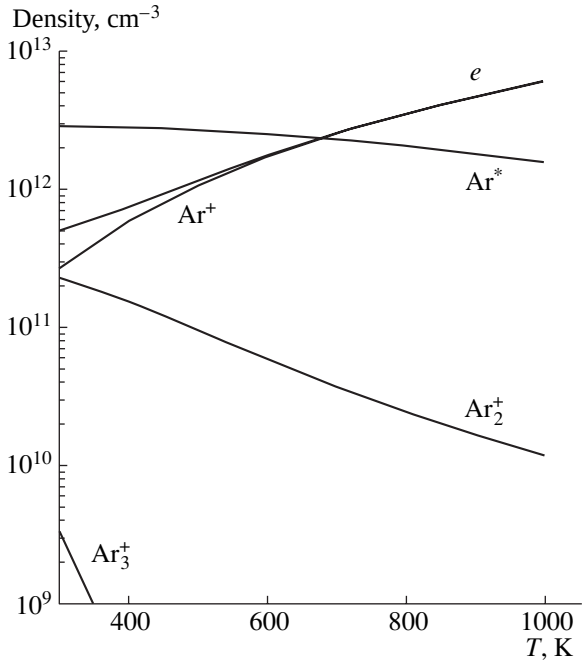

Fig. 6. Calculated densities of charged and excited particles in pure argon as functions of the temperature at a pressure of 10 torr for a specific electron-beam energy deposition of $Q = 10^{17}$ eV cm^{-3} s^{-1}.

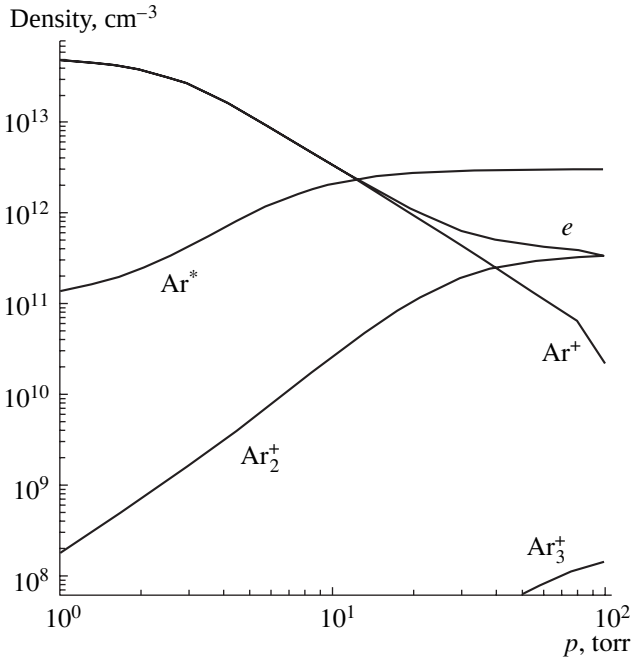

Fig. 7. Calculated densities of charged and excited particles in pure argon as functions of the gas pressure for a gas temperature of 800 K and specific electron-beam energy deposition of $Q = 10^{17}$ eV cm^{-3} s^{-1}.

nation (reactions (7)–(9)) and are lost in collisions with plasma electrons (reaction (10)). We ignored both the production of excimer molecules (which was important under the experimental conditions in [25, 26]) and the radiation from the excited atoms. Thus, the electron density in our simulations was somewhat overestimated.

The rates of ionization (Q_{ion}) and excitation (Q_{ex}) of atoms at a given point under the action of the beam electrons were determined by simulating the beam propagation by the Monte Carlo method. The rate constants for reactions (3) and (4) at $T = 300$ K were taken from the experiment [26], whereas their temperature dependence was taken from the simulation results [27]. The rate constants for reactions (5) and (6) have not yet been measured; therefore, we estimated them using formulas from [28]. Since no data on the rate constants for reactions (12) and (13) are available in the literature, they were calculated by averaging the relevant cross sections over a Maxwellian electron distribution. The references to the papers from which we took the rate constants for the other processes are listed in the table.

In the balance equations for charged particles, we also included the ambipolar diffusion of the plasma toward the tube wall. Plasma diffusion plays an important role only in the region where the beam is injected into the chamber, because the plasma radius in this region is small and, accordingly, the density gradients of charged particles are large.

The densities of charged and excited particles were determined by numerically solving the corresponding balance equations using the Gear method. The accuracy of the solutions obtained was verified using the quasineutrality condition. When modeling the kinetic processes in argon with an air admixture, the above set of equations was supplemented with the equations for the densities of O_2^+ and N_2^+ ions.

7. SIMULATION RESULTS

7.1. Electron Density as a Function of the Gas and Beam Parameters

The plasma in our experiments had a number of specific features as compared to the plasma consisting of electrons and singly charged positive ions. Let us illustrate this using a homogeneous plasma produced by an electron beam in pure argon at elevated gas temperatures as an example (hereafter, the electron temperature T_e is assumed to be 1 eV, which is close to the temperature calculated in [31] for pure argon).

The calculated densities of charged and excited particles in such a plasma for a given gas pressure and a given energy deposited by the electron beam are shown in Fig 6 versus gas temperature. It can be seen that, as the temperature increases, the molecular ions decompose because of thermal dissociation; thus, Ar^+ atomic ions become dominant. However, it is seen from the table that, under our experimental conditions, the rate

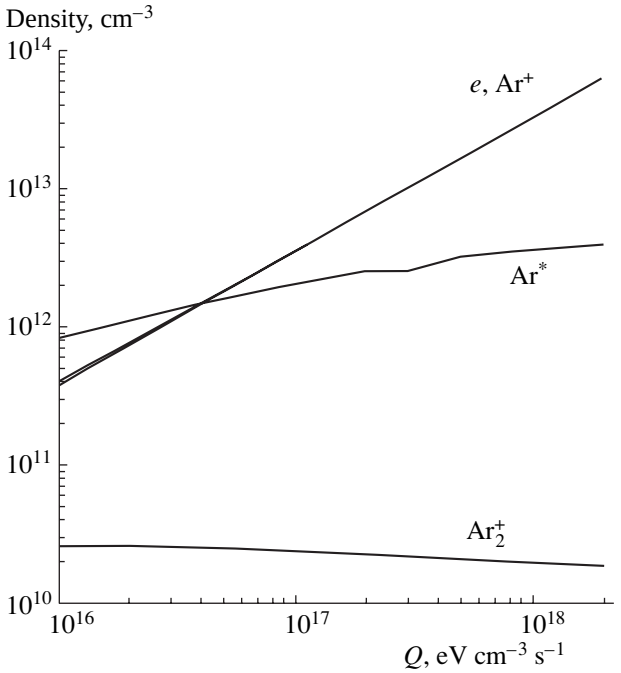

Fig. 8. Calculated densities of charged and excited particles in pure argon as functions of the specific electron-beam energy deposition for p = 10 torr and T = 800 K.

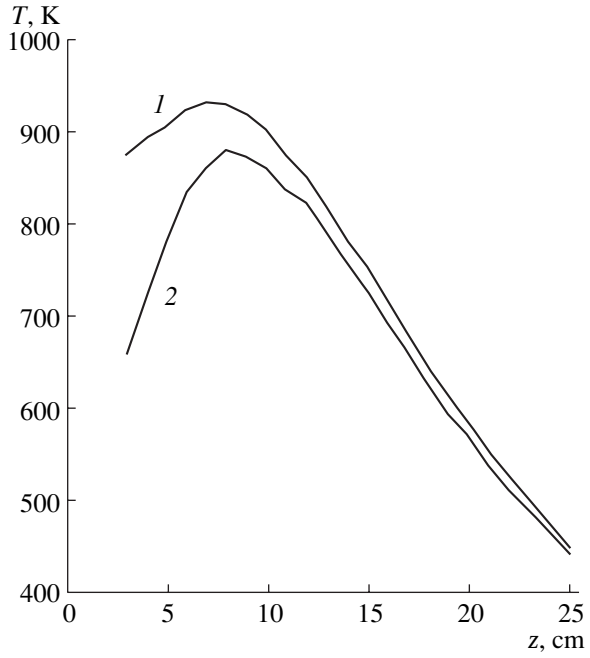

Fig. 9. Axial profile of the gas temperature (*1*) on the chamber axis and (*2*) 1.3 cm away from the axis in pure argon for a gas pressure of 11 torr, an electron-beam current of 8.8 mA, and an electron energy of 25 keV.

constant for the recombination of electrons with atomic ions (reaction (9)) is approximately seven orders of magnitude less than the analogous rate constant for Ar_2^+ molecular ions (reaction (7)); this means that the direct recombination of atomic ions can be ignored. Therefore, the electron loss rate, which determines the steady-state electron density, decreases and the electrons are lost in two stages: first, the atomic ions are converted into molecular ions (reaction (3)), which then rapidly recombine with electrons (reaction (7)). Under conditions such that atomic ions prevail and the electrons are lost via recombination with molecular ions, the effective electron loss rate is largely governed by the conversion rate of atomic ions into molecular ones. The properties of such a plasma differ significantly from the properties of a plasma with one species of positive ions.

Indeed, ignoring the processes with the participation of excited particles, the steady-state balance equation for atomic ions can be written as

$$Q_{\text{ion}} = k_3[\text{Ar}^+][\text{Ar}]^2.$$

It follows from here that the electron density is

$$[e] \approx [\text{Ar}^+] = Q_{\text{ion}}/(k_3[\text{Ar}]^2). \quad (8)$$

Note that in the beam plasma with one species of positive ions in a molecular gas, the electron density is

$$[e] = (Q_{\text{ion}}/k_{\text{rec}})^{1/2}, \quad (9)$$

where k_{rec} is the rate constant for the dissociative recombination of electrons with molecular ions.

Figure 7 shows the calculated densities of charged and excited particles versus gas pressure for a given gas temperature and given energy deposition. It can be seen that, up to pressures of ~30 torr, the atomic ions are dominant. It follows from (8) that the electron density then decreases in inverse proportion to the pressure squared. (Note that, in a plasma with one species of molecular ions, the electron density, according to (9), does not change with pressure.) This is confirmed by the calculation results of presented in Fig. 7. It is seen that the electron density decreases in accordance with formula (8) at pressures up to 30 torr and reaches a constant value at higher pressures.

Formulas (8) and (9) give different dependences of the electron density on the energy deposition Q (see also the calculated electron density as a function of the energy deposition in Fig. 8). According to formula (8), the electron density increases linearly with Q, in contrast to a weaker (square-root) dependence observed in the case where molecular ions are dominant.

In argon with a small admixture of air, N_2^+ and O_2^+ ions, which rapidly recombine with electrons, play an important role. In this case, Ar^+ is still the main ion species, whereas the electron loss is primarily determined by charge-exchange processes (8) and (9) (rather than by the production of Ar_2^+ ion, as is in pure argon).

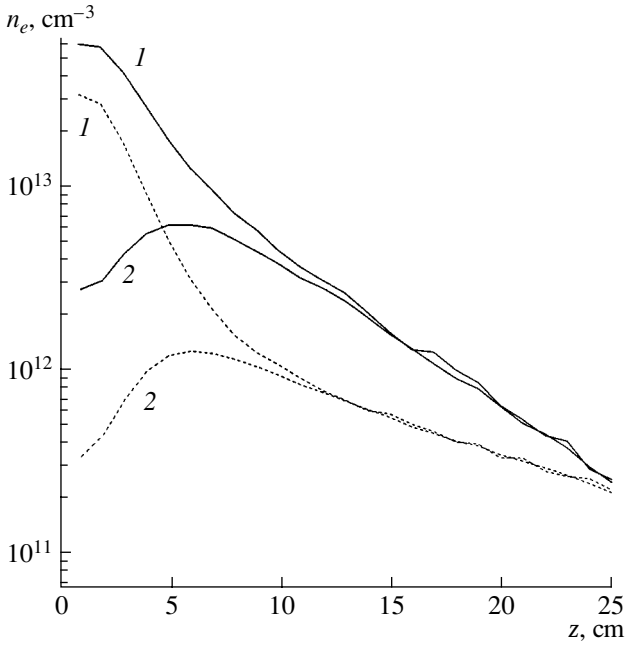

Fig. 10. Axial profile of the electron density (*1*) on the chamber axis and (*2*) 7 mm away from the axis in pure argon (solid curves) and in the mixture of argon with air at a partial air pressure of 0.014 torr (dashed curves) for a total gas pressure of 11 torr, an electron-beam current of 8.8 mA, and an electron energy of 25 keV.

7.2. Results of Self-Consistent Simulations and Comparison with the Experimental Results

When simulating the properties of the plasma produced by an electron beam under our experimental conditions, it is necessary to take into account the nonuniformity of gas heating (which leads to nonuniformities of the gas density and electron-beam scattering) and the presence of the chamber wall and a small (~0.01 torr) admixture of air that enter the chamber because of imperfect sealing. In this case, the calculated results somewhat change; however, as was mentioned above, the dependences remain qualitatively the same.

Our experimental results were compared to the results of numerical simulations performed with allowance for the above factors. It was shown above that the electron density depends substantially on the gas temperature. It can be seen from Fig. 3 that the calculated longitudinal profile of the temperature at the outer surface of the chamber wall coincides with the experimental results to within the experimental error. The calculated gas temperature at the chamber axis (see Fig. 9) reaches 1000 K. Thus, the plasma exists in a strongly heated gas. Since the chamber diameter is relatively small, gas heating is mainly caused by the absorption of the electron beam in the chamber wall. Only 2–3% of the electron beam energy is absorbed directly in the gas.

Figure 4 shows the measured and calculated electron density averaged over the chamber cross section as a function of the electron beam current I_b for different pressures and different distances z from the point of beam injection. The calculations were performed for argon with a small admixture of air (0.014 torr). This approximately corresponds to actual experimental conditions. In a plasma with one ion species, the electron density would be proportional to $I_b^{1/2}$; however, both the experiment and simulations show that the electron density increases with current much faster. This indicates that the dependence of the effective electron loss rate on the plasma density is weaker than quadratic.

Figure 5 shows the electron density averaged over the chamber cross section as a function of the gas pressure. The calculations were also performed for argon with a 0.014-torr air admixture. It can be seen that the theory adequately describes the experimental data at relatively low pressures and fails to account for the decrease in the plasma density at pressures higher than 10 torr. The simulations also predict the presence of a maximum in this dependence; however, it occurs at substantially higher pressures. This discrepancy cannot be a consequence of our assumption about a constant electron temperature (whereas the actual temperature varies throughout the plasma volume). The calculations [5] show that the dependence of T_e on the electron-beam energy deposition is very weak and the rate of electron–ion recombination also slightly depends on T_e under our experimental conditions. Estimates show that taking into account variations in the electron temperature may change the electron density by no more than 10–20%. The observed discrepancy between the experiment and theory is probably related to the presence in the plasma of dusty particles produced when the graphite surface of the gas-dynamic window is sputtered by the electron beam. This question requires separate investigation.

Figure 10 shows the axial profiles of the electron density calculated for both pure argon and argon with a small admixture (~0.1%) of air. It can be seen that even such a small admixture of air reduces the electron density by several times. It can also be seen that, at small distances from the point of beam injection, the plasma is highly nonuniform over the radius. However, as the distance from this point increases, the radial nonuniformity of the plasma significantly decreases.

8. CONCLUSIONS

(i) The density of a plasma produced in argon irradiated by a quasi-continuous electron beam has been measured under conditions where the gas temperature is a few times higher than room temperature. The plasma density has been determined as a function of the gas pressure and beam current.

(ii) A numerical model has been developed that self-consistently describes gas heating, the propagation of an electron beam in the gas and the chamber wall, and the production and loss of charged particles. The calcu-

lated results are in good agreement with the experimental data.

(iii) An analysis of collisional processes shows that, under our experimental conditions, the main channel for electron loss is dissociative recombination with molecular ions even when their density is lower than that of atomic ions. The electron loss rate depends linearly on the electron density and is determined by the conversion rate of the atomic ions into molecular ones.

(iv) Gas heating leads to a significant increase in the electron density in an argon plasma due to the conversion of molecular ions into atomic ones and, accordingly, to a decrease in the electron–ion recombination rate.

REFERENCES

1. B. F. Gordiets, A. I. Osipov, and L. A. Shelepin, *Kinetic Processes in Gases and Molecular Lasers* (Nauka, Moscow, 1980).
2. A. V. Eletskiĭ and B. M. Smirnov, *Physical Processes in Gas Lasers* (Énergoatomizdat, Moscow, 1985).
3. A. A. Ivanov and T. K. Soboleva, *Nonequilibrium Plasmochemistry* (Atomizdat, Moscow, 1978).
4. V. D. Rusanov and A. A. Fridman, *Physics of Chemically Active Plasmas* (Nauka, Moscow, 1984).
5. V. L. Bychkov, M. N. Vasil'ev, and A. S. Koroteev, *Electron-Beam Plasma: Generation, Properties, and Application* (MGOU, Moscow, 1993).
6. A. A. Valuev, A. S. Kaklyugin, G. É. Norman, *et al.*, Teplofiz. Vys. Temp. **28**, 995 (1990).
7. B. Grosswendt and E. Waibel, Nucl. Instrum. Methods Phys. Res. A **155**, 145 (1978).
8. S. V. Arlantsev, G. P. Mkheidze, A. A. Savin, and V. A. Skvortsov, Preprint No. 184 (Inst. of General Physics, USSR Acad. Sci., Moscow, 1987).
9. A. F. Akkerman, Yu. M. Nikitushev, and V. A. Botvin, *Solution of the Problems of Fast-Electron Transport in Matter by the Monte Carlo Method* (Nauka, Alma-Ata, 1972).
10. A. F. Akkerman, *Modeling of Charged-Particle Trajectories in Matter* (Énergoatomizdat, Moscow, 1991).
11. I. N. Moskalev and A. M. Stefanovskiĭ, *Plasma Diagnostics with Open Cylindrical Cavities* (Atomizdat, Moscow, 1985).
12. S. K. Srivastava, H. Tanaka, A. Chutjian, and S. Trajmar, Phys. Rev. A **23**, 2156 (1981).
13. D. Cvejanovic and A. Crowe, J. Phys. B **30**, 2873 (1997).
14. K. Tachibana, Phys. Rev. A **34**, 1007 (1986).
15. D. H. Madison, C. M. Maloney, and J. B. Wang, J. Phys. B **31**, 873 (1998).
16. J. Bretagne, G. Delouya, J. Godart, and V. Puech, J. Phys. D **14**, 1225 (1981).
17. A. Chutjian and D. C. Cartwright, Phys. Rev. A **23**, 2178 (1981).
18. L. R. Peterson and J. E. Allen, J. Chem. Phys. **56**, 6068 (1972).
19. D. A. Vroom and R. L. Palmer, J. Chem. Phys. **66**, 647 (1977).
20. D. Rapp and P. Englander-Golden, J. Chem. Phys. **43**, 1464 (1965).
21. V. F. Baranov, *Electron Radiation Dosimetry* (Atomizdat, Moscow, 1974).
22. L. Bakaleĭnikov, www.ioffe.ru/ES.
23. *Heat and Mass Transfer, Thermotechnical Experiment (Handbook)*, Ed. by V. A. Grigor'ev and V. M. Zorin (Énergoizdat, Moscow, 1982).
24. V. P. Il'in, *Numerical Methods for Solving Electrophysical Problems* (Nauka, Moscow, 1985).
25. E. Elson and M. Rokni, J. Phys. D **29**, 716 (1996).
26. S. Neeser, T. Kunz, and H. Langhoff, J. Phys. D **30**, 1489 (1997).
27. B. M. Smirnov, *Ions and Excited Atoms in Plasma* (Atomizdat, Moscow, 1974).
28. B. M. Smirnov, *Complex Ions* (Nauka, Moscow, 1983).
29. M. J. McEwan and L. F. Phillips, *Chemistry of the Atmosphere* (Halsted, New York, 1975; Mir, Moscow, 1978).
30. I. A. Kossyi, A. Yu. Kostinsky, A. A. Matveyev, and V. P. Silakov, Plasma Sources Sci. Technol. **1**, 207 (1992).
31. M. J. Kushner, J. Appl. Phys. **66**, 2297 (1989).

Translated by N.N. Ustinovskiĭ

Plasma Physics Reports, Vol. 31, No. 5, 2005, pp. 436–438. Translated from Fizika Plazmy, Vol. 31, No. 5, 2005, pp. 478–480.

BRIEF COMMUNICATIONS

Ignition of ECR Discharges in a Flaring Magnetic Field

A. V. Timofeev

Russian Research Centre Kurchatov Institute, pl. Kurchatova 1, Moscow, 123182 Russia

Received May 20, 2004

Abstract—It is shown that, due to the presence of the ponderomotive force, ECR discharges in low-density gases can be ignited in systems with a single magnetic mirror (i.e., with a flaring magnetic field) when the electron mean free path substantially exceeds the system length. The discharge ignition conditions are determined.

1. Some types of devices for etching microchips, for isotope separation, etc., make use of ECR discharges in a flaring magnetic field, i.e., a magnetic field that varies monotonically along the device axis (see, e.g., [1–4]). A flaring magnetic field does not provide a magnetic mirror and thus cannot confine the electrons that are accelerated in the ECR interaction. Nevertheless, in such devices, gas breakdown occurs and the discharge is ignited at pressures that are so low (down to 10^{-5} torr) that the electron mean free path is much greater than the system length (0.1–1 m).

Breakdowns in a low-density gas in a magnetic mirror system were considered by Suvorov and Tokman [5]. In the present paper, it is pointed out that, in a system with a single magnetic mirror (i.e., with a flaring magnetic field), the escape of electrons from the discharge chamber may be prevented by the ponderomotive force exerted on them by the microwave field. As the ECR point is approached, the magnitude of this force increases sharply because of the growth of electron oscillations in the microwave field. The increase in the ponderomotive force is accompanied by a decrease in electron scattering in both elastic and inelastic (ionizing) collisions with atoms (see below). As a result, an avalanche of electrons trapped in the ponderomotive potential wells can develop.

2. In the initial stage of breakdown (before the plasma is produced), the microwave power is not absorbed within the vacuum chamber and a standing electromagnetic wave is established there. Let us analyze the electron motion in such a wave. The geometry of the problem is illustrated in Fig. 1.

For $\omega \approx \omega_e$, the right-polarized component of the electric field has an especially strong effect on the electron motion. The Hamiltonian that describes the motion of an electron with allowance for this effect has the form (see, e.g., [6])

$$H = \mu\Delta\omega_e + \frac{p_\parallel^2}{2m} + \frac{eE}{\omega}\sqrt{\frac{2\omega_e\mu}{m}}\cos\theta. \qquad (1)$$

Here, $\mu = \dfrac{p_\perp^2}{2m\omega_e}$, $\Delta\omega_e = \omega_e - \omega$, $\omega_e(z)$ is the electron gyrofrequency, ω is the microwave field frequency, $E(z)$ is the amplitude of the right-polarized component of the microwave field, θ is the phase of electron gyration with respect to the wave phase, and z is the distance along a magnetic field line.

We assume that the phase θ varies far more rapidly than do the quantities $\Delta\omega_e(z)$ and $E(z)$ along the electron trajectory. Under this assumption, we can introduce the transverse adiabatic invariant through the relationship

$$J_\perp = \frac{1}{2\pi}\oint\mu d\theta, \qquad (2)$$

where the quantity μ is determined from expression (1) in which the variables $p_\parallel$ and z, describing the longitudinal electron motion, are assumed to be fixed.

Relationship (2) determines the dependence of the transverse invariant $J_\perp$ on the parameters of the problem, $J_\perp = J_\perp(H, p_\parallel, \ldots)$. Resolving this dependence with respect to H, we obtain the Hamiltonian for the slow longitudinal motion of an electron:

$$H = J_\perp\Delta\omega_e + \frac{p_\parallel^2}{2m} - \frac{(eE)^2}{2m\omega\Delta\omega_e}. \qquad (3)$$

Here, the last term describes the effect of the ponderomotive potential on an electron in the presence of a steady magnetic field (see, e.g., [7]).

For electrons produced by the ionization of a neutral gas, the quantity $J_\perp$ depends on the point z_0 where an

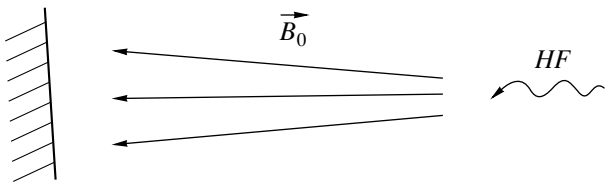

Fig. 1. Overall schematic of the experiments under discussion.

1063-780X/05/3105-0436$26.00 © 2005 Pleiades Publishing, Inc.

electron is produced and also on the initial values $\mu_0 = \frac{p_{\perp 0}^2}{2m\omega_e(z_0)}$ and θ_0. The energy of the bulk of the ionization-produced electrons does not usually exceed the ionization energy ε_{ion}. Under the condition $\varepsilon_{ion} \le \varepsilon_{HF} \approx mc^2\left(\frac{E}{B_0}\frac{\omega}{\Delta\omega_e}\right)^2$, the mean energy of the electrons is close to their oscillatory energy, $\varepsilon \approx \varepsilon_{HF}$; accordingly, we have $J_\perp \approx \frac{\varepsilon_{HF}}{\omega_e}$.

High-frequency electron oscillations in the microwave field give rise to the ponderomotive potential $U_{HF} = -\frac{(eE)^2}{2m\omega\Delta\omega_e}$, which is lower than the mean oscillatory energy by a factor of $\frac{\omega}{\Delta\omega_e}$. The ponderomotive force arises because the electric field amplitude $E(z)$ as well as the electron gyrofrequency $\omega_e(z)$ depend on the longitudinal coordinate. The first of these two factors predominates at sufficiently large distances from the resonance point, i.e., under the condition

$$\frac{\Delta\omega_e}{\omega} \ge \frac{c}{\omega L}, \tag{4}$$

where L is the characteristic spatial scale on which the steady magnetic field varies.

In a nonuniform magnetic field, an electron is subject not only to the ponderomotive force but also to the diamagnetic force. In expression (3), the diamagnetic potential is accounted for by the first term. If we assume that $J_\perp \approx \frac{\varepsilon_{HF}}{\omega_e}$ (see above), then we can see that, under condition (4), the ponderomotive force is stronger than the diamagnetic force. The total effective potential $U = U_{HF} + J_\perp\Delta\omega_e$ is shown schematically in Fig. 2 (it is assumed that the standing wave amplitude is independent of the z coordinate and that $\omega_e'(z) > 0$).

The concept of the ponderomotive potential is valid only under the adiabaticity condition, which implies that the variation in the microwave field amplitude $E(z)$ and in the quantity $\Delta\omega_e(z)$ along the electron trajectory is slower than that in the phase θ. By virtue of condition (4), the first of these two requirements is more stringent. It is satisfied under the inequalities $\Delta\omega_e \gg (a_\parallel\omega/c)^{1/2}$ and $\Delta\omega_e \gg v_\parallel\omega/c$, where $a_\parallel$ is the electron acceleration along the magnetic field. Since the longitudinal velocity of an electron oscillating in the ponderomotive potential well can be estimated in order of magnitude by $v_\parallel \approx (a_\parallel c/\omega)^{1/2}$, these inequalities are equivalent and can be reduced to a single inequality:

$$\frac{\Delta\omega_e}{\omega} \gg \left(\frac{E}{B_0}\right)^{2/3}. \tag{5}$$

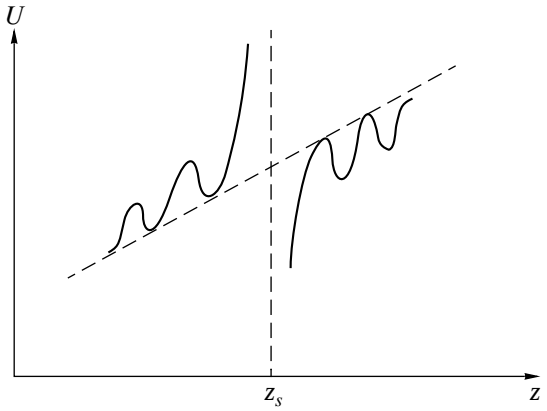

Fig. 2. Potential energy of an electron in a nonuniform magnetic field in the presence of a standing microwave: z_s is the coordinate of the ECR point.

As the microwave field amplitude increases, the secondary electrons begin to be trapped in the ponderomotive potential wells in the regions where $\Delta\omega_e \approx \Delta\omega_{e,1}$ (here, $\Delta\omega_{e,1}$ is the largest of the $\Delta\omega_e$ values satisfying conditions (4) and (5)). For this to occur, the electric field should increase to an amplitude such that $\frac{E}{B_0} \approx \left(\frac{\varepsilon_{ion}}{mc^2}\frac{\Delta\omega_{e,1}}{\omega}\right)^{1/2}$. As the microwave field amplitude increases further, the secondary electrons are confined over an increasingly wider region:

$$\frac{mc^2}{\varepsilon_{ion}}\left(\frac{E}{B_0}\right)^2 \ge \frac{\Delta\omega_e}{\omega} \ge \frac{\Delta\omega_{e,1}}{\omega}. \tag{6}$$

In Fig. 3, the region in which the conditions in question hold is hatched. It is assumed that the numerical values adopted for the parameters of the problem (see below) satisfy the inequality $\frac{c}{\omega L} > \left(\frac{\varepsilon_{ion}}{mc^2}\right)^{1/2}$.

3. Let us now discuss the development of an electron avalanche. To be specific, we consider a breakdown in argon, which is often used in experiments on discharge excitation. For estimates, we set $B_0 = 1$ kG, $L = 1$ m, and $p = 10^{-4}$ torr. In the ionization of argon, the energy of the bulk of the secondary electrons is ≤ 10 eV [8], regardless of the energy of the ionizing electrons. We set the microwave field amplitude equal to 10^3 V/cm. Under these conditions, the secondary electrons will be trapped in the ponderomotive potential wells in the region where $2 \times 10^{-2} \le \frac{\Delta\omega_e}{\omega} \le 1$.

According to [8, 9], the ionization cross section in the energy range from 30 eV to 1 keV is less than 10^{-16} cm^2. For an electron energy equal to the ionization energy, the elastic scattering cross section is about $\sigma_s \approx 2 \times 10^{-15}$ cm^2, and, in the energy range $\varepsilon \le 100$ eV,

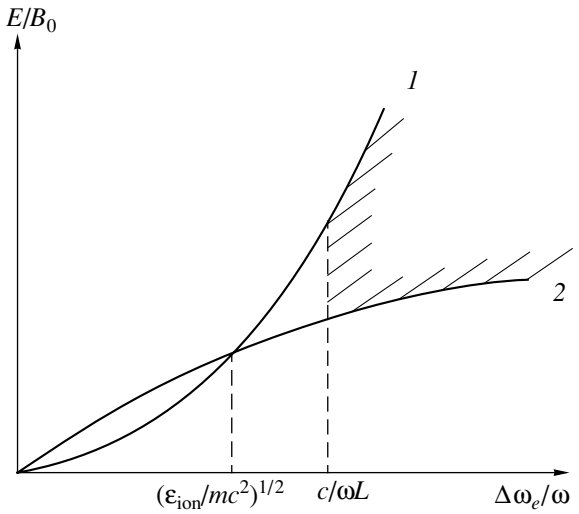

Fig. 3. Electron trapping region (hatched area) in ponderomotive potential wells for (*1*) $\frac{E}{B_0} = \left(\frac{\Delta\omega_e}{\omega}\right)^{3/2}$ and (*2*) $\frac{E}{B_0} = \left(\frac{\varepsilon_{ion}}{mc^2}\frac{\Delta\omega_e}{\omega}\right)^{1/2}$.

it is greater than the ionization cross section. However, as the energy increases, the elastic scattering cross section σ_s decreases according to the law $\propto 1/\varepsilon$ (see, e.g., [10, 11]). As a result, in the energy range $\varepsilon \geq 10^2$ eV, the ionization cross section exceeds the cross section for elastic scattering. An important point is that the scattering angle also decreases with increasing energy, $\vartheta_s \leq \sqrt{\frac{\varepsilon_{ion}}{\varepsilon}}$. An electron can escape from a ponderomotive potential well only when $\vartheta_s > \sqrt{\frac{\Delta\omega_e}{\omega}}$. Setting $\varepsilon = \varepsilon_{HF}$, we find that, when the left-hand inequality in condition (6) holds, elastic scattering does not lead to any significant escape of the electrons from the ponderomotive potential wells. The cross section for the excitation of Ar atoms is approximately one order of magnitude smaller than the elastic scattering cross section and possesses the same dependence on energy in the range $\varepsilon \gg \varepsilon_{ion}$ [8]. As for the scattering in inelastic (in particular, ionizing) collisions, the author failed to find references to exhaustive investigations of this subject in the literature. Based on the momentum conservation law, however, it can be stated that, since the energy of the secondary electrons does not exceed the ionization energy ε_{ion}, the mean scattering angle in ionization (which is the main scattering process) should be smaller than $\sqrt{\frac{\varepsilon_{ion}}{\varepsilon}}$. This is evidenced, in particular, by the results of calculating the ionization of Ar atoms by electrons with an energy of 4 keV (see [11]). These calculations show that, as the scattering angle increases from 0.025 to 0.1, the differential scattering cross section decreases by about two orders of magnitude.

The above analysis demonstrates that the effect of electron trapping in the ponderomotive potential wells can create conditions for breakdown in a low-density gas. The validity of the theory presented here can be checked in experiments with a discharge chamber one of whose ends absorbs microwaves. If the front end of the chamber is absorbing, the microwave will be a running wave and the ponderomotive potential will be a monotonic function of the longitudinal coordinate. In this case, the discharge should not develop. Gas breakdown is, however, possible in a discharge chamber in which microwaves are absorbed by the rear end. In this case, a standing microwave is established in the chamber and an electron avalanche can develop at its nodes.

Note that, if the secondary electron emission coefficient of the material of the ends of the discharge chamber is larger than unity, then the breakdown can be associated with electron accumulation (see, e.g., [12]). In this case, however, the ponderomotive potential should also have a substantial impact on the development of the discharge.

ACKNOWLEDGMENTS

This work was supported in part by the RF Program for State Support of Leading Scientific Schools, project no. 2004.2003.2.

REFERENCES

1. M. Matsuoka and K. Ono, Appl. Phys. Lett. **54**, 1645 (1989).
2. D. J. Trevor, N. Sadeghi, T. Nakano, *et al.*, Appl. Phys. Lett. **57**, 1188 (1990).
3. R. Hidaka, N. Tanaka, and Y. Kawai, J. Appl. Phys. **72**, 4461 (1992).
4. A. Compant la Fontaine and P. Louvet, Plasma Sources Sci. Technol. **8**, 125 (1999).
5. E. V. Suvorov and M. D. Tokman, Fiz. Plazmy **15**, 934 (1989) [Sov. J. Plasma Phys. **15**, 540 (1989)].
6. A. V. Timofeev, *Resonant Phenomena in Plasma Oscillations* (Fizmatlit, Moscow, 2000).
7. H. Motz and C. Y. M. Watson, Adv. Electron. Electron Phys. **23**, 153 (1967).
8. R. L. Peterson and J. E. Allen, J. Chem. Phys. **56**, 6068 (1972).
9. *Encyclopedia of Low-Temperature Plasma*, Ed. by V. E. Fortov (Nauka, Moscow, 2000), Vol. 1.
10. L. D. Landau and E. M. Lifshitz, *Quantum Mechanics: Non-Relativistic Theory* (Nauka, Moscow, 1963; Pergamon, Oxford, 1977).
11. G. F. Drukarev, *Collisions of Electrons with Atoms and Molecules* (Nauka, Moscow, 1978; Plenum, New York, 1987).
12. Yu. P. Raizer, *Gas Discharge Physics* (Nauka, Moscow, 1987; Springer-Verlag, Berlin, 1991).

Translated by I.A. Kalabalyk